Gregor Supp, Dipl.-Ing., BSc.

Bearing capacity of slender, screwed threaded rods - Experimental investigations and assesment for geotechnical applications

DOCTORAL THESIS

to achieve the university degree of

Doktor der technischen Wissenschaften

submitted to

Graz University of Technology

Supervisor

Univ.-Prof. Dipl.-Ing. Dr.techn. Roman Marte

Institute of Soil Mechanics and Foundation Engineering
Faculty of Civil Engineering

Univ.-Prof. Dipl.-Ing. Dr.-Ing. habil. Christian Moormann
Institute for Geotechnical Engineering, University of Stuttgart

Graz, April 2015

AFFIDAVIT

I declare that I have authored this thesis independently, that I have not used other than the declared sources/resources, and that I have explicitly indicated all material which has been quoted either literally or by content from the sources used. The text document uploaded to TUGRAZonline is identical to the present doctoral thesis.

Date

Signature

Acknowledgements

This dissertation would not have been possible without the consistent support and advice of Univ.-Prof. Dipl.-Ing. Dr.techn. Roman Marte. I cordially thank you for all the exciting academic discussions and conversations. I am thankful to Roman for providing the resources and the academic environment for creating this thesis.

I am grateful to Prof. Christian Moormann of University Stuttgart for reviewing this thesis.

I am grateful to Em.Univ.-Prof. Dipl.-Ing. Dr.techn. Stephan Semprich, former head of the Institute of Soil Mechanics and Foundation Engineering at Graz University of Technology. I am very grateful for being given the opportunity to work with Prof. Semprich during my first years on the Institute.

I thank all colleagues at the Institute of Soil Mechanics and Foundation Engineering for the very pleasant working environment and the many fruitful discussions. Here, I wish to highlight the colleagues of the Laboratory of the Institute for their endless support during the experiments. In particular I would like to thank Andreas Hasawend, Thomas Theißl, Daniel Vidonja and Morales-Calderon Odalys Del Carmen.

In closing, the author thanks the following associations and companies for their active respectively financial support of the experiments, in alphabetical order:

- alpS GmbH, Innsbruck, Austria *(Field test 1)*
- Austrian Society for Geomechanics ÖGG, Salzburg, Austria *(Lab test 1)*
- Energie Steiermark AG, Graz, Austria *(Field test 3)*
- Keller Grundbau Ges.mbH, Söding, Austria *(Field test 3)*
- Oberhofer Stahlbau Ges.m.b.H, Saalfelden, Austria *(Field test 1, 2, 3)*
- Otto Pregl Foundation, Vienna, Austria *(Lab test 1)*
- Spinnanker GmbH, Vienna, Austria *(Field test 1, 2, 3)*

Finally, I thank all my master students, especially Karin Poprask. I am very thankful to Karin for realizing the test set-up of the lab test 1.

Graz, April 2015 Gregor Supp

Kurzfassung

Das Tragverhalten von geschraubten und schlanken Gewindestäben – Experimentelle Untersuchungen und Bewertung für geotechnische Anwendungen

Diese Arbeit befasst sich mit schlanken und in den Untergrund geschraubten Gewindestäben. Die Gewindestäbe werden mittels einer modifizierten Eindrehmaschine und ohne Verwendung von Zementsuspension in den Untergrund geschraubt. Folglich befindet sich der Stab über die gesamte Länge in direktem Kontakt mit dem Lockergestein. Der untersuchte Gewindestab kommt im Wesentlichen für ein neues und innovatives geotechnisches Konstruktionselement zur Anwendung - dem Spinnanker. Der Spinnanker besteht aus Gewindestäben mit einem Durchmesser von 15 mm und aus einer Ankerkopfplatte. Durch die Ankerkopfplatte werden die Gewindestäbe fächerförmig mittels einer automatisierten Eindrehmaschine in den Untergrund eingeschraubt.

Die vertikale Zug-Tragfähigkeit von vertikal und geneigt eingebauten Gewindestäben wird in dieser Arbeit untersucht. Im Allgemeinen wurden folgende Fragestellungen (Qi) bearbeitet:

Q1: Wie ist das Last-Verformungsverhalten eines vertikal eingebauten Gewindestabes bei vertikalem Zug?

Q2: Wird für die Mobilisierung der Tragfähigkeit der Gewindestäbe auf Zug ein am Stab angehängter Erdkörper mobilisiert?

Q3: Welchen Einfluss hat der Stabeinbau auf die Tragfähigkeit?

Q4: Wie ist die Tragfähigkeit des geneigten Stabes bei vertikalem Zug?

Q5: Welche geotechnischen Anwendungen für den Spinnanker gibt es und ergibt sich die Tragfähigkeit des Gesamtsystems Spinnanker bei vertikalem Zug durch addieren der Tragfähigkeit der Einzelstäbe?

Zur Beantwortung der oben angeführten Forschungsfragen fanden Feld und Labor Untersuchungen statt. Für die Untersuchungen im Labor wurde ein transparenter Versuchsboden entwickelt auf Basis dessen Boden-Ankerstab-Interaktionen räumlich visualisiert werden konnten. Numerische Untersuchungen auf Basis der Diskreten Elemente Methode (DEM) fanden zusätzlich statt. Dafür wurde der Code PFC^{3D} verwendet.

Abschließend wurden fünf unterschiedliche Lastfälle für den Spinnanker und die resultierenden Lastfälle für den Einzelstab erarbeitet. Die Lastfälle Momentenbeanspruchung, vertikaler Zug und Böschungsstabilisierung wurden dabei im Detail untersucht. Hierfür fanden großmaßstäbliche Versuche satt. Ein auf Ausziehversuche des Einzelstabes basierendes Bemessungsdiagramm für den Spinnanker wurde zusätzlich erstellt.

Als Ergebnis des Lastfalls Böschungsstabilisierung wurde ein innovatives Stabilisierungs-Verfahren namens „Spinnanker Netting“ entwickelt. Eine Prototypanwendung des Verfahrens wird abschließend präsentiert.

Abstract

Bearing capacity of slender, screwed threaded rods – Experimental investigations and assessment for geotechnical applications

This thesis deals with slender threaded rods which are screwed with a modified screwing machine into a granular soil. The rods are consequently in direct contact with the granular soil over the full rod length, hence no concrete or cement mortar is used. The rod type is an essential compound of a new and innovative constructional element for geotechnical applications, called Spideranchor. A Spideranchor consists of an associated anchor head plate with inclined threaded holes and of a set of threaded rods with 15 mm diameter. The rods are installed fan-shaped into the subsoil by an automated screwing machine through the inclined threaded holes of the anchor head plate.

The load bearing behaviour of vertically and inclined installed single threaded rods which are vertically tension loaded is investigated in this thesis. In detail, the following five research questions (Qi) were addressed:

Q1: What is the magnitude of the vertical pull-out force and how does the force-displacement graph look like?

Q2: Is there a failure body attached to the threaded rod, mobilized by the applied vertical tension load (F_t)?

Q3: What is the influence of the installation process with respect to the bearing capacity?

Q4: What is the bearing capacity of inclined threaded rods which are vertically tension loaded?

Q5: What are possible applications for the Spideranchor, depending on load situations, and is it possible to describe the Spideranchor bearing capacity for vertical tension loads by adding all expected pull-out force values of each individual rod?

However, intense experimental investigations in the field and in the lab were executed in order to address the introduced research questions. A transparent soil model was developed which allowed a kind of three dimensional “insight view” into the complex behaviour of the tension loaded threaded rods. Numerical investigations based on the Discrete Element Method (DEM) were additionally carried out. The code PFC^{3D} was used therefore.

Finally, five fundamentally different load cases for the Spideranchor and the resultant load cases for the individual threaded rods are presented. The Spideranchor load cases tension and moment load as well as slope stabilization are analysed in a more detailed way. Full scale experiments were conducted therefore. A dimensioning diagram for the Spideranchor was finally developed and is based on in-situ pull-out tests of single rods.

However, as a result of the analysed load case slope stabilization, an innovative slope stabilization method called „Spideranchor Netting“ was developed and successfully tested. To conclude, a prototype application of the Spideranchor Netting is finally presented.

List of symbols and abbreviations

Capital letters

$(R_{s,cal})AVG$	[kN]	Mean value to the measured method
$(R_{t,cal})MIN$	[kN]	Lowest value to the measured method
$(R_{t,m})AVG$	[kN]	Mean value of the measured tensile resistance
$(R_{t,m})MIN$	[kN]	Lowest value of the measured tensile resistance
A	[mm^2]	Cross Section
A^*	[-]	Uplift capative factor
A	[m]	Open width
A_{10}	[%]	Ultimate elongation
A_s	[m²]	Pile shaft surface
$A_{s,i}$	[m²]	Pile shaft surface in the various strata
B	[m]	Diameter
C	[kN]	Cohesion force on the vertical slip surface
C_c	[-]	Curvature coefficient
C_F	[kN]	Vertical part of the cohesion force on the circular slip surface
C_u	[-]	Coefficient of uniformity
D	[m]	Depth
D	[-]	Soil Density
E_p	[kN/mm^2]	Young's modulus
E_s	[Mpa]	Oedometer modulus
F	[kN]	Force
F1		Field test 1
F2		Field test 2
F3		Field test 3
F_i		Field tests
F_m	[kN]	Ultimate load
F_{max}	[kN]	Maximum possible load
F_N	[N]	Contact normal force
F_{p0}	[kN]	Yield load
F_S	[kN]	Side friction force
F_t	[kN]	Tension load
$F_{t,d}$	[kN]	Design value of the applied tension load
$F_{t,k}$	[kN]	Characteristic value of the applied tension load
$F_{t,max}$	[kN]	Pull-out force
$F_{t,max,0}$	[kN]	Pull-out force of vertically installed rods
$F_{t,max,rough}$	[kN]	Pull-out force of rough rods
$F_{t,max,smooth}$	[kN]	Pull-out force of smooth rods
$F_{t,max,\alpha}$	[kN]	Pull-out force of the inclined rods (α)
G	[kPa]	Operational shear modulus of the soil
G	[kN]	Weight
G_{rod}	[kg/m]	Weight rod
H_x	[kN]	Resultant horizontal load

I_c	[-]	Consistency
I_d	[-]	Relative density
K_0	[-]	Earth pressure coefficient at rest
K_i	[-]	Coefficient of earth pressure
$K_{r,\delta=\varphi}$	[-]	Pull-out coefficient
$K_{r,\delta=\varphi,AVG,l\leq 2m}$	[-]	Average pull-out coefficient (l≤2m)
$K_{r,\delta=\varphi,l\leq 2m}$	[-]	Pull-out coefficient (l≤2m)
K_u	[-]	Uplift coefficient
L1		Lab test 1
L2		Lab test 2
L_i		Lab tests
M_y	[kNm]	Moment load in Y-direction
Q1		Research question one
Q2		Research question two
Q3		Research question three
Q4		Research question four
Q5		Research question five
Q_i		Research questions
Q_u	[kN]	Uplift force
R	[mm]	Thread radius
R	[N/mm^2]	Rough rod
R_m	[N/mm^2]	Tensile strength
$R_{p0,2}$	[kN]	Yield strength
$R_{s,k}$	[kN]	Characteristic value of the pile shaft resistance
R_t	[kN]	Tension pile resistance
$R_{t,0}$	[kN]	Pull-out resistance of vertically installed rods
$R_{t,0,l=2m}$	[kN]	Pull-out resistance of a vertically installed and 2 m long single rod
$R_{t,0,li}$	[kN]	Pull-out resistance of a vertically installed single rod
$R_{t,d}$	[kN]	Design value of the resistance to an tension force
$R_{t,d,Sp}$	[kN]	Design pull-out resistance of a Spideranchor
$R_{t,k}$	[kN]	Characteristic value of the resistance to an tension force
$R_{t,k,0}$	[kN]	Characteristic pull-out resistance of a vertically installed single rod
$R_{t,k,0,l=2m}$	[kN]	Characteristic pull-out resistance of a 2 m long and vertically installed single rod
$R_{t,k,l=2m}$	[kN]	Characteristic pull-out resistance of a 2 m long single rod
$R_{t,k,VI}$	[kN]	Characteristic pull-out resistance of the Spideranchor VI
$R_{t,k,XII}$	[kN]	Characteristic pull-out resistance of the Spideranchor XII
$R_{t,k,\alpha}$	[kN]	Characteristic pull-out resistance of the inclined threaded rods

$R_{t,\alpha}$	[kN]	Pull-out resistance of the inclined threaded rods
S		Smooth rod
S_r	[-]	Saturation
V_{mob}		Mobilized Volume
V_z	[kN]	Resultant vertical load
W	[kN]	Weight of anchor
Z		Vertical rod axis

Small letters

a	[mm]	Thread height
a	[kN/m²]	Adhesion
b	[mm]	Width
c	[mm]	Thread distance
c	[m/sec]	Speed of light in vacuum
c´	[kN/m^2]	Cohesion
c_a	[kN/m^2]	Adhesion
d	[mm]	Diameter
d_{10}	[mm]	Grain size diameter at 10 mass per cent
d_{30}^2	[mm]	Grain size diameter at 30 mass per cent
d_{50}	[mm]	Grain size diameter at 50 mass per cent
d_{60}	[mm]	Grain size diameter at 60 mass per cent
d_H	[mm]	Core- diameter
d_V	[mm]	Core- diameter
e_r	[kN]	Radial earth pressure force
h	[m]	Height
h_{layer}	[m]	Layer height
k_f	[m/s]	Permeability
k_N	[N/m]	Particle normal stiffness
k_S	[N/m]	Particle shear stiffness
l	[m]	Length
l_0	[m]	Bonded length
$l_{INSTALLED}$	[m]	Installed length
l_{rod}	[m]	Rod length
m%	[%]	Mass per cent
n	[-]	Porosity
n_bond	[N]	Contact bond normal strength
n_D	[-]	Refractive index of a material for 20°C
$n_{D,25}$	[-]	Refractive index of a material for 25°C
n_{ip}	[-]	Interparticle porosity
$n_{max,ip}$	[-]	Maximum interparticle porosity
$n_{min,ip}$	[-]	Minimum interparticle porosity
n_p	[-]	Particle porosity
n_{pt}	[kN]	Pressure ring force
$n_{rod,\alpha}$		Amound of inclined rods with angle α
n_{test}		Amound of piles/rods to be tested on the field

n_{tot}	[-]	Total porosity
n_{α}	[kN]	Vertical shell weight force
o	[m]	Distance
p'_0	[kPa]	Average effective normal pressure
pb_k_n	[Pa/m]	Parallel bond normal stiffness
pb_k_s	[Pa/m]	Parallel bond shear stiffness
pb_$n_{strength}$	[Pa]	Parallel bond normal strength
pb_radius	[-]	Parallel bond radius multiplier
pb_$s_{strength}$	[Pa]	Parallel bond shear strength
ph 1		Phase one
ph 2		Phase two
q_s	[kPa]	Constant surface friction
$q_{s,i}$	[kPa]	Constant surface friction in the various strata
r	[mm]	Radius
r_{rod}	[mm]	Rod radius
r_{tube}	[mm]	Tube radius
$r_{tube,n}$	[mm]	Tube radius after experiment
s		Interface zone
s	[-]	Shape factor
s_bond	[N]	Contact bond shear strength
t	[m]	Deepness
t_1	[sec]	Time 1
t_2	[sec]	Time 2
u	[mm]	Horizontal displacements
u_{max}	[mm]	Maximum displacements
u_N	[mm]	Particle overlap
u_P	[mm]	Settlement of the Spideranchor plate
u_r	[mm]	Radial displacements
u_T	[mm]	Heaving of the Spideranchor plate
u_x	[mm]	Translational displacement in direction of the X-axis
u_Y	[mm]	Translational displacement in direction of the Y-axis
u_z	[mm]	Vertical displacements
v	[m/sec]	Speed of light in the tested material
v		Vertical
v_z	[m/sec]	Vertical speed
w	[m]	Width
x	[m]	Horizontal distance
z	[m]	Depth

Greek letters

v	[mm^2/s]	Kinematic viscosity
α	[°]	Inclination to the vertical axis
α_s	[°]	Angle of incidence

β	[°]	Opening angel
β_s	[°]	Angle of refraction
γ'	[kN/m^3]	Effective soil weight
γ_d	[kN/m^3]	Dry weight density
γ_F	[kN/m^3]	Wet weight density
γ_i	[-]	Partial safety factor
γ_M	[kN/m3]	True weight density
γ_s	[kN/m^3]	Particle weight density
$\gamma_{s,t}$	[-]	Factor of safety for shaft friction resistance to an tension load
Δ	[-]	Difference operator
δ_f	[°]	Interface friction angle
Δr	[mm]	Radial expansion due to pile loading
$\Delta\sigma'_r$	[kPa]	Radial stress during the pile loading process
ε_{45}	[µm/m]	Inclined (45°) strains
ε_{rad}	[µm/m]	Radial strains
$\varepsilon_{rad,AVG}$	[µm/m]	Average value of radial strains
ε_v	[µm/m]	Vertical strains
η	[kg/s*m]	Dynamic viscosity
$\eta_{P,t}$	[-]	Model factor
Θ_i	[-]	Group factor
Θ_{VI}	[-]	Group factor for Spideranchor VI
Θ_{XII}	[-]	Group factor for Spideranchor XII
λ	[-]	Slenderness ratio
λ_l	[nm]	Wave length
μ	[-]	Particle friction
μ_{rod}	[-]	Rod particle friction
μ_{soil}	[-]	Soil particle friction
ξ_1	[-]	Correlation factor related to the number of piles testet
ξ_2	[-]	Correlation factor related to the number of piles testet
ξ_3	[-]	Correlation factor depend on the number of profiles of tests
ξ_4	[-]	Correlation factor depend on the number of profiles of tests
ρ_d	[g/cm^3]	Dry density
σ	[mN/m]	Surface tension
$\sigma'_ø$	[kPa]	Hoop stress
σ'_r	[kPa]	Radial stresses
σ'_v	[kPa]	Effecitve vertical stresses
$\sigma_{h,0}$	[kPa]	Earth pressure at rest
σ_h'	[kPa]	Effective horizontal stresses
σ_z	[kPa]	Vertical stresses
τ_f	[kPa]	Local shear stresses at failure
τ_x	[kPa]	Shear stresses
φ'	[°]	Internal friction angle

Abbreviations

2D	Two dimensional
3D	Three dimensional
AP	Alpinanchor
ASAP	Accelerated Surface Area and Porosimetry
AVG	Average value
BEM	Boundary Element Method
CCD	Charg-coupled Device
CPT	Cone Penetration Test
CPU	Central Processing Unit
DEM	Discrete Element Method
DPL	Dynamic probing - light
FEM	Finite Element Method
FOS	Factor of Safety
fps	Frames per second
ICP	Imperial College model pile
LL	Load level
max	Maximum
min	Minimum
MP	Megapixel
MP	Measurement Points
PFC	Particle Flow Code
PIV	Particle Image Velocimetry
PTFE	Polytetrafluoroethylene
PVC	Polyvinylchloride
SLS	Serviceability Limit State
SPT	Standard Penetration Test
SR	Investigations based on single rod pull-out tests
ULS	Ultimate Limit State

Summary

1 Introduction

1.1 General

Slender threaded rods are hot rolled, high strength thread bars with a high relation of the rod length divided by the diameter of the rod. In geotechnical engineering, and especially in ground engineering, this kind of steel rods is mainly applied as reinforcement for e.g. bored piles according to ÖNORM B 4440 (2001), micro piles according to ÖNORM EN 14199 (2013), or displacement piles according to ÖNORM EN 12699 (2013).

A basic construction method for micro piles is grouting the space between the threaded rod and the surrounding soil caused by the installation process with cement mortar, and also re-grouting it if necessary. In case of a composite displacement pile the threaded rod holds profiles which are driven into the subsoil together - for instance, hollow tubes with constant length depending on the pile producer. The space between the threaded rod and the hollow tube is finally filled with concrete or cement mortar. However, the threaded rods are neither used for the drilling process itself nor for the pile driving process of composite displacement piles. For both pile types, the micro- and the displacement pile, the threaded rods are usually not in direct contact with the subsoil.

This thesis deals with slender threaded rods which are screwed into granular soil with a modified screwing machine. Consequently, the rods are in direct contact with the granular soil over the full rod length, hence no concrete or cement mortar is used.

Until now, only little research with respect to the load bearing behaviour of these rods or of a set of these rods has been done and it has mostly been published by the author of this thesis himself, e.g. Fink and Supp (2008), Supp, Semprich, Breymann, Deutinger, Ghetta, Katzenbach, Kolymbas, Leppla, Mayrhofer and Zangerl (2010), Mayrhofer, Oberhofer, Deutinger, Zangerl, Ghetta, Katzenbach, Leppla, Semprich, Supp, Kolymbas and Breymann (2010), Supp and Semprich (2010), Supp and Semprich (2012), Lienhart, Lackner, Supp and Marte (2013), Marte, Supp and Lienhart (2014), Supp, Poprask and Marte (2014), Supp and Marte (2014).

The load bearing behaviour of vertical and inclined threaded rods with a vertical tension load is investigated in this thesis. Yet, time-dependent behaviour, e.g. creeping, and the load bearing behaviour in fine grained, soft soil is not subject of this research. The key subject of research is the load bearing behaviour in coarse grained soil.

Several threaded rod types with different geometrical properties, e.g. diameter or thread and different physical properties, e.g. strength of the material, are available on the market, depending on the application. The threaded rod type which is investigated in this thesis is an essential element of a new constructional element for geotechnical applications. Both the threaded rod and the new constructional element are introduced in the following chapters.

1.2 Threaded rod

The main subject of research in this thesis is the hot rolled, threaded steel rod of the type SAS 900/1100 FA, produced by "*Stahlwerk Annahütte*", Germany, Tab. 1, Fig. 1.

Tab. 1: Threaded rod properties, type SAS 900/1100 FA, Stahlwerk Annahütte (2011)

Geometrical properties			Physical properties		
Diameter	d [mm]	15.0	Weight	G_{rod} [kg/m]	1.41
Core diameter	d_H [mm]	14.8	Yield strength	$R_{p0,2}$ [N/mm²]	900
Core diameter	d_V [mm]	14.7	Tensile strength	R_m [N/mm²]	1100
Cross section	*A* [mm²]	173	Yield load	F_{p0} [kN]	156
Thread height	*a* [mm]	1.0	Ultimate load	F_m [kN]	190
Thread distance	*c* [mm]	10.0	Ultim. elongation	A_{10} [%]	7
Thread width	b [mm]	4.8	Young's modulus	E_p [kN/mm²]	195
Thread radius	*R* [mm]	1.5			
Inclination	Ψ [°]	78.5			

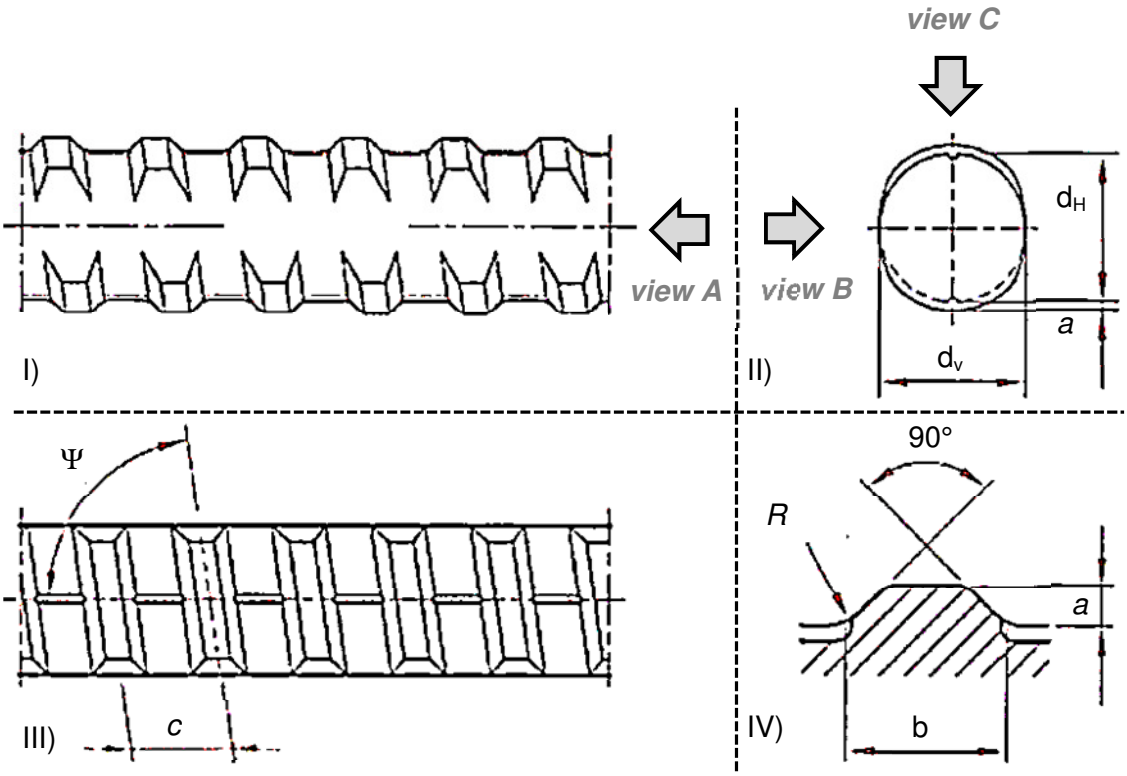

Fig. 1: Threaded rod geometry, type SAS 900/1100 FA, modified after Stahlwerk Annahütte (2011), I) longitudinal direction (view B), II) cross section (view A), III) longitudinal direction (view C), III) thread geometry (cross section)

The tip of the rod is inclined with 45°. For the installation process, a modified screwing machine is used. The threaded rod is screwed clockwise, through a plate or a bushing where an inner thread is included into the granular soil until the final depth (z) is reached, Fig. 2.

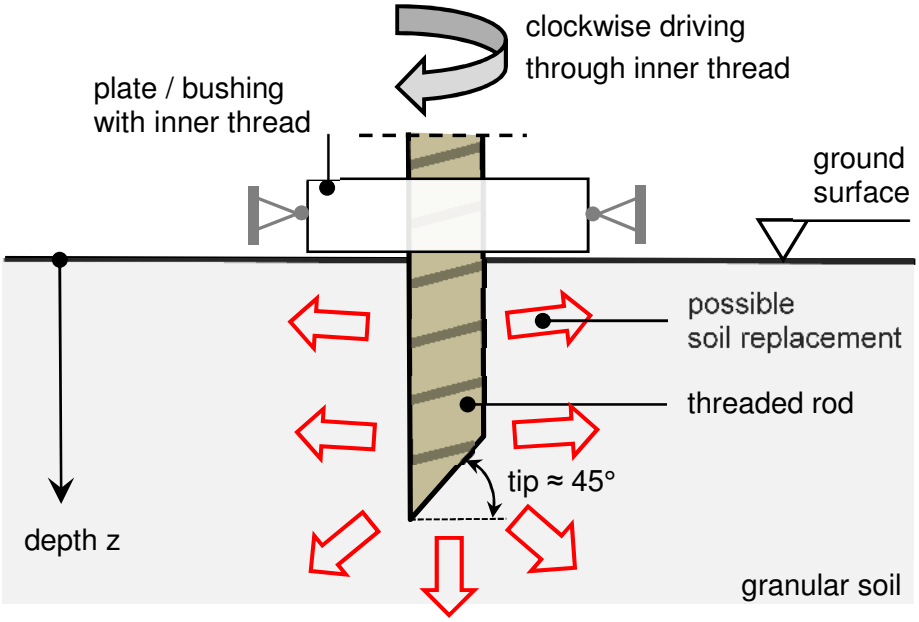

Fig. 2: Schematic sketch of the threaded rod installation process

The introduced threaded rod is an essential component of a new constructional element for variable geotechnical applications, called Spideranchor.

1.2.1 Spideranchor

A Spideranchor is a new, highly innovative structural element for geotechnical applications and has been developed by the steel company *Stahlbau Oberhofer*, Saalfelden, Austria.

The Spideranchor consists of an associated anchor head plate with inclined threaded holes, currently 30° and 45° normal to the plate and of threaded rods from the type SAS 900/1100 FA, Stahlwerk Annahütte (2011), with a diameter of 15 mm, Fig. 3. The rods are installed fan-shaped into the subsoil by an automated screwing machine of the type LDO-06E by "*Lösomat*", Austria, operating voltage 220 V, weight ≈ 9 kg with a maximum torque of ≈ 550 Nm - through the inclined threaded holes of the anchor head plate, Fig. 4. Currently two Spideranchor systems are available: System VI and System XII. The difference between these systems is defined by the amount of threaded rods and the diameter of the anchor head plate – system XII: Ø = 380 mm and system VI: Ø = 280 mm. For the system XII, six rods are installed inclined with 30° and the other six rods with 45° normal to the head plate and for the system VI three rods with 30° and the other three rods with 45°. To avoid uplift from the

anchor head plate during the installation process, the plate is fixed with a fit up aid called Alpinanchor on the surface. The length of the rods is usually constant for all rods and differs between 2 to maximum 8 m, depending on the application.

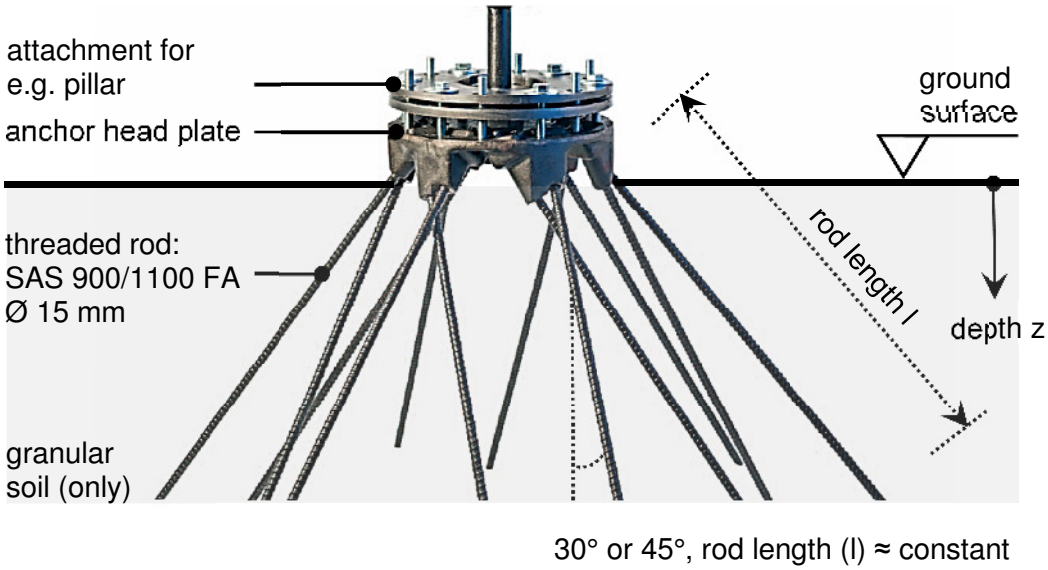

Fig. 3: Spideranchor system XII

The Spideranchor can be loaded immediately after the installation process because no concrete or slurry is needed. For that reason the anchor plate and the rods can easily be removed if needed. Geotechnical applications based on the Spideranchor technology are presented in the Chapter 6 of this thesis.

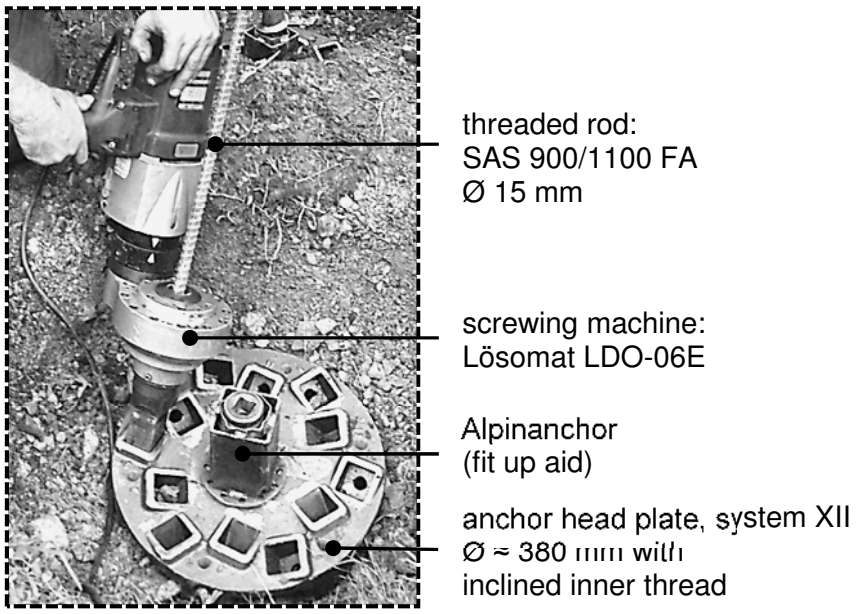

Fig. 4: Installation process, Spideranchor System XII

2 Literature review, summarising assessment, open issues, methodology and outline of the thesis

2.1 General

Before starting with a literature review on the load bearing behaviour of threaded rods with vertical tension load which are screwed in to the subsoil, a classification of these rods with respect to tension- loaded constructional elements in foundation engineering, e.g. anchorage and foundation piles, is done. Anchorage is used for instance for building pits, retaining structures or slopes. There are basically three categories of anchorage according to the Austrian national standard ÖNORM B 1997-1-1 (2013) and Martak, Breit (2014), Fig. 5:

a) Micro-piles and displacement piles which are grouted and behave like single elements. The tension load is transferred into the subsoil through surface friction over the full pile length, ÖNORM EN 14199 (2013), ÖNORM EN 12699 (2013).
b) Grouted anchors which can be pre-stressed. A free steel section is therefore installed. The load is transferred through surface friction over the grouted section only into the subsoil, ÖNORM EN 1537 (2000).
c) Nails are bar-shaped elements and behave as soil reinforcement which bonds the soil body to a monolithic body, depending on the nail spacing (common spacings are: 1.5 * 1.5 to 1.75 * 1.75 m), ÖNORM EN 14490 (2010). A soil nail wall does not behave like a single constructional element, it acts collectively.

The threaded steel rods which are investigated in this thesis do not have a free steel section, they do not act collectively and are not grouted, Fig. 5. Therefore, the rods are not classified into the group of anchorage as mentioned above. Therefore, the rods are classified into the group of foundation piles (with tension load) consistent with the ÖNORM B 1997-1-1 (2013); respectively, similar behaviour is expected. Figure 6 illustrates the basic classification of foundation piles after EA-Pfähle (2014) with special attention to displacement piles.

In EA-Pfähle (2014), bored piles are characterised "… *by ground being loosened and transported during installation. The excavated ground volume can correspond to the total or part of the pile volume…"*. Displacement piles are, according to EA-Pfähle (2014), *"…characterised by being installed without excavation or removal of soil material …"*.

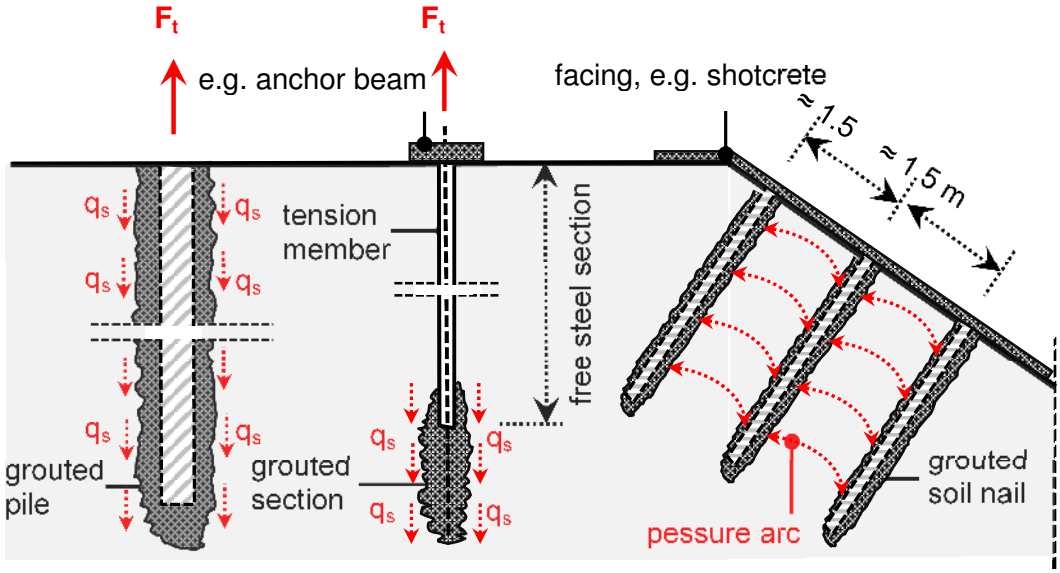

F_t: tension load; q_s: surface friction

Fig. 5: Schematic sketch of anchorage elements according to ÖNORM B 1997-1-1 (2013) and Martak, Breit (2014)

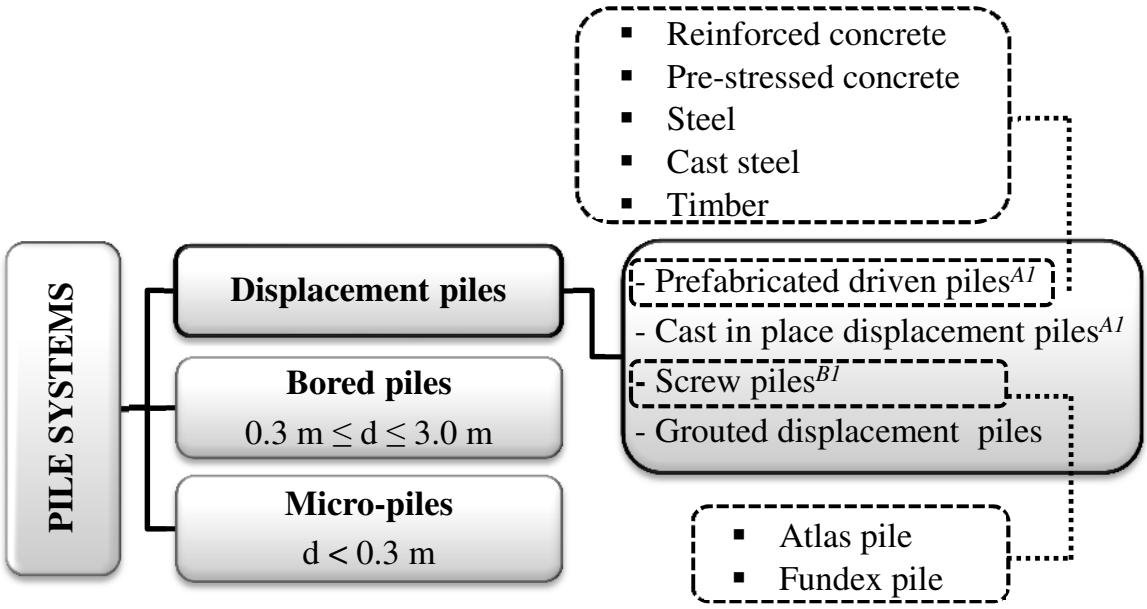

A1: installation by driving
B1: installation by screwing / pressing

Fig. 6: Overview of foundation pile systems with special attention to displacement piles according to EA-Pfähle, Recommendations on Piling (2014)

According to ÖNORM EN 14199 (2013) micro-piles are piles where a drill head is needed for the installation process and the diameter range is less than 0.3 m.

However, taking the classification after EA-Pfähle (2014) into account, it is most reasonable that the threaded rods investigated in this thesis are classified into the group of prefabricated, full displacement screw piles, Fig. 6.

To summarize the state of knowledge and to point out open research questions a literature review on the load bearing behaviour of tension piles in coarse grained soil is done.

2.2 Literature review on design approaches for vertically installed tension piles

2.2.1 General

EUROCODE 7 mentions three different options of how to design a pile:

- Based on load tests e.g. static, dynamic
- Based on recognized values given in a set of tables e.g. empirical data depending on CPU or SPT tests
- Based on calculations e.g. analytical, numerical

EUROCODE 7 design rules are introduced in chapter 2.2.2.

Poulos (1989) counts three main categories for predicting the load bearing behaviour of a pile:

1. Empirical methods, e.g. correlations from CPU or SPT tests as well as from soil mechanical parameters, e.g. relative density of the soil, to the pile friction (q_s)
2. Simplified mechanical theories, based on soil mechanical principles and the consideration of equilibrium conditions
3. Numerical methods, e.g. FEM, BEM, DEM

Intense comprehensive literature review on empirical and simplified mechanical theories for predicting the load bearing behaviour of primarily pressure-loaded displacement piles can be found in Witzel (2004).

In chapter 2.2.3, a literature review on simplified mechanical theories for predicting the load bearing behaviour of tension piles can be found. Because of almost no knowledge about the bearing capacity of the threaded rods, empirical methods to predict the load bearing behaviour are not considered.

In order to describe the effect of installation on the bearing capacity, a literature review on displacement pile installation effects is done in chapter 2.2.4.

2.2.2 Design based on EUROCODE 7

Two types of limit states must be checked according to EUROCODE 7 (2004, +AC: 2009) to design a tension pile:

1) Ultimate limit state (ULS) to check the safety level against failure e.g. pull-out of the pile
2) Serviceability limit state (SLS) to verify service requirements e.g. allowable displacements due to an applied load

This thesis deals mainly with research of the ULS for tension loaded, slender, screwed threaded rods.

According to EUROCODE 7 (2004, +AC: 2009) the bearing capacity of a tension pile (R_t) in the ULS is covered by surface friction (q_s) on the pile shaft (A_s). This is caused e.g. by a axial tension force (F_t) applied at the top of the pile, Fig. . The average surface friction (q_s) is assumed to be constant along the embedded pile length.

$$R_{t,k} = \sum A_{s,i} * q_{s,i} = R_{s,k} \tag{1}$$

$R_{t,k}$	characteristic value of the resistance to a tension force
$R_{s,k}$	characteristic value of the pile shaft resistance
$A_{s,i}$	pile shaft surface in the various strata
$q_{s,i}$	characteristic and constant pile friction in the various strata

In the ULS the design of a tension pile can be done as follows, EUROCODE 7 (2004, +AC: 2009):

a) Based on characteristic values of the tension pile resistance determined with pile load tests on the field:

$$R_{t,k} = MIN\left\{\frac{(R_{t,m})AVG}{\xi_1}, \frac{(R_{t,m})MIN}{\xi_2}\right\} \tag{2}$$

$(R_{t,m})$AVG	mean value of the measured tensile resistance
$(R_{t,m})$MIN	lowest value of the measured tensile resistance

ξ_1	correlation factor related to the number of piles tested, for details and given values see table 8, ÖNORM B 1997-1-1 (2013)
ξ_2	correlation factor related to the number of piles tested for details and given values see table 8, ÖNORM B 1997-1-1 (2013)

b) Based on characteristic values of the tension pile resistance determined with results from ground tests, e.g. correlation between the results of the SPT and the pile friction in the various strata:

$$R_{t,k} = MIN\left\{\frac{(R_{s,cal})AVG}{\xi_3}, \frac{(R_{s,cal})MIN}{\xi_4}\right\} \quad (3)$$

$(R_{s,cal})$AVG	mean value to the measured method, e.g. correlations with SPT
$(R_{t,cal})$MIN	lowest value to the measured method, e.g. correlations with SPT
ξ_3	correlation factor depend on the number of profiles of tests, for details and given values see table A.10, EUROCODE 7 (2004, +AC: 2009)
ξ_4	correlation factor depend on the number of profiles of tests, for details and given values see table A.10, EUROCODE 7 (2004, +AC: 2009)

The design based on ground tests also covers the design based on physical models to predict the bearing capacity of a tension pile, which is in general based on soil properties. In such a case it may be necessary to apply equation 1 to calculate the characteristic value of the tension resistance. In order to determine the tension pile resistance based on a set of tables depending on results from ground tests it may also be necessary to apply equation 1.

The design value of the tension pile resistance in general is given:

$$R_{t,d} = \frac{R_{t,k}}{\left(\eta_{P,t} * \gamma_{s,t}\right)} \quad (4)$$

$R_{t,k}$	characteristic value of the resistance to a tension force
$R_{t,d}$	design value of the resistance to an tension force
$\gamma_{s,t}$	factor of safety for shaft friction resistance to an tension load, for details and given values see table A.7, ÖNORM B 1997-1-1 (2013)

$\eta_{P,t}$	model factor to ensure that the predicted resistance is sufficiently safe

The design value of the applied force is given:

$$F_{t,d} = F_{t,k} * \gamma_i \quad (5)$$

$F_{t,d}$	design value of the applied force
$F_{t,k}$	characteristic value of the applied force
γ_i	factor of safety, depends on design situation and the duration of the applied force

Finally, the design for the ULS can be done as follows:

$$F_{t,d} \leq R_{t,d} \quad (6)$$

$F_{t,d}$	design value of the applied force
$R_{t,d}$	design value of the resistance to a tension force

Anyway, it is pointed out that presently at this time, EUROCODE 7-based pile design is only possible in Austria if the design is based on pile load tests in the field. For a design based on results of ground tests see ÖNORM B4440 (2001) for bored piles.

According to EUROCODE 7, a design-based bearing capacity forecast, e.g. a design based on results of ground tests, has to be verified with pile load tests on the field. The amount of piles to be tested on the field (n_{test}) depends on the total amount of piles to be constructed and the complexity of the site ($1 < n_{test} > 2\%$).

2.2.3 Simplified mechanical theories

Basically two types of simplified mechanical theories to predict the load bearing behaviour of tension-loaded piles are available in the literature:

I. Taking especially interlocking effects (pile-soil) into account, mostly based on cavity expansion theory along the shaft
II. Assuming a mobilized failure body and applying equilibrium conditions to calculate the pull-out force

These theories are introduced in the following.

Theories based on interlocking (dilatation) effects:

Lehane et al. (1993) performed instrumented in-situ pile tests with driven displacement piles in sand, cone ended rigid steel piles; length: 6 m; diameter: 102 mm. He recognizes that at failure the local shear stress (τ_f) on the pile shaft follows the Coulomb failure criterion, depending on the effective radial stress(σ'_{rf}), the interface friction angle (δ_f) and adhesion (a):

$$\tau_f = \sigma'_{rf} * \tan(\delta_f) + a \tag{7}$$

The interface friction (δ_f) depends on the pile surface and the grain size (d_{50}) and can maximally reach the internal friction angle of the soil (φ') and the adhesion (a) maximum the cohesion (c') of the soil, König (2008). For rough piles the interface friction reaches the friction angle of the soil ($\delta_f = \varphi'$), Jardine et al. (1993). The effective radial stress (σ'_{rf}) during the state of failure is compounded of the radial stress after the installation process (σ'_{rc}) and the increased radial stress during the pile loading process ($\Delta\sigma'_r$), Lehane et al. (1993), Fig. 8:

$$\sigma'_{rf} = \sigma'_{rc} + \Delta\sigma'_r \tag{8}$$

Wernick (1978) developed an idealised model to illustrate the wedging effect of an axially loaded anchor being pulled out.

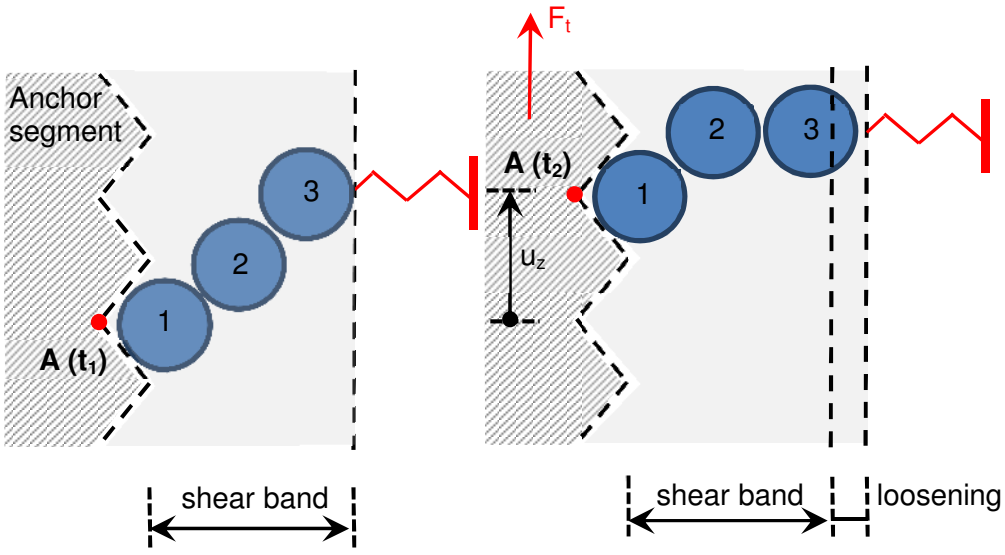

Fig. 7: Wedging effect caused by dilation of a shear band, modified after Wernick (1978), left: initial state (time: t_1) and right: after applying a tension load (time: t_2)

He observed that the vertical displacement of an anchor (u_z) due to an axial tension load (F_t) leads to a movement of soil particles in a thin shear band between anchor and soil, Fig. 7. These movements enforce an expansion of the shear band and the soil outside of the shear band, idealised by springs, is consequently densified. This leads to an increase of the radial stresses active on the anchor.

According to Lehane et al. (1993) the increase of the radial stress ($\Delta\sigma_r'$) due to the dilatant behaviour in the shear zone can be calculated depending on the radial expansion (Δr), the shear modulus (G) and the pile diameter (d), Fig. 8. The given equation is based on the cavity expansion theory, Boulon and Foray (1986).

$$\Delta\sigma_r' = \Delta r * \frac{4G}{d} \tag{9}$$

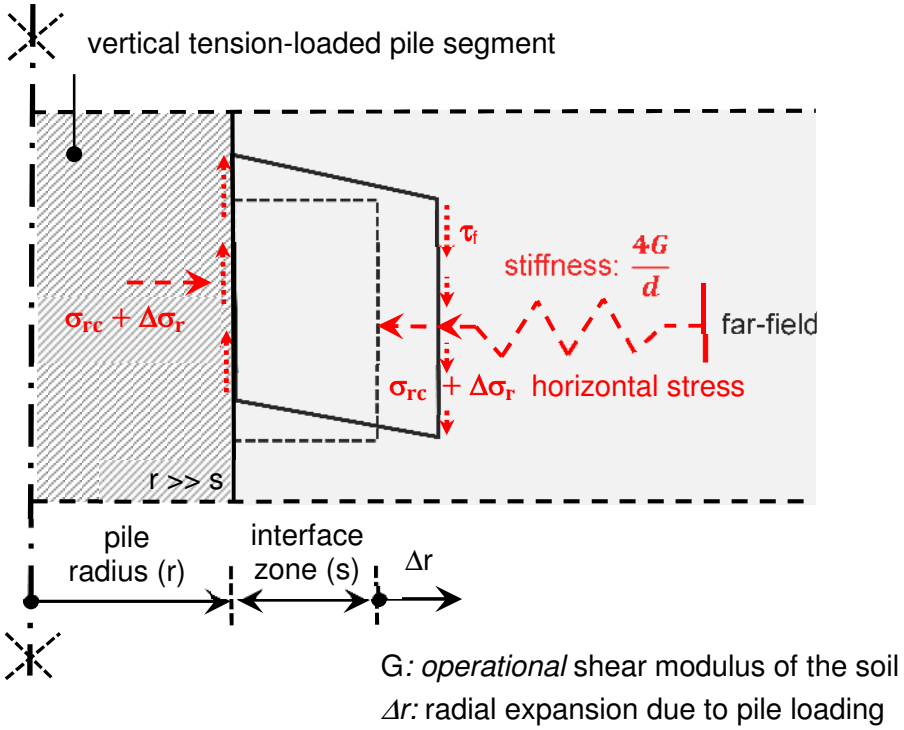

Fig. 8: Sketch of the pile-soil interface, modified after Lehane and White (2005)

The diameter of the pile is under the fraction line of the equation. For this reason the increase of the radial stresses due to dilatant behaviour is greater for piles with smaller diameter. Several authors e.g. Lehane, Gaudin and Schneider (2005), Marandi and Karimzadeh (2009) observed this phenomenon by conducting experiments.

Ostermayer and Werner (1972) observed the same kind of phenomenon by pulling out grouted anchors from dense to medium-dense sand. He back-calculated the average surface friction (q_s) from the pull-out force F_t, depending on the bonded length (l_0) of the tension member and the outer diameter (d) of the grouted anchor, Figure 9, Equation 10. However, no separation between the effects due to the installation process and the dilatant behaviour are given.

$$q_s = \frac{F_t}{d * \pi * l_0} \tag{10}$$

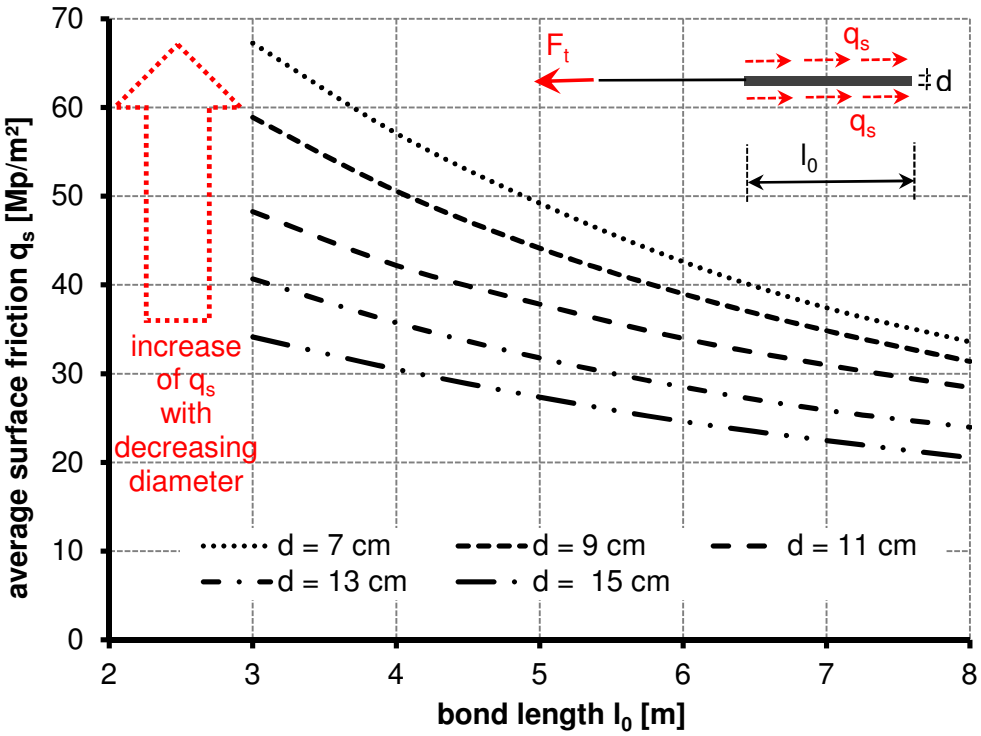

Fig. 9: Average surface friction (q_s) depending on bond length (l_0) and diameter (d) of grouted anchors in a dense to medium dense sand, modified after Ostermayer and Werner (1972)

Radial stress after the pile installation process (σ_{rc}') is not constant and changing with the embedded pile length. The stress depends on the installation process itself and the soil density. The installation process is basically distinguished between methods which replace the soil and which don't, Lehane et al. (1993).

Theories based on mobilized failure bodies:

Several authors e.g. Jelinek and Ostermayer (1964), Meyerhof and Adams (1968), Chattopadhyay and Pise (1986), Quarg-Vonscheidt (2000) have developed a design approach for axially loaded tension piles based on simplified mobilized failure bodies in the ultimate limit state (ULS).

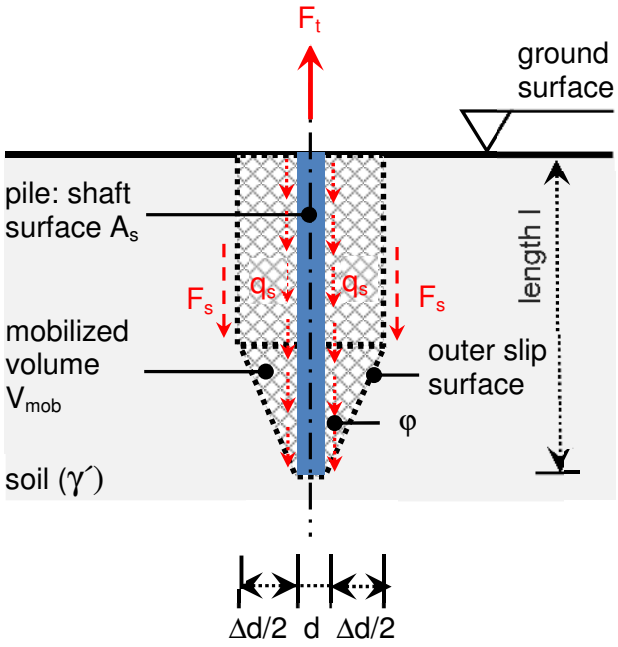

Fig. 10: Sketch of a possible, rotationally symmetric failure body in the ULS due to an axial tension load (F_t)

This mobilized failure body is basically, at least in most of the cases, lifted upwards with the pile. The volume (V_{mob}) is multiplied by the average effective soil weight (γ') and is assumed to be the resistance against the tension pile pull-out force (F_t).

$$R_t = \left[V_{mob} * \gamma' + \sum F_s\right] = \sum A_s * q_s \geq F_t \qquad (11)$$

The weight of the pile is often neglected. However, some authors are taking additional side friction forces (F_s) - active on the outer slip surface - into account to calculate the resistance against the pull-out force (F_t), Figure 10, Equation (11).

Table 2 shows a comparison of four different design approaches for tension piles with focus on mobilized soil volume and activated side friction forces on a possible slip surface. These four most- mentioned approaches in the literature are introduced in the following.

Tab. 2: Comparison of design approaches for tension-loaded piles

Author:	(year)	Assumptions: mobilized volume V_{mob}	side friction F_s
Jelinek and Ostermayer	1964	☑	☒
Meyerhof and Adams	1968	☑	☑
Chattopadhyay and Pise	1986	☑	☑
Quarg-Vonscheidt	2000	☑	☒

Jelinek and Ostermayer (1964) executed pull-out tests of displacement piles in a sand. They observed a mobilized soil body in the ultimate limit state (ULS) which is truncated cone shaped and lifted upwards, Figure 11. The opening angle (β) is between $\beta = 0$ ($l = \infty$) and $\beta = \varphi$ ($l = 0$). The final shape of the mobilized soil body depends on the pile length (l), the pile diameter (d) and the internal friction angle (φ´) of the surrounding soil. By assuming plane stress conditions they calculated the transferable shear stresses (τ_x) on the pile shaft with the help of Mohr´s circle, Equation. (12).

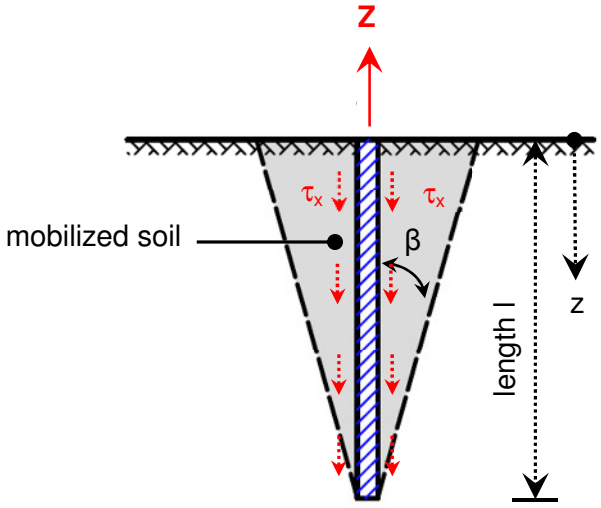

Fig. 11: Truncated cone shaped failure body which reaches the ground surface, after Jelinek and Ostermayer (1964)

Jelinek and Ostermayer suppose that in the ULS no side friction forces (F_s) on the slip surface are activated.

$$\tau_x = \sigma_z * \left[\frac{cos\,\varphi * sin\,\varphi + 2 * sin\,\varphi * sin\,\varphi * sin(\varphi - \beta)}{2 - cos^2\varphi - 2 * sin\,\varphi * sin\,\beta * cos(\varphi - \beta)}\right] \quad (12)$$

In case the slip surfaces reaches the ground surface the weight (*G*) of the truncated cone shaped sliding mass can be calculated with Equation (12) by knowing the opening angle (β).

$$G = Z = \gamma' * \ \pi * \left[(tan\,\beta * r * l^2) + \left(\frac{tan^2\beta}{3} * l^3\right)\right] \quad (13)$$

However, Marks (1997) pointed out that three-dimensional, rotational symmetric stress conditions on the pile shaft are reduced to two-dimensional plane stress conditions for calculating the shear stresses (τ_x). In addition, he noted that the β-inclined slip surface without side shear stress-resistance is kinematically questionable.

Meyerhof and Adams (1968) carried out a series of model uplift tests in loose and dense sand and in soft and stiff clay as well. In detail, plate anchor pull-out tests with a diameter (B) which varies from B ≈ 2.5 – 10 cm and slenderness ratios from ≈ 1-16. With visual observations they derived from the tests a mobilized failure body depending on the depth (*D*), Fig. 12. For small depths (*D*) the slip surface reaches the ground surface and for great depths (*D*) the slip surface does not reach the ground surface necessarily. The uplift force (Q_u) for *D* > H can be calculated with Equation (14). The uplift force is composed of the mobilized soil weight including the weight of the anchor (W) and the activated side friction forces on the slip surface. The side friction forces are calculated by assuming passive earth pressure on a vertical slip surface. However, the calculated side friction force is finally transferred to a friction force acting on a circular slip surface. This is done by introducing a shape factor (*s*). Meyerhof and Adams are further simplifying that the resultant cohesion force on the vertical slip surface (C) has approximately the same value as the vertical part of the cohesion acting on the circular slip surface (C_F), C ≈ $C_{F,vertical}$, Fig. 12.

The passive earth pressure coefficient is called uplift coefficient of earth pressure (K_u) and depends hardly on the friction angle (φ´) of the soil. The shape factor (*s*) depends on the ratio (H/B) respectively (*D*/B) for shallow depths and also from the friction angle (φ´) of the soil.

$$Q_u = \pi * B * c * H + s * \left(\frac{\pi}{2}\right) * \gamma' * B * (2D - H) * H * K_u * tan\varphi + W \quad (14)$$

It is pointed out that the experimental results by Meyerhof and Adams (1968) show uplift coefficients up to a value of seven in dense sand.

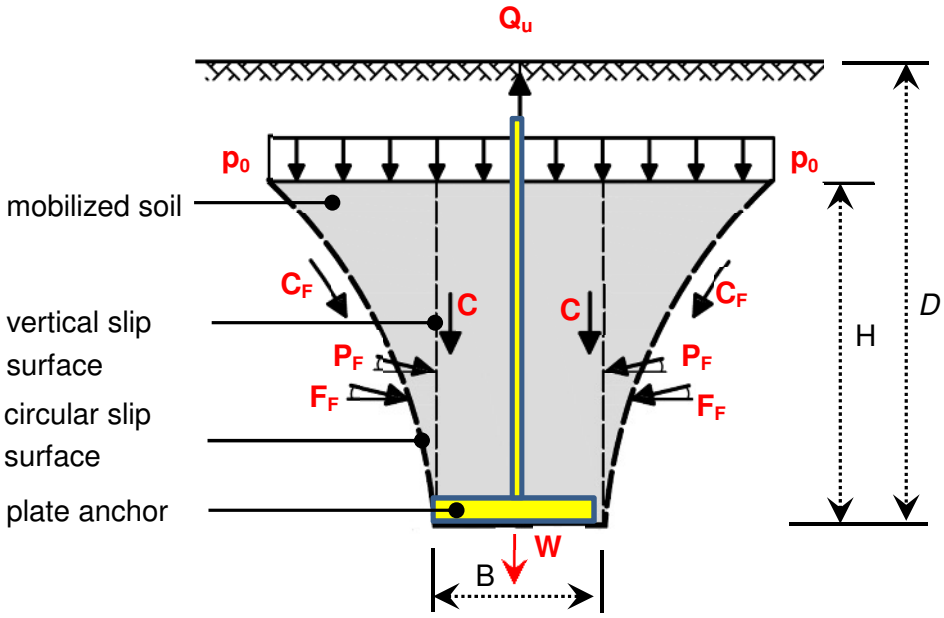

Fig. 12: Failure of soil above a plate anchor under tension load for great depth: $D > H$, Meyerhof and Adams (1968)

Full scale tests ($D \approx 0.3$ m and B ≈ 1.8 – 3.6 m) show reasonable agreement with the small scale experiments.

Based on the theory expressed by Meyerhof and Adams (1968), Meyerhof (1973) developed uplift coefficients (K_u) for piles which are axially loaded. He assumes that the mobilized soil mass has a similar shape like for plate anchors. The pull-out resistance (Q_u) can be calculated using equation (15), with the adhesion c_a, the interface friction angle δ, the average effective normal pressure p'_0, the embedded pile surface area A_s and the uplift coefficient K_u.

$$Q_u = (c_a + p'_0 * K_u * \tan(\delta)) * A_s \quad (15)$$

Meyerhof mentions that for driven piles the uplift coefficient (K_u) is greater. However, the given K_u values for bored piles are theoretical and bases on passive earth pressure theory, Fig. 13. A comparison with field and model tests was done where higher K_u values up to $K_u = 5$ ($\varphi' = 45°$) were recognized.

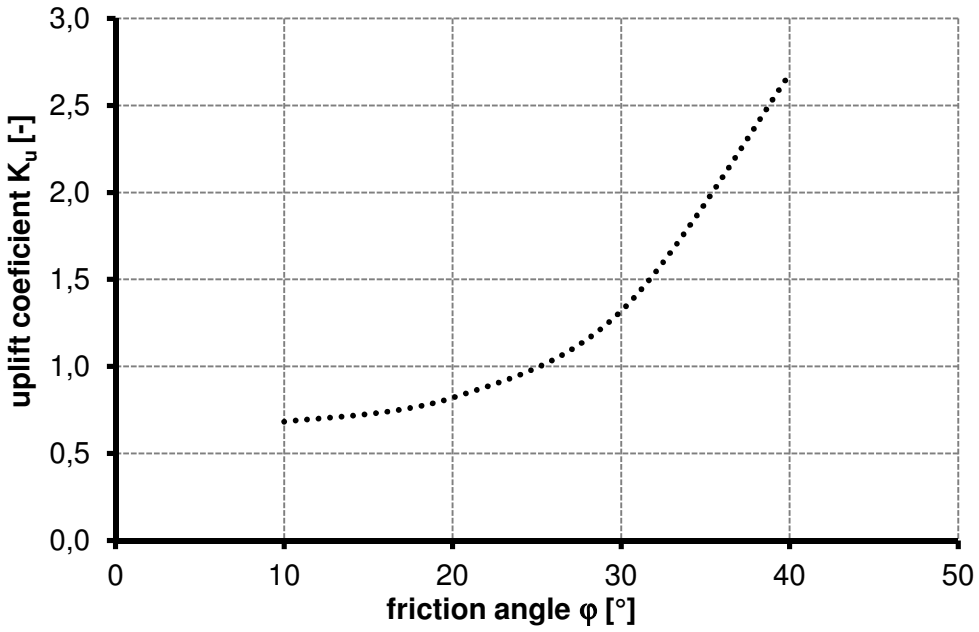

Fig. 13: Uplift coefficient for vertical bored piles according to Meyerhof (1973)

Chattopadhyay and Pise (1986) improved the approach of Meyerhof and Adams (1968) which resulted in an analytical model to calculate the pile pull-out force (F_t). The analytical model bases on a mobilized soil body for the ultimate limit state (ULS). The related pull-out force (F_t) is the result of friction resistance (F_s) active on the slip surface of the mobilized and axisymmetric soil body, the weight of the soil body and the weight of the pile, Fig. 14. The shape of the failure surface depends on the slenderness ratio (λ=l/d) of the pile and is parallel to the pile surface at the end of the pile. For greater pile slenderness ratios and greater pile interface friction values (δ) the horizontal distance (x) on the ground level of the failure body increases and the length of the failure surface parallel to the pile too.

$$\frac{x}{d} = \frac{1}{2} + \left(\frac{2\delta}{50-\varphi}\right)^2 * \frac{e^{\left[-\lambda * \frac{(50-\varphi)}{2} * \delta\right]}}{\lambda * \tan\left(45 - \frac{\varphi}{2}\right)} + \frac{2\delta}{(50-\varphi) * \tan\left(45 - \frac{\varphi}{2}\right)} * e^{\left[\frac{-\lambda*(50-\varphi)}{2\delta} * \left(1 - \frac{z}{l}\right)\right]} * * \left[\frac{z}{l} - \frac{2\delta}{(50-\delta)} * \frac{1}{\lambda}\right] \quad (16)$$

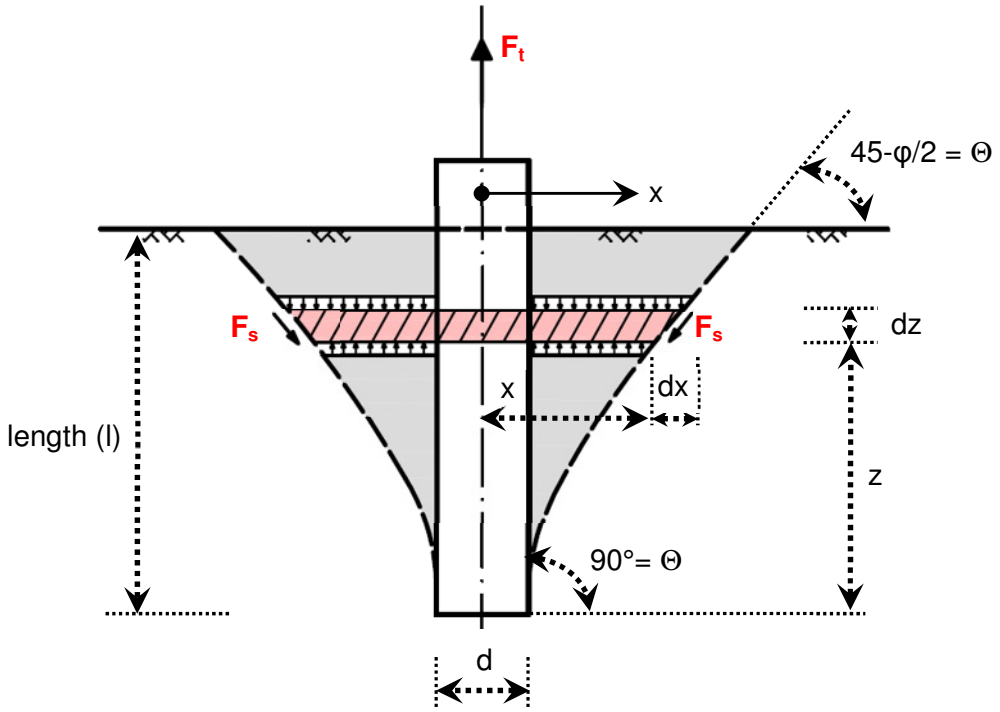

Fig. 14: Mobilized, axisymetric failure surface of a tension pile according to Chattopadhyay and Pise (1986)

The pile pull-out resistance (R_t) can be calculated with Equation 17. The associated uplift capacity factor (A^*) is given with Equation 18 and covers basically the resultant shape of the failure body and the side friction, which depends on the net weight of the soil. The ratio (x/d) is given with Equation 16.

$$R_t = A^* * \gamma' * \pi * d * l^2 - \frac{\pi * d^2}{4} * \gamma' * l \tag{17}$$

$$A^* = \frac{1}{l} * \int_{z=0}^{z=l} \left\{ \frac{2x}{d} * \left(1 - \frac{z}{l}\right) * * [\cot(\Theta) + (\cos(\Theta) + K * \sin(\Theta))] * \tan(\varphi) \right\} dz \tag{18}$$

$$K = (1 - \sin(\varphi)) * \frac{\tan(\delta)}{\tan(\varphi)} \tag{19}$$

However, Chattopadhyay and Pise (1986) did a sufficiently precise comparison of their theoretical approach with a selected set of results from small and large scale tests.

Quarg-Vonscheidt (2000) considers a radial symmetric soil body lifted up due to an axial tension load applied on the top of a pile. He assumes that the tension pile resistance (R_t) is basically covered by the weight of a set of thin nested arc-like shells of granular material which are clamped in each other. For the initial condition, after the pile installation process, the thin nested shells are cylindrically oriented around the pile with the resultant radial earth pressure force (e_r), the pressure ring force (n_{qt}) and the vertical shell weight force (n_α), Fig. 15. In order to transfer a vertical tension load into the subsoil a re-orientation of the thin nested shells from vertical to arc-like is done. The pile serves as shell-support at the end of the arc-like shells. The radial earth pressure force (e_r) and the pressure ring force (n_{qt}) are increasing consequently and preventing a run-off of the granular material shells. Quarg-Vonscheidt (2002) derived from his approach and small scale tests - as well as large and small scale tests from the literature - that the geometry of the mobilized soil body in sand depends on the pile length (l), the radial displacement (u_r) and the pile radius (r).

An open width (A) of the mobilized soil body, Fig. 15, is finally determined for sand and depends on the length (l) and the radial displacements (u_r). The radial displacements are approximately the average grain size diameter ($u_r = d_{50}$) for composite piles or the absolute roughness for friction piles.

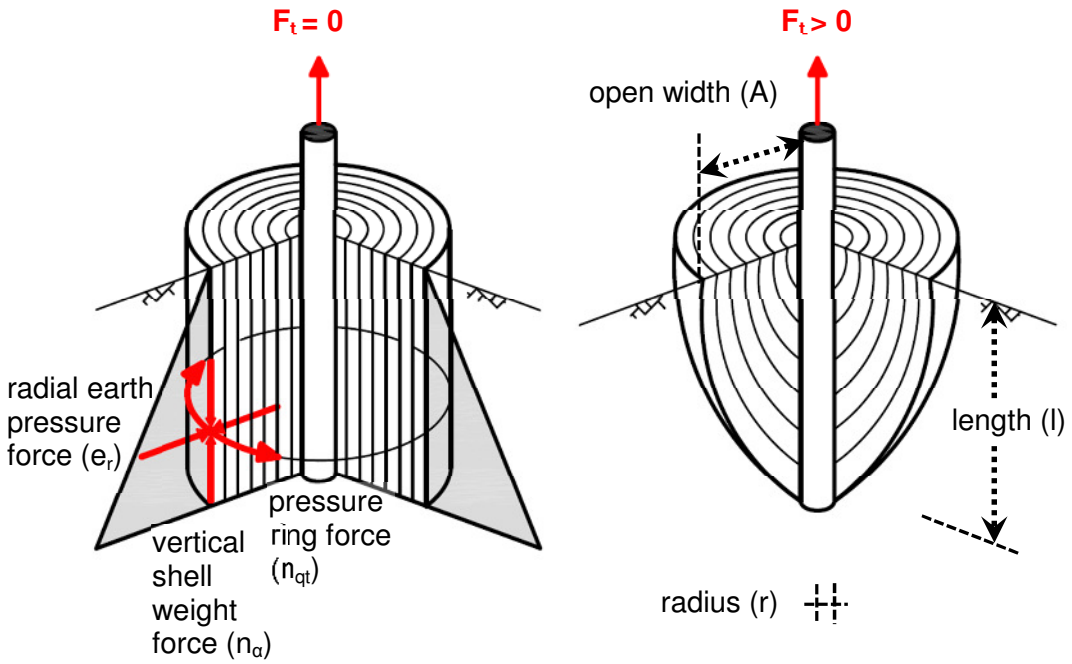

Fig. 15: Thin nested arc-like shells of granular material according to Quarg-Vonscheidt (2000), left: initial condition (after installation process), right: after applying a tension load to the pile

For composite piles in sand the open width (A) is given with:

- fine sand (d_{50} = 0.1 mm): A = 0.30 * $\sqrt{l}$
- medium sand (d_{50} = 0.4 mm): A = 0.52 * $\sqrt{l^{1.1}}$
- coarse sand (d_{50} = 1.2 mm): A = 0.64 * $\sqrt{l^{1.3}}$

The pull-out force (F_t) can be calculated with Equation 20 based on an idealised geometry of the mobilized soil body:

$$F_t = \gamma'_{soil} * \pi * 0.71\, l * [(A + r)^2 - r^2] + \gamma'_{Pile} * \pi * l * r^2 \qquad (20)$$

The design approach is limited for pile lengths from l = 3 to l = 30 m and sandy material. The approach has shown reasonable agreement with the design approach by Meyerhof (1973), but only for pile groups.

2.2.4 Installation process

Depending on the pile installation method the stress condition in the subsoil changes and a serious rearrangement of the soil grains can occur, especially close to the pile shaft. The radial stresses after a displacement pile installation (σ'_{rc}) are greater compared to the initial conditions but not constant and consequently changing with the embedded pile length, Lehane et al. (1993). In general, a distinction between two kinds of installation methods is done, Figure 16:

a) Methods which replace the soil due to the installation process e.g. driving, vibrating, screwing
b) Methods which do not replace the soil during the installation process e.g. bored piles

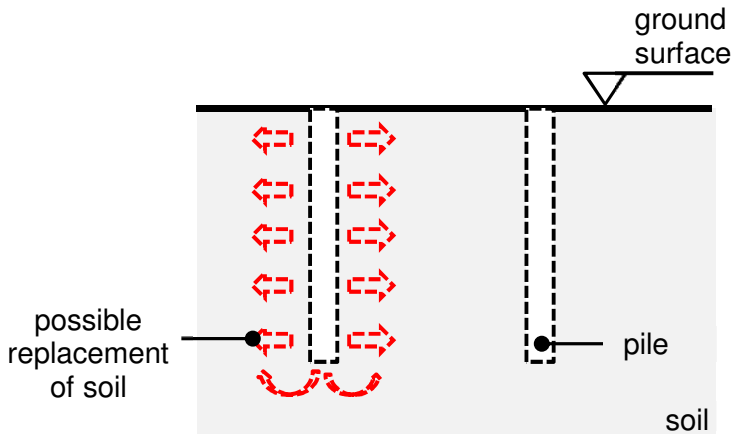

Fig. 16: Sketch of soil replacement after a pile installation, on the left side the soil is replaced and on the right side not

In the following only the influence of pile installation methods which replace the soil are considered.

Chow et al. (1998) consider a thin "sleeve" of loose sand around a displacement pile, created due to the high degree of densification at the tip of the pile during pile driving. The thin layer of loose sand is surrounded by highly compacted sand and supported by arching, which finally leads to high hoop stresses ($\sigma_{\varnothing}'$) around the pile, Fig. 17. The theory is supported by the observed increase of the pile shaft capacity with increase of time, where a reduction of the arching leads to an increase of radial stresses (σ_r') close to the pile shaft.

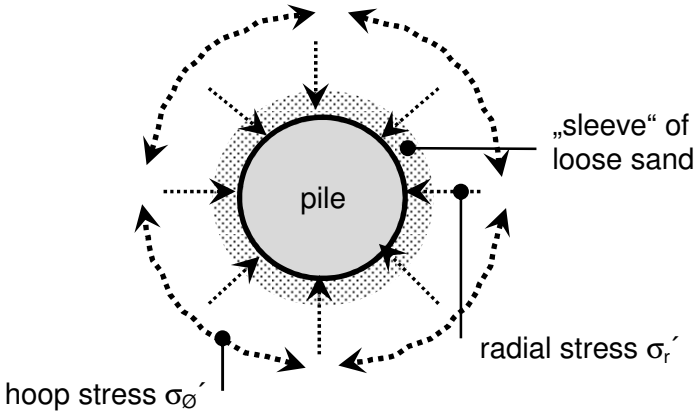

Fig. 17: Layout of arching around a pile shaft due to pile driving, Chow et al. (1997)

Augustesen (2006) mention that during or immediately after jacking displacement piles into the subsoil a remoulded zone very close to the pile shaft with low relative density (I_d) occurs. Far outside of the pile shaft a so called initial zone with almost initial undisturbed conditions is present. Between the remoulded and the initial zone a so called unstable transition zone with great hoop stresses and great relative density arises, Fig. 18. Augustesen (2006) consider that particle re-orientation in the transition zone occurs immediately after pile driving and over time too. High hoop stresses are developed in the transition zone. However, the high hoop stresses decrease with time, which finally leads to higher radial stresses acting on the pile shaft, similar to the assumptions of Chow et al. (1998).

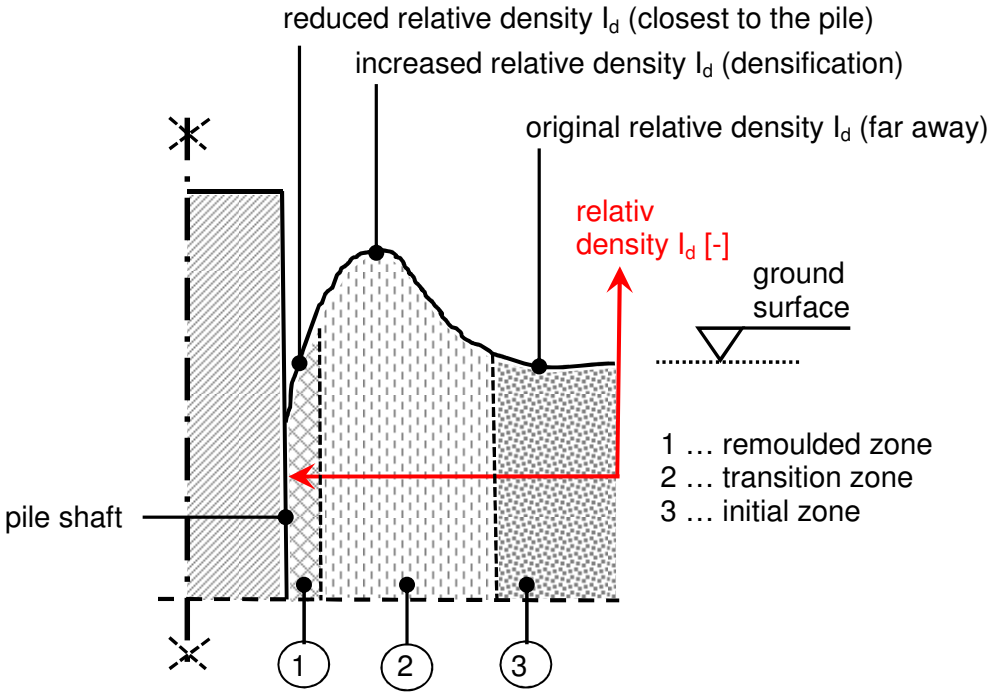

Fig. 18: Sketch of change of the relative soil density due to pile driving. Close to the pile shaft the relative density (I_d) is reduced and - after an increase - reaches the initial relative density far away from the pile again; modified after Augustesen (2006)

White and Bolton (2004) investigated the influence of the pile installation in sand of monotonic (constant driving), jacked (2 mm downward and complete unloading) and pseudo-dynamic (2 mm downward and 1.5 mm withdrawn) installation processes. The pile installations can be described by means of an interface contraction between the pile shaft and the soil. *"The mechanism of interface contraction provides the initial conditions for "set-up" of displacement piles in sand, where "set-up" refers to a time-related increase in shaft capacity. Immediately after passing the pile tip the distribution of radial stresses is as shown by the curve (OA) in Fig. 19 created as the soil is pushed outwards during flow around the pile tip. As the interface zone contracts, there is a sharp reduction in radial stress of the soil close to the pile shaft from the high value created during soil flow around the pile tip. As a result, the radial stresses acting on the pile shaft is lower than outside the zone influenced by the contraction (B). Over time the high stresses around the pile relax, creating the radial stresses shown as curve (OC) in Fig. 19,* White and Bolton (2004)".

Witzel (2004) executed small-scale pile driving experiments, to determine the change of the radial stresses around a driven pile. Model piles (d = 5 cm, l = 0.6 – 1.4 m) were driven into dense sand therefore and the change of the radial stresses was measured with a set of pressure gauges situated around the pile with variable distance to the pile axis.

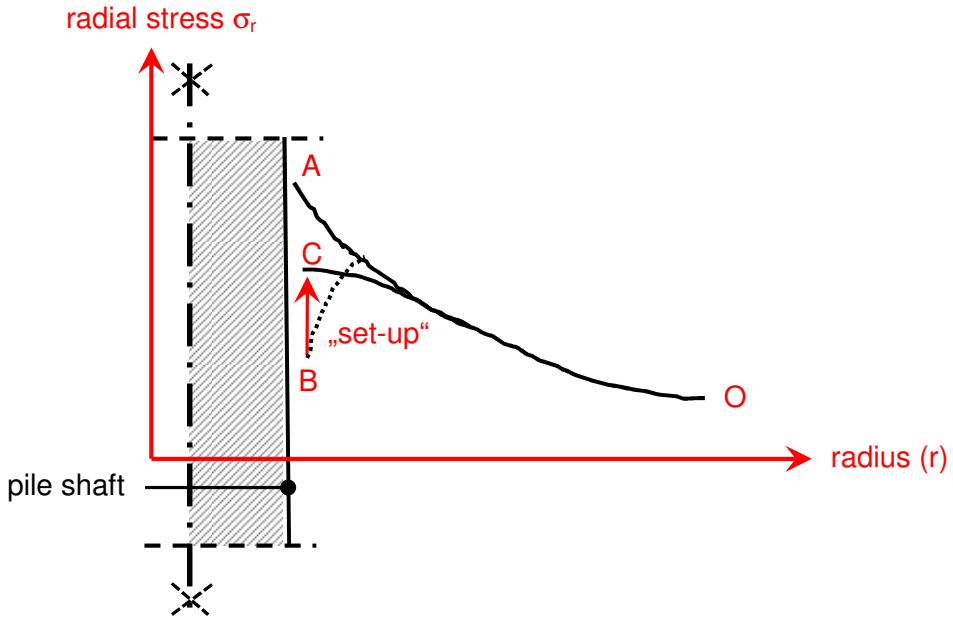

Fig. 19: Sketch of radial stress distribution due to interface contraction arising from the installation process, White and Bolton (2004)

Similar to the result of White and Bolton (2004), Fig. 19 curve OA, a significant reduction of the earth pressure (measured immediately after pile driving) with increasing distance to the pile axis was observed, Fig. 20.

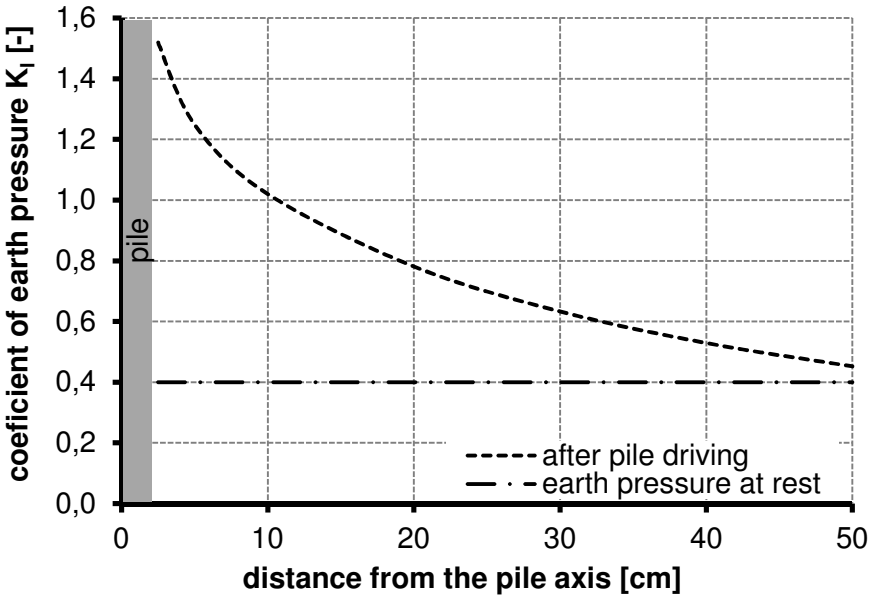

Fig. 20: Coefficient of earth pressure K_i (σ'_h/σ'_v) after pile driving depending on the distance to the pile axis, Witzel (2004)

Closest to the pile shaft the coefficient of earth pressure (K_i) is almost four times higher compared to the earth pressure coefficient at rest (K_o) and consequently the resulting stresses too.

Henke (2008) did FEM simulations based on a complex hyperplastic constitutive model, to determine the influence of pile driving and pile vibrating on a pile. An intense increase of the horizontal stresses close to the pile shaft was observed due to the installation process. The horizontal stresses decrease continuously until the stresses reach almost the initial state again around two meters away from the pile shaft, $l_{INSTALLED}$ = 4 m, d = 16 cm. This was independent from the density of the investigated "*Karlsruher"* sand. It is pointed out that for displacement piles with a full section the increase of horizontal stresses due to the installation process is significantly greater compared to piles with an open section e.g. steel pipe. After Henke (2008), the increase of the horizontal stresses is also greater for driven piles compared to piles installed by vibrating. Example: full section pile with d = 16 cm, medium dense sand, simulation results: $\sigma_h/\sigma_{h,0} \approx 13$ for driving and ≈ 3.1for vibrating a pile (σ_h horizontal stress after the installation process, $\sigma_{h,0}$ earth pressure at rest).

However, several authors, e.g. Jardine (1991), Chow (1997), White and Lehane (2004), White and Bolton (2004) as well as Gavin and Gallagher (2005), recognize that there is a reduction of the shaft friction as the pile tip penetrates further which is called "friction fatigue", Fig. 21. Friction fatigue is basically considered due to cyclic shearing during the pile installation process. The phenomenon is strongly influenced by the method of installation and the embedded pile length, White and Lehane (2004). The degradation of the horizontal stresses on the pile shaft was investigated by White and Lehane (2004). Four horizontal stress transducers were therefore installed on the pile shaft to measure the horizontal stresses during the pile installation of an Imperial College model pile (ICP, d = 101 mm, length ≈ 6 m). The pile was jacked in dense sand and the results are shown in Fig. 21, White and Lehane (2004). It is pointed out that friction fatigue is greater for greater embedded piles compared to smaller embedded piles.

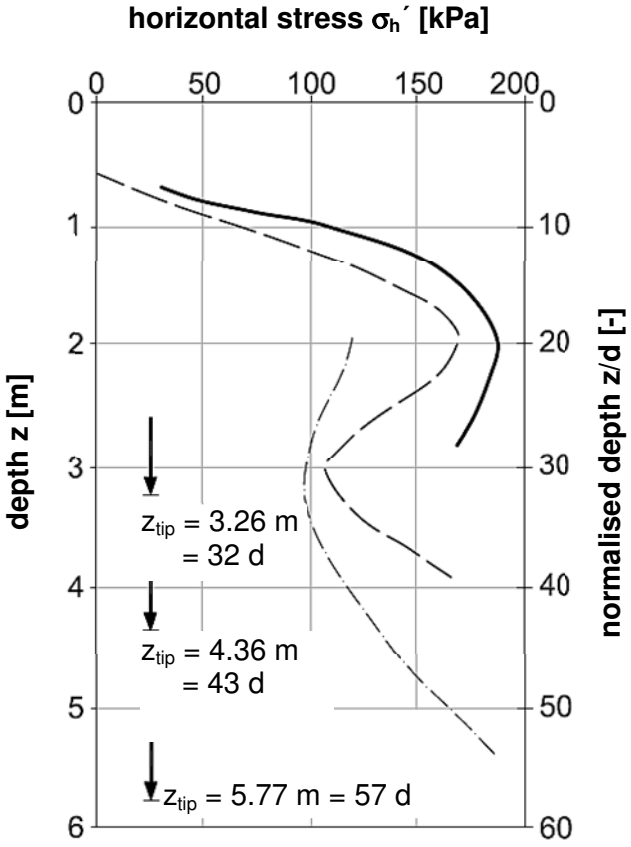

Fig. 21: Friction fatigue caused by driving an ICP pile into dense sand, White and Lehane (2004)

It is well known that due to displacement pile installation processes a densification zone with higher vertical stresses at the lower end of the pile is developed, Linder (1977), Witzel (2004), Lüking (2010), Henke (2013).

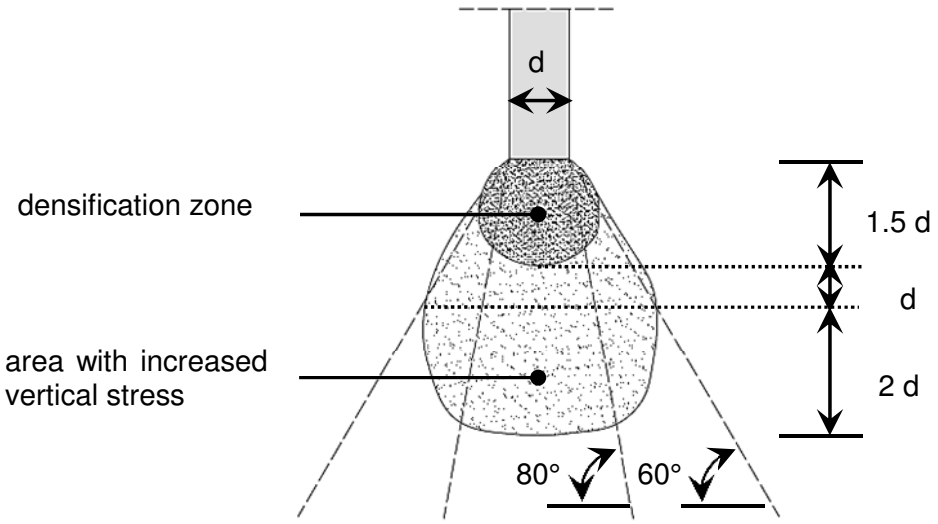

Fig. 22: Situation below the pile tip due to pile driving, Witzel (2004)

Due to this effect an increase of the pile base resistance for pressure piles and especially for open ended piles is caused. The influence of the densification zone on the bearing capacity of tension piles remains unclear and is neglected because little or no influence is expected. However, the situation below the pile tip due to pile driving is shown in Figure 22.

2.2.5 Summarising assessment and open issues

Intense research on the load bearing behaviour of tension-loaded piles was executed by many authors in the last decades. Several phenomena as well as the mechanical behaviour of tension loaded piles have been researched. In terms of the slender, threaded rods five research questions are elaborated in the following.

By reflecting the increase of the pile friction with decreasing pile diameter, Ostermayer and Werner (1972), Boulon and Foray (1986) and Lehane et al. (1993), a relatively high bearing capacity of the threaded rod is expected because of the small diameter. This leads to the following research question for a slender, threaded rod:

Q1: *What is the magnitude of the vertical pull-out force and how does the force-displacement graph look like?*

Witzel (2004) and König (2008) mention that the pile bearing capacity mainly depends on the following five factors:

- Pile type and geometry e.g. material, diameter, smooth or rough surface, length, section
- Pile installation e.g. bored, driven, screwed
- Soil type e.g. coarse and fine grained soil, density
- Service life of the pile e.g. short and long time, temporary
- Load type, e.g. static, dynamic, pressure or tension load, load direction

Transferring these factors to the threaded rod to be investigated in this thesis following restrictions to address the research question one (Q1) are done, while all other factors are kept constant:

- Pile type: rod: SAS 900/1100 FA, d = 15 mm, variable rod length
- Soil type: primarily coarse grained soil, variable density
- Pile installation: screwing only
- Service life of the pile: short time, (possible) creeping effects are not investigated
- Load type: vertical tension load only

A clear separation between three methods to predict the load bearing behaviour, with special attention to simplified mechanical theories, is introduced. However, simplified mechanical theories are categorized in two groups, either based on cavity expansion theory, or based on a mobilized failure body theory, which lead to the next research question:

Q2: *Is there a failure body attached to the threaded rod, mobilized by the applied vertical tension load (F_t)?*

It has to be pointed out that the pile installation process can lead to a significant change of the earth pressure around the pile shaft and that a densification zone is observed by many authors. However, the pile installation due to screwing only is researched in this thesis.

Q3: *What is the influence of the installation process with respect to the bearing capacity?*

The main application of the screwed threaded rods is the Spideranchor, see Chapter 1.2.1. The rods which are applied to the Spideranchor are usually not installed vertically, they are installed inclined. The bearing capacity of inclined single rods vertically tension-loaded, is therefore additionally investigated. Meyerhof (1973), Hanna and Afram (1986) and Chattopadhyay and Pise (1986) developed different functions and relationships to describe the bearing capacity from vertically to inclined installed piles.

Q4: *What is the bearing capacity of inclined threaded rods which are vertically tension-loaded?*

The final research question deals with applications of the threaded rods in general geotechnical applications of the Spideranchor.

Q5: *What are possible applications for the Spideranchor, depending on load situations, and is it possible to describe the Spideranchor bearing capacity for vertical tension loads by adding all expected pull-out force values of each individual rod?*

2.3 Methodology and outline of the thesis

The flowchart in Figure 23 outlines the methodology of the thesis. The main goal of the thesis is to understand and to describe the bearing capacity of single threaded rods which are vertically tension-loaded after the installation by screwing. As already mentioned, these rods are classified into the group of full displacement piles, respectively a similar kind of behaviour is expected.

Several research questions are highlighted in the previous chapter to understand the fundamental behaviour of the tension loaded rods, inter alia. It is pointed out that it is not the goal to derive a new mechanical theory to describe the bearing capacity of the introduced rods. Moreover, it is tried to fit the rods into existing theories and to modify these theories if necessary. For this reason, a literature review has been presented in the previous chapter.

The principal research method is experimenting, particularly rod pull-out tests in granular soil whereby variable objectives are considered, Fig. 23. This is necessary to collect a set of data for enabling a comparison with mechanical theories and possible parameter identification by means of back calculations, e.g. uplift capacities (K_u) values according to Meyerhof (1973). A three dimensional "insight view" into the granular soil is given by visualizing soil-rod interactions due to the rod installation and the pull-out process, therefore a transparent soil model is developed.

However, it is finally tried to transfer the knowledge gained about single rods to vertically loaded Spideranchors by introducing a group factor if required. For that reason pull-out tests in the field have been executed with single rods and with different Spideranchor systems, e.g. system VI and system XII.

Brief overviews of the content of the main chapter are given below:

- **Multi-scale experimental investigations**

  Intense pull-out tests of single rods and Spideranchors with variable length have been executed to address the introduced research questions. These experiments are described, summarized and discussed, and the results are compared with existing theories in this chapter. The influence of the material, the rod length and the installations process is also worked out.

- **Numerical investigation**

  For a better understanding of the experimental results gained and phenomena of the single rods observed, numerical investigations based on the DEM have been executed. The particle contact parameters e.g. particle stiffness (k_N, k_s), particle friction (μ), of the DEM simulations are gained from an inverse parameter identification based on a field experiment, Fig.23. However, a comparison of the numerical and experimental investigations is finally done in this chapter and special attention is paid to the shape of the mobilized failure body.

- **Design approach**

  Based on the experiments and the numerical investigation as well as the existing literature, a mechanical theory is presented to describe the bearing capacity of the individual rods which are vertically tension-loaded.

- **Assessment for geotechnical applications**

  This chapter deals with geotechnical applications for the Spideranchor, depending on the load situations. The design approach for single rods is transferred to the Spideranchor for applied vertical tension loads. New load cases, e.g. bending moment, are introduced and the suitability for such loads cases is proved in an experimental way.

  A new Spideranchor head plate has been developed for the bending moment load case. In closing, "Spideranchor Netting" is introduced as a modified slope stabilization method. However, Spideranchor Netting is tested based on full-scale experiments and a prototype case study is finally presented.

- **Conclusions and further research**

  In the final chapter, the most important results of this thesis are highlighted and problems that occurred when applying the Spideranchor are presented. Visions and open research questions for further research are also worked out.

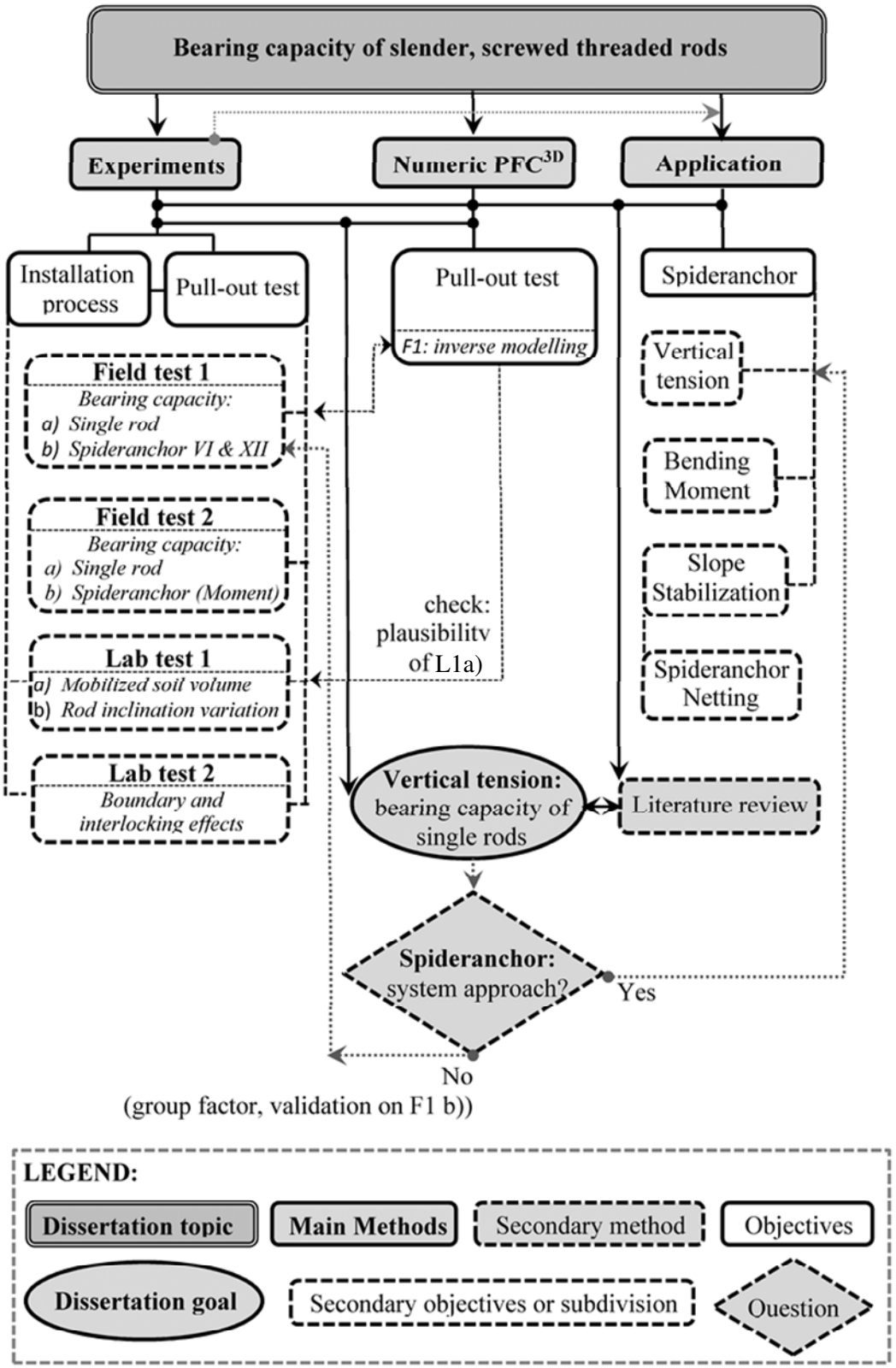

Fig. 23: Flow chart: methodology of the dissertation

3 Multi-scale experimental investigations

3.1 Introduction

In this chapter, a couple of experimental investigations to address the introduced research questions and to collect a set of data to gain a better understanding of the rod bearing capacity are presented. An overview is given in Table 3.

Tab. 3: Overview on experimental investigations

Research-questions (Q_i)	Experimental investigations				
	Field tests (F_i)			Lab tests (L_i)	
	F1	F2	F3	L1	L2
Q1 – bearing capacity: SR	☑	☑	☒	☑	☑
Q2 – attached soil body: SR	☒	☒	☒	☑	☒
Q3 – installation process : SR	☒	☒	☒	☑	☑
Q4 – inclined rod: SR	☒	☑	☒	☑	☒
Q5 – application: Spideranchor	☑	☑	☑	☒	☒

SR … investigations based on single rod pull-out tests

Experiments are executed in the field and in the lab; basically threaded rod pull-out tests with variable rod length and subsoil conditions. In this context, the term “multi-scale” in the heading refers to the variability in the slenderness ratio (λ) for the different experiments. The slenderness ratio (λ) is defined by the ratio of the rod length (l) divided by the rod diameter (d). However, in Chapter 1.2, Tab. 1, the rod to be investigated is introduced, by keeping the diameter (d) of the rod constant “multi-scale” refers also to the variability in rod length (l).

Several load cases for the Spideranchor are included within the research question five (Q5), depending on the associated application. Vertical tension load behaviour is addressed by field test 1 (F1) for the single rods and the Spideranchor, which is included in Chapter 3.2. Field test 2 (F2) deals with vertical and inclined installed single rod experiments included in Chapter 3.3. In addition, the load case bending moment is investigated within F2. This load case is included in Chapter 6. Within field test 3 (F3), an innovative slope stabilization method is tested. This experiment is included in Chapter 6.

Lab test 1 (L1) addresses several research questions (Q1 – Q4). These experiments are based on a transparent soil model and are included in Chapter 3.4. The addressed research questions within lab test 2 (L2, Q1 & Q3) can be found in Chapter 3.5.

Because of the relatively widespread research questions each chapter is organized into the following scheme: Firstly, a short introduction including a link to the defined research questions is given and, if essential, a very brief literature review is also included. Secondly, an overview of the experiment including setup and experimental procedure is given. Thirdly, the applied (lab) or existing (field) material is defined. Fourthly, the results gained are presented, compared, and discussed. Finally, a comparison of the results with the introduced literature and a final discussion is given.

3.2 Field test 1

3.2.1 Introduction

The main objective of field test one (F1) was to address research question one (Q1) for single rods by conducting pull-out tests: *"What is the magnitude of the vertical pull-out force and how does the force-displacement graph look like?"* In this context, particular consideration was given to record the caused pull-out force and displacements due to the test, continuously. Only this enables to investigate the post-peak behaviour in the force-displacement graph. For a better fundamental understanding of the rod behaviour, the experiments were conducted in coarse and fine grained soil. This was done, even though the research within this thesis is mostly limited for coarse grained soil.

The secondary objective of field test one (F1) was to address a part of research question five (Q5): *"What are possible applications for the Spideranchor, depending on load situations, and is it possible to describe the Spideranchor bearing capacity for vertical tension loads by adding all expected pull-out force values of each individual rod?"* Spideranchor pull-out tests were conducted with variable slenderness ratio (λ) respectively variable rod length, for that reason. The results are presented in this chapter. However, research question five is finally addressed in Chapter 6.

It is underlined that field test one (F1) was executed as part of a research project dealing with the examination of the Spideranchor applications for protective constructions (natural hazards). The Institute and Laboratory of Geotechnics, Technical University Darmstadt, Germany; the Institute of Soil Mechanics and Foundation Engineering, Graz University of Technology, Austria; the Division of Geotechnical and Tunnel Engineering, University of Innsbruck, Austria and the Spideranchor Company were involved in this research project led by alp▲S, Centre of Natural Hazards and Risk Management, Austria. The results of the

experimental part of this research project are summarized in a final report by Ghetta, Koler and Zangerl (2009). The results are presented, analysed and discussed for vertical tension loads only in the following subchapters. However, a master thesis written by Fink (2008) and the author of this thesis had been done before the research project started. The thesis included experimental investigations in the area of F1 and delivered a first, very rough insight into the complex structural behaviour of Spideranchors. To conclude, F1 was not executed by the author of this thesis himself. The author was responsible for the numerical investigations within the mentioned research project.

3.2.2 Overview, setup and experimental procedure

A traverse, Figure 24, Fink, Supp (2008), was developed to investigate the load-displacement behaviour of single rods and the Spideranchor due to an applied vertical tension load. In detail, pull-out tests were performed path-controlled (max. vertical displacement $u_z \approx 250$ mm). A hollow piston cylinder from Enerpac (RACH 3010, max. force 286 kN, max hub 250 mm) guided by an electronically controlled hydraulic pump with constant flow rate, Enerpac (ZE3), was used for applying the vertical tension load through the traverse. The forced vertical displacement (u_z) of the single rod or the Spideranchor was measured with the help of an immovable fixed measurement bridge. The bridge was situated around the rod or Spideranchor head plate.

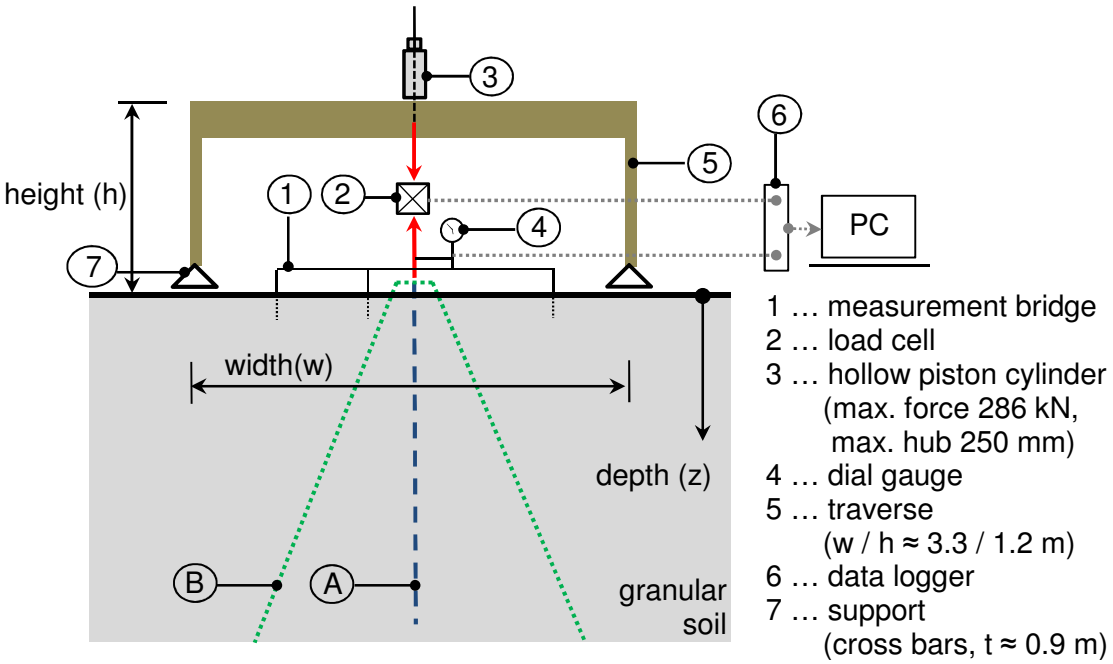

Fig. 24: Setup for pull-out tests; A) single rod pull-out tests, B) Spideranchor pull-out tests

A digital load cell (HBM, C6A) and dial gauge (HBM, WA T) were connected with a data logger (HBM, Spider 8) and a laptop for collecting the produced

data. These were in general the vertical displacements (u_z) and the vertical tension force (F_t). The full setup can be seen in Fig. 25.

Pull-out tests were performed in two different soils for field test one, coarse grained soil (material A) and fine grained soil (material B). These materials are specified in Chapter 3.2.3. However, details concerning the field tests can be found in Ghetta, Koler and Zangerl (2009) respectively in Fink, Supp (2008).

In the following, the experimental procedure for each experiment is given:

a. Installation of the Spideranchor (test B) or the vertical single rod through a bushing (test A), Figure 2, by screwing only
b. Positioning of the traverse, axially over the anchor head or the rod centre
c. Installation of the load devices, e.g. hollow piston cylinder, and connecting them to the load cell and the single rod or the Spideranchor
d. Installation of the measurement bridge and the dial gauge
e. Connecting the load cell and the dial gauge with the data logger and starting the experiment by activating the electronically controlled hydraulic pump for the hollow piston cylinder until approximately 250 mm vertical displacements (u_z) were reached

An overview of the experimental investigations is given in Tab. 4.

Tab. 4: Overview of experimental investigations in field test one (F1)

Rod length (l)	Material		Vertical pull-out tests			
			single rod[B)]		Spideranchor	
	A	B	vertical	inclined	VI	XII
2.0 m	☑	☑	☑	☒	☑	☑
3.0 m	☑	(☑)	☒	☒	☑ A[*)]	☑
4.0 m	☒[A)]	☑	☒	☒	☑	☑

[A)] aborted or not executed, maximum possible load for the traverse ($F_{max} \geq 200$ kN) was reached or expected
[B)] type: SAS 900/1100 FA, d = 15 mm, see Tab. 1
[*)] material for the executed experiments, if limited

In total, more than 30 pull-out tests were carried out. Results of 15 single rod pull-out tests and 13 Spideranchor pull-out are presented in Chapter 3.2.4

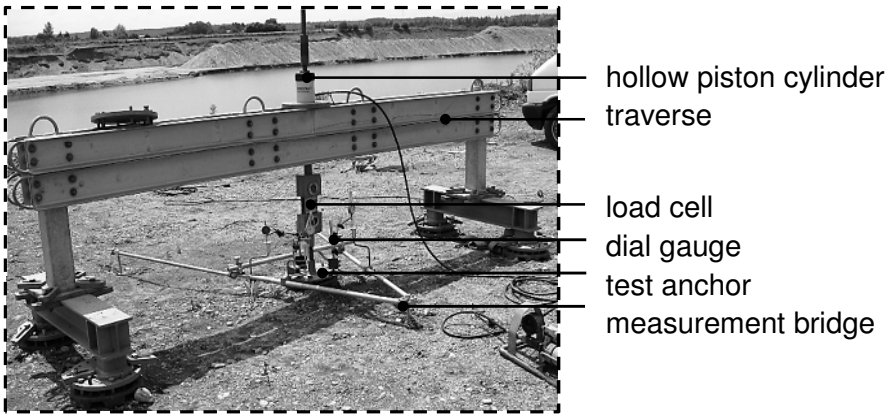

Fig. 25: Realized setup for the pull-out tests

3.2.3 Materials

Two testing locations in Austria were chosen for field test one, both of them with soil layers with almost constant properties within each test area. This was verified by dynamic probing (DPL, light) Fink and Supp (2008) and Ghetta, Koler and Zangerl (2009). The location for material A (coarse grained soil) was a gravel pit near Graz, Austria and the location for material B (fine grained soil) was a brick factory near Salzburg, Austria. For details see Ghetta, Koler and Zangerl (2009).

An extensive soil testing program, composed of field and lab tests, was executed for both materials. In detail, the following tests were carried out in the field: water replacement tests to determine the in-situ density of the soil (γ_F) and load plate tests.

Tab. 5: Material properties of the field test 1

Properties	Material type	
	Material A	Material B
Wet weight density γ_F [kN/m³]	23.0	19.4
Dry weight density γ_d [kN/m³]	22.4	15.8
Particle weight density γ_s [kN/m³]	27.2	28.2
Porosity n [-]	0.18	0.44
Density D [-] or *consistency I_c [-]*	0.92 (very dense)	*0.8 (stiff)*
Saturation S_r [-]	0.33	0.82
Cohesion c´ [kN/m²]	0	52
Peak friction angle φ´ [°]	36.9	22.4
Load plate test E_{v2}/E_{v1} [-]	not executed	3.2

The following tests were carried out in the lab: direct shear tests (material A: 30 * 30 and material B: 10 * 10 cm shear surface), variable lab tests and calculations to determine physical properties, e.g.: dry density (γ_d), particle density (γ_s), saturation (S_r), porosity (n), density (D) or consistency (I_c). Sieving and finally calculating the coefficient of uniformity ($C_u = d_{60} / d_{10}$) and the curvature coefficient ($C_c = d_{30}^2 / (d_{10}*d_{60})$) of the resultant grading curves was also done in the lab. The soil characterisation is summarized in Tab. 5 and the corresponding grading curves of the materials can be found in Fig. 26.

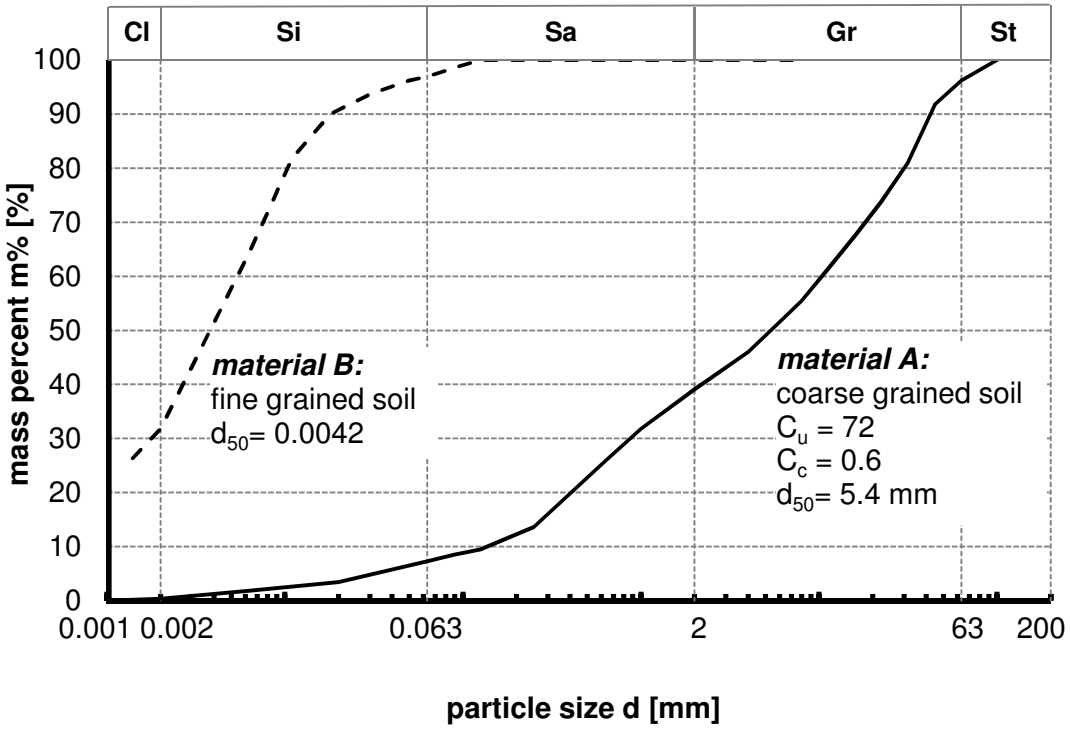

Fig. 26: Grading curve of the materials

3.2.4 Results: Vertical rod pull-out tests

- **Material A:**

Seven pull-out tests of vertically installed threaded rods with 2 m rod length were conducted in material A. The results are relatively widespread and given in Table 6. An exemplary force-displacement graph of the experiments is shown in Fig. 27. In order to define a pull-out force, the (first) maximum of the generated force-displacement graph is called pull-out force ($F_{t,max}$), Fig. 27.

The average pull-out force value for the material A is $F_{t,max,} \approx 32$ kN (min ≈ 17.5 kN; max ≈ 46.3 kN) and the average vertical displacements are $u_z \approx 7.6$ mm (min ≈ 5.4 mm; max ≈ 10.6 mm). The force-displacement graphs of the different pull-out tests show a massive reduction of the tension force (F_t) after reaching a peak value. This can be interpreted as (partly) loose of strong

interlocking effects of the single rod with the surrounded subsoil due to the rising vertical displacements.

Tab. 6: Single rod pull-out test results, material A, rod length (l) = 2 m, slenderness ration (λ) = 133, according to Ghetta, Koler and Zangerl (2009)

Test no.:	Results:	
	pull-out force $F_{t,max}$ [kN]	displacement u_z [mm]
1	17.5	5.7
2	18.1	5.4
3	34.5	10.6
4	38.2	10.0
5	45.1	9.0
6	46.3	7.2
7	24.1	5.6

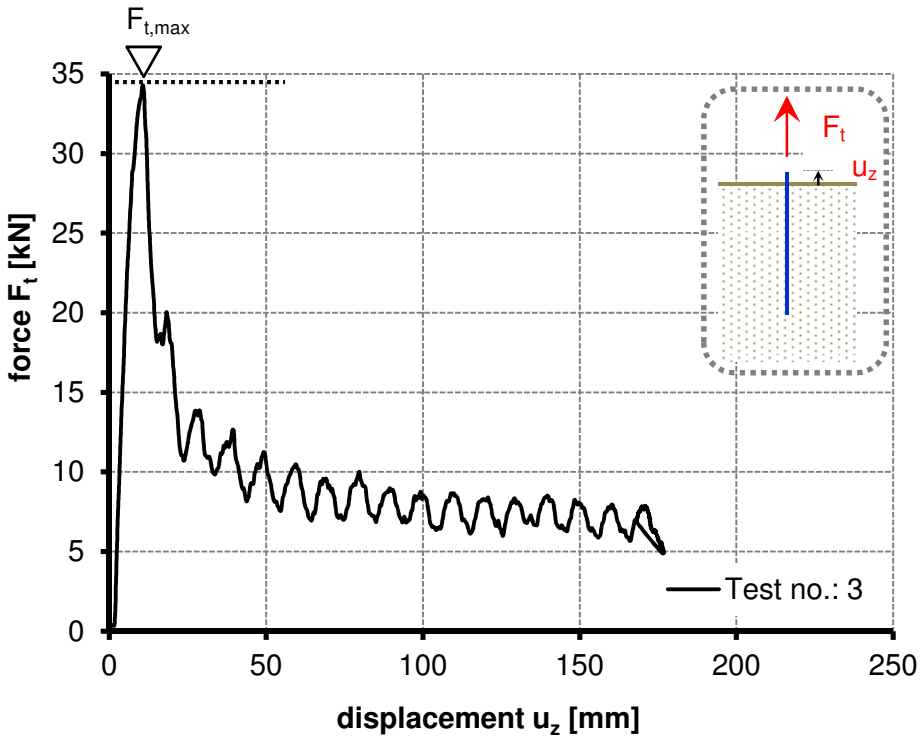

Fig. 27: Force-displacement graph of the rod pull-out test number 3, material A, rod length (l) = 2 m, slenderness ration (λ) = 133, modified after Ghetta, Koler and Zangerl (2009)

It is interesting to note that the post-peak behaviour of the force displacement graph, hence the graph after reaching the pull-out force ($F_{t,max}$), shows a "wave-like" behaviour, consisting of up and down of the applied tension force (F_t).

One possible reason for this are the threads of the rod which interlock (up) with soil particles and partly lose the interlocking (down) with further developed vertical displacements.

- **Material B**

Seven pull-out tests of vertically installed threaded rods with 2 m rod length were conducted in material B. The results are relatively widespread too, Tab. 7. An exemplary force-displacement graph of the test is shown in Fig. 28.

Tab. 7: Single rod pull-out tests result, material B, rod length (l) = 2 m slenderness ration (λ) = 133 according to Ghetta, Koler and Zangerl (2009)

Test no.:	Results:	
	pull-out force $F_{t,max}$ [kN]	displacement u_z [mm]
1	6.9	2.7
2	6.8	7.3
3	7.4	6.4
4	3.8	6.3
5	5.1	3.7
6	9.5	8.6
7	5.9	5.8
8	8.3	2.6

The average pull-out force value for the material B is $F_{t,max} \approx 6.7$ kN (min ≈ 3.8 kN; max ≈ 9.5 kN) and the average vertical displacements are $u_z \approx 5.4$ mm (min ≈ 2.8 mm; max ≈ 8.6 mm).

The force-displacement graphs of the different pull-out tests also show a massive reduction of the tension force (F_t) for material B after reaching a peak value. However, it is noted that the post-peak behaviour is also “wave-like” for material B after reaching greater vertical displacements.

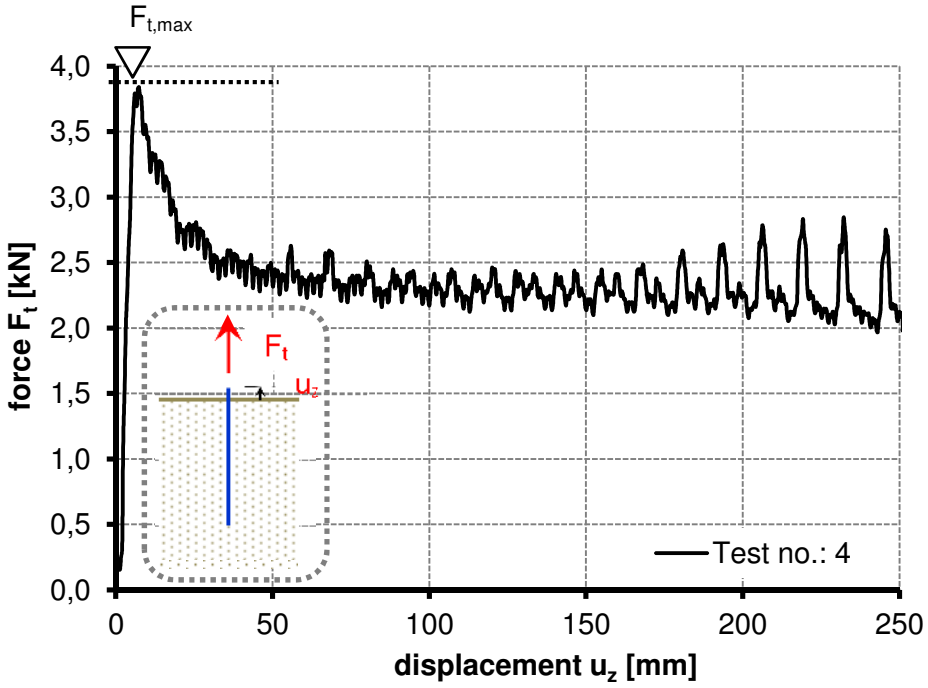

Fig. 28: Force-displacement graph of the rod pull-out test number 4, material B, rod length (l) = 2 m, slenderness ratio (λ) = 13, modified after Ghetta, Koler and Zangerl (2009)

3.2.5 Results: Spideranchor VI and XII pull-out tests

- **Material A:**

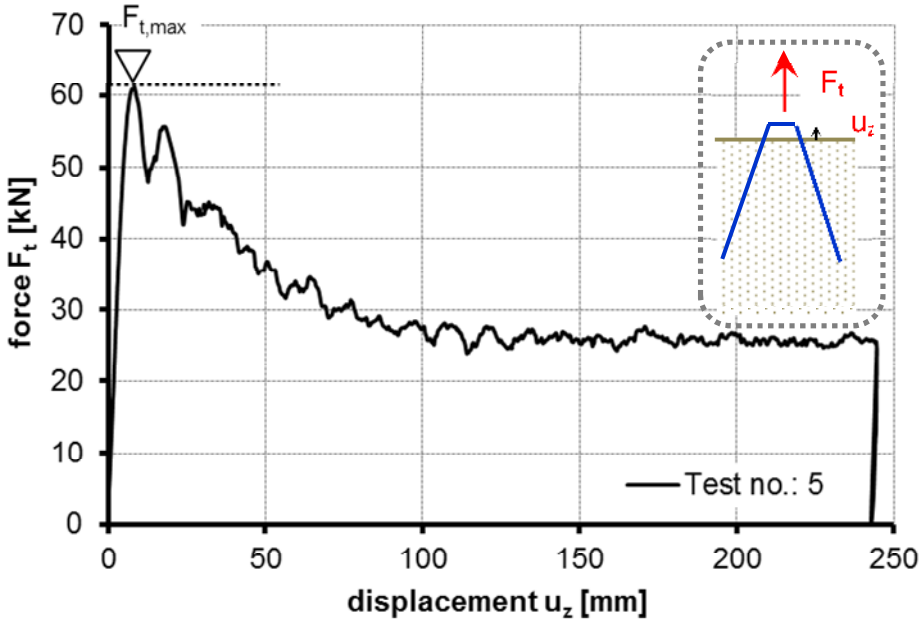

Fig. 29: Force-displacement graph of the Spideranchor VI pull-out test number 5, material A, rod length (l) = 2 m, slenderness ratio (λ) = 133, modified after Ghetta, Koler and Zangerl (2009)

Thirteen pull-out tests of the Spideranchor were conducted in material A, eight Spideranchor VI and five Spideranchor XII pull-out tests with variable rod length (l), Tab. 8. An exemplary force-displacement graph of the experiments is shown in Fig. 29.

Tab. 8: Results of the Spideranchor pull-out tests, material A, according to Ghetta, Koler and Zangerl (2009)

Test no.:	Results:				Geometrical properties: threaded rod	
	Spideranchor VI		Spideranchor XII			
	pull-out force $F_{t,max}$ [kN]	displacement u_z [mm]	pull-out force $F_{t,max}$ [kN]	displacement u_z [mm]	l [m]	λ [-]
1	57.8	15.8			2.0	133
2	49.3	17.6				
3	64.6	9.8				
4	60.6	13.6				
5	61.3	8.2				
6			103.9	12.5		
7			115.5	10.1		
8			93.8	8.8		
9			102.3	7.7		
10	141.2	9.8			3.0	200
11	124.0	9.0				
12	125.5	9.1				
13			191.7	12.7		

The force-displacement graphs of the different pull-out tests show a significant reduction of the tension force (F_t) after reaching the pull-out force ($F_{t,max}$). This is observed for both the Spideranchor VI and XII, but not as distinct as during the single rod pull-out tests. However, it is noted that for the Spideranchor pull-out tests the post-peak behaviour of the force-displacement graph shows almost no “wave-like” behaviour compared to the graph of the single rod pull-out tests. One possible reason for this is that the activation of all Spideranchor rods does not occur simultaneously. A load transfer from rods with less bearing capacity to rods with greater bearing capacity occurs because of the rigid anchor head plate. This seems very reasonable especially when looking on the relatively wide spread single rod pull-out force results.

In addition, a clockwise rotation (layout) of both Spideranchor plates (VI and XII) during the vertical pull-out experiments was observed, Fig. 30. This is because of an imbalance of horizontal forces, by looking at the force equilibrium conditions after a free cutting of the Spideranchor rods. This leads to an additional torsion moment load in addition to the applied vertical load.

- **Material B:**

Eight pull-out tests of Spideranchors were conducted in material B, one Spideranchor VI and seven Spideranchor XII pull-out tests with variable slenderness ratio (λ), Tab. 9. An exemplary force-displacement graph of the experiments is shown in Fig. 31. The force displacement graphs of the different pull-out tests show a very surprising increase of the tension load (F_t) in some cases after reaching a first peak value or a slightly distinct reduction. This happens for both the Spideranchor VI and the Spideranchor XII. However, a "wave-like" post-peak behaviour cannot be observed at all.

Tab. 9: Spideranchor pull-out tests results, material B, according to Ghetta, Koler and Zangerl (2009)

Test no.:	Results:				Geometrical properties: threaded rod	
	Spideranchor VI		Spideranchor XII			
	pull-out force $F_{t,max}$ [kN]	displacement u_z [mm]	pull-out force $F_{t,max}$ [kN]	displacement u_z [mm]	l [m]	λ [-]
1			52.0	12.1	2.0	133
2			33.5	10.9		
3			54.6	11.9		
4			53.5	13.7	3.0	200
5			71.9	7.2		
6			60.3	13.8	4.0	266
7			92.4	11.0		
8	32	11.8				

The post-peak behaviour of the Spideranchor is not the same compared to the post-peak behaviour of a single rod. To conclude, a clockwise rotation around the vertical axis of the anchor head-plate (VI and XII) was observed for the experiments in material B as well.

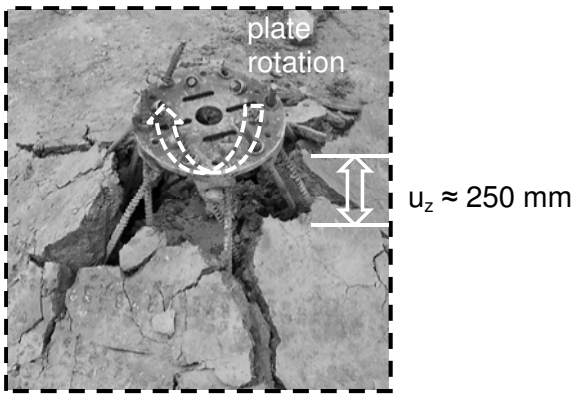

Fig. 30: Spideranchor XII after 250 mm vertical pull-out displacements u_z. The observed clockwise rotation of the plate is marked and a material uplift close to the anchor head plate can also be observed.

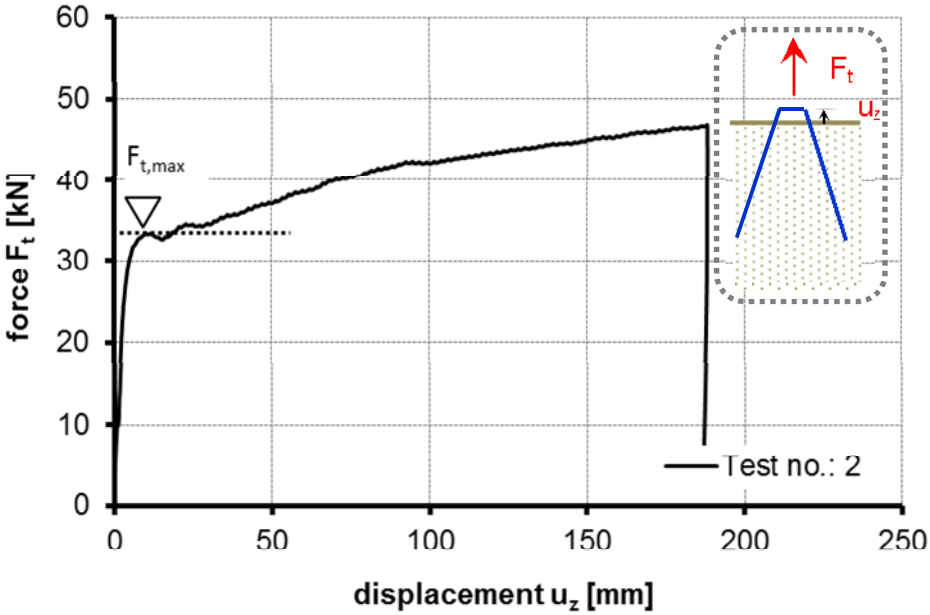

Fig. 31: Force-displacement graph of the Spideranchor XII pull-out test number 2, material B, rod length (l) = 2 m, slenderness ratio (λ) = 133, modified after Ghetta, Koler and Zangerl (2009)

3.2.6 Comparison of results and discussion

- **Single rod:**

Figure 32 illustrates the spectrum of the tension force (F_t) normalised to the individual pull-out force ($F_{t,max}$) for all executed rod pull-out tests of the field test one. The post-peak behaviour of the force-displacement graph shows a massive reduction for both materials, but significantly less for material B (material A: $\Delta \approx 0.7$; material B: $\Delta \approx 0.4$).

The necessary vertical displacements (u_z) to reach the pull-out force ($F_{t,max}$) are between 5 to 11 mm for both materials. The rods in material B reach the pull-out force with slightly less vertical displacements (u_z). One possible reason for this may be a slip between the soil particles of material A and the rod. This possibly occurs due to the change of the principle stress orientation after the installation process, by applying a tension load.

On the whole, a similar shape of the normalised pull-out graphs is observed for both materials.

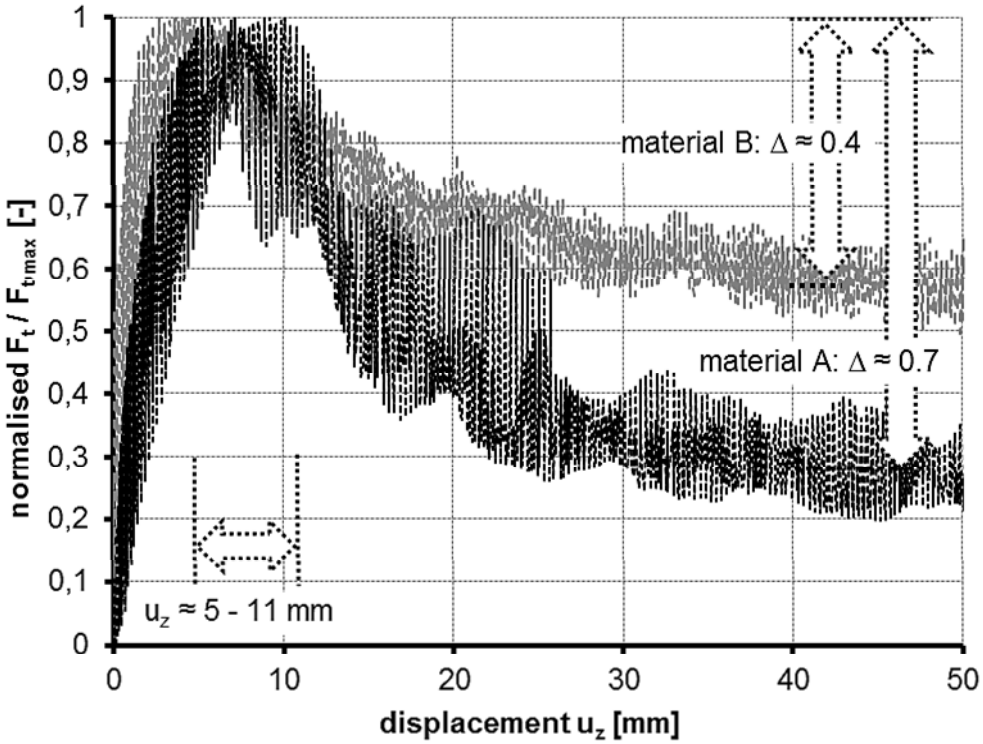

Fig. 32: Spectrum of the normalised rod pull-out forces (F_t / $F_{t,max}$) for material A and material B

- **Spideranchor:**

Figure 33 illustrates the spectrum of the tension force (F_t) normalised to the individual pull-out force ($F_{t,max}$) for all executed Spideranchor XII pull-out tests of the field test one. The post-peak behaviour of the force-displacement graph shows a reduction for material A and an increase as well as a slightly reduction for material B.

It is pointed out that independently from the type of the Spideranchor, VI or XII, the force-displacement graph looks similar for the corresponding soil type.

The necessary vertical displacements (u_z) to reach the pull-out force ($F_{t,max}$) are between 7 to 13 mm for the Spideranchor XII for both materials which is slightly higher compared to the single rod pull-out tests.

The graph of Figure 35 shows a linear increase of the pull-out force ($F_{t,max}$) by increasing the slenderness ratio (λ), respectively the rod length (l). This is valid for the given slenderness range for material B. However, only two data points are available for the graph of Figure 34, the linear increase is therefore not verifiable for material A at this point.

It can be observed very well that an intelligible decrease of the pull-out force per single rod is reached by increasing the amount of rods with constant rod length, e.g.: material A and l = 2 m: single rod: $F_{t,max}$ = 32 kN; Spideranchor VI: $F_{t,max}$ = 59 kN and Spideranchor XII: $F_{t,max}$ = 104 kN, average values are given for the example.

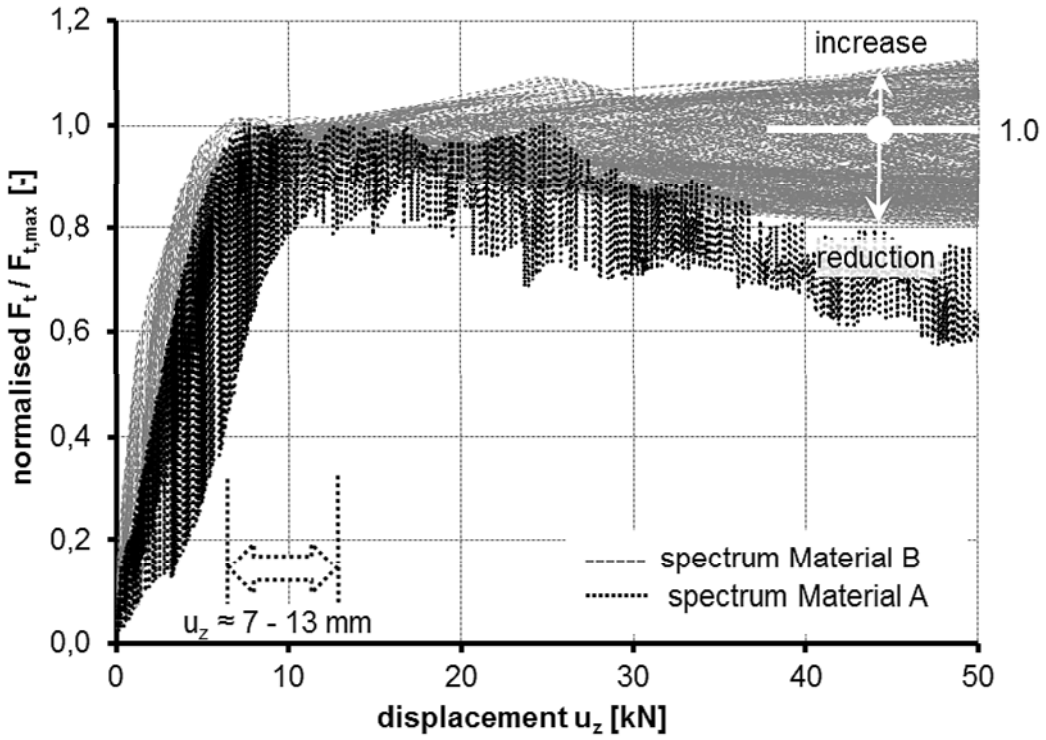

Fig. 33: Spectrum of the normalised Spideranchor XII pull-out forces (F_t / $F_{t,max}$) for material A and material B. The slenderness ratio (λ) is variable, see Table 8 - 9

A possible reason for this is the additional torsion moment, which is caused by the applied vertical tension load. This can be especially recognized by reflecting the observed plate rotation during the experiments, Fig. 30. Another possible reason is the greater final depth (z) of the vertically installed rod compared to the inclined installed rods of the Spideranchor and the resultant different stress level. Moreover, both the vertically installed rod and the inclined installed rods of the Spideranchor are finally vertically tension-loaded. In addition, an activation of all Spideranchor rods probably does not happen simultaneously. However, it is more economical to install a Spideranchor VI with longer rod length than a Spideranchor XII with shorter rod length, e.g.: $F_{t,max}$ ≈ 104 kN for

the Spideranchor XII with a rod length of 2 m (sum of the rod lengths: 12 * 2 = 24 m) and $F_{t,max} \approx 130$ kN for the Spideranchor VI with a rod length of 3 m (sum of the rod lengths: 6 * 3 = 18 m). This seems logical because the stresses in the subsoil increase with greater depth (z).

Figure 36 illustrates the necessary vertical displacements to reach the pull-out force ($F_{t,max}$) for both the Spideranchor and the soil types and with changing rod length. A best fit line is applied and almost constant average vertical displacements are determined with $u_z = 11.5$ mm ($\approx$ ¾ d).

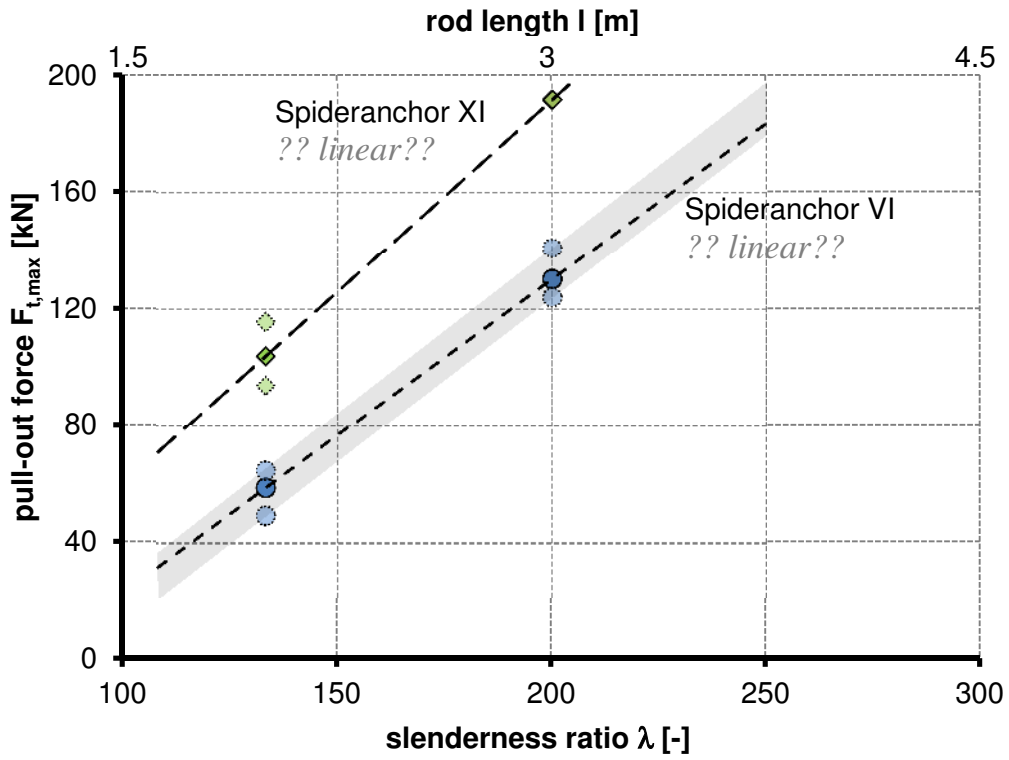

Fig. 34: Influence of the rod length (l) and the pull-out force $F_{t,max}$ for material A and the Spideranchor VI and XII. The spectrum (min, max) of the different results is given in grey, if existing

In general, it can be concluded that the load-displacement graphs of the single rod pull-out tests and the Spideranchor pull-out tests have a similar shape. The necessary displacements to reach the pull-out force are as well in a similar range even if the value of the pull-out force is different.

It is underlined that a more detailed discussion of Spideranchor applications, depending on variable load cases is part of Chapter 6, including the vertical tension load case which is based on field test one (F1).

Finally, to partly address research question five (Q5), it is reasonable to assume a relation between the pull-out forces of the single rod and the Spideranchor and this will be worked out in more detail in Chapter 6.

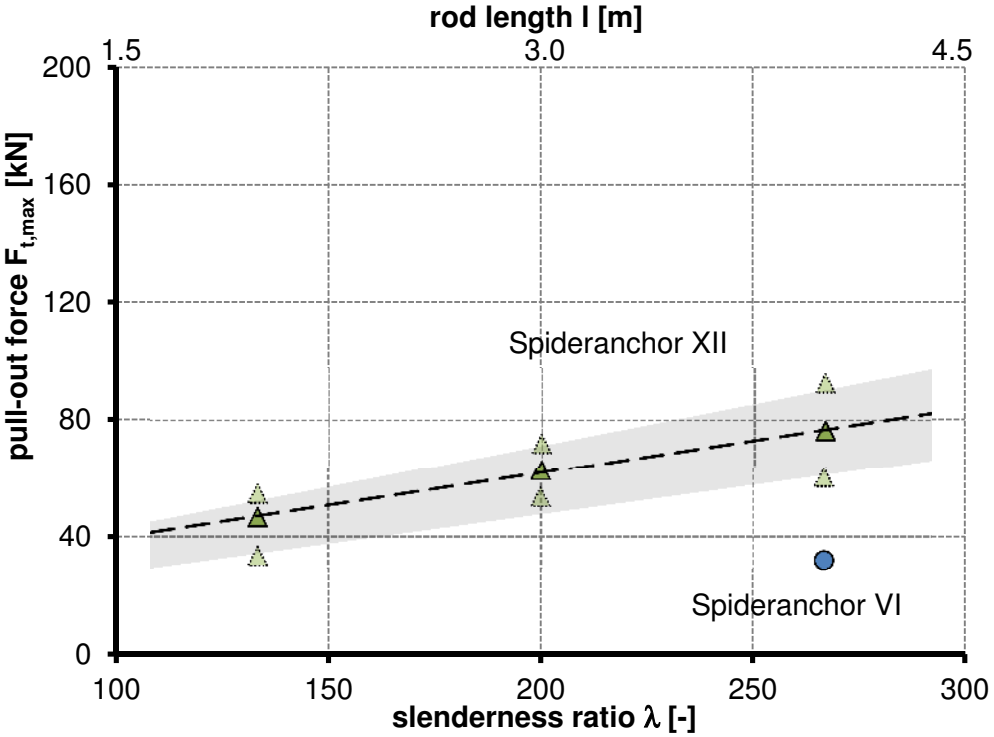

Fig. 35: Influence of the rod length (l) and the pull-out force $F_{t,max}$ for material B and the Spideranchor VI and XII. The spectrum (min, max) of the different results is given in grey, if existing

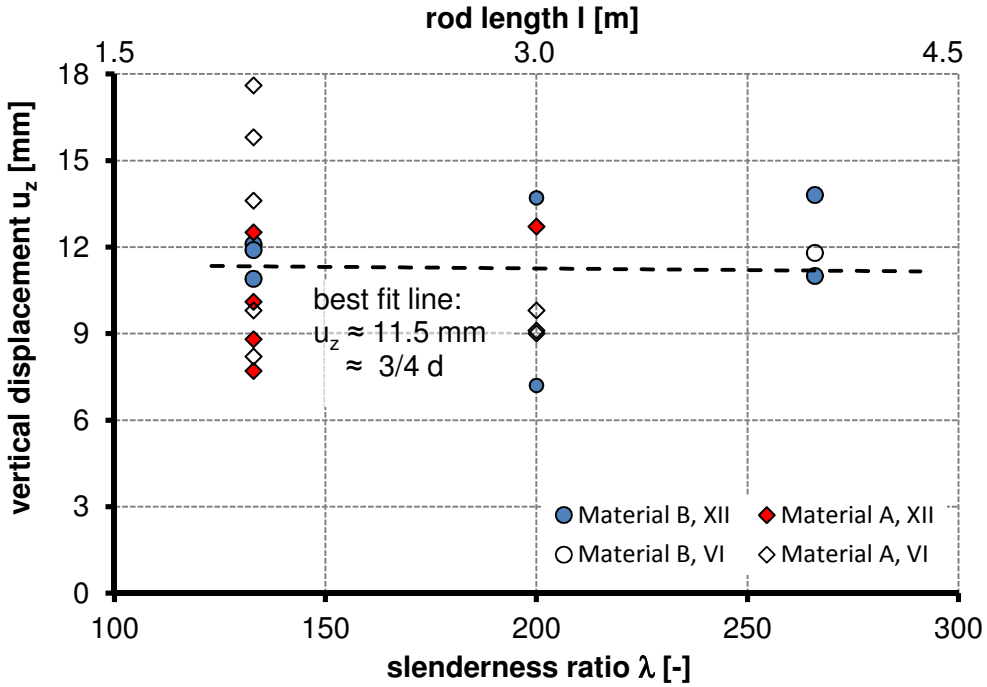

Fig. 36: Influence of the rod length (l) and the vertical displacement (u_z) which are necessary to reach the pull-out force $F_{t,max,}$ for material A and B and the Spideranchor VI and XII

3.2.7 Comparison of literature and discussion

In this chapter, a comparison of calculated pull-out forces - based on the introduced simplified mechanical theories in Chapter 2 - with the average single rod pull-out force for both materials is done. To calculate the pull-out force according to the expressed theory the following general assumptions or simplifications are done. Additional assumptions are summarized in Tab. 10:

I. Surface area rod ≈ d * π * l = 0.015 * 3.14159 * 2.0
II. Rod surface friction (δ) ≈ friction angle (φ´)
III. The rods are fully vertically installed, no rod imperfection or rod distraction due to an obstacle in the subsoil, e.g. bigger stone, is considered.
IV. The corresponding material properties from field test one (F1) are applied, see Table 5.

Tab. 10: Additional assumptions or data to calculate the pull-out force according to the expressed theory

Theory, author: (year)		Soil type	
		Material A	Material B
Jelinek and Ostermayer	1964	$\beta^{*)} \approx 3.5°$	$\beta^{*)} \approx 3.2°$
Meyerhof	1973	K_U values only for bored piles available, those values are applied, see Fig. 13	
Chattopadhyay and Pise	1986		
Quarg-Vonscheidt	2000	The approach is only applicable for sandy material and rod lengths from 3 to 30 m	
		assumption,(real): d_{50} = 1.2 (5.4) mm	assumption,(real): d_{50} = 0.1 (0.0042) mm

*) calculated

Figure 37 illustrates the different results of the calculations and the average results of field test one for both materials. The pull-out forces ($F_{t,max}$) are illustrated in logarithmic scale because of the extensive variety of results. For material A, $F_{t,max}$ = 0.9 - 105 kN and for material B, $F_{t,max}$ = 0.4 - 52.9 kN.

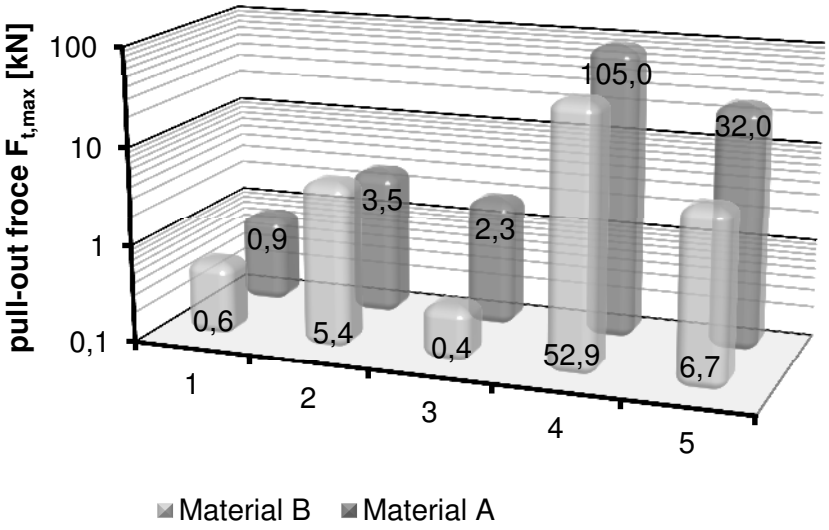

Fig. 37: Comparison of different design approaches (log scale): (1) Jelinek and Ostermayer (1964); (2) Meyerhof (1973); (3) Chattopadhyay and Pise (1986); (4) Quarg-Vonscheidt (2000), (5) average pull-out force $F_{t,max}$ of field test 1 (F1)

For material A, the approaches of Jelinek and Ostermayer (1964), Meyerhof (1973) and Chattopadhyay and Pise (1986) are very strongly underestimating and the approach of Quarg-Vonscheidt (2000) is strongly overestimating the pull-out behaviour of the threaded rods. Possible reasons for this are discussed below.

The approach of Meyerhof (1973) is only applicable for bored piles. However, Meyerhof expects much greater K_u values for displacement piles. The approach of Jelinek and Ostermayer (1964) is based on two-dimensional plane stress conditions and three-dimensional effects are not taken into account. All approaches above, except Quarg-Vonscheidt (2000), do not really consider interlocking effects between the rod and the surrounding subsoil. These are strongly observed by looking at the force-displacement graphs of the single rod pull-out tests. However, the approach of Quarg-Vonscheidt (2000) is only valid for sandy material, which is not the case for field test one.

For material B, the approaches of Jelinek and Ostermayer (1964) and Chattopadhyay and Pise (1986) are strongly underestimating and the approach of Quarg-Vonscheidt (2000) is strongly overestimating the real pull-out behaviour. The approach of Meyerhof (1973) leads to reasonable results because adhesion, respectively cohesion, is considered.

To conclude, it is clearly demonstrated that the introduced simplified mechanical theories in Chapter 2 - especially those which are based on a mobilized failure body - cannot reflect the real pull-out behaviour of the slender, screwed and tension-loaded threaded rods.

3.3 Field test 2

3.3.1 Introduction

The main objective of field test two (F2) was to address research questions one and four (Q1 and Q4) for single rods by conducting pull-out tests: "*What is the magnitude of the vertical pull-out force and how does the force-displacement graph look like?"* and "*What is the bearing capacity of inclined threaded rods which are vertically tension-loaded?"* Field test two was conducted load controlled with variable slenderness ratio (λ) for the vertical rods because the shape of the force-displacement graph had already been investigated. However, research question one has already been partly addressed in field test one, and in field test two, additional data have been gained, e.g. pull-out behaviour in sandy material and influence of the rod length, to get a better and more detailed understanding of the load bearing behaviour of single rods.

The second objective of field test two (F2) was to address a part of research question five (Q5): *"What are possible applications for the Spideranchor, depending on load situations, and is it possible to describe the Spideranchor bearing capacity for vertical tension loads by adding all expected pull-out force values of each individual rod?"* As already mentioned, research question five is addressed in Chapter 6, including the load case "bending moment" which has been verified in field test two.

3.3.2 Overview, setup and experimental procedure

An easy portable traverse, Figure 38, was designed and constructed to perform load-controlled pull-out tests in the field. A hollow piston cylinder by Enerpac (RACH 3010, max force 286 kN, max. hub 250 mm) controlled by a manual hand pump (WILLE, piston area 14.5 cm²) was used to apply a vertical tension load to the rod. The forced vertical displacements (u_z) of the single rods were measured with the help of an immovable fixed measurement bridge situated around the rod. However, a load cell (HBM) and an analogue dial gauge (KÄFER, u_{max} = 80 mm, resolution: 0.01 mm) was used to measure the applied tension load (F_t) and the vertical displacement (u_z). The full setup can be seen in Fig. 40.

However, an installation tool was developed for the rod installation process which was made of two basic elements, a balance contact area and an installation template. The balance contact area was necessary because of uplift forces due to the rod installation; one person can stand on it as a counterbalance. The installation template was made of 10 cm long iron bushings with an inner thread which fits to the rod threads.

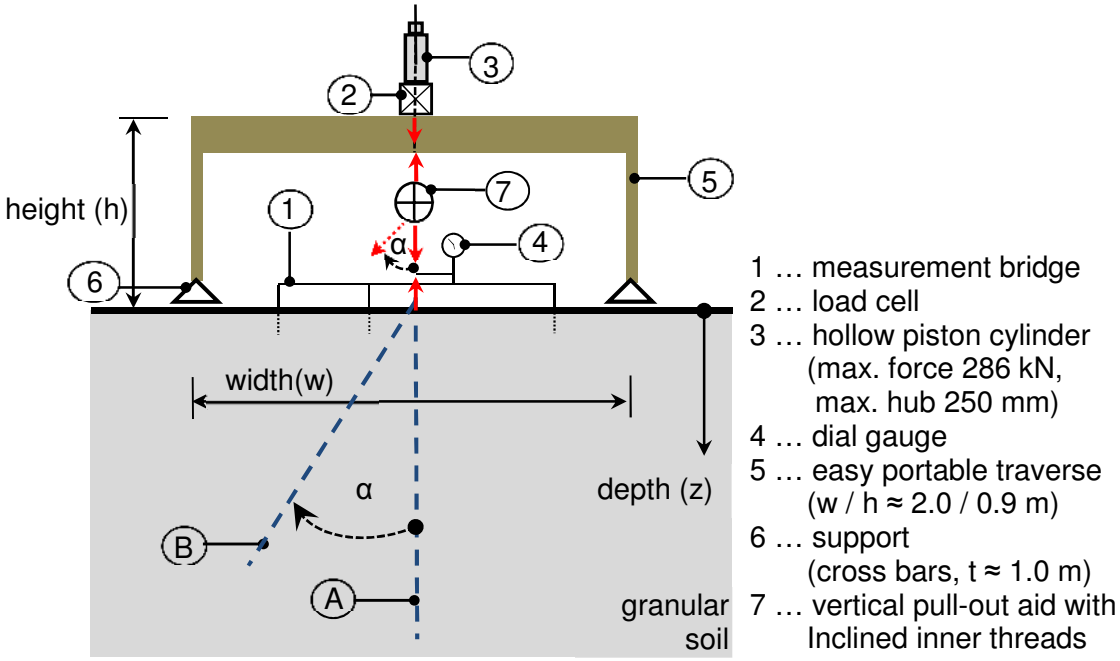

Fig. 38: Setup for the vertical pull-out tests with vertically installed rod, B) inclined installed rod

In order to investigate the bearing capacity of rods with variable inclination, multiple inclined bushings were installed, e.g. inclination (α) is 0 (vertical), 10, 20 and 30. The rods were finally screwed into the subsoil through the bushings with a defined inclination, Fig. 39. In order to pull-out the inclined rods vertically, a stiff vertical pull-out aid was finally developed, Fig. 40.

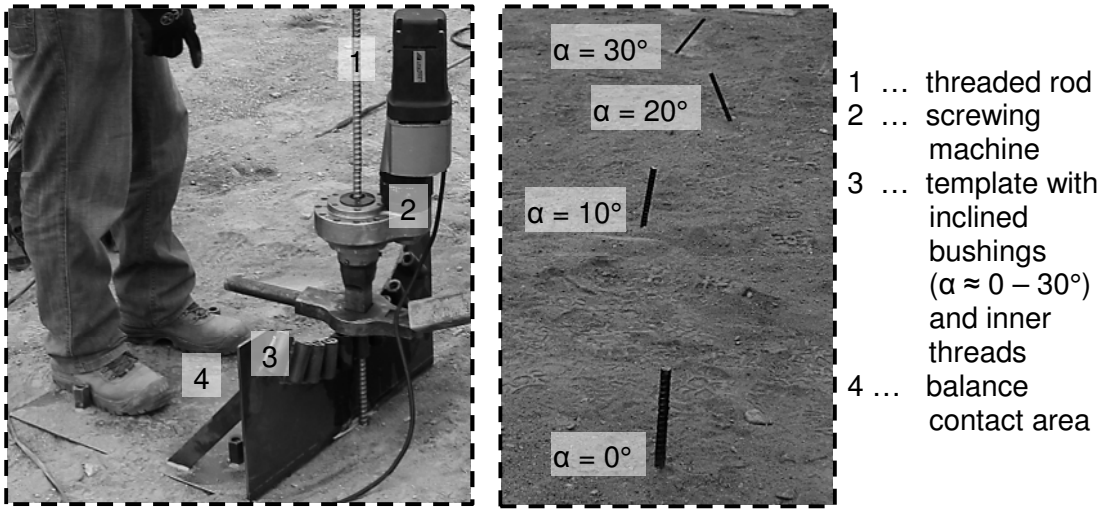

Fig. 39: Left: rod installation process, Right: inclined and vertically installed rods

Pull-out experiments were performed in two different materials, material C and material D. These granular materials are specified in Chapter 3.3.3. A dam was built and compacted in layers by applying material C. This was done to ensure reproducible and mostly homogenous soil properties. This was necessary to

determine the influence of the rod length (l) to the pull-out force with almost homogenous subsoil conditions.

An overview of the experimental investigations within field test two is given in Tab. 11.

Tab. 11: Overview on experimental investigations within field test two

Rod length (l)	Material		Rod pull-out tests[A)] rod inclination (α[B)])			
	C	D	vertical (0°)	10°	20°	30°
2.0 m	☑	☑	☑	☑	☑	☑
2.5 m	☑	☒	☑	☒	☒	☒
3.0 m	☑	☒	☑	☒	☒	☒
4.0 m	☑	☒	☑	☒	☒	☒

[A)] vertical pull-out, type: SAS 900/1100 FA, d = 15 mm, see Tab. 1
[B)] measured normal to the ground surface, Fig. 39

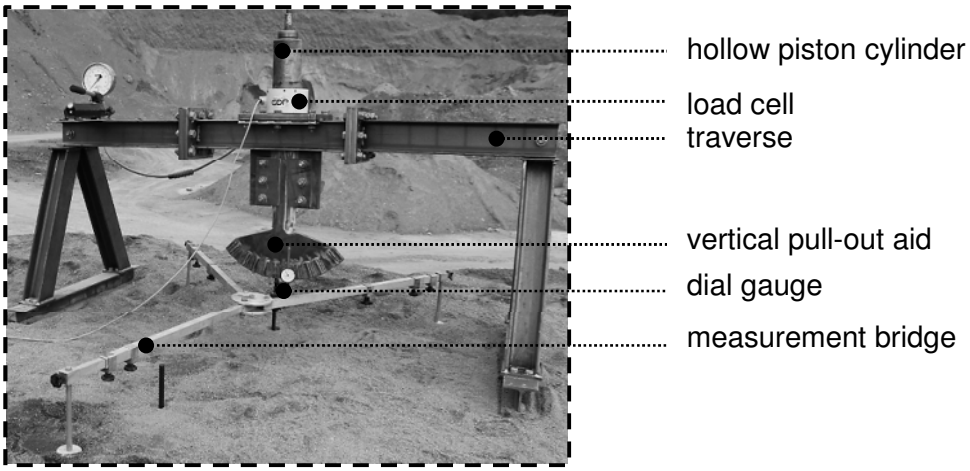

Fig. 40: Realized setup for the pull-out test of field test two

In the following, the experimental procedure of each experiment is given:

a. Installation of the vertical rod (test A) or the inclined rod (test B) by screwing only with the help of an installation template, Fig. 39
b. Positioning of the traverse axially over the rod head and connecting the rod installed before with the vertical pull-out aid, Fig. 40
c. Installation of the load devices, e.g.: hollow piston cylinder, and connecting them with the load cell and the vertical pull-out aid
d. Installation of the measurement bridge and the dial gauge
e. Starting the experiment with the first load step by activating the hydraulic hand pump for the hollow piston cylinder

f. Measuring the vertical displacement after each load step; we waited until the vertical displacements were constant over a period of five minutes. Creeping effects were not investigated
g. Repeating the steps f and g until the final load step could not be applied due to continuously rising displacements. In most of the cases it was not possible to apply the last load step completely

3.3.3 Materials

A testing location in Austria was chosen for field test two, a gravel pit near Murau, Austria. Two different coarse grained materials, material C was gravelly sand and material D was sandy gravel. Material D was naturally grown available with almost constant properties until several meters depth (z). A roughly four meters height dam was built and compacted in layers ($h_{layer} \approx 0.4$ - 0.5 m) with material C.

An extensive soil testing program composed of field and lab tests was executed for both materials. In detail, the following tests were carried out in the field: water replacement tests to determine the in-situ density of the soil (γ_F) and load plate tests.

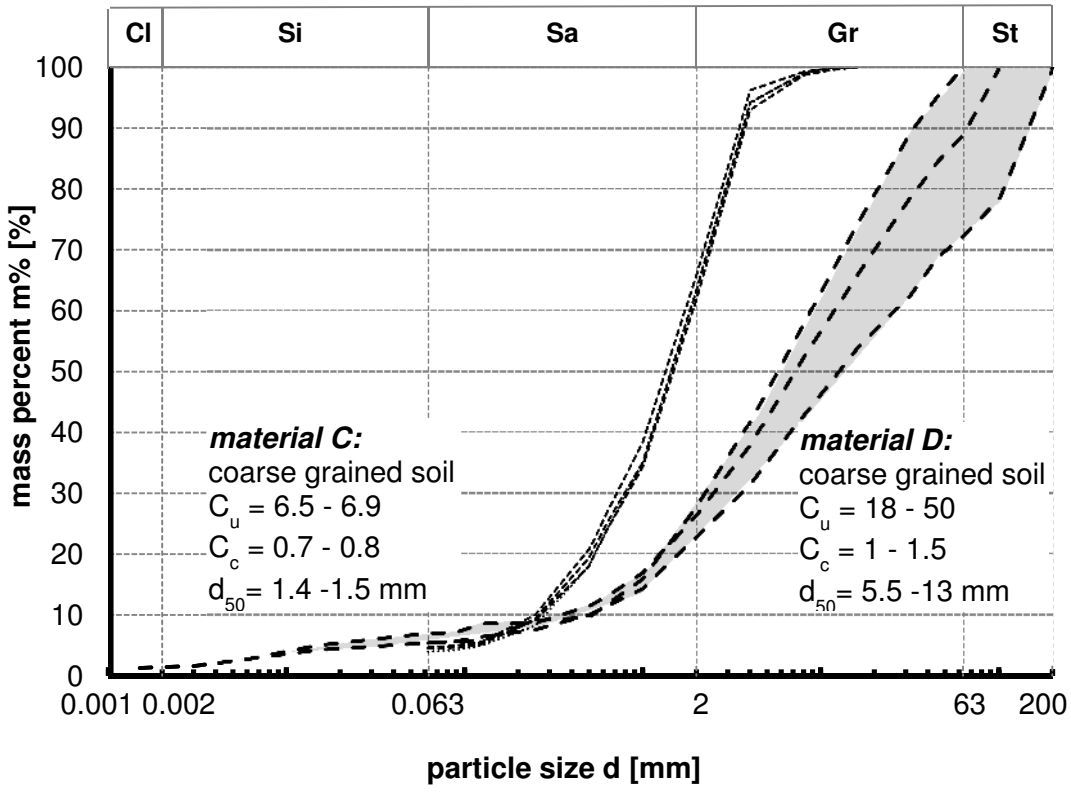

Fig. 41: Grading curve of the material C (left) and the material D (right)

Tab. 12: Material properties of field test 2

Properties	Material type	
	Material C	Material D
Wet weight density γ_F [kN/m³]	19.6	21.2
Dry weight density γ_d [kN/m³]	18.9	20.6
Particle weight density γ_s [kN/m³]	27.8	27.5
Porosity n [-]	0.32	0.25
Density D [-]	0.66 (dense)	1 (very dense)
Saturation S_r [-]	0.22	0.23
Cohesion c´ [kN/m²]	27*)	2.8
Peak friction angle φ´ [°]	37.6	38.9
Load plate test E_{v2}/E_{v1} [-]	2.40 (2.1 - 2.7)A)	2.45 (2.3 - 2.6)B)

A) four tests, one test per meter dam height; B) three tests on the surface
*) Cohesion was measured in direct shear tests and probably forced by interlocking of grains due to the testing procedure

The following tests were carried out in the lab: direct shear tests (material C, 10 * 10 and material D, 30 * 30 cm shear surface), variable lab tests and calculation of physical properties, e.g. dry density (γ_d), particle density (γ_s), saturation (S_r), porosity (n), density (D), sieving and finally determination of uniformity ($C_u = d_{60} / d_{10}$) and curvature coefficient ($C_c = d_{30}^2 / (d_{10} * d_{60})$) of the resultant grading curves. The soil specification is summarized in Tab. 12 and the corresponding grading curves of the materials can be found in Fig. 41.

3.3.4 Results: Vertical and inclined rods

- **Material C:**

Seven single rod pull-out experiments with a vertically applied tension load were conducted in material C, four vertically installed rods and three inclined installed rods pull-out tests, Tab. 13. The slenderness ratio, respectively the rod length (l) of the vertically installed rods and the inclination (α) of the inclined installed rods was varied for the experiments. The force displacement-graphs of the pull-out tests are shown in Fig. 42 and Fig. 43. However, the experiments were executed load controlled with different load levels. The penultimate load level, hence the last fully applicable load level with completed displacements is called pull-out force $F_{t,max}$.

Tab. 13: Single rod pull-out test results, material C

Test no.:	Results: Vertical installed rods		Inclined installed rods		Geometrical properties: threaded rod		
	pull-out force $F_{t,max}$ [kN]	displacement u_z [mm]	pull-out force $F_{t,max}$ [kN]	displacement u_z [mm]	l [m]	λ [-]	α [°]
1	8	9.01			2.0	133	0
2	11	5.36			2.5	167	
3	16	6.15			3.0	200	
4	20	6.00			4.0	267	
5			8	2.70	2.0	133	10
6			7	7.59			20
7			6	6.50			30

The displacements (u_z) to reach the pull-out force ($F_{t,max}$) were measured between 5 to 8 mm. This is comparable to displacements of the rod pull-out tests from field test one (F1, material A) with $u_z \approx 5 - 10$ mm.

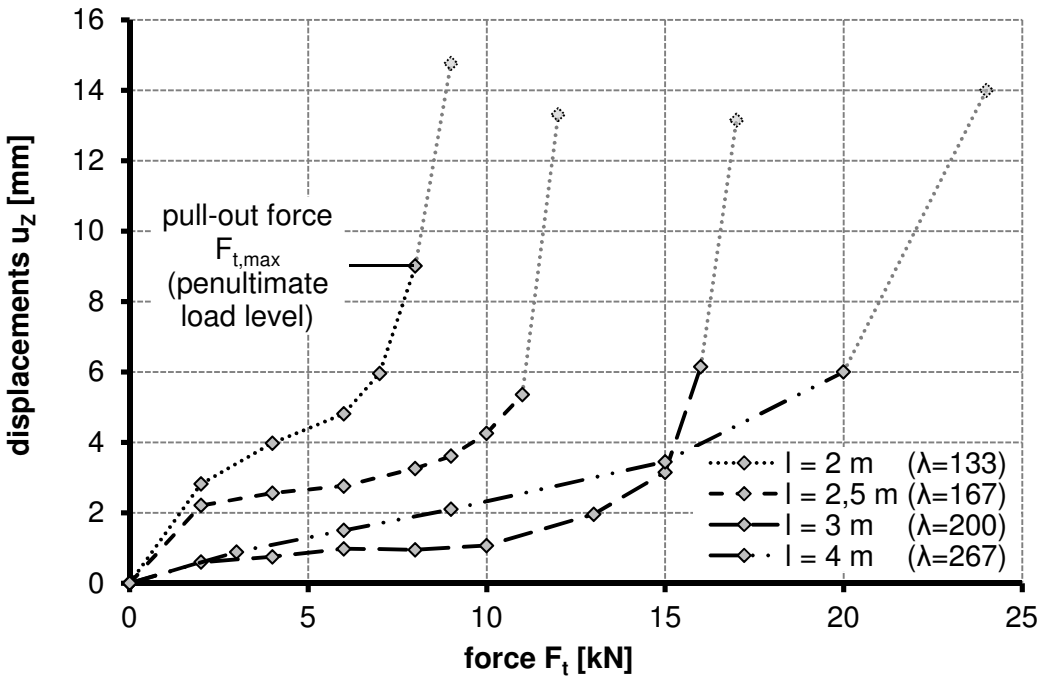

Fig. 42: Results of the vertical rod pull-out tests for material C and variable rod length (l). The last load level is displayed in grey because the forced displacements were still rising up or the load was not completely applicable

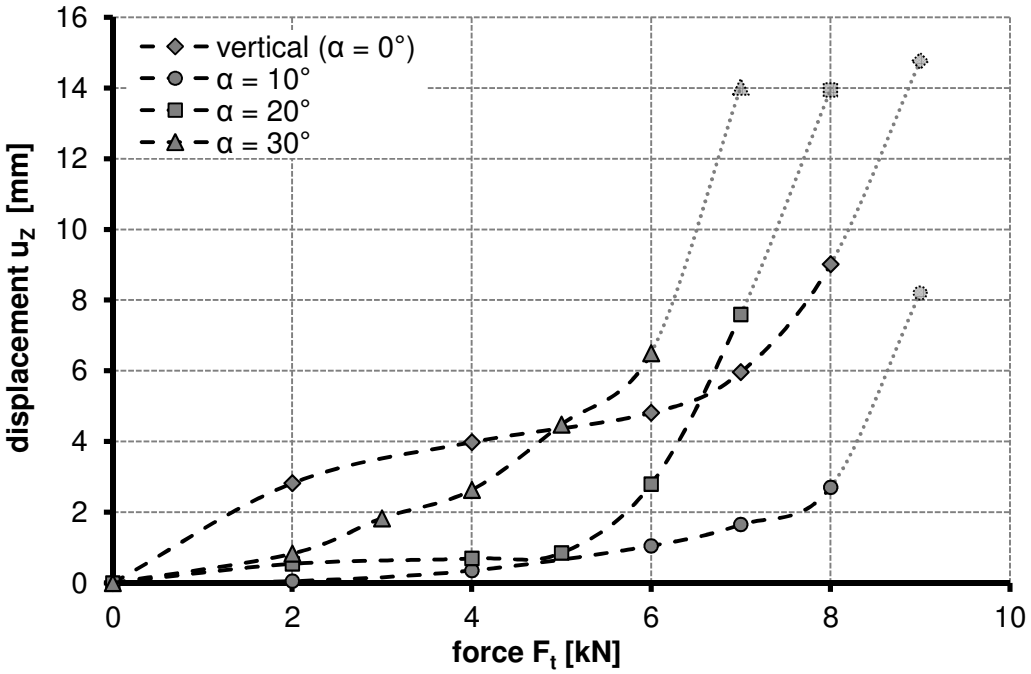

Fig. 43: Results of the inclined rod pull-out experiments for material C and variable inclination (α) , l = 2 m and λ = 133. The last load level is displayed in grey because the forced displacements were still rising up or the load was not completely applicable

It is noted that the pull-out force ($F_{t,max}$) decreases with increasing rod inclination (α), if the rod length (l) is constant. Hence, the bearing capacity of inclined rods is significantly weaker compared to the bearing capacity of vertically installed rods.

- **Material D**

Four single rod pull-out tests with a vertically applied tension load were conducted in material D, one vertically installed rod and three inclined installed rods, Tab. 14.

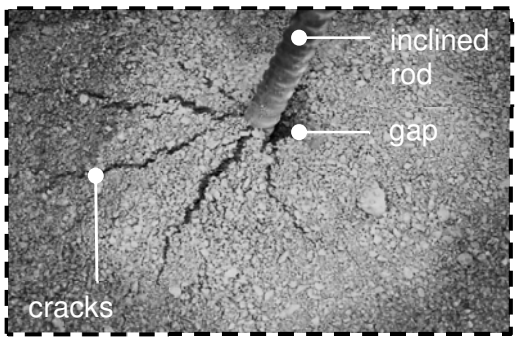

Fig. 44: Observed cracks on the surface (passive side) of material D after pulling out an inclined rod. A superficial gap opens on the backside of the rod (active side)

Tab. 14: Single rod pull-out test results, material D

Test no.:	Results:				Geometrical properties: threaded rod		
	Vertically installed rods		Inclined installed rods				
	pull-out force $F_{t,max}$ [kN]	displacement u_z [mm]	pull-out force $F_{t,max}$ [kN]	displacement u_z [mm]	l [m]	λ [-]	α [°]
1	56	8.12			2.0	133	0
2			56	4.08			10
3			48	7.54			20
4			33	10.00			30

The inclination (α) of the inclined installed rods was varied for the experiments and the force displacement-graphs of the pull-out tests are shown in Fig. 45.

It is impressive to note that the rod bearing capacity in material D is very high, especially when considering the relatively short rod length (l) of only two meters. A possible reason for this is the highly compacted testing material. The displacements ($u_z \approx 4 - 8$ mm) are also in a similar range like the displacements of the pull-out tests in material A and C.

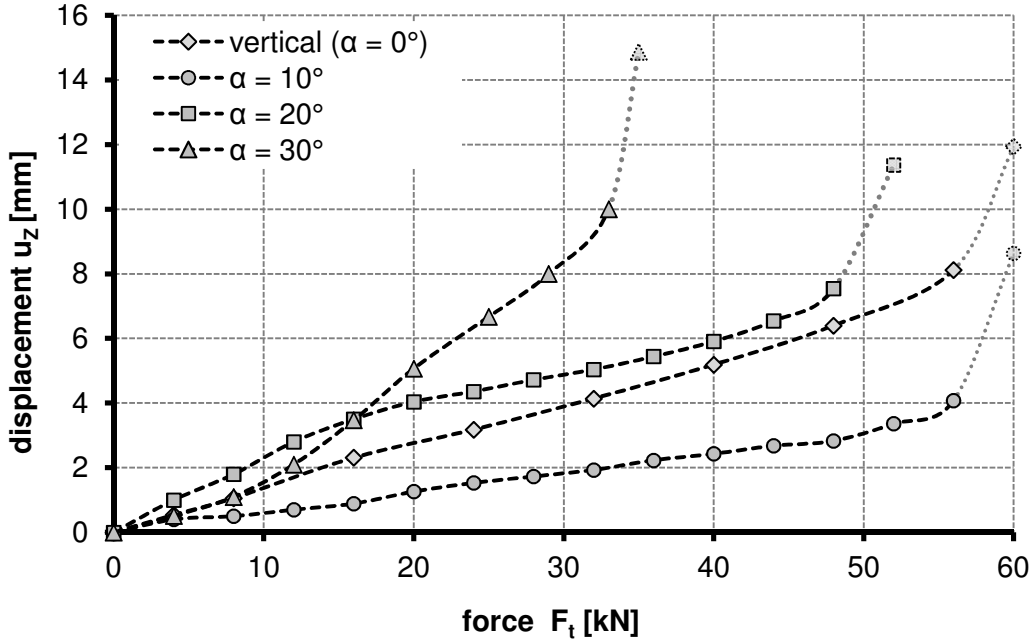

Fig. 45: Results of the inclined rod pull-out experiments for material D and variable inclination (α), l = 2 m and λ = 133. The last load level is displayed in grey because the forced displacements were still rising up or the load was not completely applicable

To conclude, a superficial gap between the backside of the rod and the subsoil opens (active side) and cracks (passive side) on the surface created by conducting pull-out tests of inclined rods, Fig. 44. The soil placed directly above the inclined rod was partly lifted up during the vertical pull-out experiments. It is pointed out that the cracks were also observed after the inclined rod pull-out tests in material C.

3.3.5 Comparison of results and discussion

Figure 46 illustrates the influence of the rod length (l) and the pull-out force $F_{t,max}$ for material C and vertically installed rods. A linear increase of the pull-out force with increasing rod length until $l \approx 3$ m is observed. For longer rods the increase is significantly weaker and it seems that for rod length longer than $l > 4.5$ m no relevant increase can be expected. This is also observed for grouted anchors in coarse grained granular material. Only a minor increase of the pull-out force for longer grouted sections than 8 m can be expected, Ostermayer (1975).

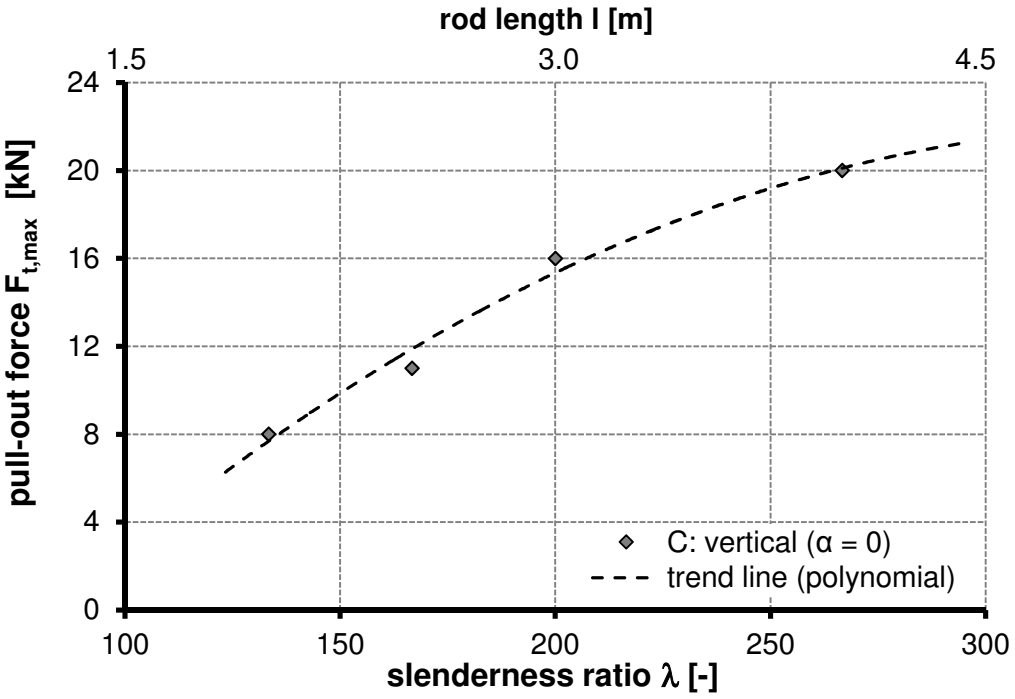

Fig. 46: Influence of the rod length (l) and the pull-out force $F_{t,max}$ for material C.

To conclude, a reason for an almost constant pull-out force of rods with longer rod length could be a progressive shear failure process. In other words, the shear stresses on the rod's surface are not fully mobilized simultaneously along the rod, depending on the normal stresses level, the elastic rod elongation and the relative displacements. However, details about the progressive shear failure can be found in Iten (2011).

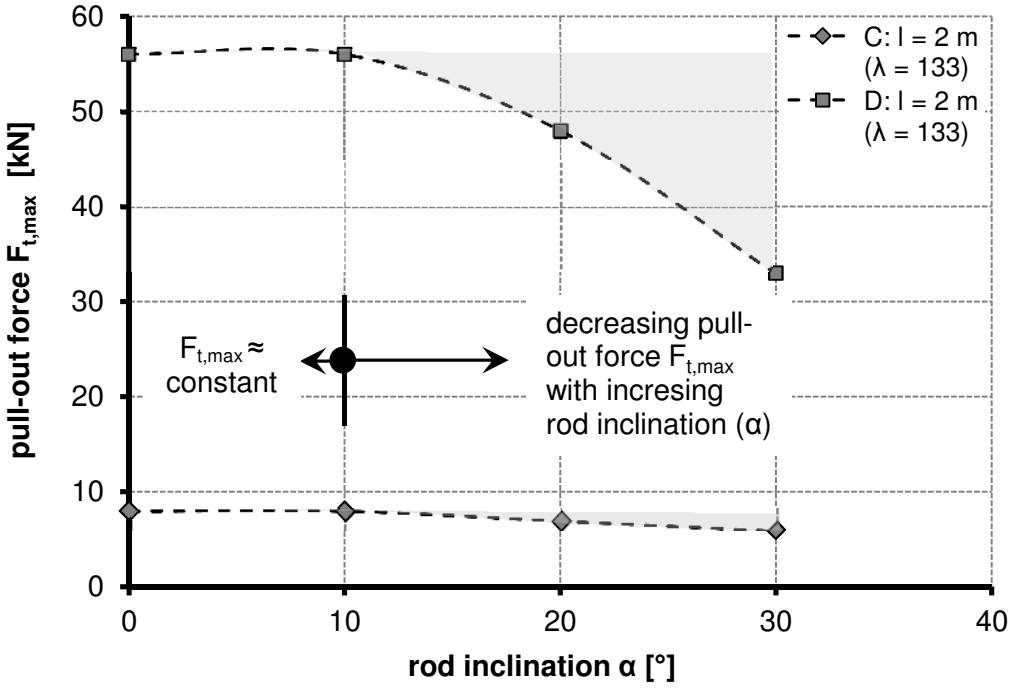

Fig. 47: Influence of the rod inclination (α) and the pull-out force $F_{t,max}$ for both materials, l = 2 m and λ = 133.

Figure 47 shows the influence of the rod inclination (α) and the pull-out force ($F_{t,max}$) for both materials (C and D) and constant rod length (l). The pull-out force remains almost constant until a rod inclination of α ≈ 10. This is reasonable because the final depth (z) of the rod end is nearly constant for all rod inclinations with less than 10°. Moreover, the resulting normal and horizontal stresses on the rod's surface change insignificantly compared to the stress conditions of vertically installed rods. For greater rod inclinations of α > 10° a significant decrease of the rod pull-out force can be observed e.g.: Material D: $F_{t,max}$ ≈ 56 kN for α = 0° and $F_{t,max}$ ≈ 32 kN for α = 30°.

In general, to address research question four (Q4), a relationship between pull-out forces of vertically and inclined installed threaded rods is worked out for sandy and gravelly material.

3.3.6 Comparison of literature and discussion

In Chapter 3.2.7, a comparison of calculated pull-out forces based on different design approaches and the results of field test one was done with little success. The calculated pull-out forces did not fit the testing results. In this context, a comparison of test results for vertically installed rods gained from field test two with calculated pull-out forces has been done, because no conformity has been expected.

However, a literature comparison on the influence of the rod inclination to the pull-out force is done in this section. In detail, the test results are compared with the results by Hanna and Afram (1986) because similar boundary conditions like for field test two were available. Hanna and Afram (1986) conducted axial pull-out tests in the lab of variable inclined, driven steel piles with a constant pile length (l) of l ≈ 1.5 m. The smooth surface of the tested piles was prepared by gluing sand paper on it and the diameters of the steel piles were d = 76 (λ ≈ 20) and d = 38 mm (λ ≈ 40). A medium uniform sandy material called "Morie sand" was applied for the tests with the following properties: peak friction angle φ´ = 39° and a unit weight of γ_F = 15.6 kN/m³ (D = medium density). Figure 48 illustrates the results of the comparison between Hanna and Afram (1986) and field test two.

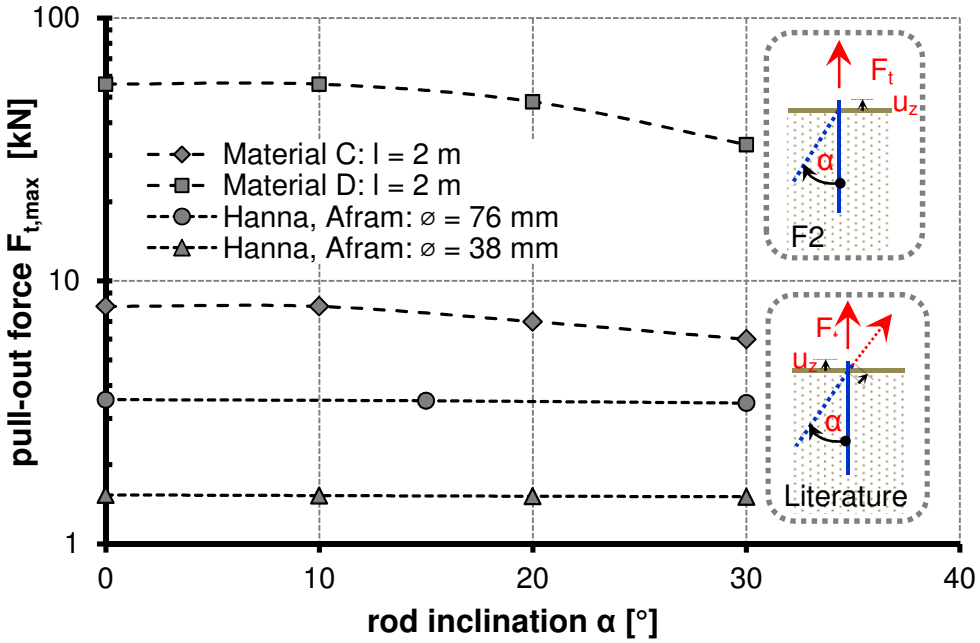

Fig. 48: Influence of the rod inclination (α) and the pull-out force $F_{t,max}$ (log-scale) of the field test two (F2) and of Hanna, Afram (1986). The pulling direction is vertically for the field test two and axial for Hanna and Afram. The rod length is constant for F2 (l = 2m; λ = 133) and for Hanna and Afram (l = 1.5 m; λ = 20-40).

The pull-out force decreases slightly or remains almost constant with increasing rod inclination for both tested pile diameter of Hanna and Afram e.g.: Ø 76: $F_{t,max}$ = 3536 N for α = 0 and $F_{t,max}$ = 3430 N for α = 30°. In contrast to field test two where the pull-out force decreases significantly with increasing rod inclination, for both materials. The main reason for this can be the load direction which is always vertical for field test two but axial for Hanna and Afram.

The pull-out forces of the driven steel piles in the sandy material ("Morie sand") are significantly lower compared to the tested threaded rods in the sandy

material C. This is especially of interest for the vertical rods, which were pulled out axially for F2 and the literature. However, the diameter of the threaded rod of F2 is between 2.5 and 5 times smaller compared to Hanna and Afram and the rod length of F2 is 50 cm longer compared to Hanna and Afram.

To conclude, the soil density (D) is different for F2 (dense) and Hanna and Afram (medium dense), which can be a reason for the different test results.

3.4 Lab test 1

3.4.1 Introduction and literature review

The main objective of lab test one (L1) was to address the research questions one to four (Q1 – Q4). This was done by conducting pull-out tests of single rods. Particular attention was paid to the soil displacements due to the installation and pull-out process. In detail and in addition to the field tests (F1 & F2) further data on the load bearing behaviour of vertically (Q1) and inclined (Q4) installed rods were gained. However, the soil-rod interactions due to the installation (Q3) and the pull-out process (Q2) were additionally analysed. In particular, it was tried to visualize an attached soil body due to the rod pull-out process, if existing. For that reason, a transparent soil model was developed which allowed a three-dimensional insight into the soil in order to understand the complexity of the soil-rod interactions. This was especially useful because three-dimensional effects occur due to the rod installation and pull-out process, by reflecting the results of the literature review in Chapter 2.1.

Half or quarter symmetric experimental models as well as plain strain experimental models are in the authors point of view only suited with restrictions to investigate the actual rod behaviour. The necessary boundary conditions for such an experiment, e.g. completely smooth model side border, are very difficult to realize and can only be seriously addressed with a reasonable numerical model, e.g. FEM. In this context, it is pointed out that the experiments in lab test one were executed with the full cross sectional area of the threaded rod.

However, a transparent soil model consists basically of two components, a double porous silica material and a suitable pore fluid. Both components have the same refractive index and the silica material becomes fully transparent if completely saturated with the pore fluid, Mannheimer and Oswald (1993), Iskander (2010). It is possible to produce two kinds of transparent soils, coarse grained and fine grained transparent soil. In general, silica gel is applied for

simulating coarse grained soil and silica powder for fine grained soil. Lab test one deals with silica gel with comparable soil mechanical properties as fine gravelly material.

To visualize the soil displacements within a transparent soil model, a laser light sheet producing laser source is needed. The laser light sheet illuminates the rigid silica gel particles of the transparent soil and so called “speckles”, Figure 49, can be observed through an observation window by using a CCD-camera. The laser light sheet moves through the transparent soil model before (time t_1) and after (time t_2) an experiment has been done. Pictures of the same laser light sheet position are analysed and compared with PIV (Particle Image Velocimetry). Details concerning the PIV method can be found in Raffel et al. (2007). Finally, the analysed pictures of many slices are put together and a kind of three dimensional insight is given, Liu and Iskander (2009), Hird and Guymer (2010), Iskander (2010), Ahmed and Iskander (2011), Siemens and Peters (2011), Ezzein and Bathurst (2011).

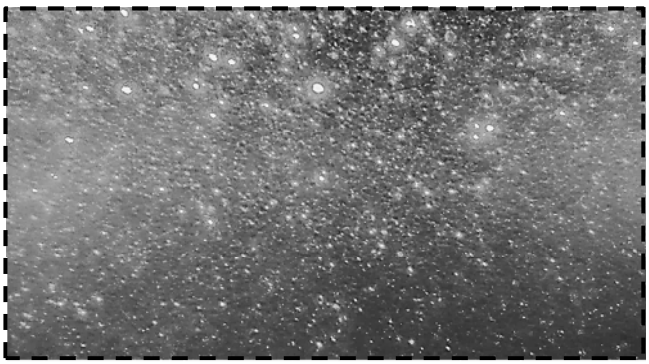

Fig. 49: Picture of observed “speckles”

Several investigations based on a transparent soil model were executed in the last years. A very brief overview is given in the following.

The displacements under a model footing in a fine grained transparent soil model were observed from Liu and Iskander (2009). The model box size was about h * w * t ≈ 50 * 300 * 150 mm (height h, width w, deepness t) and the footing about w * t ≈ 50 * 25 mm.

Hird and Guymer (2010) investigated the effects of pile driving of cylindrical model piles in a fine grained transparent soil model. The model box size was about h * w * t ≈ 300 * 100 * 100 mm and h * w * t ≈ 300 * 100 *50 mm, the model pile radius was about r ≈ 4 mm and the corresponding length was up to 80 mm.

Ahmed and Iskander (2011) analysed tunnelling-induced ground movements by shallow tunnels in a coarse grained transparent soil model. The test box size was approximately h * w * t ≈ 200 * 300 * 250 mm and the tunnel tube was made of PVC with a diameter of 25 mm.

Siemens and Peters (2011) investigated a drawdown in a granular transparent soil model. The model size was about h * w * t ≈ 1300 * 45 *45 mm.

By reflecting the dimension of the transparent soil models above it is pointed out that the model size is limited. This is because of transparency degradation which occurs with greater model deepness, Mannheimer and Oswald (1993), Iskander (2010). The reason for this is the container material or the observation window which does not fit into the refractive index of the transparent soil and small bubbles of air which have not risen to the surface yet, Ezzein and Bathurst (2011). Further reasons are the strong temperature dependence of the refractive index and the fact that the refractive index of the pore fluid and the silica material do not match to one hundred percent, Iskander (2010). Ezzein and Bathurst (2011) mentioned that the clearly visible deepness (t) is limited to approximately 120 mm for coarse grained transparent soil.

3.4.2 Overview, setup and experimental procedure

A traverse with a spindle-gear on the top was constructed to perform path-controlled (velocity ≈ 0.33 mm/s) vertical pull-out tests in the lab, Fig. 50. A load cell (HBM, max. force 10 kN, measurement error ± 0.2 %) and an inductive displacement transducer (HBM, 1-WA/50MM-T, max. displacement 50 mm, measurement error ± 0.2 %) were applied for the experiment to measure the forced vertical displacements (u_z) and the vertical tension load (F_t). The load cell and the displacement transducer were finally connected to a data logger (HBM, Spider 8). The data logger was connected to a computer to collect the data produced during the pull-out experiment.

Moreover, a model container (w * h * t ≈ 50 * 100 * 25 cm) made of steel was built for the experiments with a black polytetrafluoroethylene (PTFE, commercially known as “Teflon”, thickness $t^* = 0.13$ mm) film inner-lining. The PTFE film was especially useful to prevent possible reflections of the laser light on the steel surface of the container. The front of the container was made of glass and is called observation window, Fig 52.

In order to guide a laser light sheet through the transparent soil model a laser guide bar with a laser source including a line generator (constant wave (cw), 3.7 W, $\lambda_l = 532$ nm → green laser beam, opening angle 75°) was installed above the model container, Fig. 52. A CCD-camera (Prosilica GX 1910, 2 *MP*, 63 fps) was positioned in front of the observation window to make pictures of the moving laser light sheets. A specially developed informatics program and a

motion detector ensured that the laser position was synchronized with the CCD-camera and that finally only pictures of the same laser light sheet position were compared and analysed with PIV. However, more details concerning the experimental set-up can be found in Poprask (2014).

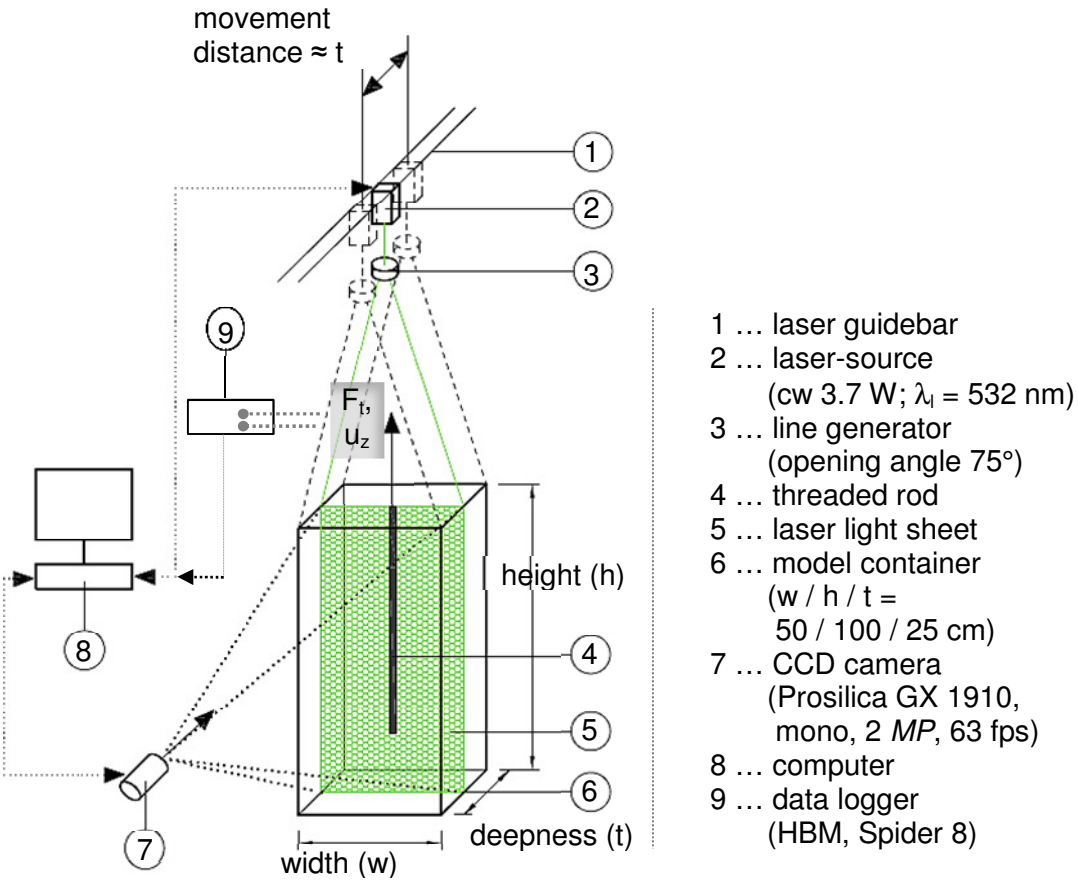

Fig. 50: Setup for the investigations based on a transparent soil model

The model container was filled in layers ($h_{layer} \approx 5$ cm) with the transparent soil and the silica gel was therefore pre-saturated with the pore fluid. In order to ensure best transparency effects, fine powder and smallest impurities were removed from the silica gel in advance by sieving. A shake motor installed underneath the model container was activated after each installed layer to ensure constant density. Anyway, the maximum and minimum inter-particle porosity vary only little ($n_{max,ip} = 0.28$ and $n_{min,ip} = 0.26$), almost constant density can be assumed for that reason.

The rods were installed inclined and vertically through a bushing for lab test one, similar to the field tests, Fig 51.

Pull-out experiments were performed with variable rod length (l = 0.5 – 0.7 m) and variable inclination. The inclination was only varied for the 50 cm long rod. Two kinds of rod types were investigated a rough (threaded rod: SAS 900/1100 FA, d = 15 mm) and a smooth (d = 15 mm) one. However, the installation process was only investigated for the rough rod with 50 cm length.

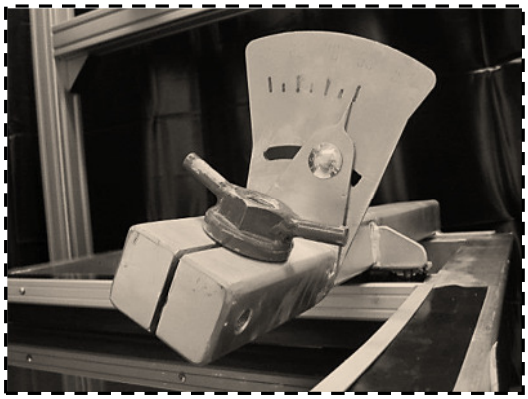

Fig. 51: Installation aid for lab test one

It is pointed out that the model container was only filled with the transparent soil once; hence all experiments were conducted with the same transparent soil model. An overview of the experimental investigations within lab test one is given in Tab. 15.

Tab. 15: Overview on experimental investigations of lab test one

Rod length (l) *(λ)*	Rod type[A]		Rod pull-out tests rod inclination					
	rough[B]	smooth[C]	vertical (0°)	5°	10°	15°	25°	30°
50 cm *(33)*	☑ +i	☑	☑	☑	☑	☑	☑	☑
70 cm *(46)*	☑	☑	☑	☒	☒	☒	☒	☒

[A] diameter d = 15 mm; [B] threaded rod type: SAS 900 / 1100 FA; [B] completely smooth steel rod without threads or rips; +i including rod installation process

In the following, the experimental procedure for each experiment is given:

a. In case no installation effect has been investigated, starting with b, otherwise: Activating the laser and guiding the laser light sheet through the transparent soil model while the CCD-camera made pictures
b. Installation of the relevant rod through the bushing by using a screwing machine
c. Connecting the top of the rod with the spindle-gear and installing the load cell and the inductive displacement transducer
d. Activating the laser and guiding the laser light sheet through the transparent soil model while the CCD-camera made pictures
e. Starting the pull-out experiment until $u_z \approx 2.5$ mm vertical displacement was reached by activating the spindle gear
f. Deactivating the spindle gear
g. Activating the laser and guiding the laser light sheet through the transparent soil model while the CCD-camera made pictures
h. Repeating step e to g each $\Delta u_z \approx 2.5$ mm until $u_z \approx 50$ mm total displacements were reached
i. Removing the tested rod from the transparent soil model

j. Activating the shake motor installed underneath the model container for five minutes
k. Starting the next experiment

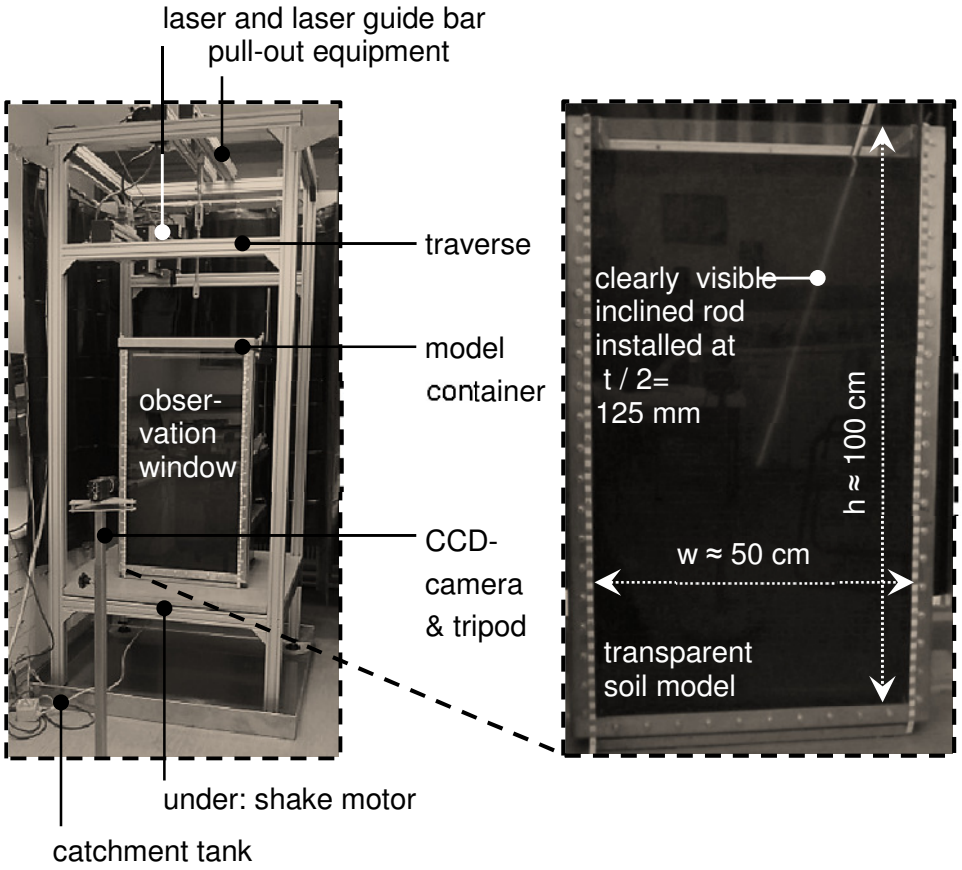

Fig. 52: Setup realized for the transparent soil experiments

3.4.3 Material

In this chapter, the materials applied for lab test one are specified and the refractive index n_D of the materials is introduced.

- **Refractive index**

The refractive index of a material (n_D) is defined by the ratio of the speed of light in vacuum (c) and the speed of light in the tested material (v), Equation 21. By assuming that the speed of light in vacuum is approximately the same as in air, the refractive index of a material can also be understood as the ratio between the angle of incidence (α_s) and the angle of refraction (β_s) of light if entering a material, Snell´s law. The refractive index is highly dependent on the temperature level of the material. However, usually the refractive index of a material is measured with a room temperature of 20 °C, in case a different temperature is chosen it is indicated as follows, e.g.: for 25°C, $n_{D,25}$.

$$n_D = \frac{c}{v} = \frac{\sin(\alpha_s)}{\sin(\beta_s)} \tag{21}$$

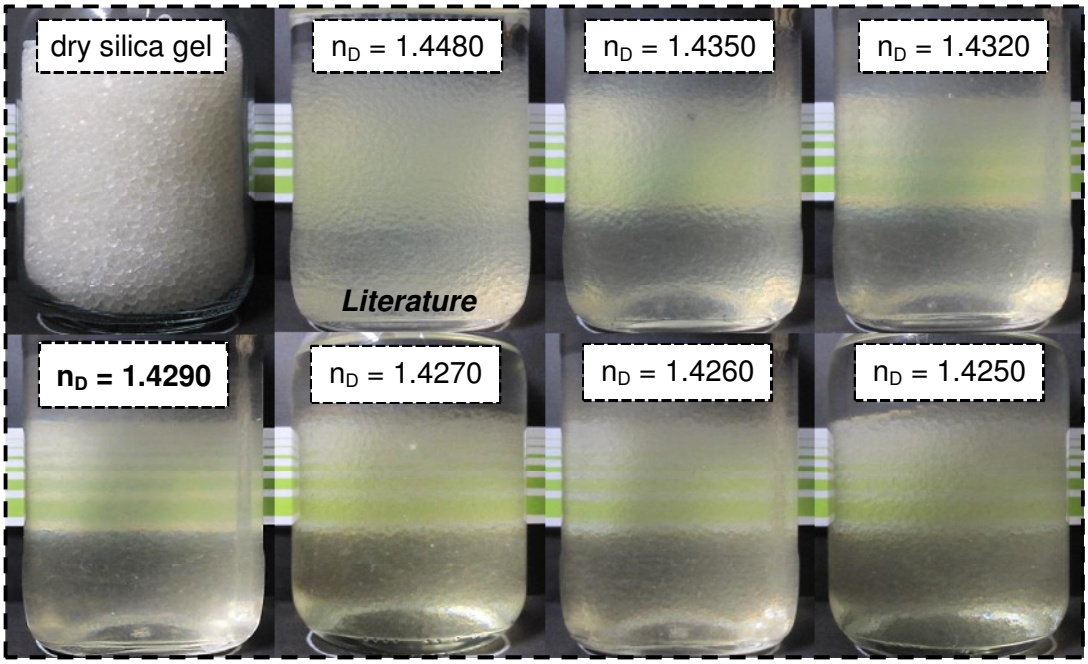

Fig. 53: Influence of refractive index (n_D) to the transparency effect, Poprask (2014). The best match of the refractive index from the pore fluid and the silica gel was found with n_D = 1.4290, in contrast to the literature with $n_{D,25}$ = 1.4480, Iskander (2010)

To determine the refractive index of a solid material following modified procedure according to Mannheimer and Oswald (1993) was applied: Firstly, a defined fluid was prepared. Secondly, the refractive index of the fluid was determined. Thirdly, a small amount (≈ 400 g) of silica gel was saturated with the prepared pore fluid. Fourthly, the transparency effect was checked, Fig. 53. Finally, repeating step one to four until the best match of the refractive index was found, where the saturated silica gel visually almost completely disappears.

The determined refractive index of the applied silica gel is n_D = 1.4290 ($n_{D,25}$ = 1.4255) and different compared to the literature $n_{D,25}$ = 1.4480. This fact can be the result of slightly different additives for the silica gel production because a different manufacturer of the silica gel in comparison to other researchers was chosen.

- **Silica gel**

Silica gel is an amorphous granular form of silicon dioxide (SiO_2) which is synthetically produced and usually spherical shaped, Fig. 54. It is insoluble in water, inert, relatively light weighted and highly porous with a very large surface area, Liu and Iskander (2009). The pores of the silica gel particles are

connected and open and the result of interconnected nano-particles with measured diameters between approximately d = 3 – 6 nm, Mannheimer and Oswald (1993).

The silica gel applied within lab test one is commercially produced by the company "ThoMar OHG, Germany" and generally used as a desiccant.

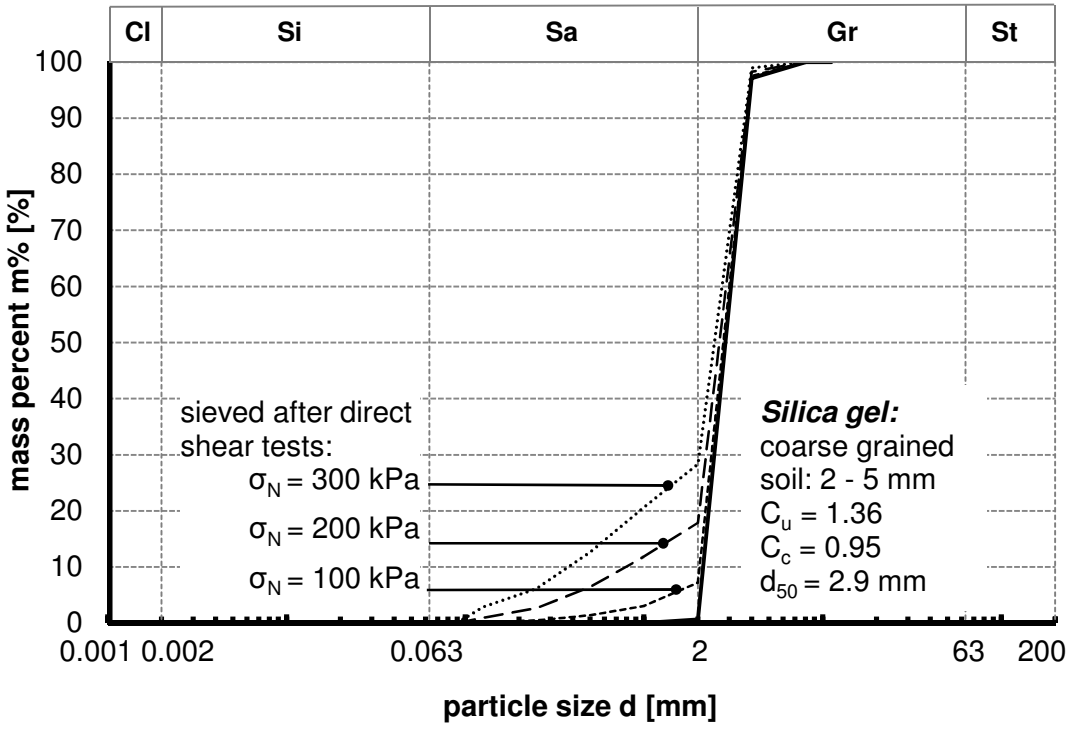

Fig. 54: Grading curve of the applied silica gel, including the sieving results after the direct shear tests. Variable normal stress (σ_N) levels were applied

An intense soil testing program was executed to determine the soil mechanical properties of the silica gel, Tab. 16. An accelerated surface area and porosimetry (ASAP) analyser was applied to determine the particle porosity of the silica gel.

The grading curve was determined by sieving and can be found in Fig. 54. However, after executing direct shear tests (10 * 10 cm shear surface) the sieving of the material was repeated and particle breakage was observed which increases with increasing normal stress level.

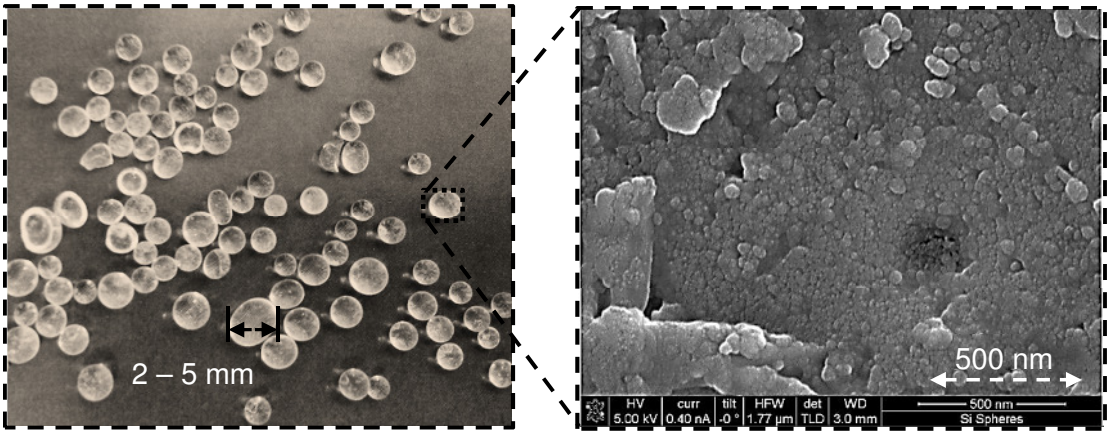

Fig. 55: Left: Dry silica gel particles; Right: Very strong enlargement of the particle surface

Tab. 16: Material properties of the lab test 1

Properties		Material type Silica gel
Dry weight density γ_d [kN/m³]		8
Particle weight density γ_s [kN/m³]		11
True weight density γ_M [kN/m³]		20.6
Refractive index n_D [-]		1.4290
Porosity:	total n_{tot} [-]	0.61
	particle n_p [-]	0.34
	inter particle n_{ip} [-]	0.27
Density D [-]		0.5 – 0.67 (medium dense)
Particle pores [cm³/g][B)]		0.425
Particle surface area [m²/g][B)]		759.6
Cohesion c´ [kN/m²]		≈ 0
Peak friction angle φ´ [°]		35.5
Oedometer modulus[A)] E_s [MPa]		30.6

[A)] normal stress level σ_N = 80 – 160 kPa
[B)] measured with ASAP (Accelerated Surface Area and Porosimetry analyser)

- **Pore fluid**

As already introduced, transparent soil is a mixture of two components with the same refractive index, the silica gel and the pore fluid. In order to apply a pore

fluid for a soil mechanical model following conditions must be met: *"(1) Kinematic viscosity identical to or close to that of water; (2) surface tension close to that of water; (3) incompressibility; (4) affordability; (5) low or no interaction with the silica gel and the model container,* Zhao (2007)*"*. At this time there is no pore fluid commercially available which matches the refractive index of the silica gel. A two-component pore fluid was therefore produced which is made of a base fluid with a greater refractive index and a secondary fluid with a lower refractive index as necessary. However, very intense investigations were executed to check several pore fluids and their suitability for a transparent soil model. The results of the investigations are summarized by Poprask (2014). The best-suited pore fluid which was finally applied for lab test one was made of 53.5 m% of Toulon (C_7H_8) and 46.5 m% of 2-Propanol (C_3H_8o) and was made of the same fluids as the transparent soil models of e.g.: Zhao (2007) and Iskander (2010).

After identifying the best suited pore fluid, an intense fluid characterisation was done, Poprask (2014). The pore fluid properties were analysed for a room temperature of 20°C and summarized in Table 17.

Tab. 17: Properties of water and the applied pore fluid, according to Poprask (2014)

Properties	Fluid type	
	Pore fluid	Water
Density ρ [g/cm³]	0.82	1.0
PH-value [-]	7	7
Surface tension σ [mN/m]	19.76	72.75
Dynamic viscosity η [kg/s*m]	0.0011	0.0010
Kinematic viscosity v [mm²/s]	1.312	1.004
Permeability [A)] k_f [m/s]	6.32e-4	8.26e-4
Refractive index n_D [-]	1.4290[B)]	1.3330

[A)] through silica gel of Table 16; [B)] $n_{D,25} = 1.4255$

It is pointed out that it is harmful to health when dealing with the pore fluid especially inhaling and contact with the skin. Safety regulations are required therefore e.g.: wearing of protective suits and breathing protection. However, nowadays new transparent soil developments can be found where new materials are applied with less or no safety concerns, Bathurst (2014).

3.4.4 Results

The results of lab test one are subdivided into the following investigation categories:

a) Installation effect
b) Pull-out process

The results of the installation effect investigations are basically the visualized soil-rod interactions, hence, the soil-displacements due to the rod installation.

The results of the pull-out investigations are the force-displacement graph and the visualized soil – rod interactions. In accordance with field test one, the (first) maximum of the force-displacement graph is called pull-out force ($F_{t,max}$).

In order to visualize the soil-rod interactions, a PIV-software (PIVlab a time-resolved digital Particle Image Velocimetry tool for MATLAB; Version: 1.35) was used. In general, four slices of the executed experiments - depending on the model deepness (t) - were analysed with PIV and total displacements are shown. For the final slice of the PIV analysed soil-rod interactions slices a separation between the vertical and horizontal displacements is shown and a section is marked for the vertical rods. The displacements along the section plane are finally additional analysed and visualized. However, the end of the threaded rod is marked with a bright dot.

It is pointed out that all rods were installed axially at half deepness of the model container, hence at t = 12.5 cm deepness. The laser light sheet slices were analysed until a maximum deepness of t =11 cm, approximately 7 mm before the rod surface. The reasons for this are laser light reflexions on the surface of the rod and the mentioned transparency degradation, which also prevents the analysis of the slice which belongs to the rod axis.

- **Installation effect:**

As already mentioned, the installation effect was investigated for the rough rods only and the results are presented for the 50 cm long rod, vertically and inclined ($\alpha = 15°$) installed.

a) Vertical rod

Figure 56 illustrates the total displacements of the PIV analysed slices (t = 0.2; 4 and 8 cm) after the full rod installation of the 50 cm long vertical rod. The vertical (v) and horizontal (u) displacements due to the soil-rod interactions are separately visualized for the slice corresponding to the deepness t = 8 cm. Settlements (+v) close to the rod end and material heaving (-v) around the upper

rod section are observed when looking at the illustrated vertical displacements. The horizontal displacements show relative symmetrical horizontal soil replacements which are present slightly deeper than the rod end. However, the analysed displacements along the marked section plane A-A can be found in Fig. 57. A so called neutral level at approximately z / l ≈ 0.8 where the vertical displacements are zero (v = 0) occurs. Settlements occur below the neutral level until approximately, z / l ≈ 1.5, 25 cm below the rod end. However, the investigated vertical displacements (v) are especially present in the upper section of the rod. Almost 2/3 of the vertical displacements are activated in the first third of the rod length only, hence in the first 17 cm of the rod.

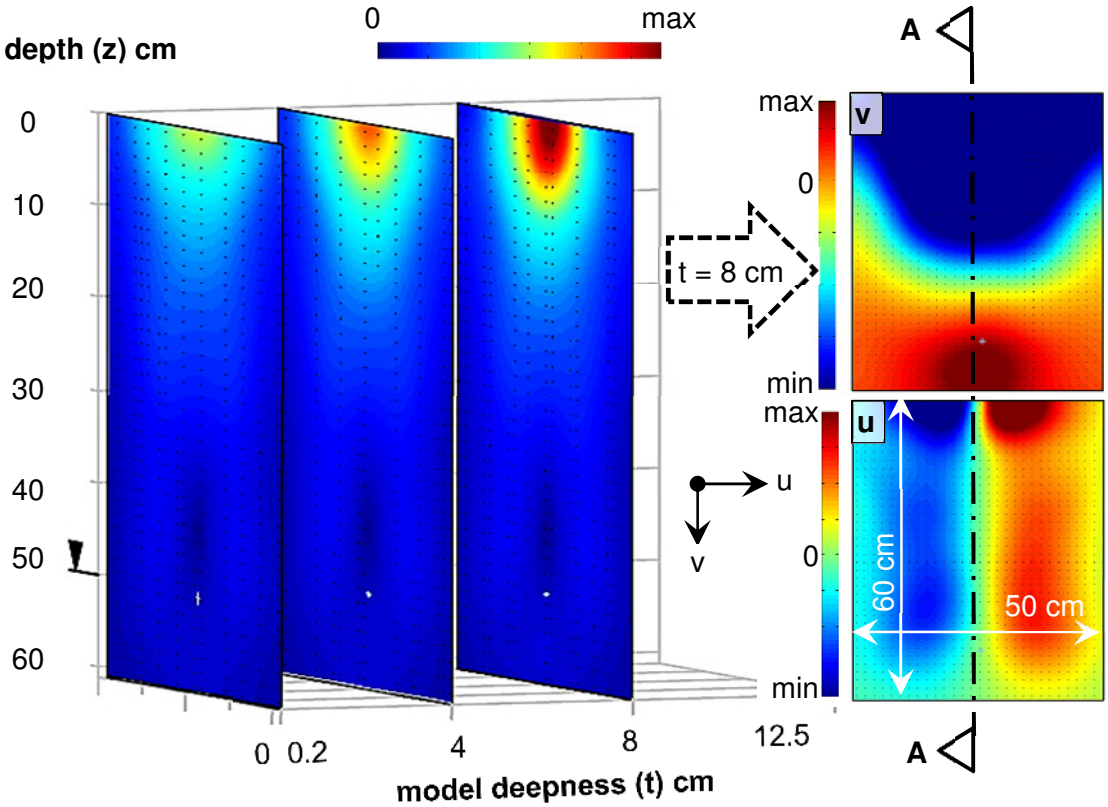

Fig. 56: Visualized soil-rod interactions due to the installation of the vertical threaded rod, l = 50 cm and λ = 33. Left: total displacements for the different slices, depending on the model deepness (t); Right: separation between the vertical (v, +v settlements; -v heaving) and horizontal (u) displacements for the slice which belongs to the model deepness t = 8 cm.

The vertical displacements below the first third of the rod length are drastically reduced. The same effect can be observed for the horizontal displacements as well, which are maximum 10 % of the vertical displacements. A possible reason for this is a small crater or little mounts which occur on the ground surface due to the installation process of the rod, depending on the density (D) of the soil.

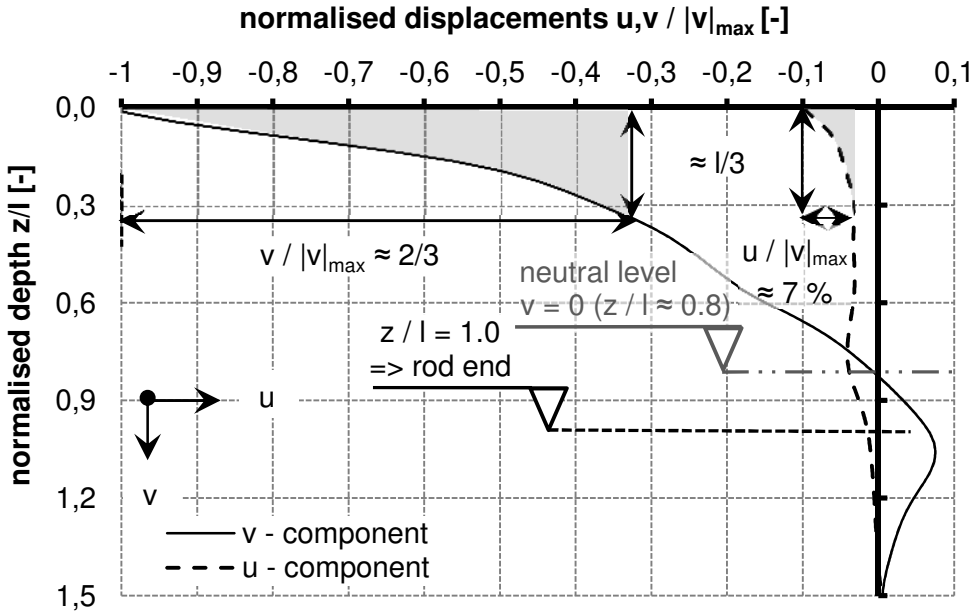

Fig. 57: Horizontal (u) and vertical (v) displacements along the section plane A-A of Figure 56

b) Inclined rod

Figure 58 illustrates the total displacements of the PIV analysed slices (t = 0.2; 4; 8 and 11 cm) after the full rod installation of the 50 cm long and inclined (α = 15°) rod. The vertical (v) and horizontal (u) displacements due to the soil-rod interactions are separately visualized for the slice corresponding to the deepness t = 11 cm. Phenomenological similarities to the vertically installed rod can be observed, especially when considering the visualized vertical (v) and horizontal (u) displacements. The vertical displacements show settlements (+v) close to the rod end and the upper section shows heaving (-v) in the form of material which moves upwards, similar to the vertically installed rod

To conclude, horizontal soil replacements which are present slightly deeper than the rod end can be observed for the inclined rod as well.

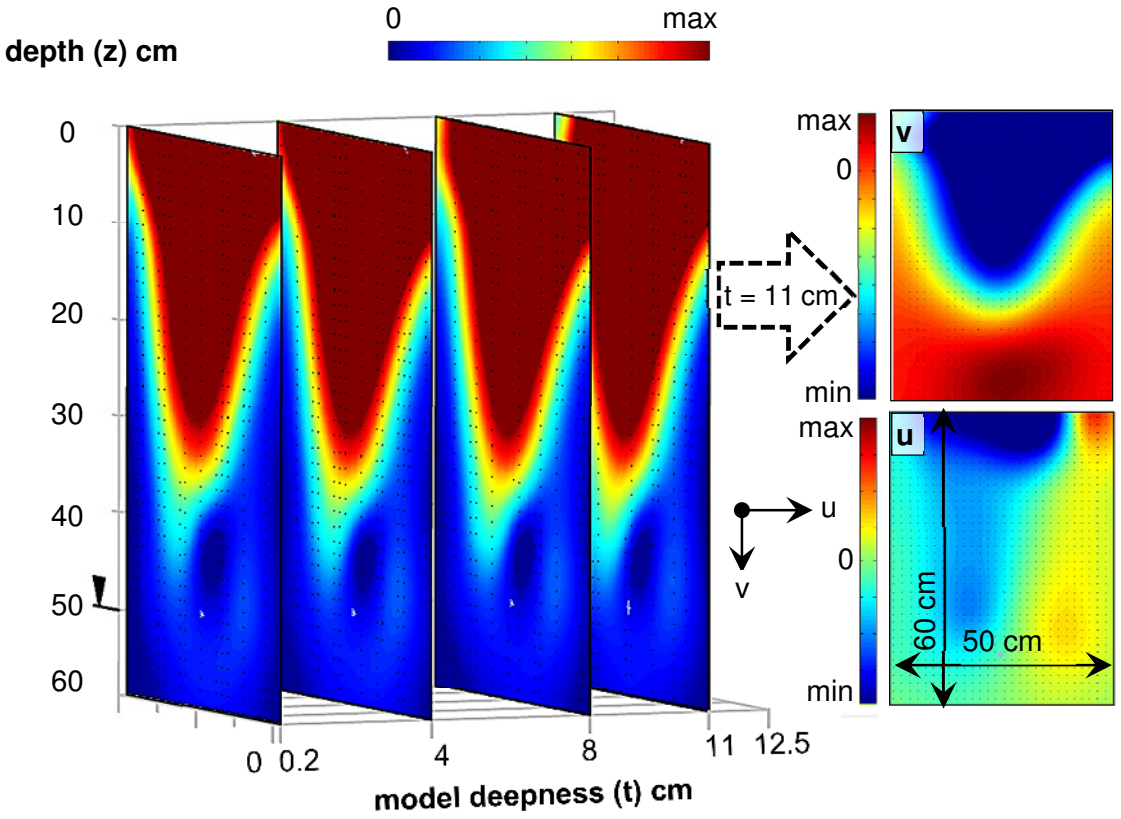

Fig. 58: Visualized soil-rod interactions due to the installation of the inclined threaded rod, $\alpha = 15°$, $l = 50$ cm and $\lambda = 33$. Left: total displacements for the different slices, depending on the model deepness (t); Right: separation between the vertical (v, +v settlements; -v heaving) and horizontal (u) displacements for the slice which belongs to the model deepness t = 11 cm.

- **Pull-out process:**

Twenty-six pull-out tests of single rods were conducted for lab test one (L1), eight vertically installed and eighteen inclined installed rod pull-out tests. The vertically installed rod pull-out tests were conducted with variable rod lengths (l = 0.5 & 0.7 m) and with variable rod surfaces. As already mentioned above, a completely smooth (S) and a rough (R) rod surface was investigated. However, only the rod surface varies for the executed inclined installed rod pull-out tests, whereas the rod length (l) remained unchanged. The results of the different pull-out tests are summarized in Table 17. An exemplary force-displacement graph for the vertically installed rods is shown in Figure 59 and for the inclined installed rods in Figure 60. A reduction of the tension force of the force displacement-graph is observed after reaching a peak value. This happens in a comparable way like for field test one (F1).It is interesting to note that also the force-displacement graph of the smooth rod pull-out test shows a significant reduction of the tension force after reaching a peak value, which was not expected. This can be observed for the pull-out tests with the inclined installed rod as well, Figure 59 & 60.

Tab. 17: Pull-out test results, strongly modified after Poprask (2014)

Test no.:	Results: Vertically installed rods		Inclined installed rods		Geometrical properties: rod			
	pull-out force $F_{t,max}$ [N]	displacement u_z [mm]	pull-out force $F_{t,max}$ [N]	displacement u_z [mm]	l [m]	λ [-]	α [°]	R*) S
1	346	6.5			0.5	33	0	R
2	320	6.0						
3	100	2.6						S
4	88	3.9						
5	659	5.2			0.7	47	0	R
6	648	8.5						
7	174	4.5						S
8	176	3.0						
9			330	7.24	0.5	33	5	R
10			101	2.49				S
11			94	3.39				
12			311	7.26			10	R
13			316	7.51				
14			92	3.73				S
15			303	8.05			15	R
16			293	7.57				
17			89	3.49				S
18			97	8.18				
19			270	6.44			25	R
20			273	9.70				
21			65	11				S
22			70	5.74				
23			230	10.14			30	R
24			223	7.83				
25			69	5.62				S
26			60	15.22				

*) R … rough rod: SAS 900/1100 FA; S … smooth rod; for all rods: d = 15 mm

A possible reason for this is the installation process of the smooth rod which was done by screwing and pushing.

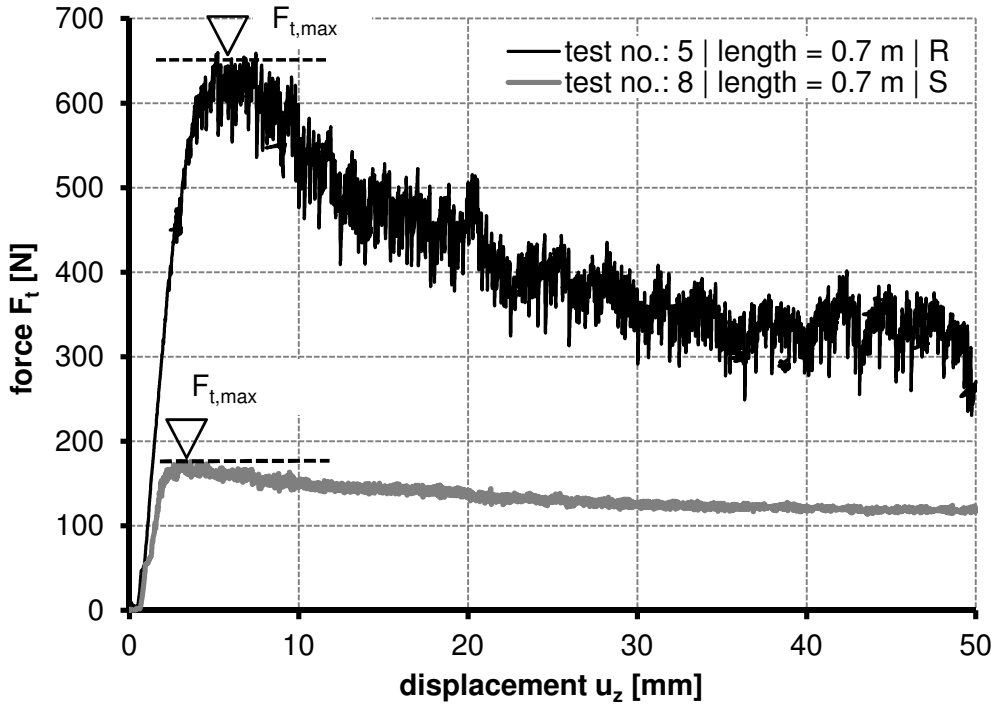

Fig. 59: Force-displacement graph of the single rod pull-out test numbers 5 and 8 (R … rough rod, S … smooth rod), rod length (l) = 0.5 m, modified after Poprask (2014)

The pull-out forces ($F_{t,max}$) of the executed tests under the same technical boundary conditions vary only a little, in comparison to the results of field test one (F1). This may be due to the fact that the laboratory conditions are controlled and reproducible. In addition, the density (D) of the transparent soil is relatively uniform over the full height of the model container. The necessary vertical displacements (u_z) to reach the pull-out force are significantly lower for the tests with the smooth rod surface, Table 17. Anyway, the necessary displacements (u_z) to reach the pull-out force of the inclined rods are slightly increasing with increasing inclination, depending on the rod type, Table 17.

Generally, a relatively constant ratio between the pull-out force of the rough rod and the smooth rod independently from the executed experiment is obtained, $F_{t,max,smooth}$ / $F_{t,max,rough}$ ≈ 3 / 11, if all technical boundary conditions are kept constant, e.g.: rod length (l), inclination (α). Therefore it can be concluded that the threads of the threaded rods have an intense influence on the bearing capacity of the rods, which was expected and is now confirmed with reasonable confidence.

In the following, the results of the soil-rod interactions due to the pull-out process are presented and discussed for the vertically and inclined installed

rods. It is expressly pointed out that the soil-rod interactions are only displayed for the rough rod because almost no soil displacements were observed for the smooth rod by applying the introduced testing and measuring equipment, see chapter 3.4.2 and Poprask (2014).

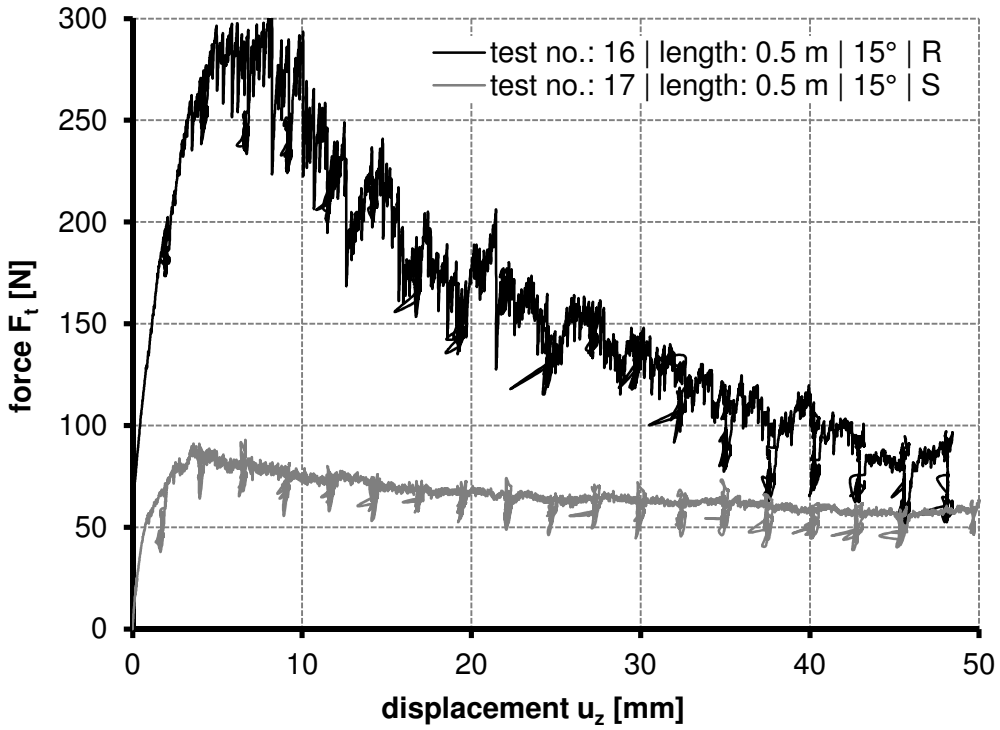

Fig. 60: Force-displacement graph of the rod pull-out test numbers 16 and 17 (S … smooth rod, R … rough rod), rod length (l) = 0.5 m, inclination α = 15°, modified after Poprask (2014)

To conclude, in order to visualize the soil-rod interactions due to the pull-out process, the pictures of laser-light sheets after the full rod installation process and after some defined pull-out displacements (u_z) are compared and analysed with PIV.

a) Vertical rod

Figure 61 illustrates the total displacements of the PIV analysed slices (t = 0.2; 4; 8 and 11 cm) after approximately $u_z \approx 7.5$ mm vertical pull-out displacements, for the rough rod with 50 cm rod length. The PIV analysed slices are belonging roughly to the displacements (u_z) to reach the pull-out force $F_{t,max}$. The vertical (v) and horizontal (u) displacements due to the soil-rod interactions are separately visualized for the slice corresponding to the deepness t = 11 cm. Streamlines outline the mobilized soil body and specify the moving direction of the failure body.

Total displacements are mostly noticed in the upper 20 cm of the rod and almost no total displacements are noticed for the area below.

It is pointed out that no vertical movements are recognizable for depths (z) greater than 20 cm.

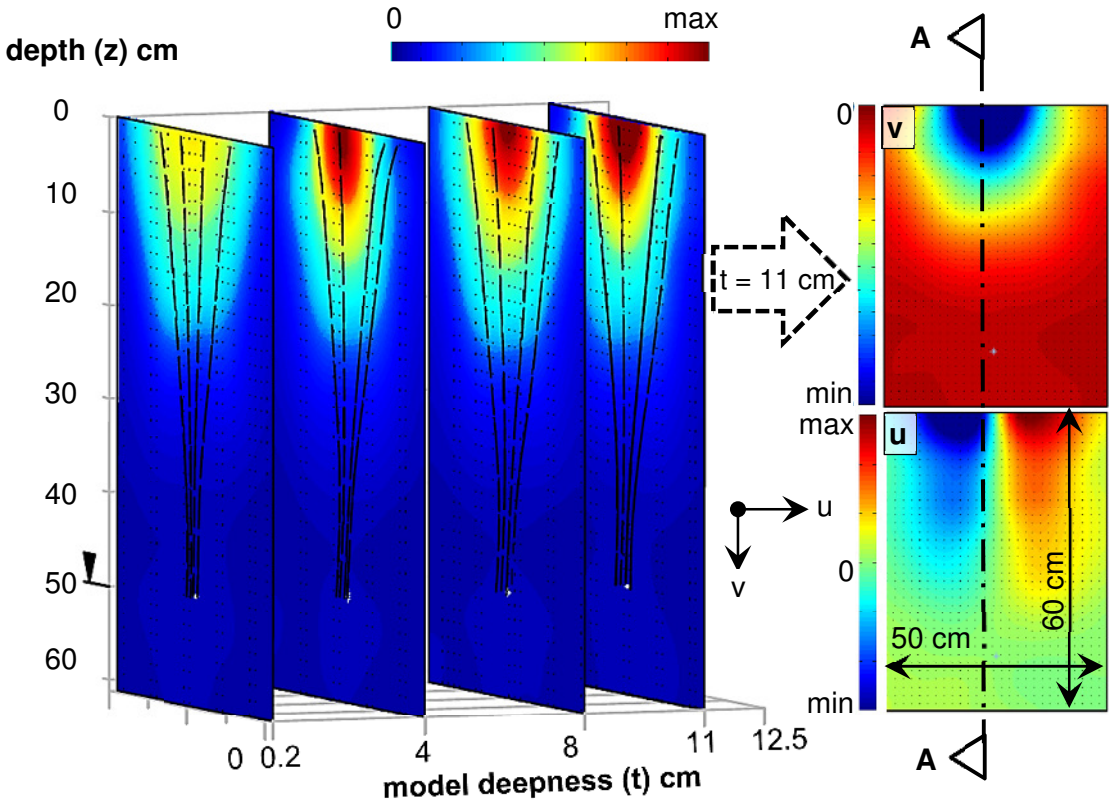

Fig. 61: Visualized soil-rod interactions due to the pull-out process of the vertical threaded rod, l = 50 cm and λ = 33. The analysed slices belong to the vertical displacements (u_z) to reach the pull-out force $F_{t,max}$. Left: total displacements for the different slices, depending on the model deepness (t); Right: separation between the vertical (v, +v settlements; -v heaving) and horizontal (u) displacements for the slice which belongs to the model deepness t = 11 cm

Heaving in the form of material which moves upwards is observed for the very shallow region when looking at the illustrated vertical displacements. The horizontal displacements show relatively symmetrical horizontal soil replacements.

However, the analysed displacements along the marked section plane A-A can be found in Figure 62. The investigated vertical displacements (v) are especially present in the upper section of the rod, almost 70% of the vertical displacements are activated in the first 20 cm rod length only. Similar effects are noticed for the analysed horizontal displacements along the section plane. The horizontal displacements are maximum 10 % of the vertical displacements and mostly activated in the first 10 cm of the rod, Fig. 62.

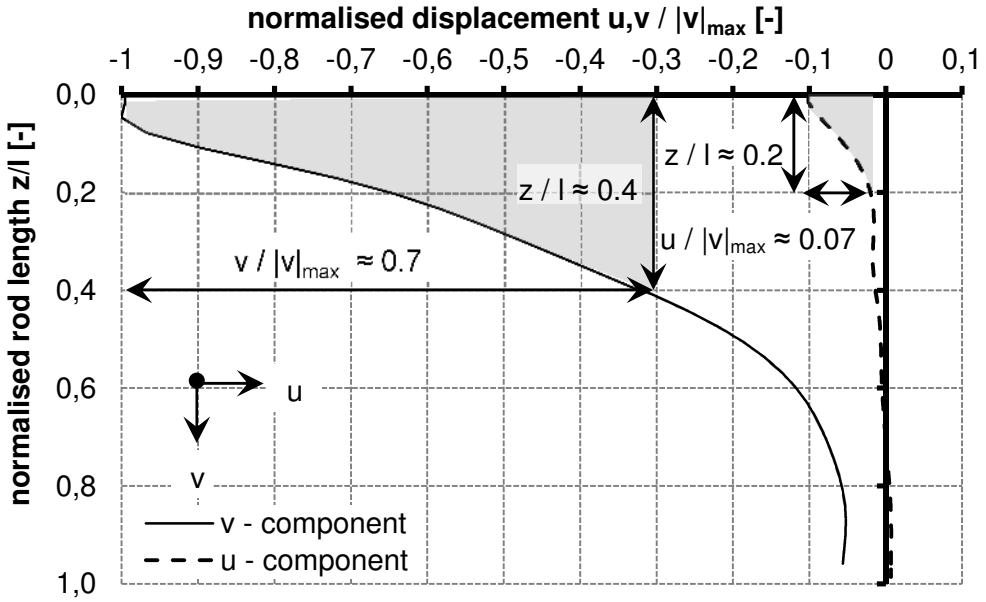

Fig. 62: Horizontal (u) and vertical (v) displacements along the section plane A-A of Figure 61 and the slice corresponding to the deepness t = 11 cm.

b) Inclined rod

Figure 63 illustrates the total displacements of the PIV analysed slices (t = 0.2; 4; 8 and 11 cm) after approximately $u_z \approx 7.5$ mm vertical pull-out displacements for the rough rod with 50 cm rod length and 15° inclination. The PIV analysed slices roughly belong to the displacements (u_z) to reach the pull-out force $F_{t,max}$. Streamlines additionally outline the mobilized soil body. The vertical (v) and horizontal (u) displacements due to the soil-rod interactions are separately visualized for the slice corresponding to the deepness t = 11 cm.

Displacements (u, v, total) are mostly noticed in the first 20 cm depth (z), similar like for the vertical rod. It appears that the mobilized soil body is placed and interlocked over the upper part of the inclined rod. Underneath the lower rod section almost no displacements are observed.

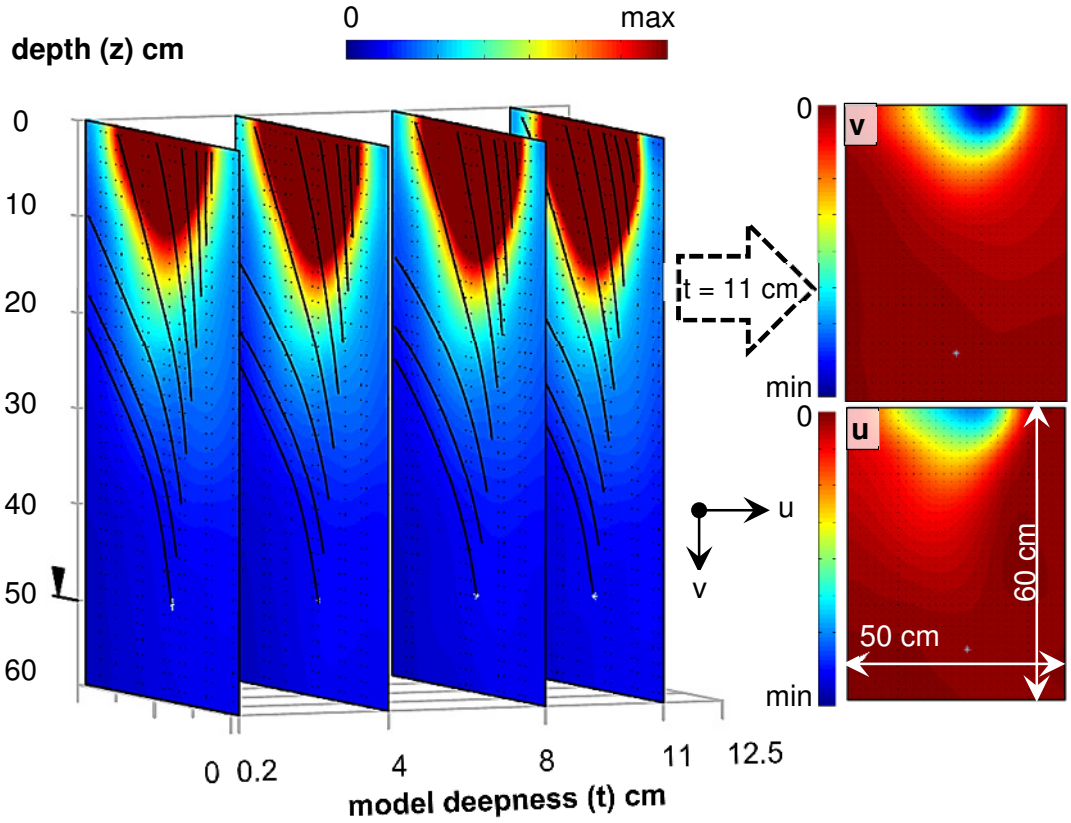

Fig. 63: Visualized soil-rod interactions due to the pull-out process of the inclined threaded rod, $\alpha = 15°$, $l = 50$ cm and $\lambda = 33$. The analysed slices belong to the vertical displacements u_z to reach the pull-out force $F_{t,max}$. Left: total displacements for the different slices, depending on the model deepness (t); Right: separation between the vertical (v, +v settlements; -v heaving) and horizontal (u) displacements for the slice which belongs to the model deepness t = 11 cm.

3.4.5 Comparison of results and discussion

- **Vertically installed rods**

Figure 64 illustrates the spectrum of the tension force (F_t) normalised to the individual pull-out force ($F_{t,max}$). This is done for all executed pull-out tests of the vertically installed and rough rod of lab test one (L1) and of field test one (F1). The force-displacement graph shows a reduction of the tension force (F_t) after reaching a peak value, similar to field test one, F1, material A, chapter 3.2.6, Figure 32. For material A the reduction is $\Delta \approx 0.7$ and for the transparent soil: $\Delta_{L1} \approx 0.65$. This fact confirms the assumption that the pull-out behaviour in a transparent soil model is comparable to the one in a "real" coarse grained soil model. The necessary displacements to reach the pull-out force are between $u_{z,L1} \approx 5$ to 8 mm and in a similar range as for field test one for both materials (material A and material B, $u_z \approx 5$ to 11 mm, Figure 32).

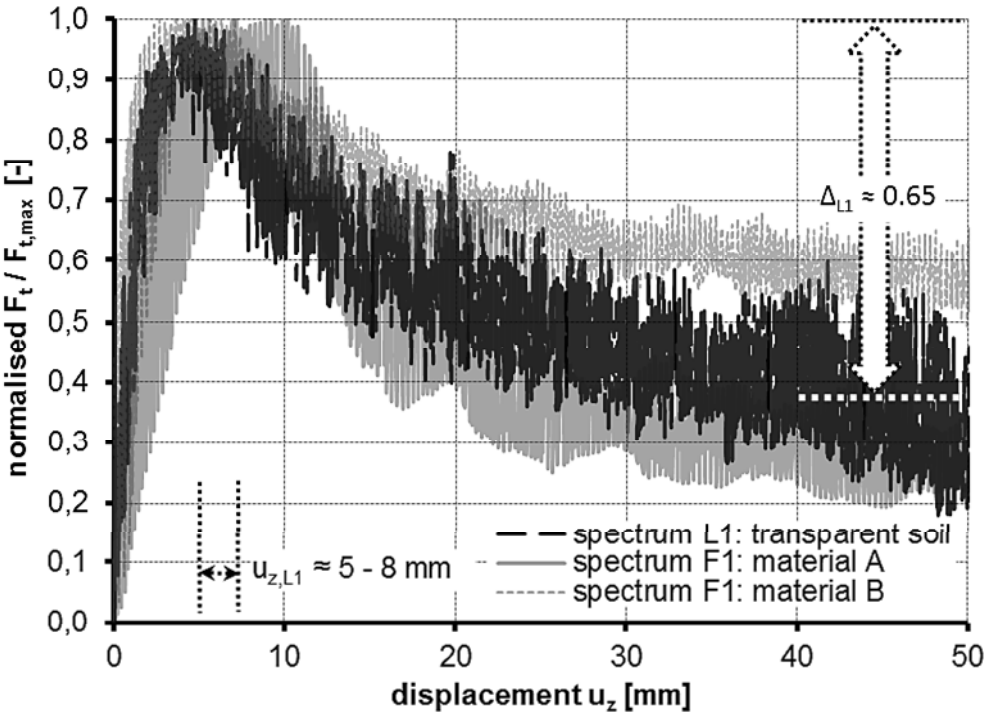

Fig. 64: Spectrum of the normalised single-rod pull-out forces (F_t / $F_{t,max}$) for the vertical in silica gel installed threaded rods. A softening can be observed in a similar way like for the field test one (F1, material A). The rod length is variable (l= 0.5 -0.7 for L1 and l = 2 m for F1)

To address research question two (Q2), a mobilized failure body due to an applied vertical tension load which is attached on the threaded rod is only slightly observed. Most of the analysed displacements are very superficial and for greater depths (z) the failure is almost parallel to the threaded rod axis. Hence, almost no particle movements are observed beneath the superficial area. However, nearly no displacements are noticed due to the pull-out process of the smooth rod, see Poprask (2014).

Due to the installations process of the threaded rod a distinct change of the initial conditions in the subsoil occurs. This happens especially in the immediate vicinity of the rod when reflecting the results of the visualized soil-rod interactions. These effects are very difficult to quantify especially the increase of radial stresses as a result of replacement effects due to the rod installation. However, this will be worked out in more detail in lab test two (L2).

To conclude, the visualized soil-rod interactions show for all analysed cases (installation and pull-out process) displacements which are developed very close to the observation window of the model container. Therefore, boundary conditions may influence the test results.

- **Inclined installed rods**

Figure 65 depicts the influence of the rod inclination (α) to the pull-out force ($F_{t,max}$) for lab test one (L1) and field test two (F2). The rod length (l) is constant for each graph. The pull-out force remains almost constant for all executed experiments until a rod inclination of α ≈ 10° and decreases afterwards with increasing rod inclination. This can be observed independently from the rod length, the rod surface and the soil type, Figure 65.

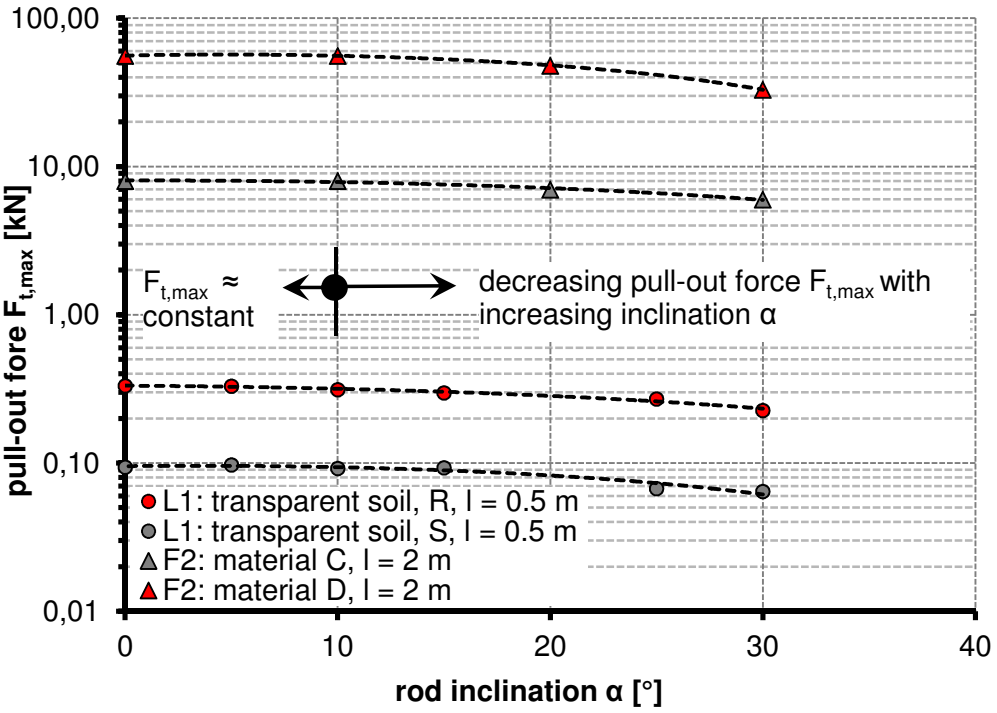

Fig. 65: Influence of the rod inclination (α) and the pull-out force $F_{t,max}$ (log-scale) for lab test one (L1) and field test two (F2) . A black dotted polynomial trend line is applied (quadratic). It is interesting to note that the relative decrease of the pull-out force ($F_{t,max}$) with increasing rod inclination (α) is almost similar for the rough (R) and smooth (S) rod of lab test one and for the rods of field test two as well (F2, material C and material D).

This suggests that a geometrical relationship between vertical pull-out forces of vertically and inclined installed threaded rods is existing. This will be worked out in more detail in Chapter 5 to address research question four (Q4).

Strong similarities are noticed when comparing the PIV analysed slices of displacements due to the vertically and inclined rod installation process. This reasonably explains the relationship between the pull-out forces of the vertical and inclined rods, especially when considering the smooth rods. However, the

pull-out force is strongly influenced by the rod installation process, which leads to a change of the initial conditions and consequently of the radial stresses.

To conclude, a kind of mobilized soil body attached to the threaded rod is slightly observed for the inclined rods. Most of the analysed displacements are very superficial and displacements for greater depths (z) do not exist.

3.4.6 Comparison of literature and discussion

In this chapter, a comparison of literature - with respect to the shape of the mobilized soil body - with the results given by the presented PIV analysis is done. Additionally, the soil-rod interactions caused by the installation process are compared with the literature. A comparison of the pull-out forces ($F_{t,max}$) gained from lab test one (L1) with calculated pull-out forces for vertically installed piles is waived. The reason for this is that the pull-out forces ($F_{t,max}$) given by field test one (F1) did not meet the calculated pull-out forces. However, the influence of the rod inclination (α) and the pull-out force $F_{t,max}$ is already carried out within the field test two (F2) and discussed with the results of Hanna, Afram (1986), see Chapter 3.3.6, with satisfactory results. The relative load-drop behaviour between the inclined and vertically installed rods of lab test one is similar to the load-drop behaviour of the rods for field test two (F2), as further explained above.

The results of the comparison of literature are subdivided into following categories:

a) Installation effect
b) Pull-out process

a) Installation process

Figure 66 illustrates the radial displacements (u_r) and radial stresses (σ'_{rc}) due to the pile installation by driving for a displacement pile with full section. The radial displacements (u_r) and radial stresses (σ'_{rc}) due to the rod installation are additional illustrated.

The feed rate of the threaded rod is given via the threads and is continuous, hence, no impulsive “stop and go” like for pile driving. In this context, the visualised radial displacements (u_r) can be understood in a way similar to the horizontal displacements (u) of Figure 56 - 57.

However, settlements underneath the tip of the threaded rod are discovered after the full rod installation. This is observed in a shape similar to a driven pile. The soil is radially replaced over the full length of a driven pile and a wedge-shaped settlement zone below the pile-tip can be found, White et al. (2005). The

settlement zone increases the base-resistance of a pressure pile. However, due to the radial displacements along the rod shaft, an increase on the bearing capacity of a tension pile is expected.

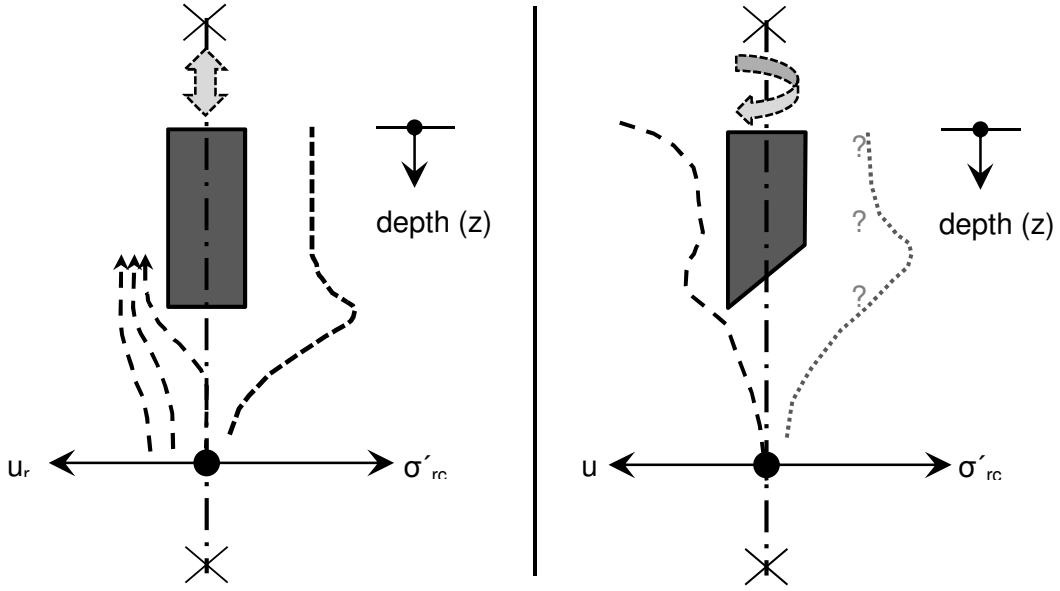

Fig. 66: Rotationally symmetrical, qualitative presentation of the radial displacements and the radial stresses caused by a pile or the threaded rod installation. Left: pile driving (full section), White et al. (2005); Right: threaded rod installation by screwing, feed rate is given via the threads

A deflected part of radial displacements close to the rod tip and a steeper cone wedged settlement zone can be observed for the threaded rod in comparison to a driven pile. This can be the result of the unilateral 45° inclined rod tip which replaces the surrounded soil more effectively in radial direction by screwing.

To conclude, an increase of the radial stresses due to the rod installation is unquestionable and worked out in more detail within lab test two (L2).

b) Pull-out process

A comparison of differently shaped soil bodies according to the expressed theory and the PIV investigated mobilized soil body is shown in Figure 67. Details concerning the expressed theories can be found in Chapter 2 and additional specifications with respect to the comparison can be found in Table 18.

The shape of Jelinek´s and Ostermayer´s (1964) failure body for vertical tension piles is cone-shaped with a low opening angle (β). For this reason, the outer sliding surface is very close to the pile shaft for greater depths (z) and the greatest expansion of the failure body occurs superficial, similar to the results of L1. For this approach no side friction forces (F_s) are considered, see Table 2,

and the pull-out force is mobilized due to the weight of the mobilized soil body only, which is not reasonable. Only a relatively low volume of soil is mobilized, which cannot explain the relatively high pull-out forces ($F_{t,max}$) by applying the threaded rods.

Tab. 18: Additional assumptions or data to draw sketches of mobilized soil bodies with different shape, according to the expressed theory

Theory, author: (year)		Soil type Transparent soil
Jelinek and Ostermayer	1964	$\beta^{*)} \approx 6.9°$
Meyerhof	1973	
Chattopadhyay and Pise	1986	$\delta = \varphi$
Quarg-Vonscheidt	2000	The approach is only applicable for sandy material and rod length from 3 to 30 m *assumption,(real): d_{50} = 1.2 (2.9) mm*

*) calculated

Quarg-Vonscheidt (2000) developed a failure body which does not consider side friction forces. For this reason, the mobilized volume is relatively large, especially the opening with (A), Figure 15. However, the shape of the failure body does not match the one observed of the rod. Consequently, Quarg-Vonscheidt's (2000) approach is not applicable for slender and screwed threaded rods, Table 1.

The shape of Chattopadhyay's and Pise's (1986) mobilized failure body is almost similar to the observed one of L1. For greater depths (z) the failure occurs on the pile shaft, hence parallel to the pile axis, and the largest expansion can be observed superficial. However, Chattopadhyay and Pise (1986) consider both side friction forces (F_s) and the weight of the mobilized failure body to calculate the pull-out force. It is pointed out that for greater pile lengths, and especially for great slenderness ratios (λ), the failure occurs along the pile shaft over a larger area and that a maximum expansion is reached superficial, by applying Equation 15, see Example 1 - 2.

⇨ **Example 1**: *Given:* l = 0.5 m (λ =33); r = 0.0075 m; $\delta = \varphi = 35.5°$
Result: x/d ≈ 9 and around 40 % of the failure occurs along the pile shaft

⇨ **Example 2**: *Given:* l = 2.0 m (λ =133); r = 0.0075 m; $\delta = \varphi = 35.5°$
Result: x/d ≈ 10 and around 75 % of the failure occurs along the pile shaft

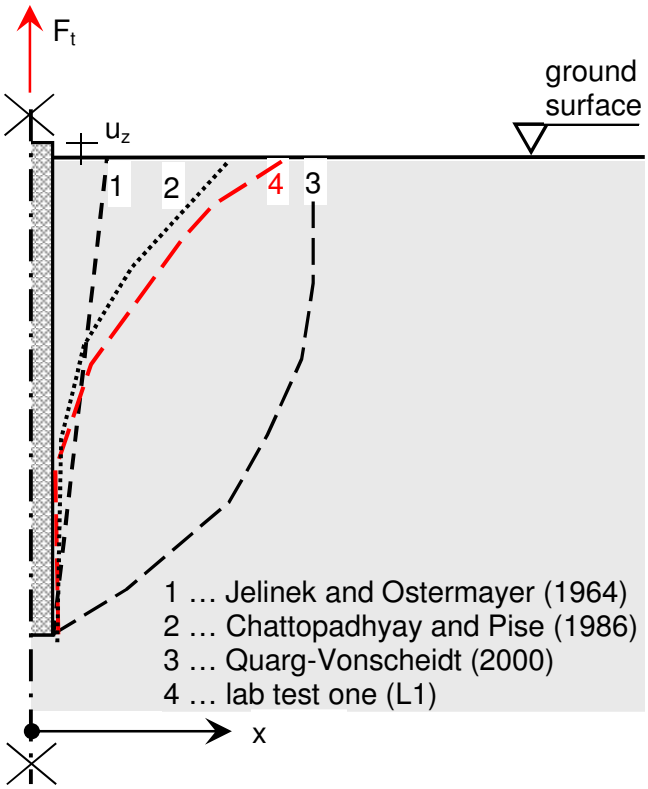

Fig. 67: Rotational symmetrical, schematic sketch of the different approaches of mobilized failure bodies for vertical tension loaded and vertically installed threaded rods with a rod length of 0.5 m ($\lambda = 33$)

To conclude, strong similarities of the observed failure body and the failure body of Chattopadhyay's and Pise's (1986) approach can be found, at least for the rod with 50 cm length. This observation is worked out more extensively in chapter 4, with the help of numerical simulations.

3.5 Lab test 2

3.5.1 Introduction

The main objective of lab test two (L2) was to address research question one (Q1) for single rods by conducting pull-out tests: *"What is the magnitude of the vertical pull-out force and how does the force-displacement graph look like?"* Research question three (Q3): "*What is the influence of the installation process with respect to the bearing capacity?"* was also addressed. It is underlined that research question one (Q1) was already partly addressed in F1, F2 and L1 and research question three (Q3) in L1. In this context, particular consideration was given to determine interlocking effects due to the installation and pull-out process of the vertically installed threaded rods, depending on the distance to the vertical rod axis and the depth (z).

3.5.2 Overview, setup and experimental procedure

Centrifugally cast fiberglass tubes with variable diameter (Hobas, SN 10.000 PN 06: d = 25, 50 and 60 cm) were filled with three different types of material over the full height of h =2 m. Threaded rods were installed vertically in the centre of the tube afterwards and finally pulled out. In order to determine the increase of the radial tube expansion caused by interlocking effects - due to the installation and pull-out process - the tubes were equipped with strain gauges (HBM, 6/350 RY81). The strain gauges were arranged on the airside of the tube on three different levels (z_1= 40, z_2= 90 and z_3= 140 cm). Each level in the ground plan (arrangement: 0°, 90° and 180°) consisted of three measurement points (MP1 – MP3), Figure 68. However, three strain gauges where applied for each measurement point, measuring direction: radial ε_{rad}, inclined ε_{45} and vertically ε_v, Fig. 68c). In total, 27 strain gauges were applied to each tube.

The relevant tubes for the corresponding experiment was finally placed below and clamped within the modified traverse of lab test one (L1). Finally, the test setup of L1, e.g.: spindle gear (velocity ≈ 0.33 mm/s) was applied. The measuring equipment consisted of a load cell (HBM, max. force 10 kN, measurement error ± 0.2 %), an inductive displacement transducer (HBM, 1-WA/50MM-T, max. displacements 50 mm, measurement error ± 0.2 %), a data logger (HBM, Spider 8) as well as a computer, for more details see Chapter 3.4.2.

The traverse height of L1 was too low for L2 and a raised support frame was therefore placed on the top of the traverse in order to apply a tension load to the rod, Figure 69. To conclude, the laser guide bar and the laser source where removed from the traverse in advance for lab test two (L2). The full setup can be seen in Figure 69.

Pull-out tests were performed path controlled with variable rod lengths (l = 50, 100 and 150 cm) and variable ground conditions, material E - G. The strains due to the interlocking effects were measured continuously during the experiments.

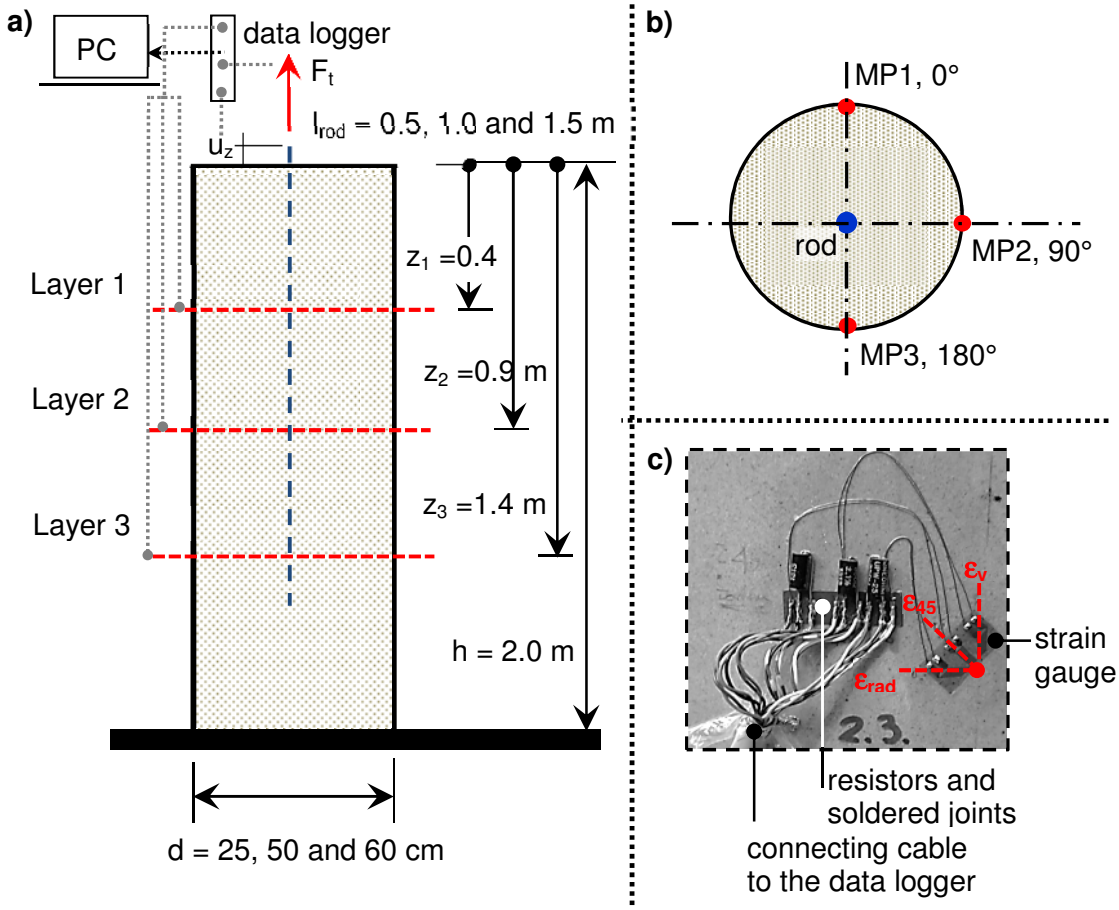

Fig. 68: Setup and overview of lab test two. a) side view; b) ground plan; c) detailed side view of each measurement point (MP)

In the following, the experimental procedure for each experiment is given:

a. Filling and compacting of the relevant material by layers into the relevant tube, depending on the experiment
b. Placing the tube below and jamming the tube within the traverse
c. Connecting the strain gauges with the data logger
d. Installing the threaded rod through a bushing into the tube which was filled with material. The strains of the applied strain gauges were recorded
e. Connecting the top of the rod with the spindle-gear and installing the load cell and inductive displacement transducer
f. Activating the spindle gear until approximately 50 mm pull-out displacements u_z were reached. The strains of the different strain gauges and the forced tension force F_t, as well as the displacements u_z were recorded continuously
g. Weighing and emptying the applied material from the tube
h. Starting the new experiment

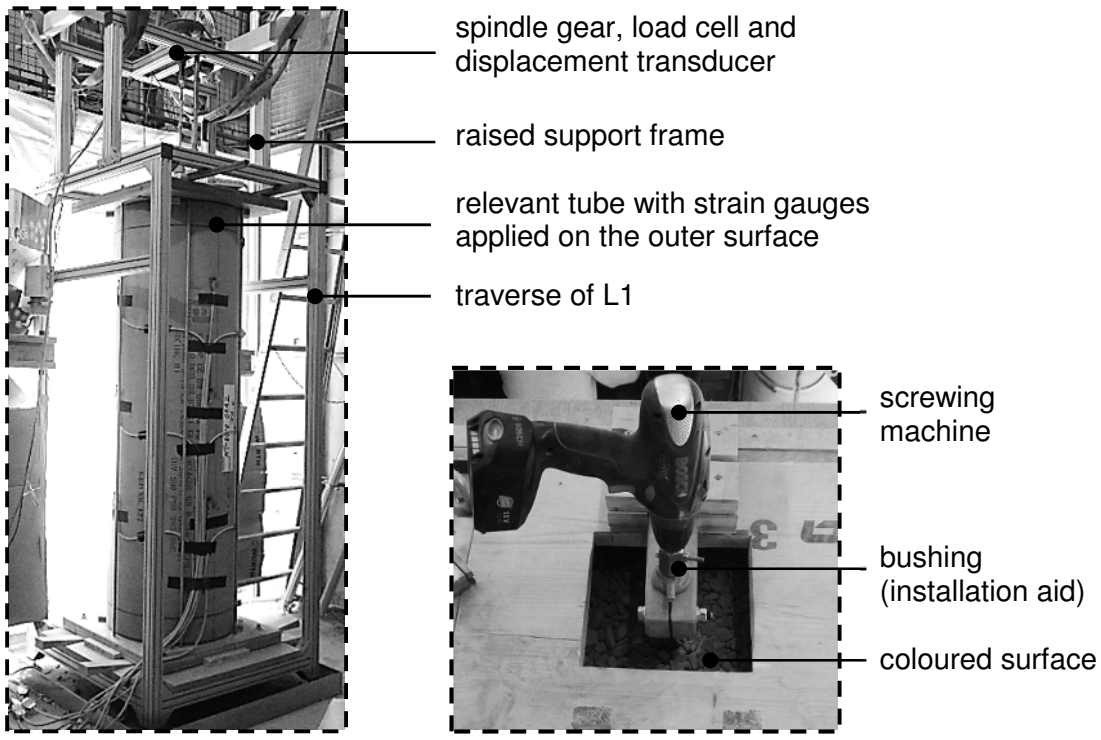

Fig. 69: Left: setup realized for the pull-out tests; Right: vertical rod installation through an axial positioned bushing

An overview on the experimental investigations is given in Table 19.

Tab. 19: Overview on experimental investigations for L2

Tube diameter d [m]	Material			Rod length l [m] and *(λ)*			Pull-out test: rod installation	
	E	F	G	0.5 *(33)*	1.0 *(67)*	1.5 *(100)*	vertical	inclined
0.25	☑	☑	☒	☑	☑	☑	☑	☒
0.50	☑	☑	✂	☑	☑	☑	☑	☒
0.60	☒	☑	✂	☑	☑	☑	☑	☒

✂ not considered - vide infra

In total, more than 47 pull-out tests were carried out, 25 pull-out test of this quantity are presented and discussed in the following. The rod installation into the tube with 25 cm diameter and filled with the material G was not possible. The reason for this was the weak engine of the screwing machine which was not able to overcome the surface friction resistance between the rod and the surrounding soil during the installation process. However, the pull-out test results from the tube with 50 and 60 cm diameter and filled with material G were discarded. They were not evaluable due to untypical stepwise behaviour of the produced load-displacement graphs. This may be the result of highly scattered and irreproducible soil density (D) inside the tube, vide infra.

To conclude, pull-out tests results from the tube with 60 cm diameter and filled with material E were finally not executed; see Chapter 3.5.4.

3.5.3 Materials

Three different kinds of coarse grained soils were applied for L2, sand (material E), sandy gravel (material F) and gravel (material G), Fig. 70. In order to execute the introduced experiments, see Table 19, a defined amount of material was filled into the tube and compacted by layers ($h_{layer} \approx 0.4$ m). A shake motor installed below the contact area of the tube, Figure 52, and an additional frequency-adjustable vibrator where used therefore.

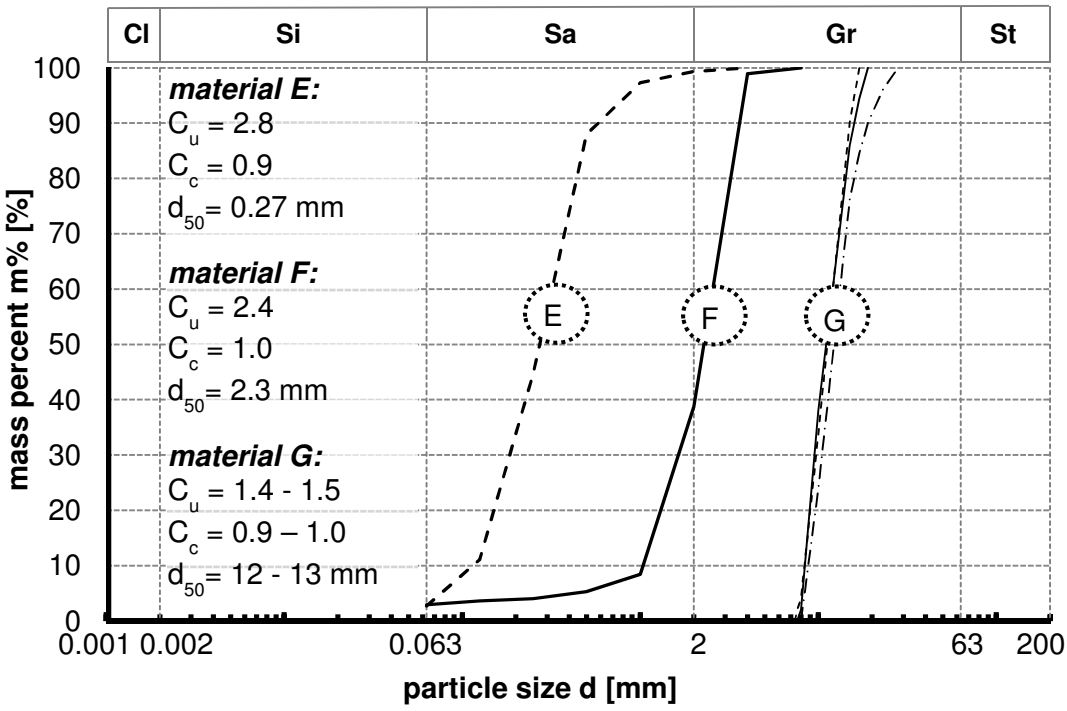

Fig. 70: Grading curves of the different materials E, F and G. The material G was analysed by Lackner (2012)

It is underlined that filling by layers and compacting of material inside the 2 m high tube was difficult to handle because of especially cramped conditions.
In some cases and especially when dealing with the greater tubes it was not possible to build in the defined amount of material. Constant soil density (D) could not be guaranteed therefore. However, the tube was emptied after the experiment was executed and the material was weighed in order to control the density (D).

An extensive soil testing program was executed to characterise the materials E and F. Material G corresponds to the material of Lackner (2012).

The following tests were carried out in the lab: oedometer test, direct shear tests (material E and F, 10 * 10 cm shear surface), variable lab tests and calculations to determine physical properties, like: dry density (γ_d), particle density (γ_s), saturation (S_r), porosity (n), density (D). Sieving and calculating the coefficient of uniformity ($C_u = d_{60} / d_{10}$) and the curvature coefficient ($C_c = d_{30}^2 / (d_{10}*d_{60})$) of the resultant grading curves was also done. The soil characterisation is summarized in Table 21 and the corresponding grading curves of the materials can be found in Figure 70.

Tab. 21: Material properties of lab test 2

Properties	Material type		
	Material E	Material F	Material G[1)]
Wet weight density γ_F [kN/m³]	15.9	16.13	16.3
Dry weight density γ_d [kN/m³]	14.8	14.66	16.0
Particle weight density γ_s [kN/m³]	27.4	26.9	26.4
Porosity n [-]	0.45 – 0.47	0.45 – 0.46	0.39 – 0.40
Density D [-]	0.4 – 0.5 (loose)	0.45 – 0.55 (loose)	0.75 – 1 (dense to very dense)
Saturation S_r [-]	0.24	0.3	0.08
Peak friction angle φ´ [°]	39.0[2)]	44.0[3)]	40.1 - 46
Stiffness E_s [MN/m²] ($\sigma_N = \sigma_{N1}/\sigma_{N2}$ kN/m²)			10 / 40 (10/100)

[1)] according to Lackner (2012); [2)] γ_d = 15.5 kN/m³ (very dense);
[3)] γ_d = 15.0 kN/m³ (very dense)

3.5.4 Results

The results of L2 are basically load-displacement graphs of the pull-out tests and the continuously measured strains of the applied strain gauges caused by the installation and pull-out process. As already introduced, the (first) peak of the produced load-displacement graph is called pull-pout force ($F_{t,max}$). Finally, the results are subdivided between the installation and the pull-out process.

Due to the anisotropic material behaviour of the centrifugally cast fiberglass tubes a conversion from the measured strains to stresses was not exercised. Additionally, the jamming of the tube within the traverse led also to unclear boundary conditions.

However, an additional boundary condition which influences the experimental results significantly is the stiffness in longitudinal direction of the tube. This fact results in lateral tube contractions if the tube is expanded above or below

due to interlocking effects. Splitting the tube into multiple segments would have eliminated or at least lowered this effect.

In this context, the inclined strains (ε_{45}) and the vertical strains (ε_v) measured on the airside of the relevant tube, Figure 68, are not visualized. The reason for this is that especially the measured vertical strains (ε_v) are highly influenced by the jamming of the tube within the traverse. The inclined strains (ε_{45}) were measured in order to convert the strains to stresses when knowing three strain directions, which was finally not exercised. The radial strains (ε_{rad}) are measured at three defined measurement points, Figure 68, and the average values of the measured strains ($\varepsilon_{rad,AVG}$) depending on the measurement layer (layer 1 - 3) are visualized. The expanded or compressed tube radius after the experiment ($r_{tube,n}$) can be calculated with Equation (22) when knowing the measured strains ($\varepsilon_{rad,AVG}$). It is pointed out that the measured strains were set to zero after the installation process.

$$r_{tube,n} = r_{tube} * \left(1 + \varepsilon_{rad,AVG}\right) \tag{22}$$

Subsequently, it is underlined that strains greater than one ($\varepsilon_i > 1$ µm/m) only occur for the tube with 25 cm diameter and almost no strains ($\varepsilon_i < 1$ µm/m) were measured outside the tubes with 50 and 60 cm diameter, for both the installation and the pull-out process. Reasons for this are the low degree of soil compaction inside the bigger tubes and the fact that such great areas are not or only slightly influenced by the applied rod. For this reason, only the measured strains outside the tube with 25 cm diameter are presented below and the measured strain results for greater tube diameters are no longer considered. Finally, the pull-out experiments from the tube with 60 cm diameter and filled with material E, were not executed for that reason.

- **Installation process**

Figure 71 & 72 depict the average value of the measured radial strains of the tube with 25 cm diameter and filled with material E, versus the elapsed time until the rods with 50 respectively 150 cm rod length were fully installed.

The installed strain gauges within layer two and three did not respond to the installation process of the rod with 50 cm length, Figure 71, because these layers were well arranged below the final rod tip state. However, a significant increase of the radial strains is observed for layer one, which was arranged around 10 cm above the final rod tip position. The strain gauges within layer one already started to respond several centimetres before the rod tip reached the layer and the measured strains were continuously increasing until the level was reached. Afterwards a decrease of the radial strains was observed.

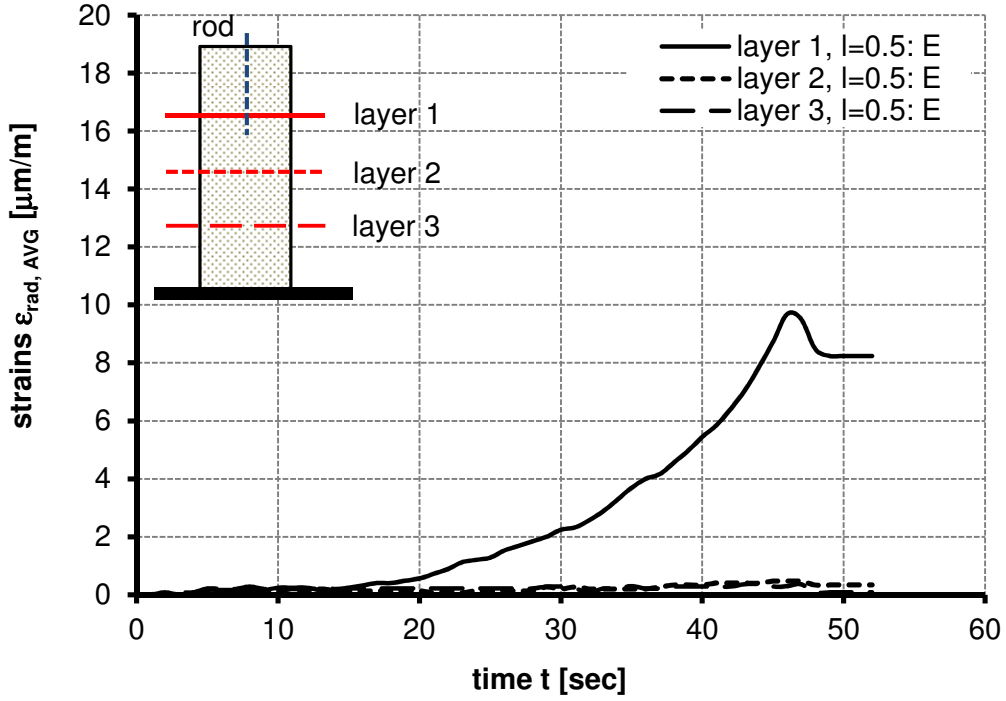

Fig. 71: Measured strains ($\varepsilon_{rad,\,AVG}$) outside the tube with 25 cm diameter, due the 50 cm long rod installation, material E.

All strain gauges responded within the different layers when installing the rod with 150 cm length, Figure 72. The strain gauges within layer one showed an intense reduction of the strains after reaching a peak value, which were finally almost gone after the rod was fully installed. Similar behaviour was observed for the strain gauges within layer two.

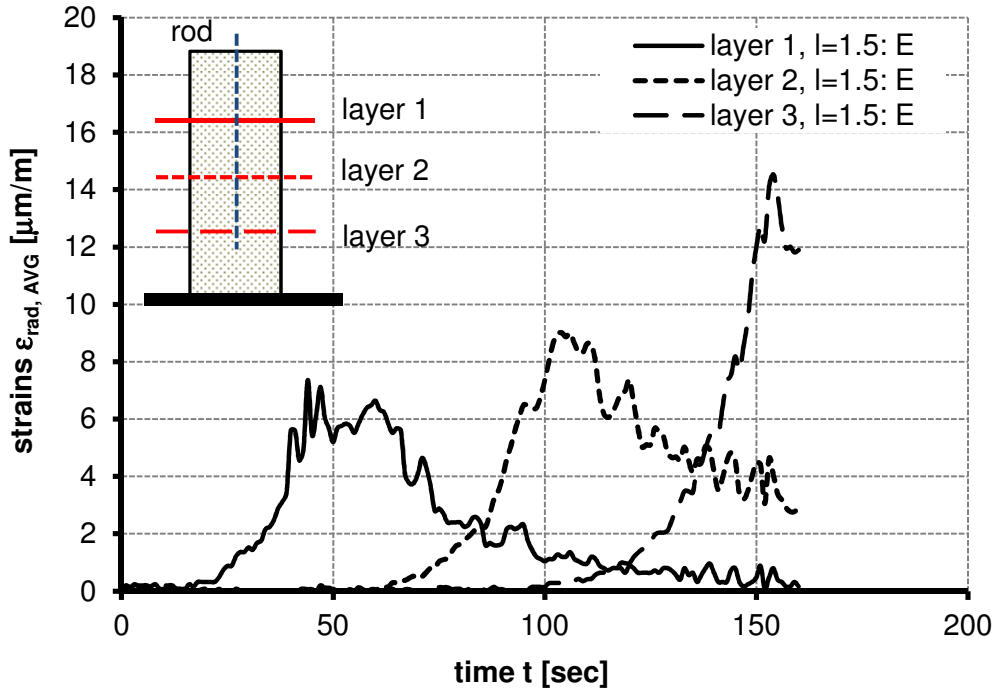

Fig. 72: Measured strains ($\varepsilon_{rad,\,AVG}$) outside the tube with 25 cm diameter, due the rod installation with 150 cm rod length in material E.

These started to respond after approximately 60 seconds, about 40 cm before the rod tip reached level two. After the rod tip passed layer two, the strains within the layer started to reduce significantly and the strain gauges within the level three started to respond in the form of an increase of strains, once again, about 40 cm before the rod tip reached level three.

However, when comparing the maximum values of the measured strains ($\varepsilon_{rad,AVG}$), layer 1: ≈ 7; layer 2: ≈ 9 and layer 3: ≈ 14 µm/m, it can be concluded that the radial strains increase with depth (z). Hence, the strains and consequently the radial stresses are not constant with increasing depth (z).

- **Pull-out process**

Figure 73, shows the load-displacement graph of the different pull-out tests for the tube with 25 cm diameter and filled with material E. An overview of all test results is given in Table 22. A reduction of the tension force (F_t) after reaching a peak value was observed for all executed experiments. The pull-out forces gained from the experiments with 25 cm tube diameter were significantly higher if material F was applied compared to material E. The pull-out forces of the rods with 50 cm and 100 cm length were nearly half of the pull-out tests within the tube of 50 cm diameter and filled with material F in comparison to the test in material E. This was the opposite for the rods with 150 cm length.

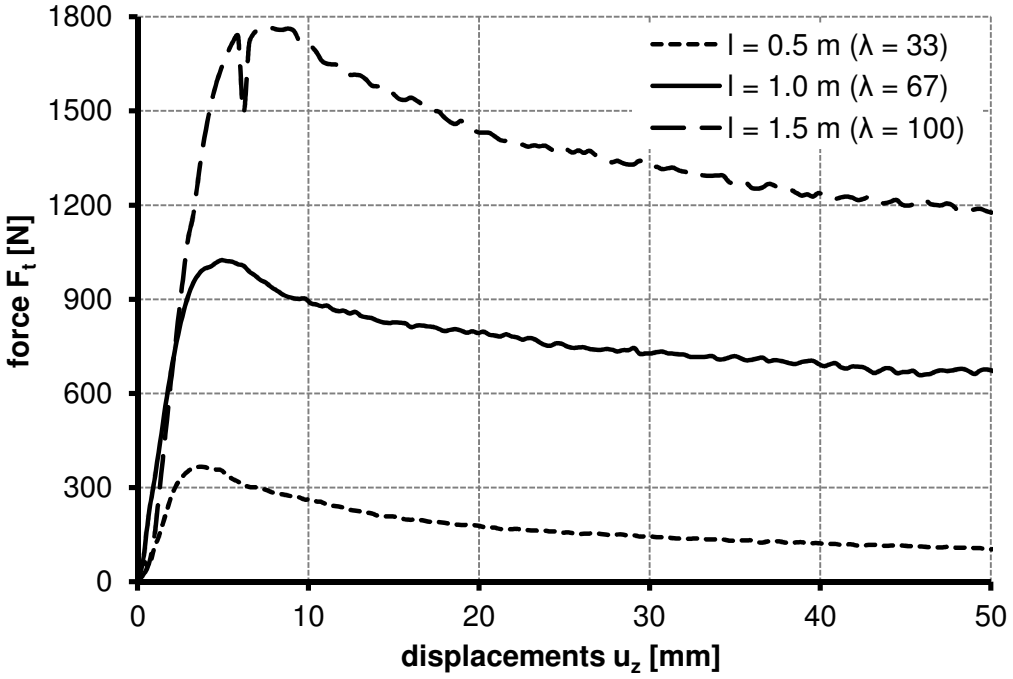

Fig. 73: Load-displacement graphs of the executed pull-out tests from the tube with 25 cm diameter and the material E. The rod length (l) is variable.

Tab. 22: Pull-out test results

Test no.:	Results: Vertically installed rods		Tube diameter d [cm]			Geometrical properties: rod		Material	
	pull-out force $F_{t,max}$ [N]	displacement u_z [mm]	25	50	60	l [m]	λ [-]	E-G	dry density *)╬ ρ_d [g/cm³]
1	577.8	3.6				0.5	33		1.464
2	366.0	3.8							1.467
3	1024.6	4.9				1.0	67		1.467
4	924.6	5.88						E	1.444
5	1764.4	8.62	☑			1.5	100		1.488
6	1082.6	6.87							1.434
7	1318.0	14.38				0.5	33		1.451
8	510.6	7.19						F	1.461
9	2278.6	15.37				1.0	67		1.476
10	1928.2	15.07							1.452
11	154.8	4.58				0.5	33		◙
12	130.8	4.25							◙
13	483	3.6				1.0	67		◙
14	362.4	4.58						E	◙
15	433.2	5.56				1.5	100		◙
16	435.6	4.91		☑					◙
17	108.6	15.04				0.5	33		◙
18	99.6	13.08							◙
19	264.6	8.83				1.0	67		◙
20	161.4	10.0						F	◙
21	670.8	6.05				1.5	100		◙
22	971.6	7.17							◙
23	241.2	10.13				0.5	33		◙
24	171.6	12.42			☑	1.0	67	F	◙
25	886.2	12.0				1.5	100		◙

*) smeared average value, total weighted mass divided by the total tube volume;
◙ errors in measurements; ╬ the soil density (D) is for the soil types E and F and the tube with 25 cm diameter, loose and for greater diameter, D = loose to very loose

As already mentioned, the soil density (D) was lower for soil within greater tube diameters. Thus, the pull-out forces received from the tests with variable tube diameter are only comparable with restrictions in terms of the soil density (D). It is pointed out that for very low soil density (D) which was close to the loosest compaction degree, the rods could be pulled-out by hand only. This was observed even for longer rod lengths and regardless of the applied material E or F, sees test no.: 23 and 24, Table 22. The reason for this is that almost no interlocking between the soil and the rod occurs, which finally results in very low pull-out forces ($F_{t,max}$).

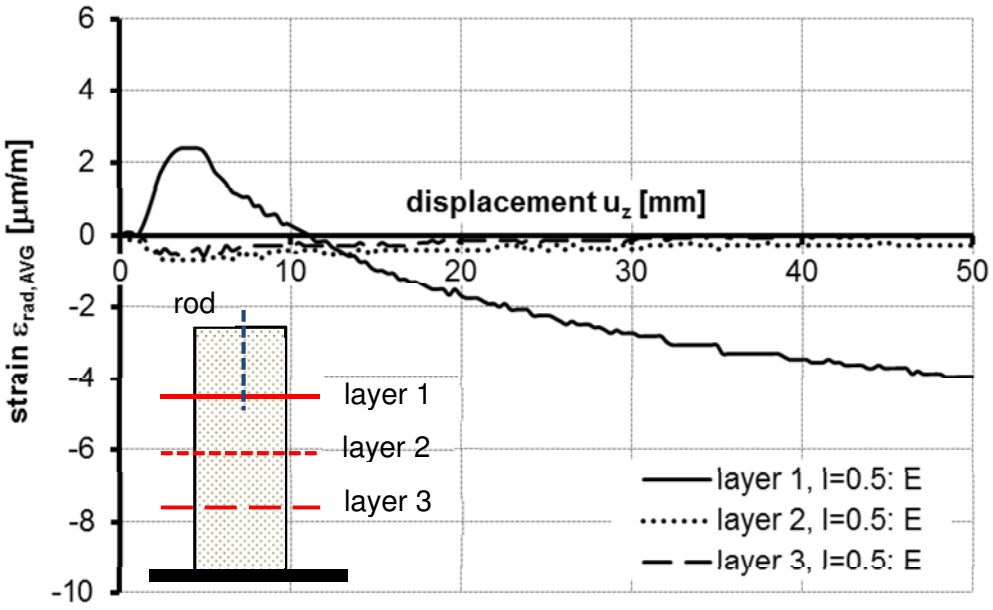

Fig. 74: Measured strains ($\varepsilon_{rad,\,AVG}$) outside the tube with 25 cm diameter, during the pull-out process of the rod with 50 cm length in material E.

Figure 74 & 75 illustrate the average value of the measured radial strains outside the tube with 25 cm diameter and filled with the material E, versus the pull-out displacements (u_z) caused by the pull-out process of the rod with 50 respectively 150 cm rod length.

Similar to the installation process, the strain gauges installed within layer two and three did not correspond to the pull-out process of the rod with 50 cm length, Fig 74. A significant increase of the radial strains was observed for layer one approximately until the pull-out force ($F_{t,max}$) was reached, u_z = 3.8 mm, see Table 22. A sharp reduction of the observed strains occurred afterwards. In other words, the strain gauges within layer one were showing an increase of the tube radius, hence, volumetric expansion until the pull-out force was reached. Afterwards, a decrease of the radius, hence volumetric compression occurred.

The strain gauges of layer three, installed slightly above the rod tip of the 150 cm long rod, show behaviour comparable to the strain gauges of level one for

the rod with 50 cm length, Figure 74 & 75. A positive peak value was reached after a few pull-out displacements (u_z). The displacements correspond to the necessary displacements to reach the pull-out force. Afterwards, a significant decrease of the observed strains occurred.

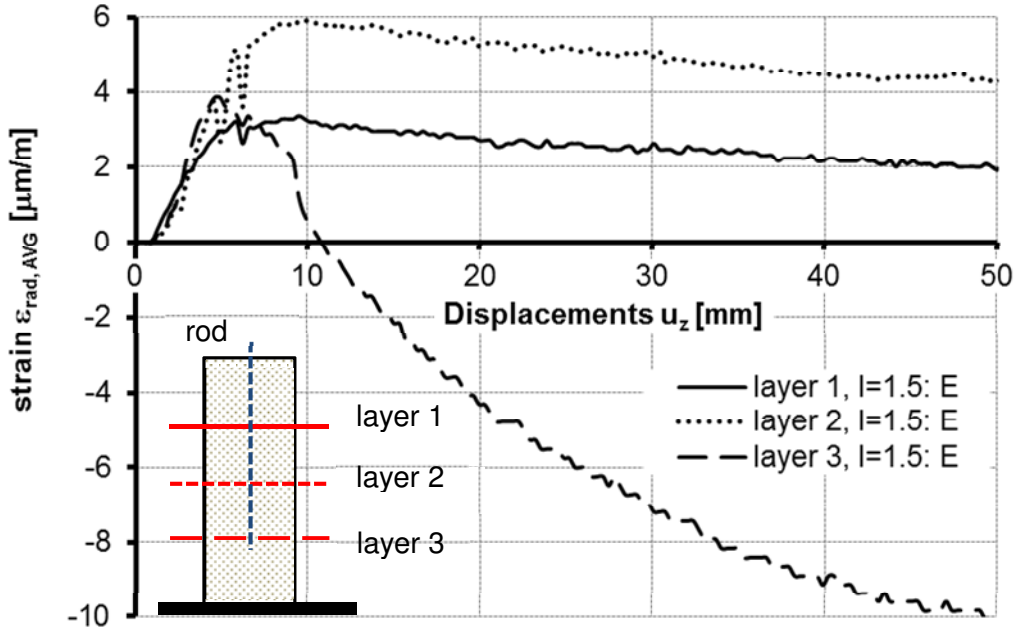

Fig. 75: Measured strains ($\varepsilon_{rad,\,AVG}$) outside the tube with 25 cm diameter, due the pull-out process of the 150 cm long rod in material E.

However, the strain gauges of layer one and two of the experiments with 150 cm rod length, behave very differently compared to layer three. A tube expansion of both layers can be observed, but significantly weaker for layer one. Possible reasons for this are the fact that the tube is fixed within the traverse, that the radial stresses increase with depth (z), and that friction between the top surface of the tube and the traverse occurred, which finally hampered an expansion.

3.5.5 Comparison of results and discussion

- **Installation process**

Figure 76 depicts the average value of the measured radial strains outside the tube with 25 cm diameter and filled with material E and F versus the elapsed time until the rod with 100 cm length was fully installed. Similar phenomena are observed for both soil types during the installation of the threaded rod. In a first phase (ph 1) the measured radial strains ($\varepsilon_{rad,\,AVE}$) begin to develop before the corresponding depth (z) of the measurement layer is reached. Shortly before the rod tip reaches the measurement layer, phase two (ph 2) starts with a

significant decrease of the radial strains, when the threaded rod is installed until much greater depths (z), Fig 76.

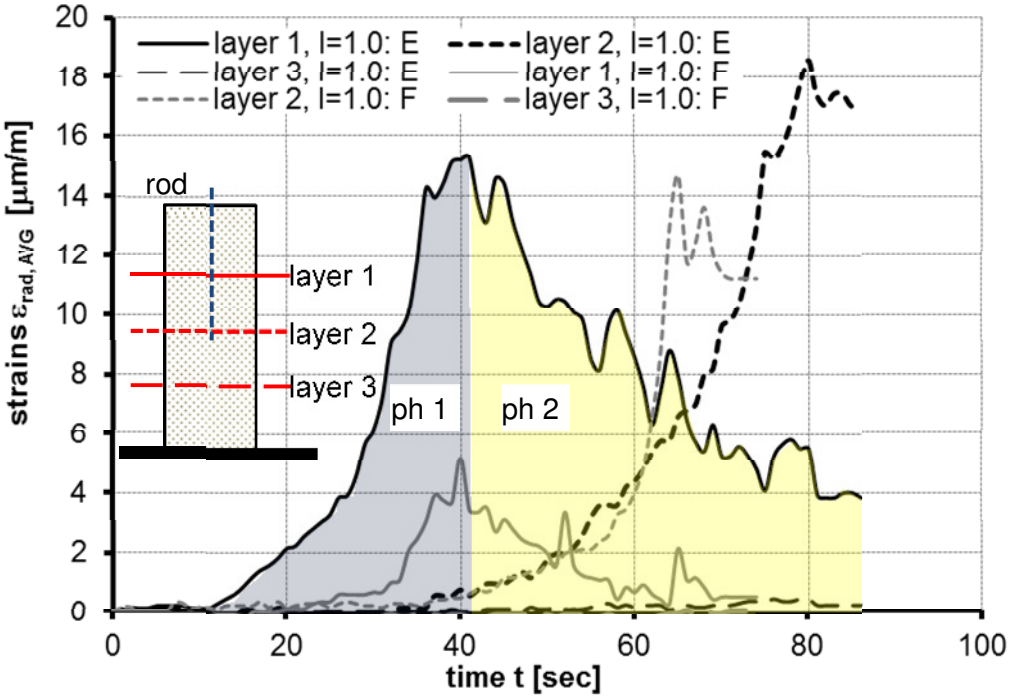

Fig. 76: Measured strains ($\varepsilon_{rad,\,AVG}$) outside the tube with 25 cm diameter, due the installation process of the rod with 100 cm length in material E and material F. The introduced phases (ph 1 development of interlocking effects and volumetric expansion – ph 2 reduction of interlocking effects and volumetric compression) are coloured for the layer 1, material E.

The observed phases can be reasonably interpreted as the beginning of interlocking effects during the installation of the first section of the rod and a reduction or even complete reduction of the interlocking effects for the first rod section when the rod penetrates much further.

However, the measured strains are bigger for deeper arranged measurement layers. Hence, stronger interlocking effects were developed.

When reflecting the results of lab test one (L1) especially the visualized soil-rod interaction due to the threaded rod installation, good comparability to the results of lab test two is given, Figure 56 & 57. For L1, a settlement zone close to the rod end and a heaving for the upper rod section was observed. This explains the loose or strong reduction of interlocking effects for the upper rod section and the development of strong interlocking effects for the final section of the rod, with a view to the measured strains ($\varepsilon_{rad,\,AVG}$), Figure 76.

To conclude and to address research question three (Q3): "*What is the influence of the installation process with respect to the bearing capacity?*" it is pointed

out that especially for deeper and medium deep installed rod sections a significant increase of radial stresses exists which results in a higher resistance against applied tension loads.

- **Pull-out process**

Figure 77 illustrates the measured strains ($\varepsilon_{rad,\ AVG}$) for the pull-out experiments within the tube with 25 cm diameter and filled with material E and F. The strain gauges within layer 3 which are arranged well under the rod tip show a volumetric tube compression for both soil types applied. This is a result of strong boundary effects, due to the great volumetric tube expansion above, vide supra. The results of these strain gauges are therefore no longer considered.

Much greater volumetric tube expansion than with material E was observed in the tests with material F. However, the maximum volumetric expansion was almost the same for layer 1 and layer 2, $\varepsilon_{rad,\ AVG,max} \approx 3$ µm/m for material E and about 15 µm/m for material F.

A significant increase of the radial strains is observed for layer two of material E and F approximately until the pull-out force ($F_{t,max}$) is reached, $u_z \approx 15$ mm for material F and about 5 mm for material E, see Table 22. Afterwards, a significant reduction is recognized.

The maximum tube expansion is almost reached simultaneously for layer one and two of material E. This cannot be observed for material F where the peak values are reached much more delayed.

To conclude and to address research question two (Q2) with particular consideration to interlocking effects, it is underlined that radial expansion over the rod shaft can be reasonably considered if a tension load is applied to the threaded rods.

Finally, it is worth remembering that the results gained from L2 are influenced by boundary conditions, as already discussed above. For this reason, the results are only considered in a phenomenological way and with restrictions.

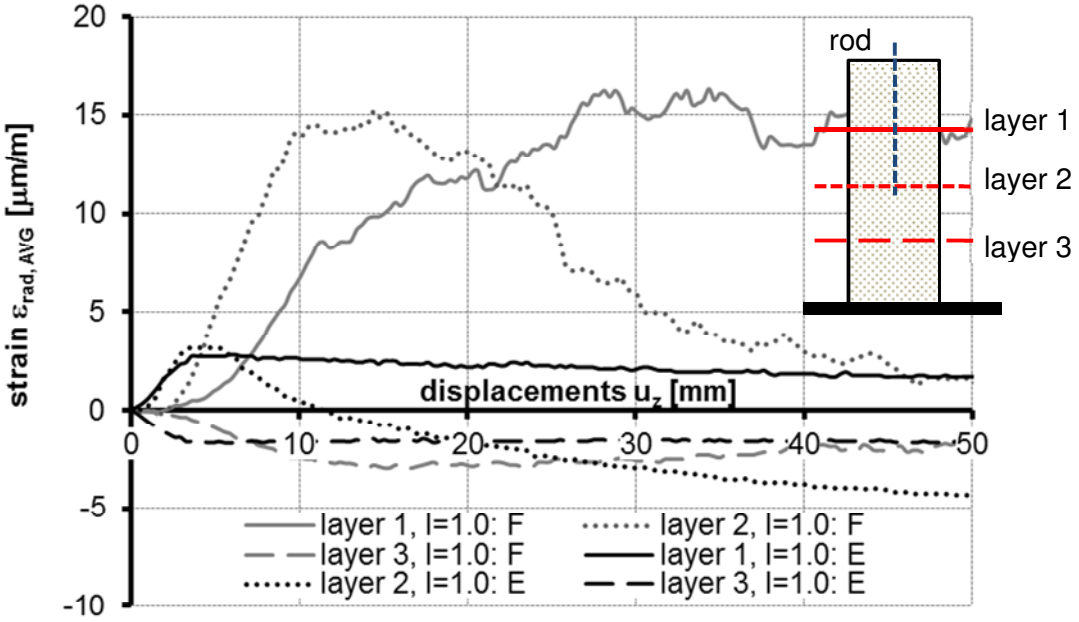

Fig. 77: Measured strains ($\varepsilon_{rad, AVG}$) outside the tube with 25 cm diameter, during the pull-out process of the rod with 100 cm length in material E and material F.

3.5.6 Comparison of literature and discussion

- **Installation process**

White and Bolton (2004), see Figure 19, and Witzel (2004), see Figure 20 in chapter 2.2.4, investigated the coefficient of earth pressure K_i (σ'_h/σ'_v) after pile driving, depending on the distance to the pile axis. The coefficient of earth pressure, and consequently the radial stresses too, are highest very close to the pile shaft and decrease significantly with increasing distance to the pile shaft. Transferring this fact to L2, where radial strains are measured relatively far away from the pile shaft, depending on the applied tube, it is pointed out that higher strain values are expected close to the pile shaft, even if the L2 results are influenced by boundary conditions.

However, friction fatigue, a reduction of the shaft friction as the pile tip penetrates further, is observed during the installation of the threaded rod too, similar to Jardine (1991), Chow (1997), White and Lehane (2004), White and Bolton (2004) as well as Gavin and Gallagher (2005). Friction fatigue is basically considered due to cyclic shearing during the pile installation process, where material is replaced and "flows" upwards around the pile if the pile penetrates further.

To conclude, strong similarities to pile driving are observed for the rod installation by screwing only.

- **Pull-out process**

Wernick (1978) and also Lehane et al. (1993) especially considered interlocking effects between the pile and the soil if a pile is being pulled out. In this context, radial tube expansions due to interlocking effects are observed for L2 until approximately the pull-out force ($F_{t,max}$) was reached. The interlocking effects are highly dependent on the soil density (D) and the medium size diameter (d_{50}) of the grading curve from the applied material.

To conclude, interlocking effects can be reasonably considered over the full rod shaft, depending on the corresponding depth (z) and the pull-out displacement (u_z). Similar to the installation process, much greater effects than measured are expected close to the pile shaft.

3.6 Summary and conclusion

The chapter focused on a rich set of experimental investigations to address the introduced research questions (Q1 – Q5), see the beginning of this main chapter. Two different field (F1 and F2) and two different lab tests (L1 and L2) have been conducted therefore, where threaded rods were basically pulled out.

At this point it is noted that field test three (F3) is described in Chapter 6. However, highly innovative and complex experimental techniques as well as extensive sets of measurement methods were applied to address the research questions. The applied, respectively available materials were exhaustively characterised in a soil mechanical way.

Comprehensive pull-out data, in general vertical displacements (u_z) and pull-out forces ($F_{t,max}$), were gained and discussed, depending on the applied material, the rod length (l) respectively the slenderness ratio (λ) and the rod inclination (α). The load-displacement graphs showed in all cases a reduction of the tension force after a peak value was reached if the experiment was conducted path controlled. In dependence of the material type and experiment, strong to weak variability of the gained pull-out forces was observed if all basic conditions were kept constant.

The necessary displacements u_z to reach the pull-out force showed low variability in all cases. Different design approaches were applied in order to calculate the pull-out forces and to finally compare the results with the gained test results, with very low success. The soil density (D), which highly influences the pull-out forces, can be identified as a key factor. For very low soil density the rods can be pulled-out by hand only and for great soil density (D) pull-out force values up to 60 kN for 2 m long rods were recognized.

For greater rod lengths a nearly constant pull-out force was reached, even when the length was further increased. In addition, a clear relation between the pull-out forces of vertically and inclined installed rods was recognized, which is worked out in a more general way in Chapter 5.

Innovative transparent and granular soil was developed for L1, which allowed an insight view into the very complex rod-soil interaction. The experiments were conducted successfully and the soil-rod interactions due to the installation and the pull-out process were visualized. Nevertheless, displacements were observed very close to the observation window of the model container and boundary conditions may influence the results therefore. Total displacements due to the pull-out experiments were mostly noticed superficial and the shape of the observed mobilized failure body is similar to Chattopadhyay's and Pise's (1986) approach, where most of the failure occurs along the pile shaft.

However, the performance of lab test two was very hard to handle, especially when greater tubes were applied, which resulted in irregularities of the soil density (D). The analysed results are influenced by boundary conditions and the measured strains are not converted to stresses for this reason. Although these influences are quantitatively unknown, the gained results are considered in a phenomenological way and show reasonable agreement with results from the literature. Especially for the investigated installation process where friction fatigue was observed. Radial expansions along the pile shaft where observed during the pull-out tests, approximately until the pull-out force was reached

In conclusion, the results of the lab tests show that most of the failure occurs along the pile shaft and that radial volumetric expansions along the shaft occur when a tension load is applied to the rod. The comparison with the design approach of Chattopadhyay and Pise (1986) was done with success for the 50 cm long rod only.

In the following chapter, numerical simulations based on a DEM are executed, in order to determine the shape of the failure body for longer rods.

4 Numerical investigations

4.1 Introduction

Numerical investigations concerning the rod-subsoil interactions are based on the Discrete Element Method (DEM) and are presented in this chapter. First, after a very brief introduction into the DEM, inverse parameter estimation is presented in order to determine the numerical properties for the DEM-model. For this, a box filled with discrete soil particles was modelled and a 2 m long numerically calibrated rod was pulled out path-controlled. The rod was placed vertically in the centre of the box. The particle properties were varied until the pull-out force of F1, where material A was applied, was reached. Second, results of lab test L1, which showed the visualization of the soil-rod interactions based on the pull-out test of the 50 cm long vertical rod, were compared with the results of the calibrated DEM-model. Additionally, the shape of the numerically determined, mobilized soil body was compared with the shape of the failure body from the design approach of Chattopadhyay and Pise (1986). Finally, the load transfer from the rod into the soil was analysed.

To conclude, the numerical investigations have been done to address research questions one and two (Q1, Q2).

4.2 Discrete Element Method

To perform research into the behaviour of granular materials, Cundall and Strack (1979) formulated the DEM. "*The method is based on the use of an explicit numerical scheme in which the interaction of rigid particles is monitored contact by contact and the motion of the particles is modeled particle by particle",* Cundall and Strack (1979). The formulation headed into a numerical code, called "Particle Flow Code (PFC)" to solve variable tasks in two and three dimensions. PFC deals with rigid spherical particles for three dimensional problems (PFC^{3D}) and with rigid disks for two dimensional problems (PFC^{2D}). However, wall elements are usually used as numerical model boundaries. For the numerical investigations within this thesis, PFC^{3D} was applied, distributed by Itasca (2008).

The rigid spherical particles modelled in PFC^{3D} are able to slightly overlap and the numerical calculation process consists of two parts for each numerical time step. *"At the start of each time step the set of contacts is updated from the known particle positions. The force-displacement law is then applied to each contact to update the contact forces based on the relative motion between the*

two entities at the contact. Next, Newton's law of motion is applied to each particle to update its velocity and position based on the resultant forces and moments arising from the contact forces and any forces acting on the particle", Itasca (2005). The following principle particle contact laws are available in PFC^{3D}:

- linear contact springs or simplified Hertz-Mindlin law
- coulomb sliding
- bonding, normal bonds for simulating adhesion respectively cohesion between particles and parallel bonds to simulate a moment resistance between particles
- user defined contact models

Fundamental principles on PFC^{3D} are exhaustively summarised by Itasca (2005) and fundamental principles in a geotechnical point of view are prepared by, e.g.: Herten (1999), Hainbüchner (2001), Halsegger (2004), Pohl (2005), Zöhrer (2006) and Lenzi (2009).

However, in principle it is possible to model variable geometrical shapes of soil particles in PFC^{3D} similar to the shape of granular particles in reality. Several spherical particles are bonded permanently together for this and are finally called clumps, Lackner (2012). It is pointed out that dealing with spherical particles is computationally the most efficient and fastest way because the computational time increases significantly with an increasing amount of spheres, Jakob and Konietzky (2012). This leads to the need of geometrical simplifications of the numerical model if dealing with larger model dimensions and small particle radii.

It is pointed out that the PFC code was completely redesigned during the last years, which lead to a new significantly faster and versatile version, which was commercially available in late 2014. However, the older version 4.00-191 based on 64-bit was used for the research in this thesis, Itasca (2008).

4.3 Inverse calibration

4.3.1 Introduction

Physical material properties in soil mechanics are basically continuum based properties and mostly cannot be applied directly for a discontinuum model, e.g.: PFC^{3D}-model. A discontinuum model needs particle contact properties, e.g. linear contact springs. The particle weight density (γ_s), the porosity (n) and the

grading curve are exceptions and can be applied more or less directly to the PFC^{3D}-model. For that reason, a numerically - based calibration process is needed to simulate the continuum - based material parameters, e.g. oedometric module (E_s), with applied particle contact parameters. Two fundamentally different calibration processes are basically possible:

(1) Modeling different lab tests, e.g. the oedometer test, to match the continuum-based material properties with applied contact properties. These contact properties are finally applied to the full numerical model, e.g. land slide model
(2) Numerical modeling of a full numerical model and matching with applied contact properties the measured physical response, e.g. pull-out force $F_{t,max}$ and vertical displacements (u_z), of a real experiment. This is called inverse calibration.

Inverse calibration, also called inverse modeling, Figure 78, was applied in order to estimate the DEM particle contact parameters for the applied soil type, material A of field test F1, see Table 5. The single rod pull-out test of F1was modeled for this. The numerical contact properties of material A were varied until the numerically determined pull-out force matched the measured physical response of F1, test no: 3 $F_{t,max} \approx 34.5$ kN, $u_z = 10.6$ mm, see Fig. 27, Tab. 6 in Chapter 3.2.4. In this context, the contact parameters were finally derived by "trial and error". This neglects the possibility of multiple combinations of the DEM parameters that could achieve the same numerical response. However, the effect of multiple parameter combinations was not investigated. Details about these effects can be found in, e.g. Zhang (2010).

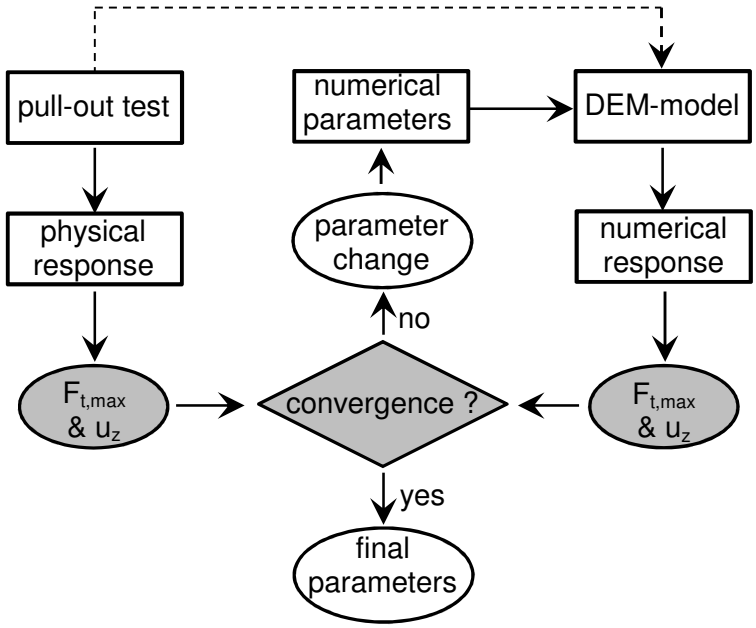

Fig. 78: Numerical parameter estimation by inverse modelling of pull-out tests, strongly modified after Steger (2010)

It is underlined that the main goal of the numerical simulations is to compare parts of the numerical response of the DEM-model - the particle rod interaction of rods with 2 m length - with the physical response of L2 with view to the mobilized soil body due to the vertical tension load, Figure 61in Chapter 3.4.4.

4.3.2 Overview on the numerical model and numerical procedure

The geometrical dimensions of the numerical model can be found in Figure 79. The 2 m long vertical rod is arranged in the centre of the box and is modelled of 133 single spheres with a diameter of d = 15 mm which are bonded together by applying normal and parallel bonds. The rod was calibrated in advance with the help of three point bending tests and vertical elongation tests to determine the numerical parameters of the different contact bonds, Fink and Supp (2008), Supp and Semprich (2010). The final parameters are summarised in Table 23.

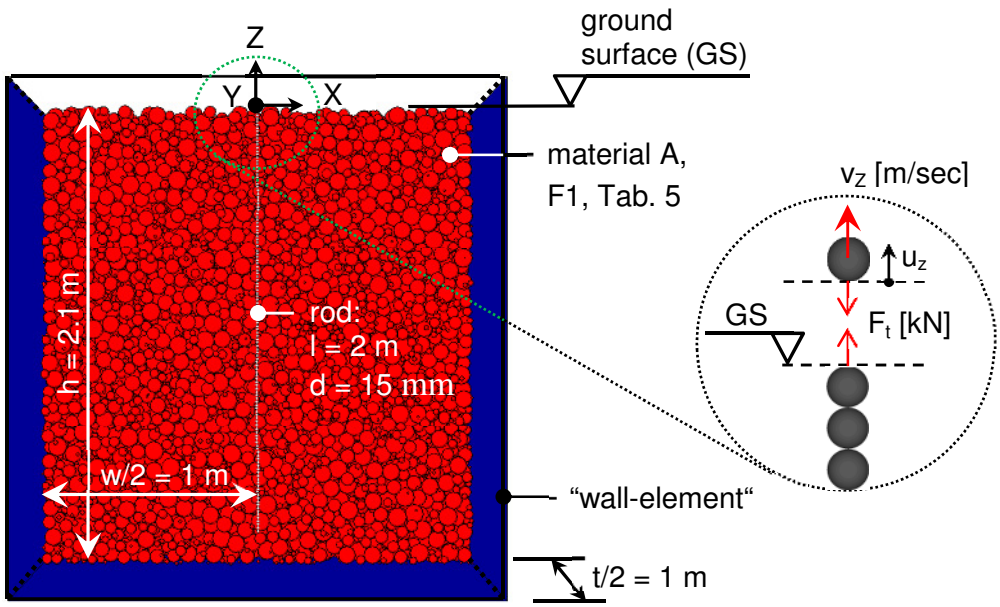

Fig. 79: Perspective view of the numerical model. The discrete soil particles are only visualized for the rear half of the model and the rod is arranged vertically in the centre of the box. Right: Numerical method for the path-controlled pull-out test

The grading curve of material A is not fully modelled because this would lead to particle amounts of several millions, which is not manageable computationally. Several authors up-scale the grading curve to address this problem. This is done by multiplying all particle radii of the grading curve with a constant factor, Zöhrer (2006). A series of numerical investigations were utilized by Lenzi (2009) to determine the effect of up-scaling on the results of tri-axial tests, which have shown low influence. Pohl (2005) neglected smaller particles, by cutting off the very left part of the grading curve, and did an

additional up-scaling of the new grading curve afterwards. Herten (1999) simplified the grading curve to a mono particle diameter and calculated the three-dimensional earth pressure on a sheet pile wall - with reasonable success. To conclude, it is underlined that doubling of all soil particle radii leads in general to a reduction of the particle amount by a factor of eight.

Tab. 23: Numerical material properties of the rod, according to Supp and Semprich (2010)

Properties		Value
Particle density	$\rho^{A)}$ [kg/m³]	14 900
Normal stiffness	k_N [N/m]	$1.7 * 10^9$
Shear stiffness	k_S [N/m]	$1.7 * 10^9$
Particle friction	$\mu_{rod}{}^{B)}$ [-]	0.75
Contact bond normal strength	*n_bond* [N]	$5 * 10^{12}$
Contact bond shear strength	*s_bond* [N]	$5 * 10^{12}$
Parallel bond radius multiplier	*pb_radius* [-]	$1.325 * r_{rod}$
Parallel bond normal stiffness	pb_k_n [Pa/m]	$4.62 * 10^{12}$
Parallel bond shear stiffness	pb_k_s [Pa/m]	$4.62 * 10^{12}$
Parallel bond normal strength	$pb\_n_{strength}$ [Pa]	$1*10^{20}$
Parallel bond shear strength	$pb\_s_{strength}$ [Pa]	$1*10^{20}$

[A)] Converted, the overall weight of a particle chain and the threaded rod is the same; [B)] rod particle friction (μ_{rod}) = soil particle friction (μ_{soil})

The grading curve of material A is cut off for particle radii smaller than 2.5 mm and the corresponding mass percentage is linearly partitioned to the remaining mass, Fig. 80. The particle radii of the numerically modelled and strongly simplified grading curve are chosen from a uniform distribution (r_{min} = 2.5 mm and r_{max} = 4.5 cm) and can be found in Figure 80.

The soil particles are generated automatically within the numerically modelled box, which was made of wall-elements, Fig. 79. For this purpose, the total amount of particles is estimated in advance. Therefore, an average particle radius is calculated and the total volume of the box, minus the inter particle pore volume, is divided by the volume of one average particle. However, the numerically calibrated rod was arranged in the centre of the box before the box was filled with particles. Meanwhile, the rod particle positions were fixed. The soil particles were generated randomly within the box and were approximately ten times smaller than the required end radius afterwards. The soil particles

were finally expanded stepwise until the end radii were reached. This method was chosen in order to ensure interlocking effects between the soil and the rod because the rod installation process was not modelled.

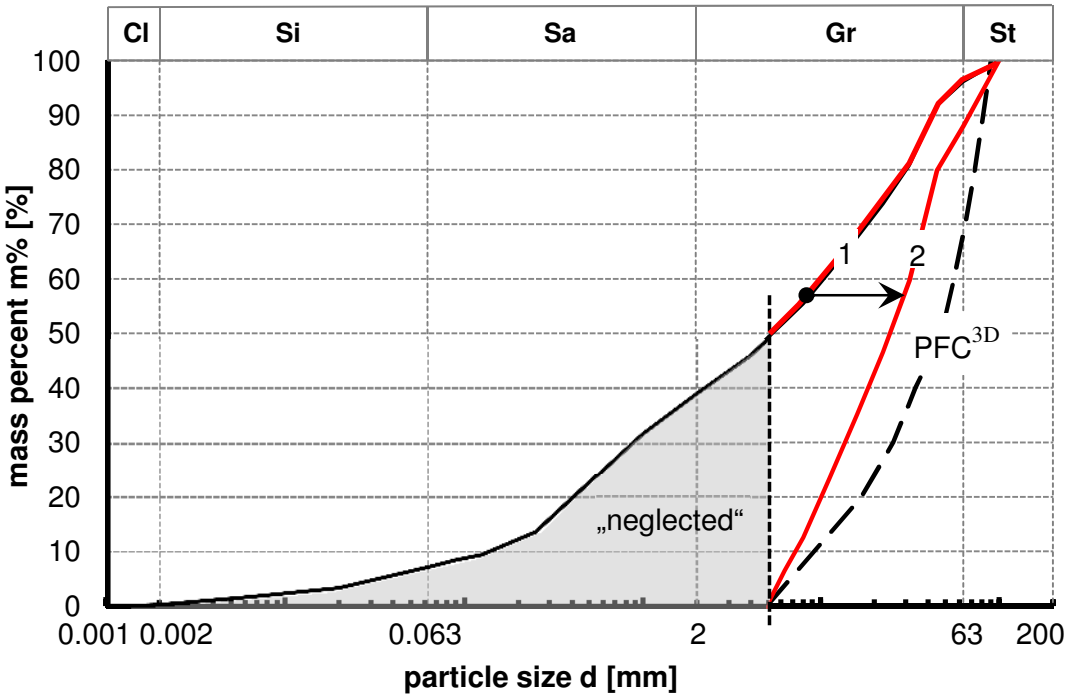

Fig. 80: Idealised grading curve of material A (F1) for the numerical simulations. 1 … grading curve cut off; 2 … idealised grading curve; PFC^{3D} … numerically applied grading curve (particle radii are chosen from a uniform distribution: r_{min} = 2.5 mm and r_{max} = 4.5 cm)

- **Numerical procedure**

In the following, the numerical procedure of the pull-out tests is shown. The soil particle generation process is not included, see procedure above:

1) Assigning the defined particle parameters to the modelled and already generated soil particles, the same parameters were also applied to the wall-elements
2) Cancelling of the rod fixing
3) Assigning a vertical velocity (v_Z = 1 mm / sec) to the first particle of the rod which was arranged at the upper model limit, Figure 79. The velocity of the first particle was fixed during the numerical simulations
4) Numerical monitoring of the vertical displacements (u_z) of the first rod particle and the (normal) force (F_t) between the first and the second rod particle
5) Generating a numerically determined force (F_t) - displacement (u_z) graph

Steps one to five were repeated until the pull-out force and the vertical displacements of F1 and material A were reached.

4.3.3 Calibration process and results

- Calibration process

A contact model based on linear springs, shear (k_S) and normal springs (k_N), and coulomb sliding (μ) was applied to model the properties of material A, Fig. 81. The shear stiffness (k_S) is assumed to be a third of the normal stiffness ($k_S = 1/3\ k_N$).

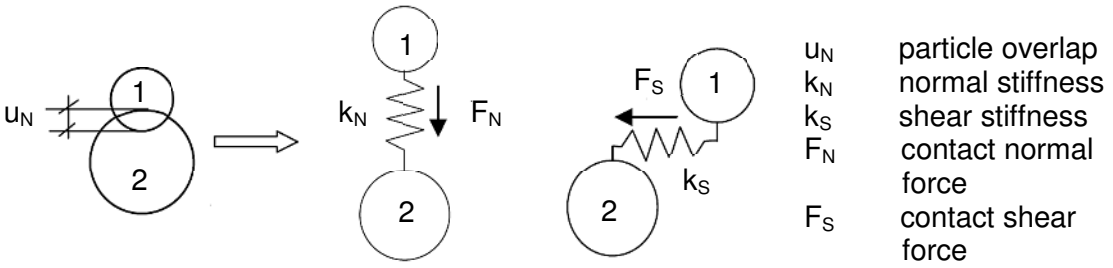

Fig. 81: Contact springs between two particles which are in contact, according to Hainbüchner (2001)

Several authors, e. g Herten (1999), Halsegger (2004), have noticed that the physical friction angle (φ) of a soil cannot be simulated numerically by applying the value to the particle contact friction ($\mu = \tan(\varphi)$), if spherical particles are applied. This is because of the rolling resistance of the spherical particles which is much lower compared to a real grain with variable shape. Bardet (1994) investigated the influence of the effects of particle rotations on the failure of granular materials, based on simulations of biaxial tests. Almost no influence was noticed to the linear spring properties but significant influence was noticed on the shear strength of the material. Therefore, particle rotations are numerically blocked for a chosen amount of particles. Lenzi (2009) concluded that blocking the rotation of 50% of the soil particles ensures optimal convergence with lab tests. In addition, he noticed that the effective friction angle (φ) is almost numerically independent from the up-scaling of the grain size distribution if spheres are applied.

For that reason, the rotation was blocked for half of the modelled soil particles of material A. Due to this, the particle contact friction (μ) was assumed to be the tangents of the friction angle (φ).

The interparticle porosity (n) of the modelled material A differs from the real material A, Table 5. This is due to the simplified grading curve which was

applied for the simulations, where the smaller particle radii were neglected, Fig. 80. Smaller particles of a grading curve are usually arranged between the interparticle pores of larger particles. This fact leads to a lower total porosity if dealing with soils with a wide-spread grading curve. However, about 100,000 particles were modelled in total and the resultant porosity was about n = 0.38. It is pointed out that a denser particle arrangement was numerically not possible when applying the particle generation method introduced above. This means that the particle arrangement can be virtually classified into a dense to very dense density (D). The particle weight density (γ_s) was modified to ensure almost the same wet weight density of the soil (γ_F) like for F1, material A.

To conclude, the final parameter to be determined for the simulations was the particle contact normal stiffness (k_N), while all other properties were known respectively assumed, see Table 24.

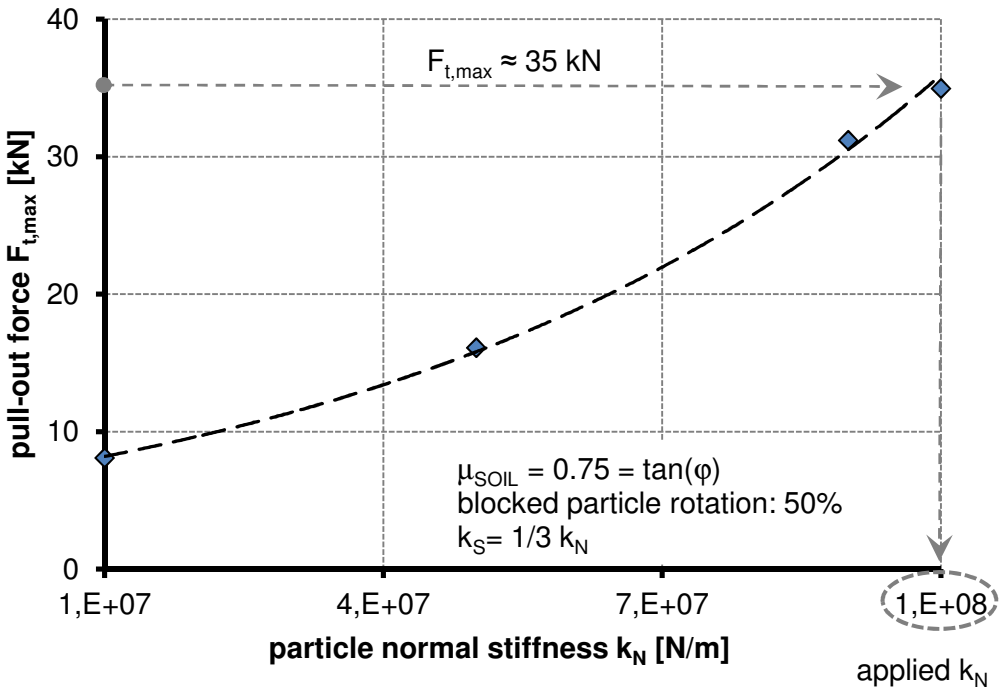

Fig. 82: Influence of the particle normal stiffness (k_N) on the numerically determined pull-out force $F_{t,max}$. An exponential best fit curve (R^2 = 0.9987) is applied.

Figure 82 illustrates the strong influence of the particle contact stiffness to the numerically determined pull-out force $F_{t,max.}$ The influence was determined by simulating pull-out tests and keeping the particle friction (μ) and other general properties (porosity, particle radii, particle density) constant, Table 24. An increase of the particle stiffness (k_N, k_S = 1/3 k_N) by a factor of ten leads to an increase of the pull-out force by a factor of four.

This highlights the fact that the influence of interlocking effects to the pull-out force is significant. In this context, the soil density (D) has a major impact on the oedometer modulus (E_s) of a soil; hence soil behaves more stiffly if the soil density (D) is higher. However, the experimental results (L2) have shown that the soil density (D) can be classified as a main influence factor to the bearing capacity of the rods. This fact can be concluded for the simulations as well.

The final contact and particle parameters of the DEM-model are summarised in Table 24.

Tab. 24: Numerical properties for the modelled material A

Properties		Value
Particle density	$\rho^{A)}$ [kg/m³]	3 700
Normal stiffness	k_N [N/m]	$1.0 * 10^8$
Shear stiffness	k_S [N/m]	$1/3 * k_N = 3.33 * 10^7$
Particle friction	$\mu_{soil}^{B)}$ [-]	0.75
Blocked particle rotation	[%]	50
Porosity	n [-]	0.38

A) Converted, the weight density of the soil (γ_F) is identical like for F1;
B) soil particle friction $\mu_{soil} = \tan(\varphi)$, see Table 5

- **Results**

Figure 83 shows the load-displacement graph comparison of F1 and the DEM-model where the parameters of Table 24 were applied. The graph produced with the DEM-model shows a great resemblance to test number three, F1, material A.

The pull-out force in the DEM-model is reached faster, hence with fewer necessary displacements ($u_z \approx 5$ mm), compared to the experiment. However, the displacements are still in the investigated range of the F1, $u_z = 5 – 11$ mm, see Fig. 32.

A relatively great load-drop of the load-displacement graph after reaching a (first) peak value, called pull-out force $F_{t,max}$, similar to the experiments can be observed for the numerical simulations as well. Furthermore, a “wave-like” post-peak behaviour of the graph is additionally observed. Presumably due to new interlocking effects between the soil particles and the rod. First, increases were developed and afterwards broken again with greater vertical displacements (u_z).

The distribution of contact forces and the translational velocities are numerically investigated additionally and Figure 84 presents the results at half model depth (t/2 = 1m) for the modelled soil only. The vertical rod axis (Z) is located at half model depth. A great contact force concentration for the lower half of the model and comparatively very low contact forces for the superficial part of the model are noticed. The translational velocities are concentrated in the upper half of the model where the contact forces are relatively low and almost no velocities occur for the lower model part, Fig. 84.

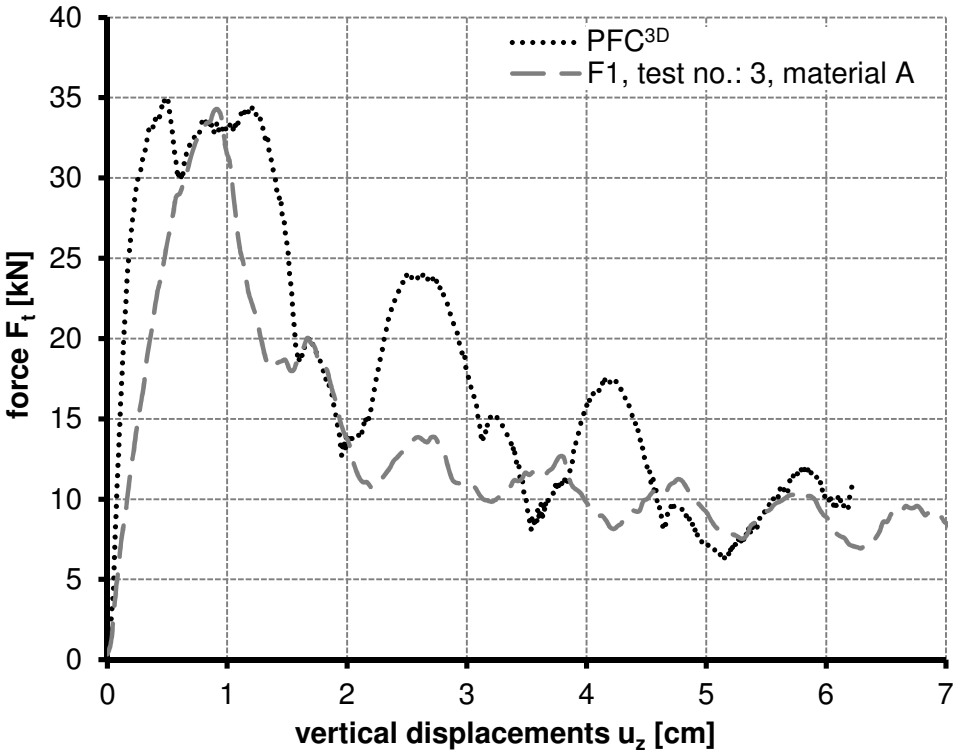

Fig. 83: Comparison of the load displacement graphs: PFC^{3D} and F1, see Figure 27 in addition

It is interesting to note that the visualized velocity vectors closest to the rod show a kind of "zigzag" arrangement, probably because of already disintegrated interlocking effects. This could also explain the very low concentration of contact forces for the upper model section. To conclude, the numerically observed failure occurs along the pile shaft only for the lower half of the rod.

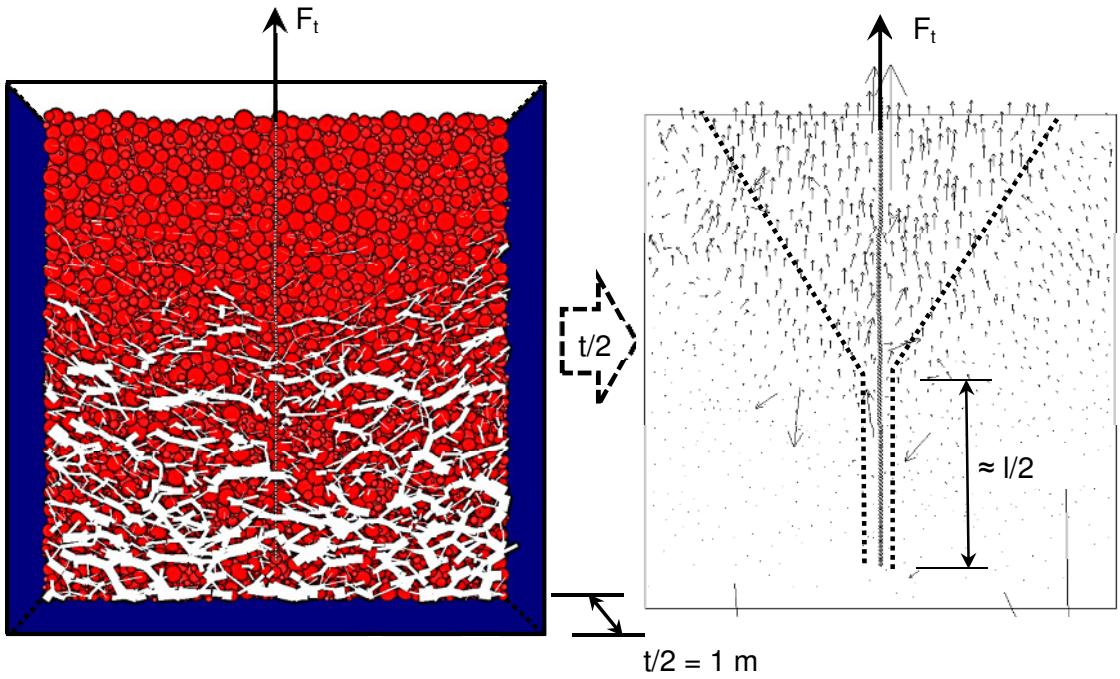

Fig. 84: Left: Distribution of the particle contact forces (white colour) at the half model depth (t/2). The discrete soil particles are visualized for the rear half of the model only (perspective view). Right: Distribution of the translational soil particle velocities (very strongly enlarged visualized). The left and the right picture corresponds to $u_z \approx 12$ mm

4.3.4 Result comparison and discussion

In this chapter, the shape of the numerically determined mobilized soil body is compared with approaches from the literature and the results of L2. This is done in order to address research question two (Q2).

- **Lab test 2**

In general, strong similarities can be observed by comparing the shapes of the mobilized soil bodies, determined from the experiment (L1, Figure 61) and the numerical investigations.

Pure sliding occurs along 40% of the rod shaft for the 50 cm long rod of L2 and pure sliding along 50% of the rod shaft occurs of the numerical investigations of the 200 cm long rod. However, pure sliding occurs only along the deeper rod section, approximately along the lower half of the rod.

Soil is mobilized in a more expanded manner when considering the first half of the rod. The largest expansion of the mobilized soil body was investigated on the top ground surface. The expansion drops finally down, approximately until the middle of the rod, where underneath pure sliding along the shaft occurs. However, a low concentration of contact forces is noticed when reflecting the

results of the numerical simulations for the upper rod half, Fig. 84. It seems that interlocking effects have already disappeared along the upper rod half.

- **Literature**

Figure 85 depicts the sketch of variable shapes of mobilized soil bodies for a 2 m long tension loaded rod and the mobilized soil body determined with PFC^{3D}. The approach of Chattopadhyay and Pise (1986) shows almost pure sliding along the rod shaft with exception of the very superficial part. It is interesting to note that the approach of Chattopadhyay and Pise (1986) reflected quiet well the shape of the mobilized soil body for the 50 cm long rod of L1. This cannot be observed for the 2 m long rod of the numerical investigations.

The approach of Jelinek and Ostermayer (1964) assumes a mobilize soil body failure which is developed very close to the rod shaft. However, it is pointed out that the calculated pull-out forces did not match the results of F1, when applying the approach of Jelinek and Ostermayer (1964) or Chattopadhyay and Pise (1986).

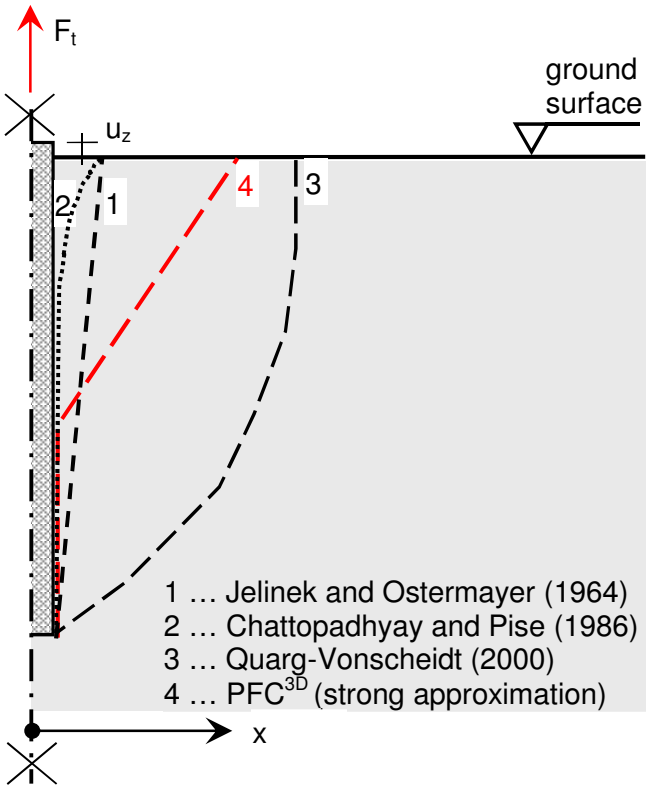

Fig. 85: Rotational symmetrical, schematic sketch of the numerically determined mobilized soil body and the shape of different approaches of mobilized soil bodies for vertically tension loaded and vertically installed threaded rods. The rod length is 2 m (λ = 133). For additional information and assumption see Table 10, Chapter 3.2.7

As already explained, see Chapter 3.2.7, the approach of Quarg-Vonscheidt (2000) is not applicable for the given boundary conditions with a view to the rod length and the material type. The shape of the mobilized soil body is very different in comparison to the numerically observed one.

The numerical one shows a sliding along the rod shaft for the lower half of the rod and an additional mobilized soil body which is attached on the upper half of the rod. A relatively strong contact force concentration along the rod shaft is observed for the lower half of the rod, where pure sliding occurs. Furthermore, a very low contact force concentration is observed along the upper half of the rod shaft. Hence, the major part of the load transfer from the rod into the soil is reasonably assumed to be along the lower half of the rod.

4.4 Summary and conclusions

A set of simplifications enabled the numerically performed pull-out tests. The threaded rod was modelled by applying a bonded particle chain and material A by applying spherical particle including up-scaling of the grading curve. The parameter set for the DEM-model was determined by inverse modelling. The particle stiffness (k_N, k_S) was varied and a great influence to the pull-out force was determined.

The load-displacement graph gained from the simulations shows a very similar behaviour, in terms of the pull-out force and the displacements, like the experiments of F1. Moreover, the post-peak behaviour of the load-displacement graph can also be compared well to the ones of this experiment.

It is highlighted that the rod length is different for L2 and the simulations, but the shape of the mobilized soil body gained fromL2 and the simulations is highly comparable. Pure sliding along the rod shaft occurred along the lower half of the rod only and for both types of investigations. A more expanded soil body is mobilized for the upper part of the rod. The expansion drops finally down, approximately until the middle of the rod. This is in a similar way observed for the experimental and the numerical investigations.

Finally, it must be stated that the influence of the numerical up-scaling of the grading-curve on the numerically determined shape of the failure body has not been investigated and is therefore unknown.

The final conclusion of chapter 4 is that great density (D) of a soil which is resulting in stiffer soil behaviour, leads to relatively high pull-out forces ($F_{t,max}$) of the rod. The reasons for this are interlocking effects with great impact to the load-transfer mechanism.

5 Design approach

5.1 Introduction

In Chapter 5, a first calculation model to estimate the pull-out resistance of vertically installed and tension-loaded threaded rods is presented.

In a first step, the most important results of the investigations carried out are summarized. Next, a geotechnical model to describe the pull-out resistance of the threaded rods is formulated. After that, empirical relationships are presented in order to estimate the pull-out resistance. Additionally, an empirical correlation between the pull-out resistance of vertically and inclined threaded rods is presented. Finally, design recommendations based on the EUROCODE 7 are given.

It is highlighted that the introduced design approach should be understood as a first design recommendation.

5.2 Estimation of the vertical pull-out force for vertically installed threaded rods

5.2.1 Fundamental basics

The experiments of lab test one as well as the numerical investigations showed that a kind of composite failure mechanism occurs when the pull-out force ($F_{t,max}$) was reached. Failure occurs along a slip surface where the relative displacements soil-rod or soil-soil are greatest and when the pull-out force ($F_{t,max}$) is exceeded. However, the composite mechanism consists of a slip surface along the lower half of the rod shaft and of a kind of mobilized soil volume surrounding the upper half of the rod at ultimate limit state, hence when the pull-out force is reached. However, the mobilized soil body is associated with losing density and the loss, respectively reduction of interlocking effects. Meyerhof (1973) and Chattopadhyay and Pise (1986) observed a relatively similar shaped failure body for piles. The failure surface respectively slip surface was more parabolic for the upper pile section and vertical as well as closest to the pile shaft for deeper sections of the pile, see Chapter 3.

The numerical investigations showed significantly higher contact force concentrations along the lower half of the rod, it seems this is a result of strong interlocking effects. A very marginal contact force concentration was noticed along the upper rod half because of the already mentioned loss of interlocking effects. It seems therefore logical that the main load transfer from the rod into the soil happens along the lower rod half. The results of the numerical investigations confirm this assumption.

The results of the numerical investigations showed a sound agreement with the results of L1, by considering the shape of the mobilized soil body. It is highlighted, that the effect of up-scaling of the grading curve to the shape of the mobilized soil body was not investigated, see Chapter 4.3.2 Figure 80.

However, by considering the load-displacement graphs of the field and lab tests, a great load-drop occurred after reaching the pull-out force ($F_{t,max}$). This is the result of the loss of interlocking effects. It is highlighted that it was not possible to estimate the pull-out force appropriate by applying design approaches known from the literature, see Chapters 2-3. It can be concluded that interlocking effects are playing a key role and must be taken into account for a design approach. Interlocking effects can be comprehended especially by considering cavity expansion theory, Boulon and Foray (1986) and Lehane et al. (1993), see Chapter 2. In this context, it is reasonable to apply cavity expansion to mechanically describe the interlocking effects caused by the threaded rod, see Chapter 2 and Equation 7-9.

The experimental investigations also showed that an influence of the depth (z) is given for the installation and pull-out process. Hence, the resultant radial stresses depend on the effective vertical stresses (σ'_v).

5.2.2 Simplified mechanical model

A simplified mechanical model to calculate the pull-out force of vertically installed threaded rods ($F_{t,max,0}$) is presented in this chapter. The mobilized soil body is neglected for this due to minor significance. The main load transfer from the rod into the soil is caused by friction and interlocking effects along the lower half of the rod shaft and the surrounding soil. For that reason, it is assumed that at ultimate limit state pure sliding along the rod shaft occurs. Lehane et al. (1993) observed pure sliding along the shaft of displacement piles at ULS. Additionally, he recognized that at failure the local shear stresses (τ_f) on the pile shaft follow the Coulomb failure criterion, see Chapter 2 and Equations 7 – 9. Considering the Coulomb failure criterion the soil resistance ($R_{t,0}$) to the pull-out force ($F_{t,max,0}$) is given by the integral of the local shear stresses at failure (τ_f) along the surface of the embedded rod, Equation 23.

$$R_{t,0} = d * \pi \int_{z=0}^{z=l} \tau_f \ \mathrm{dz} \geq F_{t,max,0} \tag{23}$$

Figure 86 illustrates the observed failure mechanism at ULS and the simplified mechanism in terms of pure sliding along the rod shaft.

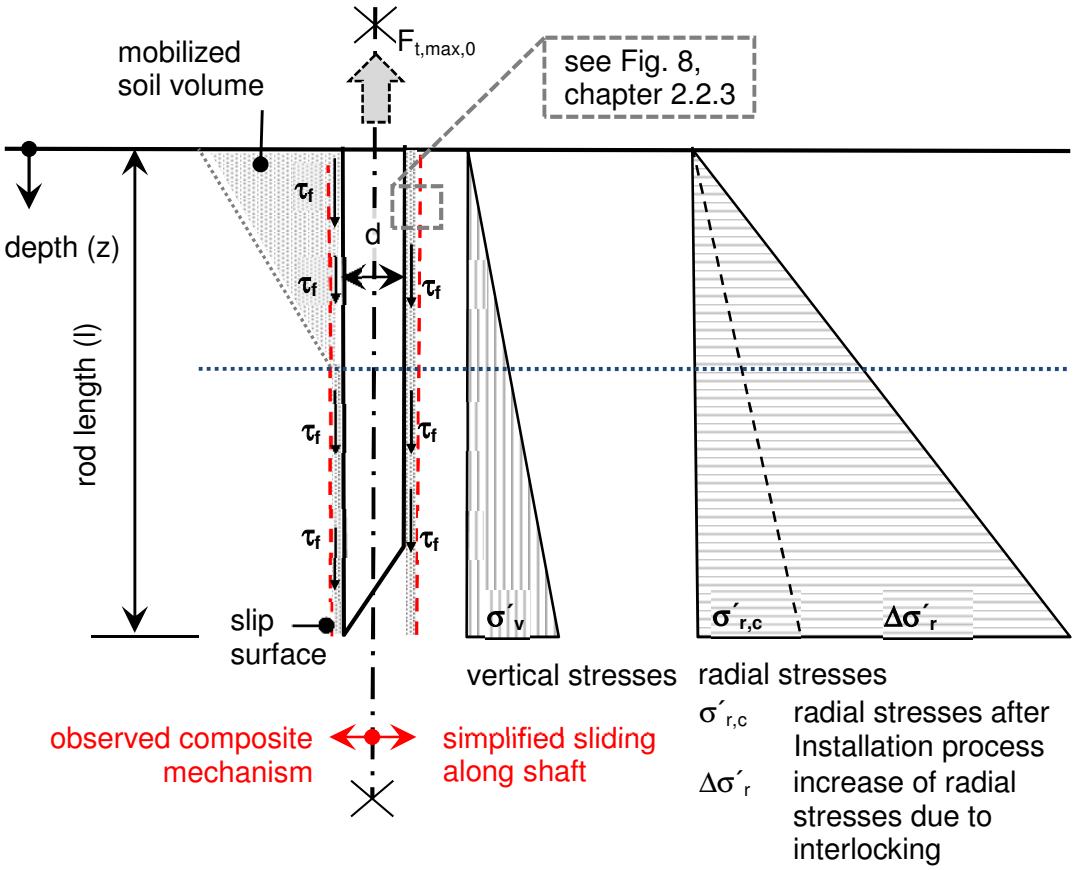

Fig. 86: Sketch of the load transfer into the soil caused by an applied tension load. Left, observed mechanism including a mobilized soil volume and right, simplified mechanism in terms of pure sliding along the shaft

The radial stresses depend on the radial stresses after the installation process ($\sigma'_{r,c}$) and the additional increase of radial stresses due to interlocking effects ($\Delta\sigma'_r$) which are caused by the pull-out process, Lehane et al. (1993). The radial stresses due to interlocking effects are - as already mentioned - more pronounced for piles with low diameters, see Equation (9). The interface friction angle (δ) at failure is assumed to be the friction angle (φ') of the soil because of the relatively rough rod surface, Jardine et al. (1993). It is underlined that the radial stresses on the pile shaft were not investigated in a quantitative way in this work.

Equation 24, reflects the relationship between the vertical and the full radial stresses. A pull-out coefficient ($K_{r,\delta=\varphi}$) is introduced, which covers the effects of the surface roughness of the rod ($\delta=\varphi'$), as well as the installation ($\sigma'_{r,c}$) and pull-out process ($\Delta\sigma'_r$) to the full radial stresses (σ'_{rf}). The full radial stresses which refer to the pull-out force ($F_{t,max,0}$) depend on the effective vertical stresses (σ'_v). This also addresses the significantly higher bearing capacity of the lower half of the rod. The resultant shear stresses on the pile shaft can be calculated with Equation 24.

$$\left(\acute{\sigma_{r,c}} + \Delta\acute{\sigma_r}\right) * \tan(\delta) = \tau_f = \acute{\sigma_v} * K_{r,\delta=\varphi} \tag{24}$$

The soil resistance ($R_{t,0}$) to the pull-out force ($F_{t,max,0}$) is finally given with Equation (25).

$$R_{t,0} = d * \pi \int_{z=0}^{z=l} \acute{\sigma_v} * K_{r,\delta=\varphi} \, dz \quad with: \acute{\sigma_v} = \acute{\gamma} * z \tag{25}$$

Boulon and Foray (1986) observed for sandy materials that the radial stresses are up to forty times higher than the vertical stresses if cavity expansion is blocked. In addition, he noticed that the ratio between radial and vertical stresses is significantly greater for low vertical stress levels (up to 100 kPa) and strongly decreasing with higher vertical stress levels. It can therefore be concluded that the pull-out coefficient ($K_{r,\delta=\varphi}$) is not constant and changing with depth (z).

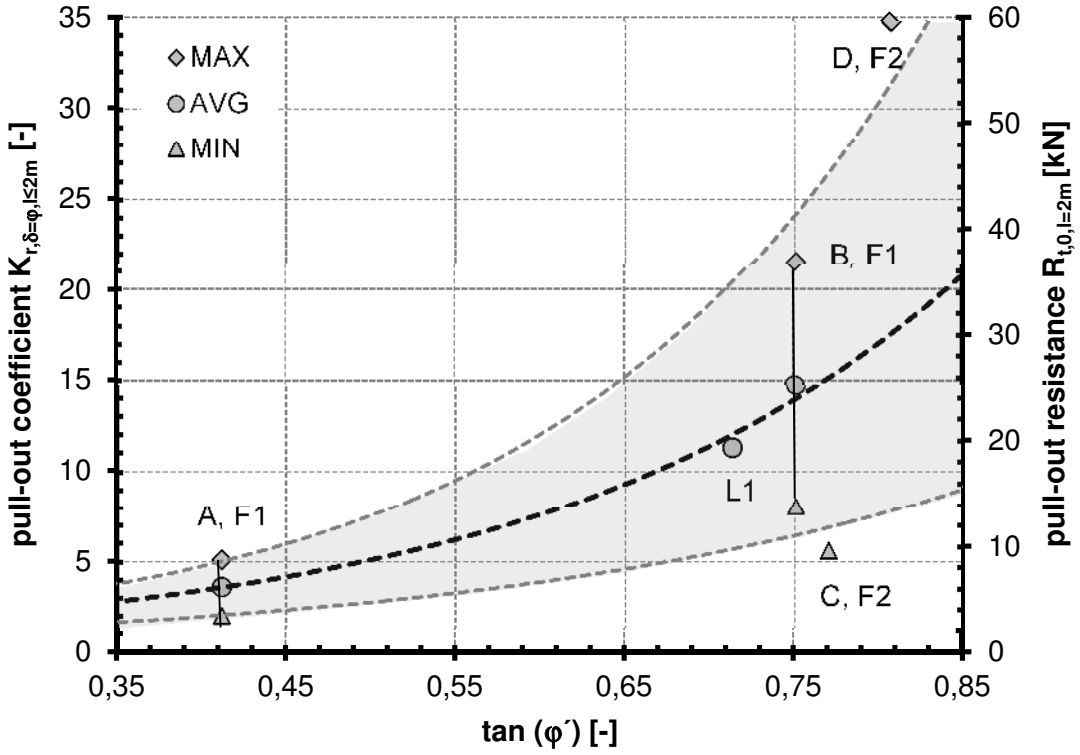

Fig. 87: Determined pull-out coefficient ($K_{r,\delta=\varphi,l=2m}$) for a maximum 2 m long rod versus the tangents of the material friction angle (φ´). The pull-out resistance for a 2 m long rod ($R_{t,0,l=2m}$) is additionally visualized along the second ordinate axis.

Based on the soil properties of the applied materials and the determined pull-out forces ($F_{t,max,0}$) of the utilized experiments, an average constant pull-out coefficient ($K_{r,\delta=\varphi,l\leq2m}$) was roughly back calculated for a rod with maximum 2 m length, by applying Equation 25. Figure 87 illustrates the range of the

determined pull-out coefficient ($K_{r,\delta=\varphi,l\leq 2m}$) and the range of the calculated pull-out resistance for a 2 m long rod ($R_{t,0,l=2m}$), depending on the tangents of the material friction angle (φ´). The pull-out resistance is calculated with Equation (25) and the effective soil weight (γ´) is assumed with γ´ = 18 kN/m³.

The average pull-out coefficient ($K_{r,\delta=\varphi,AVG,l\leq 2m}$) for a maximum 2 m long rod can be calculated with the analytical Equation (26).

$$K_{r,\delta=\varphi,l\leq 2m,AVG} = 0.6876 * e^{\left(4.01*\tan(\varphi')\right)} \tag{26}$$

The range of the pull-out resistance for a two meter long rod can be calculated with the empirical Equation (27).

$$R_{t,0,l=2m}[kN] = \begin{cases} \text{MAX: } 1.2625 * e^{(4.64*\tan(\varphi'))} \\ \text{AVG: } 1.1665 * e^{(4.01*\tan(\varphi'))} \\ \text{MIN: } 0.8697 * e^{(3.38*\tan(\varphi'))} \end{cases} \tag{27}$$

It is noted that most of the investigations are based on rods with 2 m length. However, a great range of results is given, considering all experiments. Therefore, the calculated pull-out forces have to be verified in the field. A minimum of five field tests (or 5% of all rods) have to be conducted for that reason in order to achieve reliable pull-out test results.

The analysis of the experiments showed that the soil density (D) can be classified as a key-factor of influence to the pull-out force. It may be more appropriate to give a relationship of the pull-out coefficient ($K_{r,\delta=\varphi}$) or pull-out resistance to the soil density of defined materials, e.g. sand or gravel, similar to Ostermayer (1975). However, correlations between the friction angle and the soil density (D) for defined soil materials can be found in the literature, e.g.: Holtz et al. (2010). These correlations are very sensitive referring to the grading curve and the particle shape and also show a great variety depending on the author. Further on, more research is necessary to work out a more appropriate relationship with view to the soil density and the pull-out coefficient. It is highlighted for this reason that the given relationships can be understood as a first rough estimation, Figure 87.

Jardine et al. (2005) already mentioned that theoretical calculations of the pull-out resistance of displacement piles are relatively unreliable for the reasons stated above. Correlations based on CPT or SPT tests are generally used to determine the pile resistance of displacement piles in advance. The benefit of these in-situ measurements are that correlations to the shear resistance along the pile shaft are known under reliable site conditions. These kinds of investigations were not part of this thesis. To conclude, in accordance with CPT or SPT based design methods, the energy consumption of the drilling machine - needed for

the rod installation process - can be recorded in future and correlations to the pull-out resistance can be investigated. This was also not executed within this thesis.

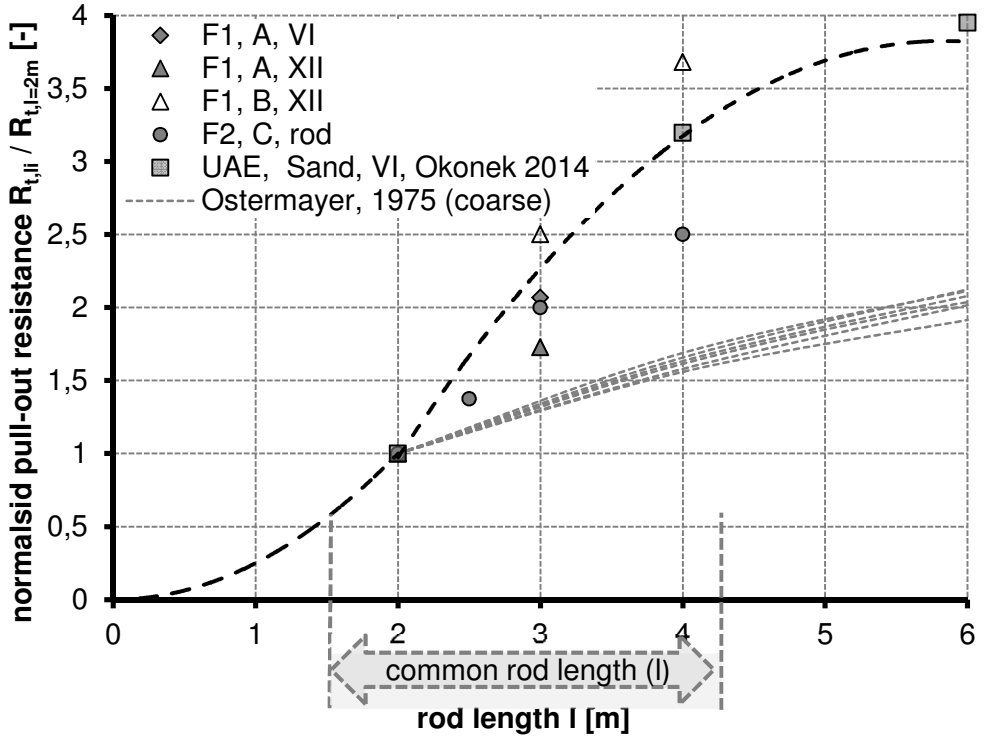

Fig. 88: Influence of the rod length (l) to the pull-out resistance. The pull-out resistance ($R_{t,0,li}$) is normalised to the pull-out resistance of a 2 m long rod ($R_{t,0,l=2m}$). The common rod length for practical application is in between l = 1.5 - 4.5 m. The range of dependency of the pull-out resistance to the bonded length for grouted anchors in different coarse grained soils is additionally visualized, according to Ostermayer (1975)

Figure 88 illustrates the average relationship - black dashed line - of the pull-out resistance referring to the rod length (l). The pull-out resistance of one rod (or a set of rods) with variable length ($R_{t,max,0,li}$) is normalised to the pull-out resistance of one rod (or a set of rods) with 2 m length ($R_{t,max,0,l=2m}$). This relationship enables the extrapolation of the pull-out resistance for rods with lengths greater than 2 m, when knowing the pull-out resistance of rods with 2 m length. However, only one data point is available for rods longer than 4 m, this data is based on pull-out tests from dense sand, Okonek (2014). In addition, a horizontal tangent is assumed at the right end of the graph. Hence, the pull-out resistance cannot be increased - or only slightly increased - in case of rods longer than 6 m.

The range of dependency of the pull-out resistance to the bonded length for grouted anchors in coarse grained soils is additionally visualized. The graphs are almost independent from the soil density (D) and material type of coarse

grained soils, Ostermayer (1975). However, the pull-out resistance of grouted anchors with bonded lengths longer than 8 m remains as well almost constant.

It is highlighted that the given correlation has to be continuously complemented with additional data, especially for rods longer than 4 m.

The pull-out resistance of rods with variable rod lengths can also be calculated with Equation (28), when knowing the pull-out resistance of a rod with 2 m length ($R_{t,0,l=2m}$). Finally, it might be mentioned that the given empirical extrapolation functions addresses the effect of the changing pull-out coefficient ($K_{r,\delta=\varphi}$) with changing depth (z), vide supra.

$$R_{t,0,li} = R_{t,0,l=2m} * * \begin{cases} 0 \leq l < 2: f_{(l)} = \frac{1}{4} l^2 \\ 2 < l \leq 6: f_{(l)} = -0.194\, l^2 + 2.27\, l - 2.78 \end{cases} \quad (28)$$

Summary of the first design approach:

I. The pull-out resistance of vertically installed rods which are vertically tension-loaded is covered by the integral of the shear stresses (τ_f) at ULS over the embedded rod surface (A_s), Equation 23. The shear stresses are depending on the full radial stresses along the rod shaft (σ'_{rf}) and the rod interface friction angle (δ). The full radial stresses depend on the radial stresses after the installation ($\sigma'_{r,c}$) and the increase of radial stresses caused by interlocking due to the pull-out process ($\Delta\sigma'_r$)

II. The shear stresses (τ_f) are simplified to the vertical stresses times an pull-out coefficient ($K_{r,\delta=\varphi}$), Equation 24. The pull-out coefficient covers the rod interface friction ($\delta=\varphi'$) and the effects of the installation as well as the pull-out process.

III. The pull-out coefficient ($K_{r,\delta=\varphi,l\leq 2m}$) was determined for a maximum 2 m long rod, depending on the tangents of the material friction angle (φ'), Figure 87, Equation 26. The pull-out test results of the field and lab tests were used for this. For this reason, the pull-out force ($F_{t,max}$) was set equal to the pull-out resistance ($R_{t,0}$).

IV. Based on the introduced pull-out coefficient ($K_{r,\delta=\varphi,l\leq 2m}$) the pull-out resistance of a maximum 2 m long rod ($R_{t,0,l=2m}$) can be calculated, Equation 27

V. Finally, the pull-out resistance of rods with variable rod lengths can be calculated with the length extrapolation function, Equation (28), when knowing the pull-out resistance of a rod with 2 m length ($R_{t,0,l=2m}$). The pull-out test results of the field and lab tests with variable rod length were used to achieve the length extrapolation function.

5.2.3 Inclined rods

The bearing capacity of inclined threaded rods which are vertically tension loaded is characterized by a decrease of the pull-out resistance with increasing rod inclination (α), see Chapter 3.3.6 and Chapter 3.4.5.

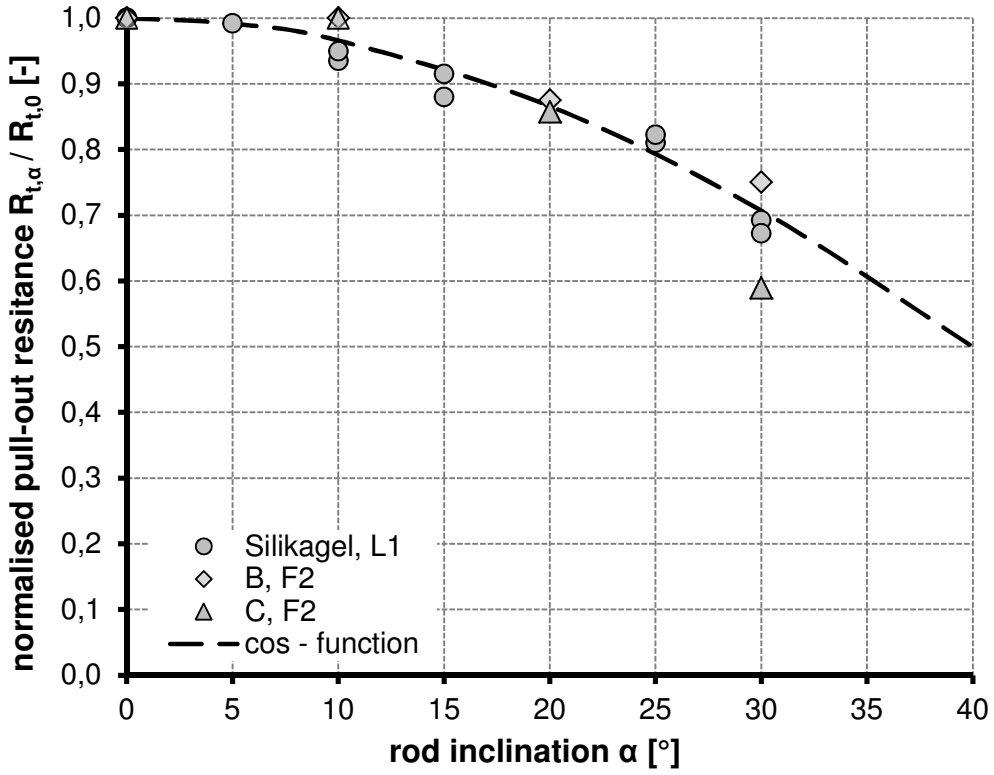

Fig. 89: Correlation between the pull-out resistance of vertically and inclined threaded rods. The length (l) of the rods is constant

Figure 89 illustrates the normalised pull-out resistance of the inclined threaded rods ($R_{t,\alpha}$) compared to the resistance of vertically installed rods ($R_{t,0}$). The maximum pull-out resistance of inclined rods ($R_{t,\alpha}$) therefore corresponds to the pull-out force of the inclined rods ($F_{t,max,\alpha}$). An empirical function (Equation 29) was developed which reflects the decrease of the pull-out resistance with increasing rod inclination. As long as the pull-out resistance of inclined rods ($R_{t,\alpha}$) is regarded to the pull-out resistance of vertical rods ($R_{t,0}$) for a certain soil type and rod length, the shape of the function is independent from the rod length and the soil type itself. The empirical function enables the estimation of the pull-out resistance for inclined rods ($R_{t,\alpha}$), when knowing the pull-out resistance of the vertically installed rod ($R_{t,0}$). This function is a helpful tool because the pull-out test of inclined rods requires special equipment.

$$R_{t,\alpha} = R_{t,0} * \cos\left(\frac{3}{2} * \alpha\right) \; valid\ for\colon\ 0° \leq \alpha \leq 45° \tag{29}$$

5.3 Design procedure

In accordance to the introduced design approach of the EUROCODE 7 (2004, +AC: 2009) the following two methods can be applied to determine the characteristic value of the rod resistance ($R_{t,k}$) against an applied tension load ($F_{t,k}$), see also Chapter 2.2.2

(1) Based on the tangents of the known friction angle (φ´) of the soil, see Figure 87
(2) Based on in-situ pull-out tests

In the following, the procedure for the given methods is described.

5.3.1 Based on the known friction angle (φ´) of the soil

Based on the known friction angle of the material the pull-out resistance ($R_{t,0,l=2m}$) of a 2 m long and vertically installed rod can be estimated by applying Figure 87. The average graph should be applied for this and can be understood as a characteristic value ($R_{t,0,l=2m} = R_{t,k}$). However, in case of poor soil density (D) or not well specifiable soil conditions, the lower boundary should be applied. It is highlighted that this method is only applicable for homogenous, primarily non-cohesive and at least medium dense (D) and proved soils.

For rods longer than two meters the extrapolation function and for inclined rods the conversion function should be applied to determine the characteristic pull-out resistance ($R_{t,k}$), Figures 88 and 89.

The design value of the applied tension force ($F_{t,d}$) must be smaller than or equal to the design value of the pull-out resistance ($R_{t,d}$), Equation (6). The design value of the applied tension force ($F_{t,d}$) can be calculated by applying Equation (5) and the design value of the pull-out resistance ($R_{t,d}$) by applying Equation (4), see Chapter 2.2.2 However, damage sceneries and design situation as described in EUROCDODE 7 are addressed by applying the partial safety factors (γ_i) as given in ÖNORM B 1997-1-1 (2013).

In order to calculate the pull-out resistance ($R_{t,d}$) with sufficient certainty, the model factor ($\eta_{P,t}$) of Equation (4) should be set to the value of $\eta_{P,t} = 1.35$. However, the calculated pull-out resistance ($R_{t,d}$) must be verified in the field with pull-out tests.
The amount of rods to be tested in the field (n_{test}) depends on the total amount of rods to be constructed and the complexity of the site and is set to ($5 < n_{test} > 5\%$).

Summary of the design procedure:

I. Estimation of the characteristic pull-out resistance ($R_{t,0,l=2m} = R_{t,k}$) of vertically installed rods with maximum 2 m length, by applying Figure 87. The friction angle of the soil must be known for this.
II. Applying the length extrapolation function to determine the resistance of rods longer than 2 m and the inclination conversion function for inclined rods, see Figures 88 and 89
III. Calculating the design value of the pull-out resistance ($R_{t,d}$), by applying Equation 4. The model factor is set to the value of $\eta_{P,t} = 1.35$ for this. The damage sceneries and design situation as described in EUROCODE 7 are addressed by applying the partial safety factors (γ_i) as given in ÖNORM B 1997-1-1 (2013).
IV. Calculating the design value of the applied tension load to the rod ($F_{t,d}$), by applying Equation 5, depending on the design situation.
V. Applying Equation 6 to check the final design

Once more, it is highlighted that the calculated pull-out resistance ($R_{t,d}$) must be verified on the field with pull-out tests ($5 < n_{test} > 5\%$). Additionally, this method is only applicable for homogenous soils.

5.3.2 Based on in-situ pull-out tests

This is the highly recommended way for the design of threaded rods and should be applied as mentioned in Chapter 2.2.2 - a). For homogeneous soil conditions pull-out tests of only two meter long vertically installed rods have to be executed. The pull-out resistance for longer rods can be determined by applying the extrapolation function, and for inclined rods the conversion function, Figure 88, Figure 89 and Equations 28-29. For heterogeneous soil conditions the rod length (l) should be the same length which is going to be applied on the site.

However, the model factor ($\eta_{P,t}$) of Equation (4) should also be set to a value of $\eta_{P,t} = 1.25$. The model factor is lower compared to the first method because of less calculation respectively simplification steps.

Summary of the design procedure:

I. In case of homogeneous soil conditions: Executing of five (or 5% off all rods) pull-out tests minimum with 2 m long rods and calculating the characteristic pull-out resistance ($R_{t,k,l=2m}$) of the single rods by applying Equation (2), see Chapter 2.2.2, depending on the amount of the tested rods n_{test}
II. In case of heterogeneous soil conditions: Executing pull-out tests in the field, minimum five (or 5% off all rods). The rod length is the same which is going to be applied on the site. Next, calculating the characteristic pull-

out resistance ($R_{t,k}$) of the single rods by applying Equation (2), see Chapter 2.2.2, depending on the amount of the tested rods n_{test}

III. In case of homogeneous soil conditions: Applying the length extrapolation function to determine the resistance of rods longer than 2 m.
IV. Applying the inclination conversion function for inclined rods, see Figure 89
V. Calculating the design value of the pull-out resistance ($R_{t,d}$), by applying Equation 4. The model factor is set to the value of $\eta_{P,t} = 1.25$ for this. The damage sceneries and design situation as described in EUROCDODE 7 are addressed by applying the partial safety factors (γ_i) as given in ÖNORM B 1997-1-1 (2013).
VI. Calculating the design value of the applied tension load to the rod ($F_{t,d}$) by applying Equation 5, depending on the design situation.
VII. Applying Equation 6 to check the final design

5.4 Summary and conclusions

A simple geotechnical model was introduced to calculate the bearing capacity of threaded rods which are vertically tension-loaded. Pure sliding along the rod shaft including the Coulomb failure criterion is assumed for this. The investigated increase of radial stresses - caused by the installation and pull-out process - is addressed by applying cavity expansion theory, Boulon and Foray (1986) and Lehane et al. (1993).

A pull-out coefficient ($K_{r,\delta=\varphi}$) was introduced which covers the effects of the surface roughness of the rod, the effects of the installation and the pull-out process to the radial stresses, depending on the effective vertical stresses. The pull-out coefficient is given for a maximum 2 m long rod, depending on the material friction angle. An extrapolation function is additionally introduced to calculate the pull-out resistance of rods longer than 2 m. The pull-out resistance of inclined rods ($R_{t,\alpha}$) can be calculated when knowing the pull-out resistance of vertically installed rods ($R_{t,0}$). An empirical function was developed for this.

To conclude, pull-out tests are highly recommended to determine the pull-out resistance under reliable site conditions.

6 Assessment for geotechnical applications

6.1 Introduction

This chapter deals with applications of the threaded rods, basically the Spideranchor technology introduced in this thesis, see Chapter 1.2.1. In a first step, variable substantial load cases for the Spideranchor and the resultant load cases for the individual threaded rods are introduced and examples for applications are given. In a next step, three different load cases are analysed in detail. A set of experiments - where the corresponding load case is applied - were conducted for this.

However, the design approach for single vertically tension loaded threaded rods introduced herein is applied for the Spideranchor. Minor extensions of the approach are done for this reason.

As already mentioned, time dependent behaviour, e.g. creeping, is not considered in this thesis. However, the application period for the Spideranchor is limited to semi-permanent applications due to corrosion effects. This means a maximum life-time of 30 years, depending on the corrosion class of the soil, see Nürnberger (2011). Several construction elements in ground engineering are in need of corrosion protections, such protections are e.g. protective coating, cathodic corrosion protection and over-dimensioning of steel components which enable a rust allowance of several millimetres. The most practical corrosion protection for the Spideranchor is the over-dimensioning of the rod. Over-dimensioning is also done for e.g. sheet pile walls ÖNORM EN 1993-5 (2008), micro piles ÖNORM EN 14199 (2013) and soil nailing ÖNORM EN 14490 (2010). In this context, it is suggested to install one additional Spideranchor VI as a so called corrosion observation anchor. Within a time interval of five years maximum one steel rod from the Spideranchor can be unscrewed and checked for corrosion. If necessary, the rods of the applied Spideranchors can be exchanged.

To conclude, corrosion leads to a reduction of the rod cross section which can be problematic with view to the interlocking effects. Chow et al. (1998) mention that corrosion also leads to bonding of grains to the pile surface which increases the pile roughness (δ) or can even force the principal displacement shear band out into the soil mass. In addition, Chow et al. (1998) mention that *"the creation of ferric oxide rust products could lead to volume increase and a rise in radial stresses"*. Finally, Chow et al. (1998) concluded that for open-ended and driven piles in dense sand an 85% increase in shaft capacity between six months and five years after the installation process was observed.

Nevertheless, the investigation of corrosion appearance and protections are not subject of this thesis and are therefore no longer considered.

To conclude, the application of Spideranchors is connected to several benefits; these are e.g.

- full bearing capacity - immediately after the installation process
- fast and simple installation process
- low weight installation equipment
- fast and simple system removal - if necessary

6.1.1 Load cases

Five fundamentally different load cases for the Spideranchor and the resultant load cases for the individual threaded rods are presented.

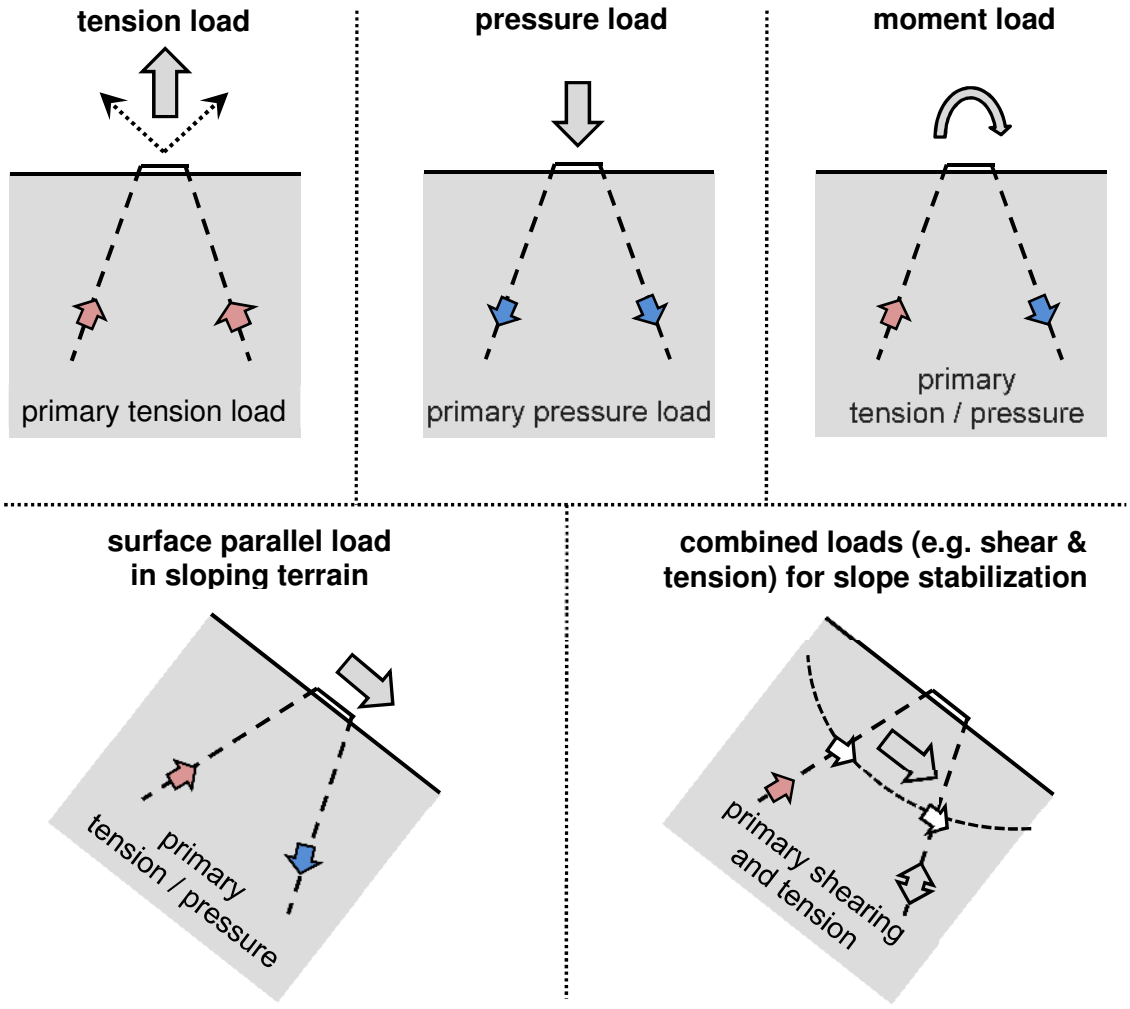

Fig. 90: Spideranchor load cases and the resultant load cases for the individual threaded rods

Possible load cases for the Spideranchor are, see Fig. 90:

- **Tension load** - the single rods are primary tension loaded as well.
  Possible applications are: different kind of anchorage - e.g.: anchorage of safety fences in disaster protection, anchorage of cranes and pylons

- **Pressure load** - the single rods are primary pressure loaded as well.
  Possible applications are: foundations for site cabins, carports, containers, wooden houses

- **Moment load** - the single rods are primary pressure and tension loaded. Possible applications are: foundations for traffic signs, overhead direction signs, crash barriers

- **Horizontal load or surface parallel load e.g. in sloping terrain** - the single rods are primary pressure and tension loaded. Possible applications are: foundations for snow groomers, anchorage points for forestry activities

- **Slope stabilization** - the single rods are primary shear loaded & tension loaded. Possible applications are: alternative to soil nailing, erosion control, stabilization of shallow landslides, temporary building pit support - especially in case of problems with neighbouring grounds because the Spideranchor system can be easily removed

The load cases tension and moment load as well as slope stabilization are analysed in more detail in the following chapters.

It is highlighted that all studies and analyses below refer to investigations with constant lengths (l) of the applied rods for the Spideranchor.

6.2 Vertical tension load

The experimental investigations of the Spideranchor load case vertical tension is included in Chapter 3.2 – field test one (F1). This chapter deals with the design approach introduced for single rods which is applied for the Spideranchor system, minor extensions of the approach are done for that reason.

The pull-out resistance of a set of threaded rods - in general the Spideranchor system - can't be estimated by summing up the individual values of the pull-out resistance of each single rod of the Spideranchor. The threaded rods of the Spideranchor influence each other, which results in a decrease of the total pull-out resistance. This decrease can be addressed by applying a group factor (Θ_i). Ries (2014) highlighted that an increase of the total bearing capacity can be expected for displacement pile groups. This is expected because of densification effects caused by the installation of the piles which influence each other.

However the experiments of F1 showed that a significant decrease of the bearing capacity happens with an increasing amount of threaded rods, see Chapter 3.2. This is probably due to the fact that the individual threaded rods of the Spideranchor are not fully activated simultaneously. A load transfer occurs between the rods because of the anchor head plate. Additionally, and as already mentioned, another reason for the decrease of the bearing capacity could be the resulting torsion moment which is caused by the vertical tension load in the Spideranchor system, see also Chapter 3.2.

Rudolf (2005) mentioned that the group factor depends on the axial distance between the piles and that a pile group behaves less stiff compared to a single pile. Therefore, it can be concluded that variable group factors for the Spideranchor VI and XII are expected because of the different geometrical rod arrangement.

Field test F1 delivered the basic fundamentals to determine the group factors ($\Theta_{i;}$ i=XII group factor of the Spideranchor XII, i=VI group factor of the Spideranchor VI) of the different Spideranchor systems at the current state. The group factor defines the ratio between the pull-out resistance of the Spideranchor ($R_{t,k,Sp}$) and the sum of the pull-out resistance of the single and inclined threaded rods ($R_{t,k,\alpha}$), Equation 30.

In order to calculate the group factors, the determined Spideranchor pull-out forces - see Figure 34 (material A) and Figure 35 (material B) - are set equal to the characteristic pull-out resistance of the Spideranchor ($R_{t,k,Sp}$). The rod length extrapolation function as well as the inclination conversion function, see Chapter 5, were additionally applied for this. The group factors (Θ_i) determined are different for the different Spideranchor systems as well as for coarse and fine- grained soil. The given group factors are a first rough estimation and are based on a few experimental data. This has to be checked and verified in more detail in further research work.

$$\Theta_i = \frac{R_{t,k,Sp}}{\sum n_{rod,\alpha} * R_{t,k,\alpha}}$$

$$\Theta_{VI} = \begin{cases} coarse\ grained\ soil: 3/5 \\ fine\ grained\ soil: \ 3/4 \end{cases} \qquad (30)$$

$$\Theta_{XII} = \begin{cases} coarse\ grained\ soil: 1/2 \\ fine\ grained\ soil: \ 2/3 \end{cases}$$

However, the vertical displacements which are necessary to reach the ultimate Spideranchor pull-out resistance are about u_z = 11.5 mm (≈ ¾ d) and are almost independent from the soil, the Spideranchor type, and the rod length, see Figure 36, Chapter 3.2.

The recommended design of the Spideranchor for vertical tension loads is introduced in the following.

6.2.1 Design recommendations

- **Based on pull-out tests of single rods**

This method is based on pull-out tests of single rods. The group factors introduced and the inclination conversion function - see Chapter 5 - are applied for this. The greatest benefit of this method is that the pull-out force resistance is determined under reliable soil conditions.

However, two ways are introduced to determine the Spideranchor pull-out resistance. Pull-out test results of vertically installed single rods are used for both methods.

The first method addresses the effects of heterogeneous soils. Pull-out tests of single rods with the same rod length as for the final Spideranchor application provide the basis for the first method.

The second method is based on pull-out tests of rods with 2 m length. It is reasonable to apply this method if homogenous soil layers are expected. For this, the rod length extrapolation function, see Chapter 5 is applied additionally. This is done in order to calculate the single rod pull-out resistance for longer rods than 2 m. The additional simplification compared to the first method is addressed by introducing a higher model factor ($\eta_{P,t}$), see Chapter 2.2.2. The model factor ensures sufficient certainty for the calculated Spideranchor pull-out resistance.

Finally, the characteristic pull-out resistance of the single rods depends on the mean and the lowest value of the rod pull-out test results and the amount of tested rods, see Equation 2 in Chapter 2.2.2. The more rods are tested, the lower are the correlation factors to calculate the characteristic pull-out resistance of one single rod ($R_{t,k,0}$). The correlation factors are reflecting the safety pattern to ensure the characteristic pull-out resistance.

To conclude, the design pull-out resistance of a Spideranchor ($R_{t,d,Sp}$) can be calculated with Equation (4) when knowing the characteristic pull-out resistance ($R_{t,k,Sp}$), see Chapter 2.2.2. Damage sceneries and design situations as described in EUROCDODE 7 are addressed by applying the partial safety factors (γ_i) as given in ÖNORM B 1997-1-1 (2013). For the final design see Equation (6) in chapter 2.2.2.

In the following, the two methods which are based on pull-out tests are introduced in more detail.

a) Heterogeneous soils

This method is recommended if heterogeneous soils and consequently changing material properties are available and tested. The following procedure is given for this:

I. Executing in-situ pull-out tests of vertically installed rods, ($5 < n_{test} > 5\%$) The rod length (l) should be the same length which is going to be applied for the Spideranchor.

II. Calculating the characteristic pull-out resistance ($R_{t,k,0}$) of the single rods, by applying Equation (2), see Chapter 2.2.2, depending on the amount of the tested rods n_{test}

III. Calculating the characteristic pull-out resistance ($R_{t,k,Sp}$) of the Spideranchor, by applying equation (X). The group factor (Θ_i) depends on the Spideranchor and soil type, vide supra. The equation (29), see Chapter 5.23., is applied in order to transfer the bearing capacity from the vertical to the inclined rod

$$R_{t,k,SP} = R_{t,k,0} * \Theta_i * \sum n_{rod,\alpha} * \cos(1.5 * \alpha) \quad (31)$$

Example: *Spideranchor XII: six rods 30° inclined and six rods with 45° inclination (see Chapter 1),* $R_{t,k,0}$ *= 25 kN, coarse grained soil*

$$R_{t,k,SP=XII} =$$

$$= 25 * \frac{1}{2} * [6 * \cos(1.5 * 30) + 6 * \cos(1.5 * 4\,5)] \approx 82 \text{ kN}$$

IV. Calculating the design value of the pull-out resistance ($R_{t,d,Sp}$) with equation (4) and finally applying equation (6) for the final design. The model factor ($\eta_{P,t}$) should be set to $\eta_{P,t}$ = 1.15 to ensure a sufficient certainty.

b) Homogenous soils

This method is recommended if homogenous soils are available and tested. The benefit of this method is that the pull-out equipment need not resist very heavy loads which results in lower equipment weight. This is due to the fact that only 2 m long rods must be pulled out in the field for this method. For this, the length extrapolation function - see Chapter 5 - is applied additionally. To conclude, easy-to-carry portable pull-out equipment can be used for this which can be handled by one person only.

Therefore the following procedure is given:

I. Executing in-situ pull-out tests of vertically installed rods with 2 m rod length (l), ($5 < n_{test} > 5\%$)

II. Calculating the characteristic pull-out resistance ($R_{t,k,0,l=2m}$) of the single rods, by applying equation (2), see Chapter 2.2.2, depending on the amount of the tested rods n_{test}

III. Applying Figure 91 – 94, depending on the Spideranchor and soil type, to determine the characteristic pull-out resistance of the Spideranchor with variable rod length (l)

IV. Calculating the design value of the pull-out resistance ($R_{t,d,Sp}$) with equation (4) and finally applying equation (6) for the final design, see Chapter 2.2.2. The model factor ($\eta_{P,t}$) should be set to $\eta_{P,t} = 1.25$ to ensure sufficient certainty.

However, the Figures 91-94 are based on the length extrapolation and inclination conversation functions, see Figure 28 – 29 in Chapter 5, and the group factors (Θ_i) introduced as well. In addition, the results of F1 are added to the diagrams. The most economic rod length is in colour in the diagram.

It is highlighted that the given dimensioning diagrams are a first design approach which must be evaluated due to further field tests with different soils and therefore have to be developed further on.

Anyway, the input value for the given diagrams is based on the characteristic pull-out resistance of one individual rod with 2 m length. In this context, the output of the diagrams is the characteristic value of the Spideranchor pull-out resistance ($R_{t,k,SP}$) for variable rod lengths (l).

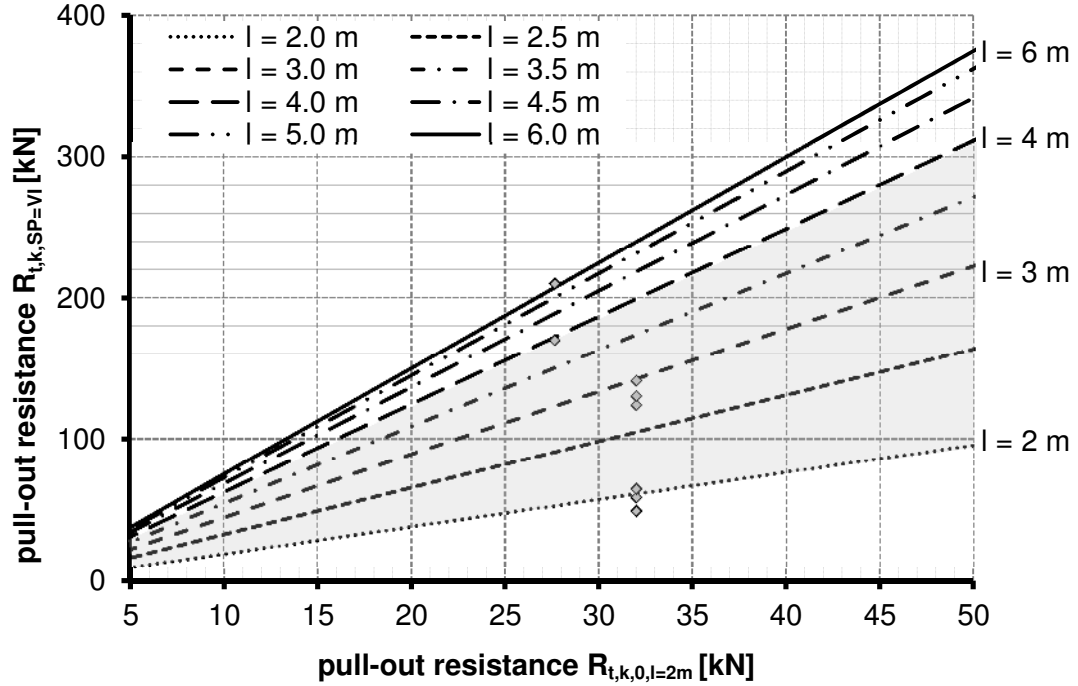

Fig. 91: Spideranchor VI – dimensioning diagram for vertical tension loads, homogenous granular soil

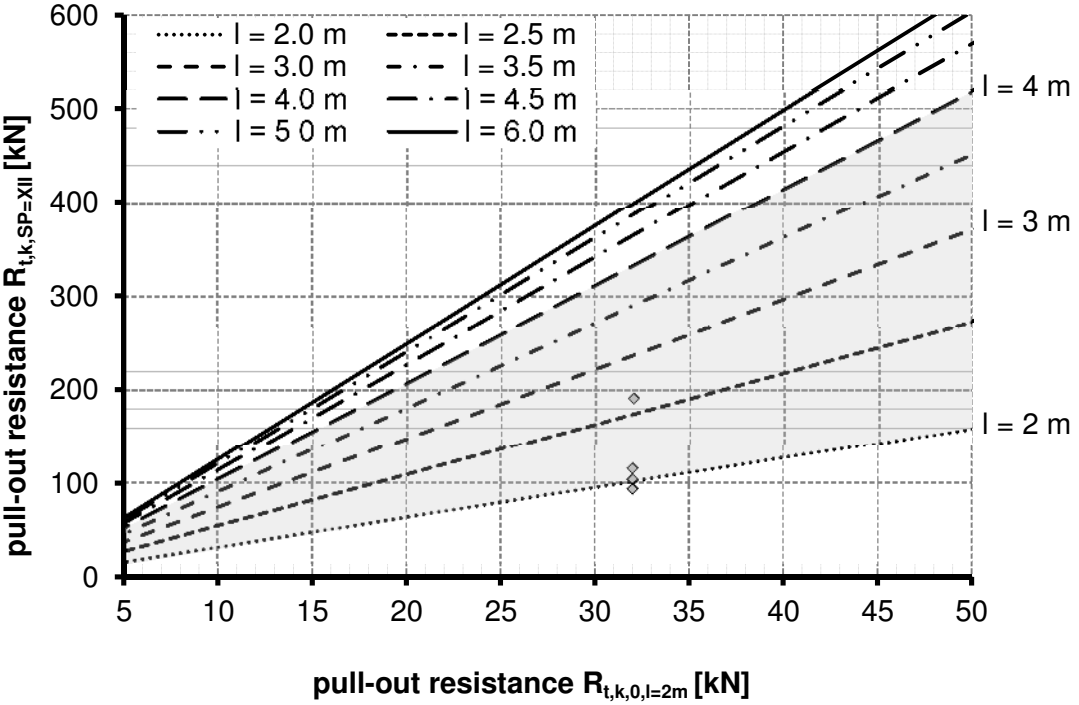

Fig. 92: Spideranchor XII – dimensioning diagram for vertical tension loads, homogenous granular soil

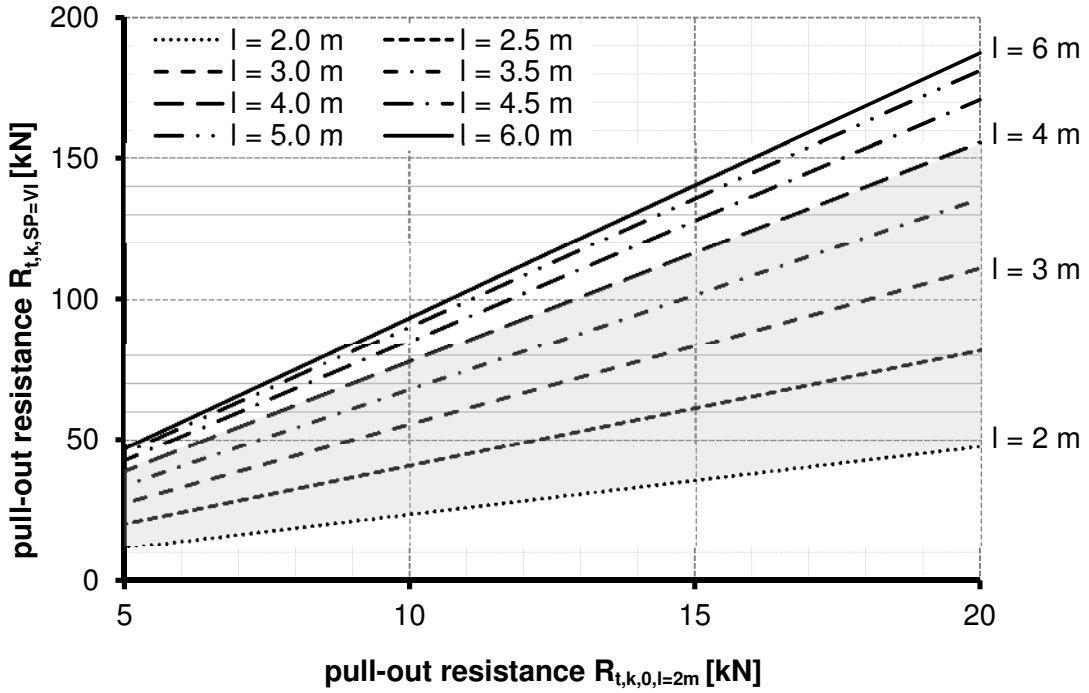

Fig. 93: Spideranchor VI – dimensioning diagram for vertical tension loads, homogenous fine grained soil

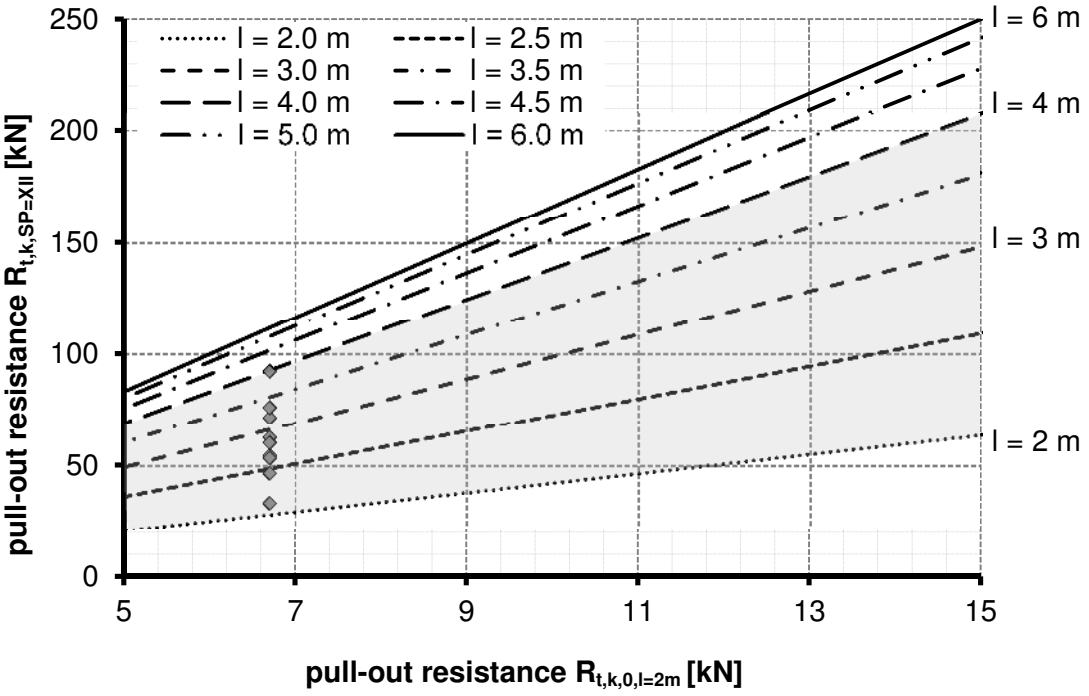

Fig. 94: Spideranchor XII – dimensioning diagram for vertical tension loads, homogenous fine grained soil

- **Based on calculations**

This method must be verified on the site with further pull-out tests and is only applicable for homogenous, basically non-cohesive and at least medium dense and proved soils. However, as introduced in chapter 5, the characteristic pull-out resistance of a single rod with 2 metre rod length ($R_{t,k,0,l=2m}$) can be estimated, based on the materials friction angle (φ').

After estimating the characteristic pull-out resistance of a single rod the following procedure should be applied.

I. Applying Figure 91 – 94, depending on the Spideranchor and soil type, to determine the characteristic pull-out resistance of the Spideranchor with variable rod length (l)

II. Calculating the design value of the pull-out resistance ($R_{t,d,Sp}$) with Equation (4) and finally applying equation (6) for the final design, see Chapter 2.2.2.

It is highlighted that additional model representations are applied for this design method to estimate the characteristic pull-out resistance of a single rod depending on the material friction angle. This results in a higher model factor ($\eta_{P,t}$ = 1.35) to ensure sufficient certainty of the design value of the Spideranchor pull-out resistance.

6.3 Moment load

In order to apply primarily moment loads to the Spideranchor, a new head plate was developed. This was necessary because the present head plates of the Spideranchor VI and XII are not very suitable for moment loads due to the threaded rod arrangement.

A moment load (M_y) can be expressed as a couple of forces (F) which are parallel to each other but with opposite effects. One side, e.g. the left side, is activated by pressure and the other side, e.g. right side, by tension, the level of pressure and tension depends on the distance (o) between the sides, M = F * o. The force couple finally results in rotational movement of the head plate, Figure 95.

A rectangular-shaped anchor head plate - including an opening in the middle to save material - was designed for this. The rods were arranged close to the left and right boundary of the plate to achieve a maximum distance (o) which resulted in a lower force couple.

The investigations of the rod inclination *(Q4)* showed that a decrease of the single rod resistance happens with increasing rod inclination (α). For this reason, low rod inclination (α = 20°) was applied to the threaded rods of the

new anchor head plate. This was done in order to achieve great resistance of the threaded rods and to address the couple of forces (F) due to the applied moment load (M_y), Figure 95. 14 rods were applied in total, six rods on the left and six rods on the right side ($\alpha = 20°$), and two additional rods with strong inclination ($\alpha = 60°$) on the right side. This was done to achieve greater resistance against translational movements of the plate. However, the tension side was additionally supported by applying a permanently and vertically installed Alpinanchor if necessary, see Chapter 1. The new head plate can be seen in Figure 95 and it is about 40 mm thick.

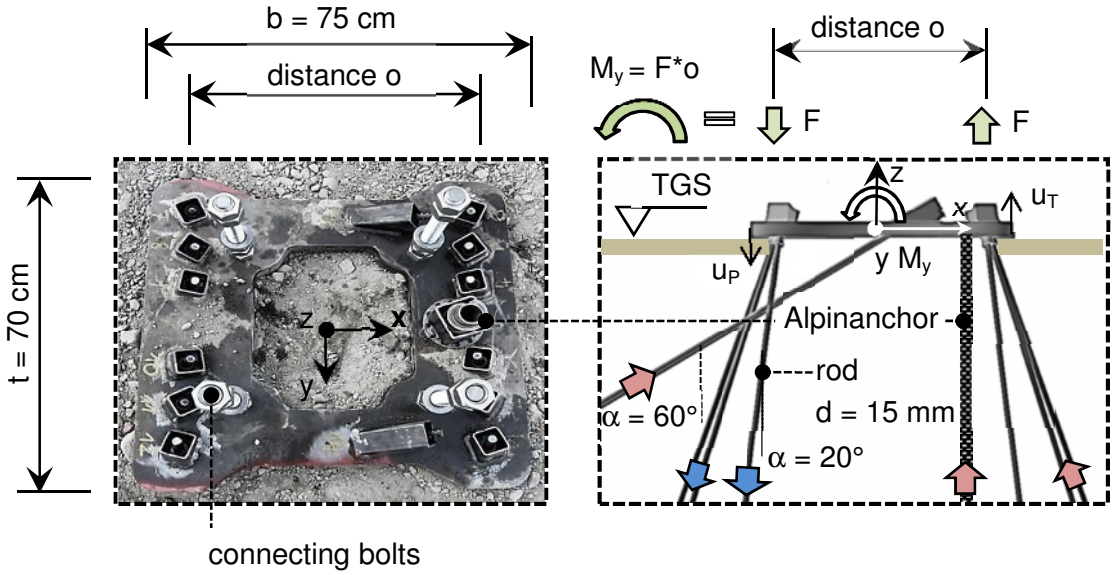

Fig. 95: Spideranchor M dimensions and sketch of the rod arrangement

In order to assess the new head plate for moment loads, experimental investigations were executed, as introduced and analysed below. The length of the rods and the Alpinanchor, if applied, was constant and is l = 4 m.

6.3.1 Overview, setup and experimental procedure

Two Spideranchors M were tested simultaneously to investigate the load-displacement behaviour of the Spideranchor M due to an applied moment load (M_y). In detail, primarily moment-load tests were performed load-controlled (max. load $M_y \approx 60$ kNm). The experimental setup was composed of two I-profiles and two steel ropes. The positioned profiles were rigidly connected to each Spideranchor M head plate via connecting bolts. However, an almost frictionless pulley was mounted at the upper end of each profile. Each of the two steel ropes was fixed horizontally on an upper profile end and finally connected to the opposite profile via the pulley. Finally, the ropes were loaded stepwise with defined weights. This resulted in simultaneous horizontal loading of the profiles, which acted as a lever arm to apply the moment load to the head plate, Figure 96.

The rotational movement of the rigid head plate due to moment load resulted in heavings (u_T) and settlements (u_P) of the plate. These were measured on the plate border with the help of an immovable fixed measurement bridge situated around each Spideranchor head plate. The translational displacements (u_X, u_Y) of the plates were additionally measured, see Figure 95. However, analogue dial gauges (KÄFER, u_{max} = 80 mm, resolution: 0.01 mm) were used to measure the displacements.

The new Spideranchor M was tested within field test 2 (F2) where two different materials were applied, material C and material D. These granular materials are characterised in Chapter 3.3.3.

It is highlighted that pure moment loading was not provided with the introduced test set-up because of additionally caused horizontal and vertical forces, see Figure 96.

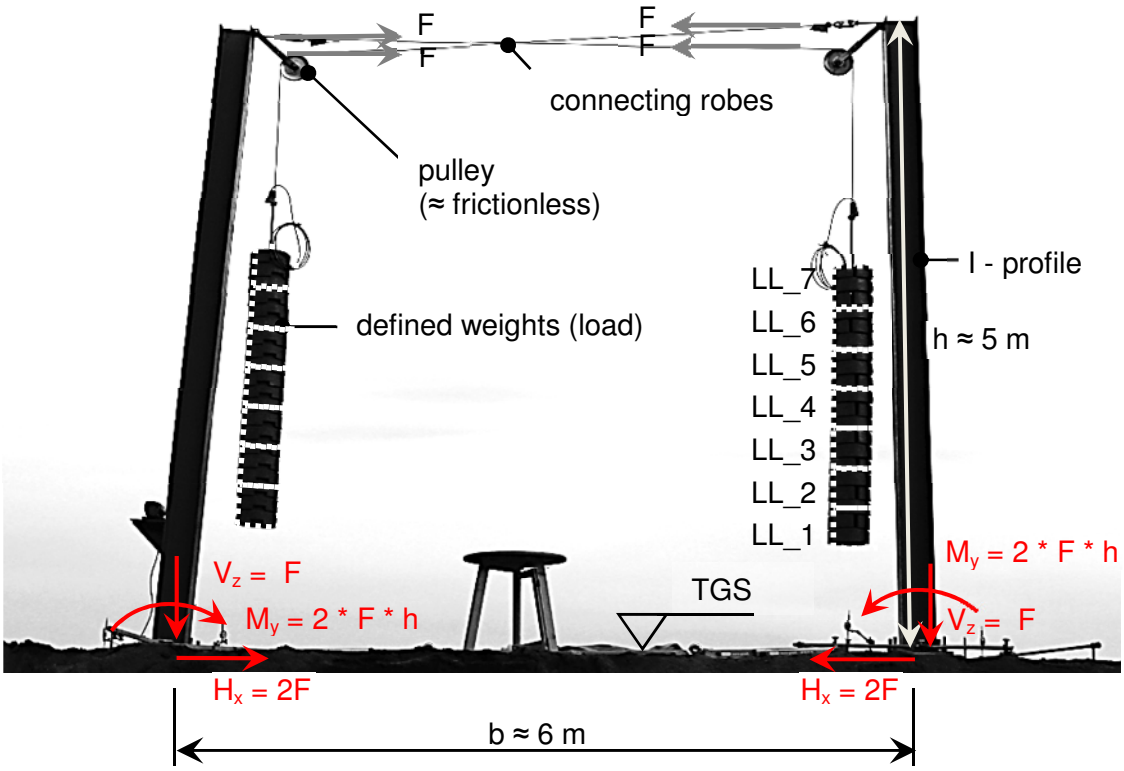

Fig. 96: Experimental set-up, the picture was made after the experiment. Left: without and right with applied Alpinanchor. LL … load level

In total, two couples of experiments were executed, one per soil material. In the following, the experimental procedure for each couple of experiments is shown:

a. Installation of two Spideranchors M, one with and one without the Alpinanchor. The length of the rods and the Alpinanchor was l = 4m
b. Connecting of 5 m high I-profiles rigidly to each anchor head plate by applying connecting bolts, Figure 96

c. Connecting the I-profiles to the steel ropes via the pulley
d. Installation of the measurement bridge around the Spideranchor M, one per side and installation of the dial gauges
e. Starting the experiment with the first load level (LL) by adding defined weights to the steel ropes, see Figure 96.
f. Measuring the displacement after each load step; we waited until the displacements were constant over a period of five minutes. Creeping effects were not detected but observed.
g. Repeating the steps e to g until the final load step was reached (M_y = 60 kNm)

6.3.2 Results

Figure 97, illustrates the moment-displacement diagram of the executed experiments. The observed displacements (u_Z = the heave or settlement of the plate on the sides) result from the rotational movements of the anchor head plate. The Spideranchor-M behaves more stiffly in material D compared to material C. This is the result of the greater bearing-capacity of the threaded rods in material D, see Chapter 3.2. However, much greater displacements occurred in material C independently if the Alpinanchor (AP) was applied or not.

The additionally caused horizontal and vertical forces due to the test set-up are not considered for the evaluation. Therefore, the results are considered and analysed for primary moment loads.

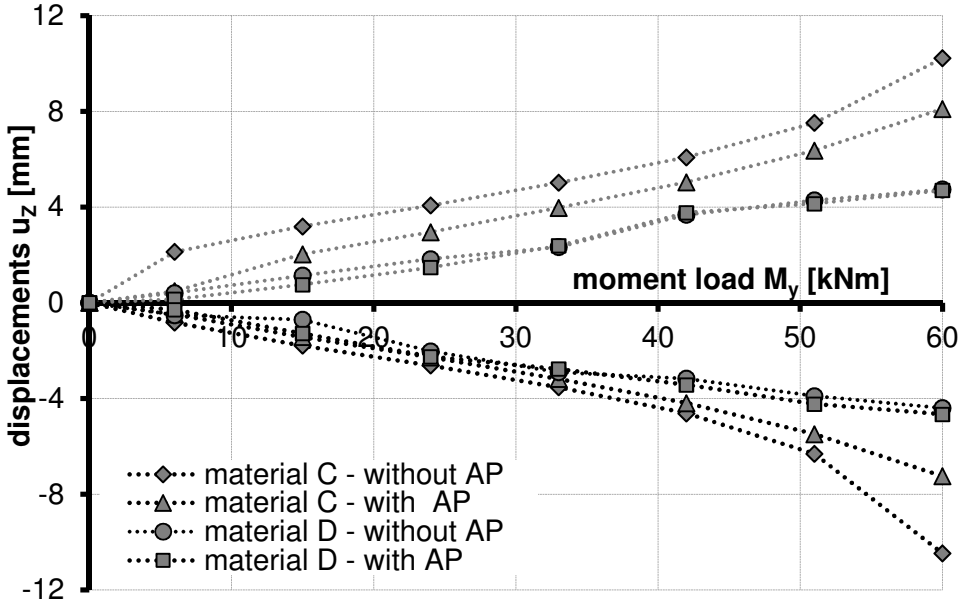

Fig. 97: Moment-displacement diagram. Positive values correspond to $+u_Z = u_T$ (heaving) and negative to $(-u_Z) = u_P$ (settlements), measured on the plate border, see Figure X for the axis. AP … Alpinanchor

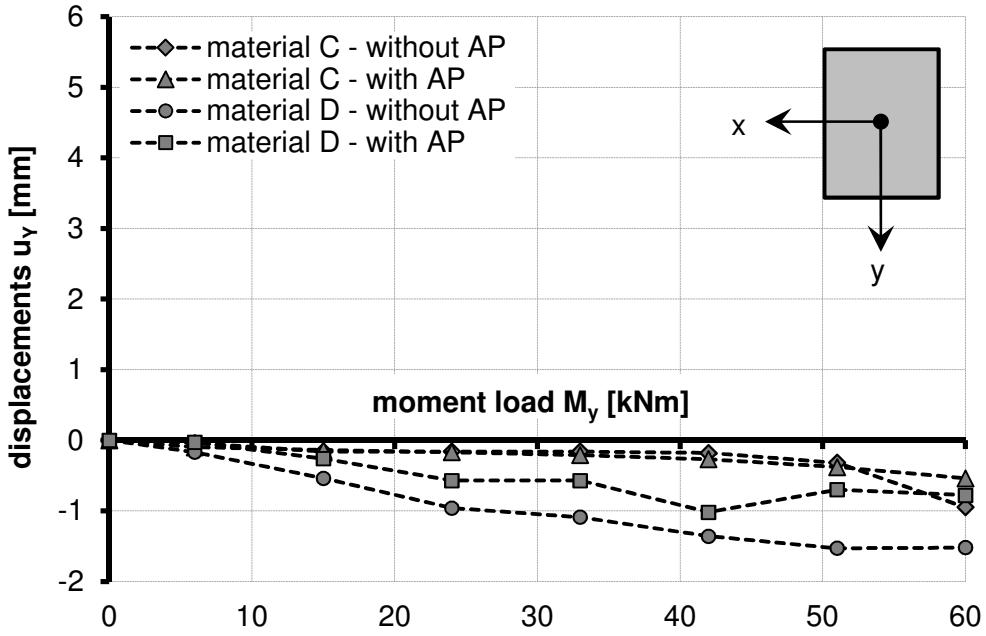

Fig. 98: Moment- translational displacements u_Y diagram, see Figure 95 for the axis. AP … Alpinanchor

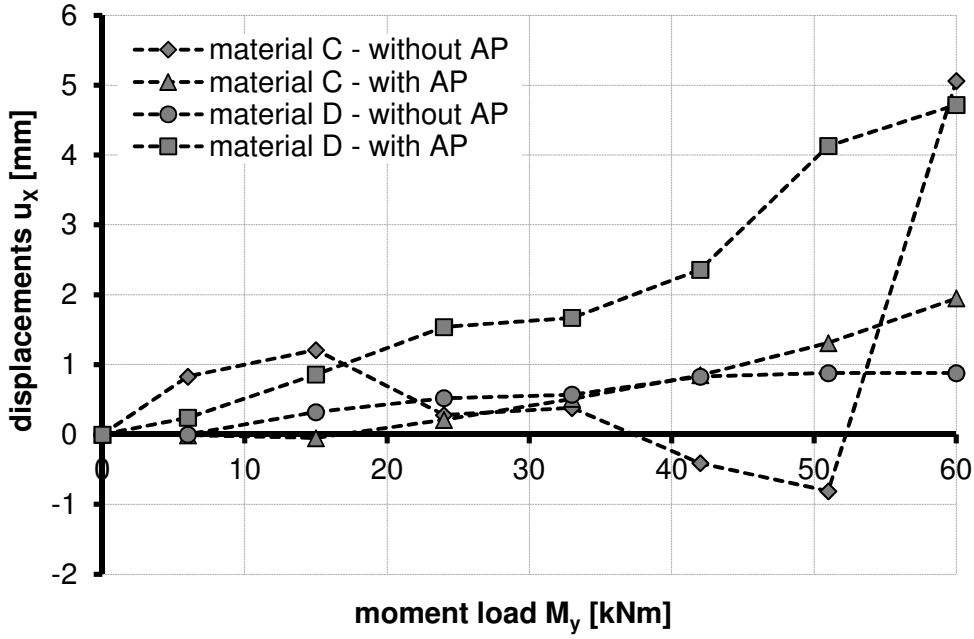

Fig. 99: Moment- translational displacements u_X diagram, see Figure X for the axis. AP … Alpinanchor

The additionally applied Alpinanchor does not result in stiffer behaviour up to the applied bending moment of 60 kNm for the material D. How much the bearing capacity of the Spideranchor M for material D is increased due to the Alpinanchor could not be evaluated in this test because at the applied bending moment of 60 kNm there were no indices of failure neither with nor without the Alpinanchor. Not so for material C. At the load step from 50 to 60 kNm, there

is a clear difference in the load-deformation behaviour between the plate with and without an Alpinanchor. Also the total amount of heave respectively settlements of the plate for material C at a momentum of 60 kNm is about twice as for material D.

The translational displacements in direction of the Y-axis, see Figure 98, are very low and therefore not further discussed. The translational displacements in direction of the X-axis are greater and confirm the necessity of the two more strongly inclined rods (α=60°) on the tension side of the anchor head plate.

To conclude, the rods were hard to install in material D, which resulted in a not plane anchor head plate position and in a slightly eccentric load transfer, especially for the experiment with the applied Alpinanchor. This could explain the greater translational movements of the plate compared to the Spideranchor without applied Alpinanchor.

6.3.3 Conclusions

In principle, the new Spideranchor M is suitable for transferring relatively great moment loads into the subsoil. An additional Alpinanchor might be necessary to support the tension side of the anchor head plate e.g. for sandy materials but not for gravelly materials with high density (D).

However, in order to apply greater loads to the new Spideranchor M than M_y = 60 kNm a second, an Alpinanchor arranged on the pressure side could be used. An increase of the rod length is not very suitable for this, with view to the influence of the rod length to the bearing capacity of the single rods, see Chapter 5.

A decrease of the translational anchor displacements especially in the direction of the X-axis could be achieved by applying a second Alpinanchor, vide supra, or by applying rods with a greater diameter than d = 15 mm. This finally results in a stiffer horizontal behaviour of the Spideranchor. It is highlighted that the installation process gets more difficult with increasing rod diameter (d), especially if the rod hits an obstacle e.g.: bigger stone.

6.4 Slope stabilization

In this chapter, the threaded rod load case “primary shearing” and an innovative method for slope protection - e.g. in case of shallow instabilities - is introduced. This innovative method is called “Spideranchor Netting” and is a modified slope stabilization method after Körner’s (1986) “Spidernetting”.

In the following, two effects are considered for this modified method. On the one hand a surface protection, e.g. a high-tensile strength geosynthetic or steel

net, is pushed against the slope surface to increase the shear resistance on a sliding plane. And on the other hand, Spideranchors stabilize the slope and are used for pushing the surface protection against the slope surface.

In the following, Spidernetting and Spideranchor Netting are presented.

6.4.1 Spidernetting and Spideranchor Netting

For Spidernetting, geosynthetics such as geonets or geogrids are placed tightly on a slope surface and anchored down by single small diameter ripped rods through openings in the geosynthetics, approximately up to 10 to 15 cm deeper than the original surface. A lock-off system is installed for this on the final part of the steel rod, which leads to a tensioning in the geosynthetics and a compression of the soil. Consolidation and settlements of the soil may occur; in this case a retensioning of the geosynthetics is necessary, Vitton and Hryciw (1991). The application of grouted nails is also possible for Spidernetting, Herold and Vollmert (2008).

For the highly innovative method of Spideranchor Netting, Spideranchors are installed in small dells, which are prepared according to the size of the Spideranchors. A high-tensile strength geotextile or mesh is tightly placed on the slope surface and above the dells and fixed on the downhill and uphill side of the slope. Finally, the geotextile or mesh is pulled down into each dell with the help of pre-stressing equipment which is installed on the head of the Spideranchor. By pulling down the geotextile or mesh into the dell the geotextile or mesh is tensioned and pressed against the slope surface in the style of the Spidernetting. If required, the stabilized slope can be vegetated afterwards, Figure 100. However, an additional separation fleece placed below the net can be applied to prevent surface erosion.

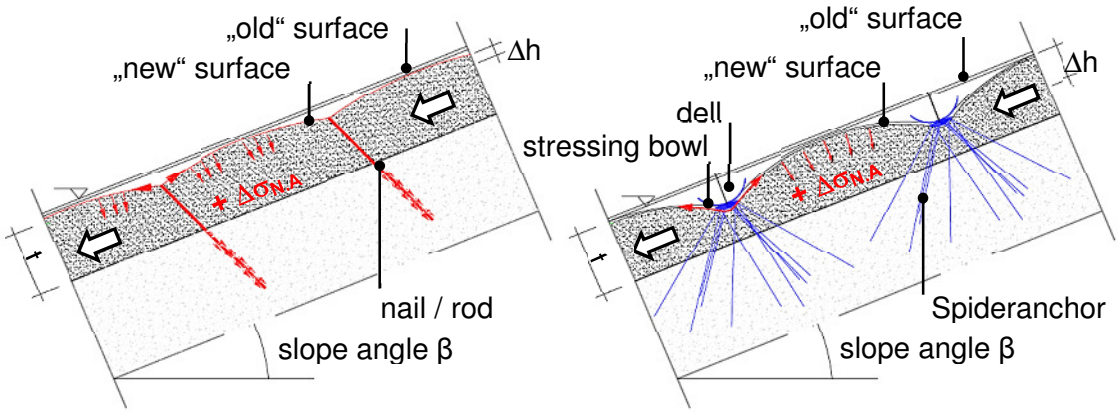

Fig. 100: Left: Spidernetting after Körner (1986) and right the modified Spideranchor Netting

To determine the effectivity of Spideranchors and Spideranchor Netting for e.g. stabilizing a slope, full scale slope failure experiments were conducted.

6.4.2 Overview, setup and experimental procedure

An embankment (b * h * l ≈ 3.5 * 3 * 27 m) built between rigid plates - plane strain model - was constructed for the full scale experiments, field test 3 (F3). The supported plates were anchored in a prefabricated concrete plate, for details see Supp et al. (2014). After the construction of the plates, an embankment was built in layers (h_{Layer} ≈ 50 cm) and compacted between the plates until the final height of 3 m was reached. The embankment crest was loaded stepwise over a loading area of 2 m² and a maximum load of 1.6 MN (σ_z ≈ 800 kN/m²) for the different tests. A horizontal beam - two welded HE-1000-B profiles - and two electronically and synchronously controlled hollow piston cylinders (max load: 2.5 MN) were used for this. The load system was self-constructed by the company Keller GmbH, Söding, Austria. The hollow piston cylinders were connected with small diameter piles (bar diameter 50 mm, anchorage length 8.5 m) which acted as an abutment for the loading process. The final test set-up can be seen in Figure 101.

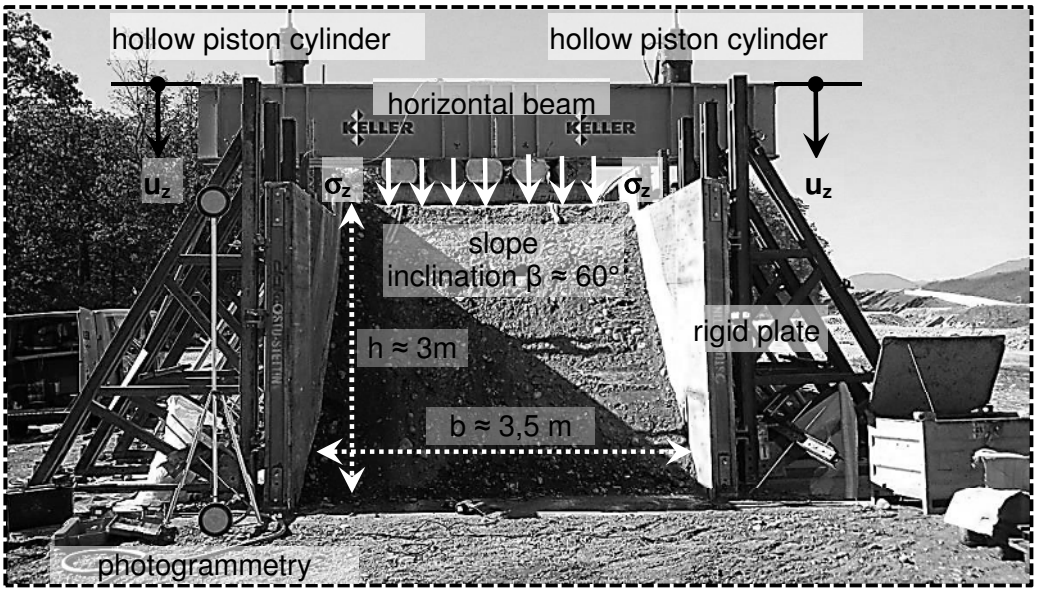

Fig. 101: Experimental set-up

The settlements of the horizontal beam - caused by the applied load (σ_z) - were measured with digital dial gauges (BALLUFF, u_{max} = 500 mm) on the upper side of the beam. For this, the gauges were placed close to the hollow piston cylinders. In order to evaluate the sliding surface after the slope failure experiments, a photogrammetric measurement system - called "ShapeMetriX3D see Gaich A. (2001)" - was used. However, the anchor head plate was monitored by applying geodetic measurement. For details see Lienhart et al. (2013).

The following full-scale slope failure experiments were conducted:

- slope without any stabilization method
- with two applied Spideranchors. Test conditions: two Spideranchors XII; rod length 2.0 m; anchor distance ≈ 1.3 m; installed axial (b/2); distance upper anchor to the slope edge ≈ 0.85
- with applied Spideranchor Netting. Test conditions: two Spideranchor XII; rod length 2.0 m; anchor distance ≈ 1.3 m; installed axial (b/2); distance upper anchor to the slope edge ≈ 0.85; dell depth Δh ≈ 40 cm; Net: woven biaxial PET geotextile; mesh size 20 * 20 mm

In the following, the experimental procedure is given:

a) Preparing the slope for the experiment
b) Applying a stabilization method a) Spideranchor or b) Spideranchor Netting - if required for the experiment
c) Applying the photogrammetric measurement system and the geodetic measurements - initial measurement
d) Starting with the first load level
e) Measuring of the vertical displacements (u_z); we waited until the displacements were constant over a period of a couple of minutes
f) Applying the photogrammetric measurement system and the geodetic measurements - follow-up measurement
g) Repeating steps d to g until the final load step was reached and the slope failed, if a slope failure was reached

6.4.3 Material

The material which was applied for the test embankment of F3 was man made by mixing fluvial gravel material (called “Murschotter”) with floodplain sand. This technology - for building a homogeneous embankment - had already been applied for the embankments of the hydro power stations in Gössendorf and Kalsdorf near Graz, Austria, Semprich et al. (2012).

An extensive soil testing program was executed to ensure almost constant properties of the material over the full length of the test embankment, Table 25. The in-situ soil strength was determined by the experiment without any protection system. The failure surface was determined after the slope failure experiment and back analysis based on the Ordinary slice method was done. The results of the back analysis showed smeared soil strength properties of a friction angle φ’ = 43° and a cohesion c’ = 15 kN/m², Marte et al. (2014). The soil characterisation is summarized in Tab. 25 and the corresponding grading curves of the mixed materials can be found in Fig. 102.

Tab. 25: Material properties - field test 3 (F3), material H

Properties	Material type Material H	
	height 2 m	height 3 m[#)]
Wet weight density γ_F [kN/m³]	24.7	24.9
Dry weight density γ_d [kN/m³]	23.3	23.9
Particle weight density γ_s [kN/m³]	27.8	27.8
Porosity n [-]	0.15 – 0.18	0.13 – 0.14
Saturation S_r [-]	0.88	0.89
Peak friction angle φ´ [°]	43[*)]	
Cohesion c´ [kN/m²]	15[*)]	
Load plate test E_{v1} [kN/m²] ; E_{v2} [kN/m²]	32.4 ; 108.6	25.2 ; 88.5
E_{v2} / E_{v1} [-]	3.4	3.5

[*)] back analysed - based on the slope failure experiment without any protection, see Marte et al. (2014)
[#)] h = 3 m → dam crest

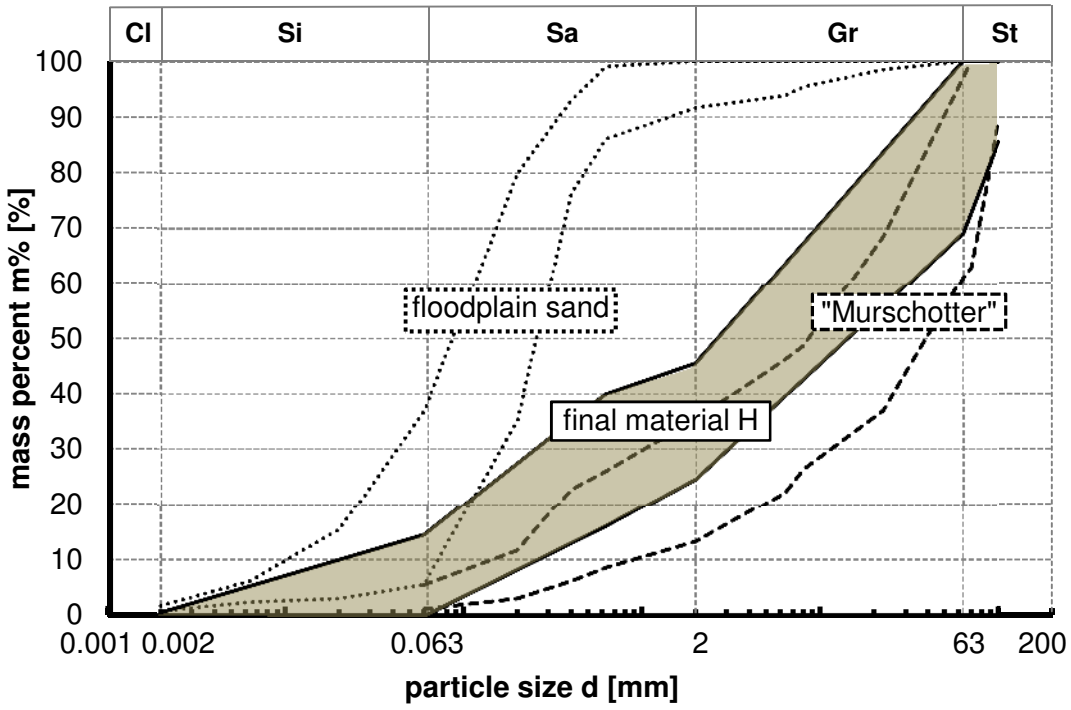

Fig. 102: Range of the different grading curves. The final grading curve of material H is shaded grey. Material H is the result of mixing the floodplain sand with the "Murschotter"

6.4.4 Results

Figure 103 illustrates the load-settlement curves of the utilized experiments. The test with applied Spideranchors only behaves in a more ductile manner compared to the test without any stabilization method. A 80 % higher load on the embankment crest could be applied and the calculated factor of safety (FOS) increases from FOS = 1.0 ($\sigma_z \approx 375$ kN/m², no protection) to FOS=1.2 by applying the Spideranchors only, Supp and Marte (2014).

However, serious problems were discovered when applying the Spideranchor Netting. First of all, the dells for tensioning the geotextile and installing the Spideranchors ($\Delta h \approx 40$ cm) were difficult to excavate because of the strong slope inclination ($\beta \approx 60°$). This led to an incorrect shape of the dells. Consequently, the shape of the stressing bowl did not fit the dells' shape and some parts of the geotextile were not in contact with the dell surface after the tensioning process. Finally, local failures above the upper anchor occurred during the experiment, and for this reason the experiment with applied Spideranchor Netting was interrupted and higher loads could be applied to the experiment with applied Spideranchors only. Also the test with applied Spideranchor Netting behaves in a more ductile manner compared to the test without any stabilization. Furthermore, an activated geotextile, in the form of clamping of the geotextile, was observed.

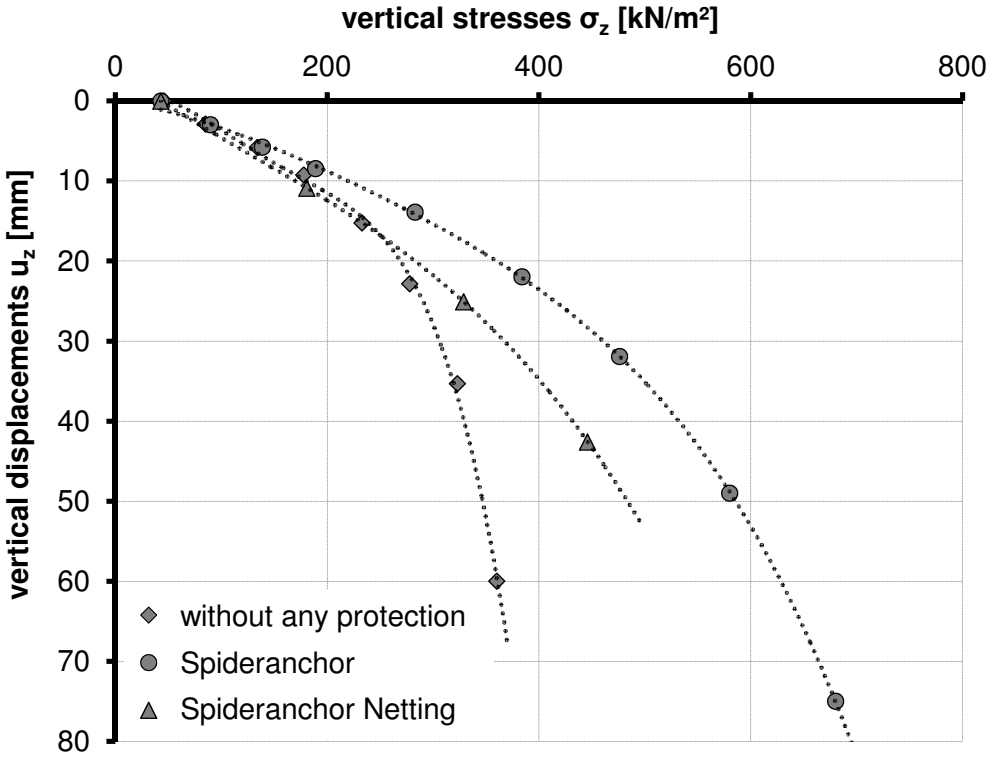

Fig. 103: Load – settlement curve of the different full scale experiments

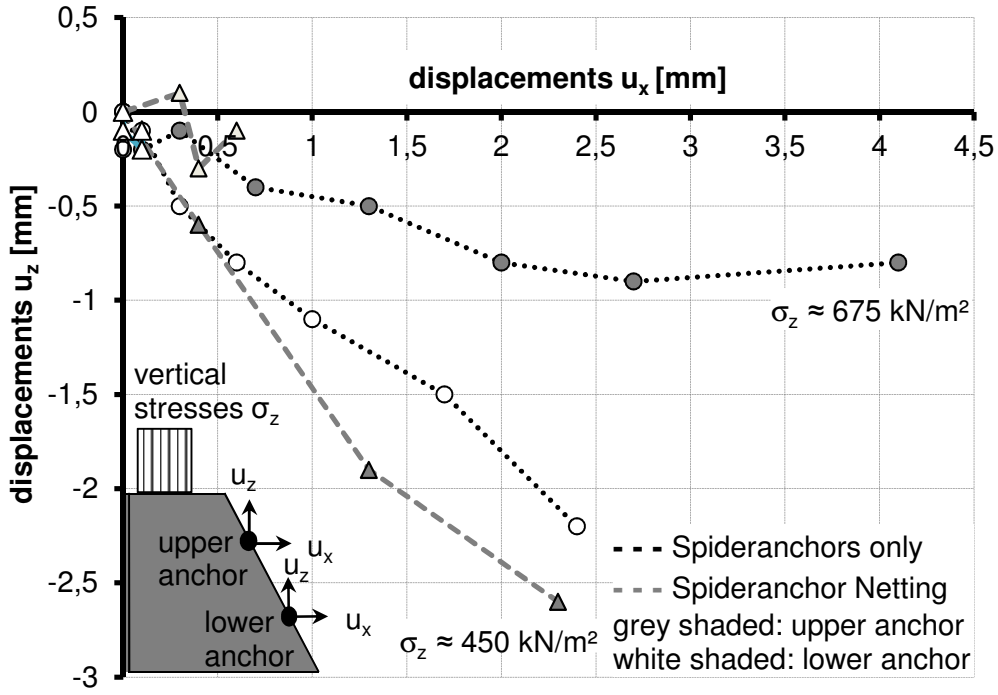

Fig. 104: Anchor head plate monitoring based on geodetic measurements

Figure 104 depicts the results of the geodetic measurements, summed up after each load level (σ_z) and modified after Lienhart et al. (2013). A kind of a composed failure mechanism occurred for both executed experiments, with applied Spideranchors only and with applied Spideranchor Netting.

The upper anchor was pushed out from the soil which resulted in a tension load for the experiment with Spideranchors only. The lower anchor was moved down almost parallel to the slope surface.

The lower anchor was not activated at all for the experiment with applied Spideranchor Netting and the upper anchor was moved down almost parallel to the slope surface. This confirms the assumption that a local failure occurred above the upper anchor due to the steep slope and the relatively deeply excavated and irregularly shaped dell.

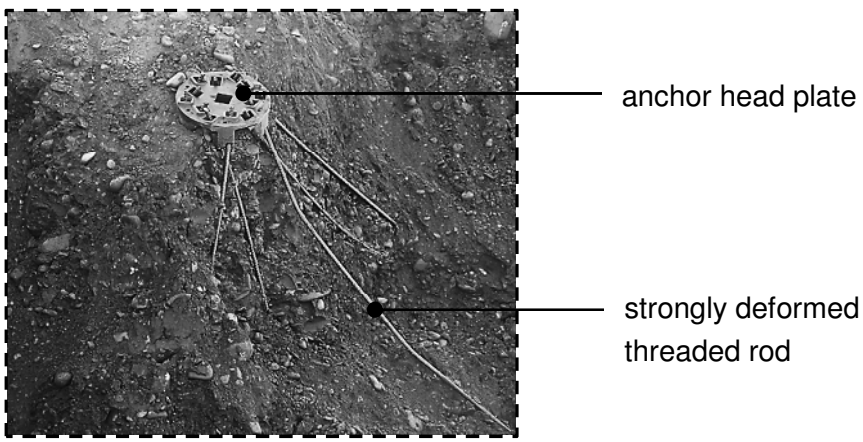

Fig. 105: Exposed Spideranchor after the utilized slope failure experiment

However, the slope was carefully exposed after the experiments to prove how the threaded rods were "really" arranged due to the installation process, Figure 105. More than half of the rods were arranged as intended and showed almost no deflection or imperfections, and about a quarter of the applied rods showed deflections or imperfections smaller than 10 cm. Nevertheless, a few rods - about 10% of the total amount - were relatively strongly deflected due to obstacles in the subsoil, e.g.: bigger stones.

6.4.5 Prototype

After identifying the problems which occurred when applying the Spideranchor Netting for the full scale experiment, a new prototype was developed. The prototype was used for stabilizing an instable slope with a sliding plane depth of about 2 – 3 m and an instable area of about 200 m². For this new prototype, five significant changes were made:

I. Special attention was paid to the excavation of the dells by using a master plate, $\Delta h \approx 40$ cm
II. spherical cap shaped stressing bowls, $h \approx 20$; $b \approx 60$ cm, were applied
III. covering the Spideranchors with asphalt cement and optimal aligning to the shape of the stressing bowl
IV. additional use of tensioning steel ropes, $d \approx 16$ mm
V. use of square net with mesh size 50 mm, $d \approx 5.1$mm, instead of the geotextile

The lengths of the steel rods from the Spideranchors XII were between 6 – 8 m and the horizontal anchor distance was approximately 3.5 m. Two anchor rows with a distance between 2 – 3 m, arranged in a triangular pattern, were installed. The steel ropes were tensioned diagonally and horizontally between the anchors. After screwing the stressing bowls down into the dells a significant surface pressure caused by tensioning, the net was obtained, Figure 106.

However, the Spideranchor Netting prototype is a semi-permanent protection system with a life time of 30 years. Components like the net and the stressing bowls were galvanized for this and the anchor heads were covered with asphalt cement. The pre-stressing equipment was covered with a heat shrink tube. Finally, a corrosion observation anchor, Spideranchor VI, was installed. Within a time interval of five years maximum one steel rod of the Spideranchor VI will be unscrewed and checked for corrosion. If necessary, the rods of the Spideranchors can be exchanged.

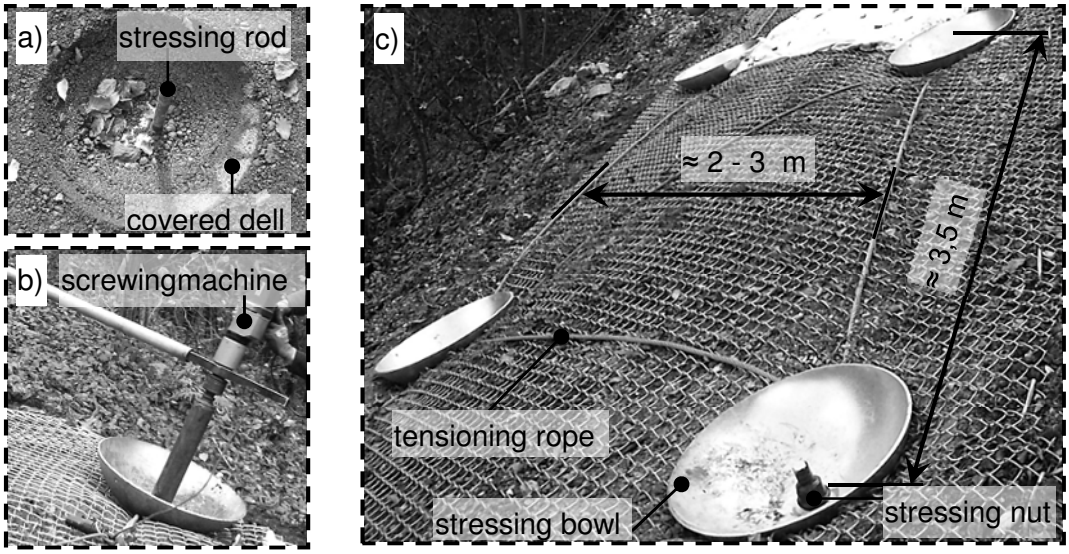

Fig. 106: a) aligned dell; b) pre-tensioning process; c) fully installed Spideranchor Netting

6.4.6 Conclusions

Spideranchors and Spideranchor Netting are powerful tools to stabilize instable slopes with shallow slip surfaces and can be classified as an alternative to soil nailing.

The stabilized slopes behave in a more ductile manner compared to a slope without any stabilization method. Local failure above the upper anchor occurred for the experiments if Spideranchor Netting was applied. This was due to the steep slope inclination and the irregularly shaped and to deeply excavated pre-stressing dell. This problem was addressed for the new prototype by applying master plates in order to excavate the dells. Additional aligning of the dells to the shape of the stressing bowl by applying asphalt cement was also very useful.

The new shaped stressing bowl was very suitable for the pre-stressing of the wire mesh. However, geotextiles tend to creep under stress and are often not UV-resistant. Therefore, it is recommended to use wire meshes instead of geotextiles for the Spideranchor Netting.

6.5 Summary and conclusions

Variable load cases for the Spideranchor and the substantive load cases for the threaded rods were introduced in this chapter.

The load case vertical tension took already place in Chapter 3.2 – field test one (F1). However, the design approach for single vertical threaded rods was successfully applied for the Spideranchor in this chapter. The bearing capacity decreases significantly with increasing amount of rods and an additional group factor (Θ_i) was introduced for this. Spideranchor dimensioning diagrams based on the results of single rod pull-out tests were introduced. However, F1 showed

only a little variety of the Spideranchor pull-out tests results, which was the opposite for the single rods. A minimum of five single rods had to be tested for that reason to reasonably apply the dimension diagram. It is highlighted that the given dimensioning diagrams are a first design approach which must be evaluated on the basis of further field tests with different soils and developed further. To conclude, it is highly recommended to check in-situ the bearing capacity of the single rods to achieve reliable rod behaviour.

A new head plate was developed to address the load case moment load for the Spideranchor. The results of the previous experimental investigations - see Chapter 3 - where used for this, especially the relationship between inclined and vertically installed rods. However, experimental investigations were executed where moment-loads up to M = 60 kNm have been applied to the new plate. An Alpinanchor might be necessary e.g. if the new Spideranchor-M is applied for sandy materials. This was not necessary for gravelly materials with high density (D).

Based on full scale experiments, the increase of overall slope stability of slopes with applied Spideranchors or Spideranchor Netting was investigated. Problems when applying the Spideranchor Netting to the test slope were solved and a new prototype developed. This new prototype was applied to an instable slope and a significant pressure on the slope surface due to the tensioned facing system was observed. The additional use of tension ropes between the anchor-heads increases the pressure effect significantly. However, the excavation of the dells which are needed for the tensioning process is of particular importance. Special care must be taken with respect to the shape of the dell and the aligning of the dell surface to the shape of the stressing bowl was very useful. Spideranchor Netting can be an effective slope stabilization method for shallow landslides and an alternative for conventional soil nailing, especially when putting structural elements on neighbouring ground is restricted, because Spideranchors are easily dismountable.

To conclude, the Spideranchor is a powerful and highly innovative constructional element for variable load cases. It is very impressive that relatively high bearing capacity can be achieved by applying a set of threaded rods with only 15 mm diameter. The easy installation process and the possible dismantling are the greatest benefits. However, more investigation is necessary for Spideranchor Netting.

7 Conclusions and further research

The main objective of this thesis has been to understand and to describe the bearing capacity of single threaded rods which are vertically tension-loaded after the installation process by screwing only. The investigated threaded rod is an essential component of a new and innovative constructional element for variable geotechnical applications called Spideranchor.

However, most of the research has been limited to granular soil and time-dependent behaviour like creeping has not been considered. In detail, five research questions were addressed by conducting pull-out tests.

More than 70 single rod and more than 20 Spideranchor pull-out tests by considering variable objectives have been performed in order to address the research questions. Pull-out tests have been executed in the field and in the lab and variable materials have been applied for this.

A first calculation model to estimate the pull-out resistance of single threaded rods has been introduced which is based on the results of the experiments and the numerical investigations utilized.

Finally, different load cases for the Spideranchor and the resultant load cases for the threaded rods have been introduced. Three load cases have been analysed in more detail and full scale experiments were conducted for this. The knowledge gained of a single rod has been transferred to a set of threaded rods - basically to the Spideranchor technology. A new head plate has been developed in order to apply a moment load to the Spideranchor. The new head plate has been successfully tested. In closing, a slope stabilization method called Spideranchor Netting has been developed and successfully tested. This resulted in a practical application of a new prototype of Spideranchor Netting.

Below, the most important findings concerning the research questions are highlighted.

Q1: What is the magnitude of the vertical pull-out force and how does the force-displacement graph look like?

- The bearing capacity has been strongly affected by interlocking effects between the rod shaft and the surrounding soil. The post peak behaviour of the force-displacement graph has shown a massive reduction of the pull-out force after reaching a peak value
- The peak-value, called pull-out force, has been reached after 5 to 8 mm pull-out displacements

- The dimension of the pull-out force highly depended on the rod length (l) and the soil type. The density (D) of granular soil delivered the most important factor of influence to the bearing capacity of the rod.
- The determined pull-out forces for a 2 m long rod have been in a range from 56 kN to 3.8 kN, depending on the applied soil type
- It seemed that the pull-out force remained almost constant for rod lengths greater than 6 m

Q2: Is there a failure body attached to the threaded rod, mobilized by the applied vertical tension load (F_t)?

- The experiments as well as the numerical investigations showed that a kind of composite failure mechanism occurred when the pull-out force was reached, consistent of a slip surface along the lower half of the rod shaft and of a kind of mobilized soil volume surrounding the upper half of the rod
- The mobilized soil body has been associated with losing density and the loss, respectively reduction of interlocking effects along the upper rod shaft

Q3: What is the influence of the installation process with respect to the bearing capacity?

- The installation process led to a significant change of the initial conditions in the subsoil and is a progressing process depending on the final installation depth
- Two phases have been observed during the installation process, by considering a soil element below the rod tip. Phase one has been characterised by the increase of horizontal stresses caused by interlocking effects due to the approaching rod tip. If the rod tip penetrates further and reaches finally the depth of the soil element, the interlocking effects achieve a maximum value. This is the end of phase one and the phase two (ph 2) starts if the rod is still penetrating further. Phase two is characterised by the loss respectively reduction of interlocking effects
- To conclude, the effect of the installation process to the bearing capacity of the rods results in higher horizontal stresses on the pile shaft and consequently higher shear resistance. The horizontal stresses are developed significantly stronger for rod sections arranged deeper and relatively poor for rod sections close to the surface.

Q4: What is the bearing capacity of inclined threaded rods which are vertically tension-loaded?

- The bearing capacity of inclined threaded rods is characterized by a decrease of pull-out resistance with increasing rod inclination

- An analytical function has been developed which describes the bearing capacity of inclined rods when knowing the bearing capacity of a vertical rod

Q5: What are possible applications for the Spideranchor, depending on load situations, and is it possible to describe the Spideranchor bearing capacity for vertical tension loads by adding all expected pull-out force values of each individual rod?

- The bearing capacity decreases significantly with an increasing amount of threaded rods. A group factor has been introduced for this.
- Design diagrams have been developed, which enable u to determine the Spideranchor bearing capacity based on single rod pull-out test results
- Variable Spideranchor load cases and applications have been introduced and three of them successfully tested. In detail, vertical tension load, moment load and slope stabilization issues.
- The Spideranchor is a powerful and highly innovative constructional element for variable load cases

In closing, the introduced design approach - for the single rod and the Spideranchor as well - should be understood as a first calculation model. The approach must be evaluated on the basis of further field tests with different soils and therefore has to be developed further.

Finally, in order to apply Spideranchor Netting to a slope, more research concerning overall slope stability is needed.

8 References

Ahmed and Iskander (2011)
Analysis of Tunneling-Induced Ground Movements Using Transparent Soil Models Journal of Geotechnical and Geoenvironmental Engineering, Vol 137

Augustesen (2006)
The Effects of Time on Soil Behaviour and Pile Capacity. PhD Thesis at Aalborg UniversityThesis No 4

Bardet (1994)
Observations on the effect of particle rotations on the failure of idealized garnular materials. Mechanics of Materials 18 (1194). Pages 159-182

Bathurst (2014)
Challenges and recent progress in the analysis, design and modelling of geosynthetic reinforced soil walls. 10th International Conference on Geosynthetics. Abstractbook of the Conference. DGGT, Berlin, Germany.

Boulon and Foray (1986)
Physical and Numerical Simulation of Lateral Shaft Friction along Offshore Piles in Sand Proceedings of the 3rd International conference on Numerical Methods in Offshore Pilling, Nantes, France

Chattopadhyay and Pise (1986)
Uplift capacity of piles in sand. Jornal of Geoetchnical Engineering, Vol. 112, No. 9, ASCE, USA

Chow (1997)
Investigations into displacement pile behavior for offshore foundations. PhD thesis, MIT, US

Chow et al. (1998)
Effects of Time on Capacity of Pipe Piles in Dense Marine Sand. Journal of Geotechnical and Geoenvironmental Engineering, Vol 124, pages 254-264

Cundall and Strack (1979)
A discrete numerical model for granular assemblies. Géotechnique 29,Vol 1, pages 47-65

EA-Pfähle Recommendations on Pilling (20014)
German Geotechnical Society. Ernst & Sohn, Berlin, Germany. ISBN 978-3-433-03018-9

Ezzein and Bathurst (2011)
A transparent sand for Geotechnical Laboratory Modeling. Geotechnical Testing Journal, Vol 34, Issue 6. ATSM USA

Fink und Supp (2008)
Experimentelle und rechnerische Untersuchungen zum Tragverhalten des Spinnankers in rolligem und bindigem Boden. Masterarbeit: Technische Universität Graz, Institut für Bodenemchanik und Grundbau

Gaich A. (2001)
Panoramic Vision for Geotechnical Analyses in Tunnelling Dissertation Technische Universität Graz, Österreich. Institut für Felsmechanik und Tunnelbau Gruppe Geotechnik Graz, Österreich

Gavin and Gallagher (2005)
Development of Shaft Friction on Driven Piles in Sand and Clay Geotechnical Society of Civil Engineering of Ireland

Ghetta, Koler and Zangerl (2009)
Forschungsbericht (Endbericht der experimentellen Untersuchungen): Überprüfung der Einsatzmöglichkeiten von Bodenankern (Spinnanker) im Schutzbereich (Naturgefahren), vergleichende Evaluierung und Optimierung.

Hainbüchner 2001
Vergleich von analytischen Berechnungsverfahren mit den Verfahren der Distinkten Element Methode bei geotechnischen Anwendungen. Master thesis at the Institute of Soil Mechanics and Foundationengineering, University of Essen, Germany

Halsegger (2004)
Experimentelle und numerische Untersuchungen zur geführten Senkkastenbauweise unter besonderer
Berücksichtigung des Eindringvorganges der Schneide und der Risiken des Verfahrens. Dissertation TU Graz, Institut für Bodenmechanik und Grundbau

Hanna and Afram (1986)
Pullout capacity of Single Batter Piles in Sand. Canadian Geotechnical Journal, Vol 23, No 3, 1986

Henke (2008)
Herstellungseinflüsse aus Pfahlrammungen im Kaimauerbau. Veröffentlichung des Institutes für Geotechnik und Baubetrieb. Heft 18, TUHH

Henke (2013)
Untersuchungen zur Pfropfenbildung infolge der Installation offener

Profile in granularen Böden, Habilitation. Veröffentlichung des Institutes für Geotechnik und Baubetrieb. Heft 29, TUHH

Herold and Vollmert (2008)
Kombination von Vernagelung und Geokunststoffen zur Sicherung von Lockergesteinsböschungen.
In Bautechnik 85 (2008), Heft 6: 420-424. Wilhelm Ernst & Sohn. Germany: Berlin.

Herten (1999)
Räumlicher Erddruck auf Schachtbauwewrke in Abhängikeit von der Wandverformung. Bergische Universität – Gesamthochschule Wuppertal – Fachbereich Bauingenieurwesen, Shaker Verlag GmbH, S 113-118

Hird and Guymer (2010)
Physical of pile penetration in clay using transparent soil and particle image velocimetry. Géotechnique,Volume 60, Issue 2, pages121 –132

Iskander (2010)
M. Iskander, Modelling with Transparent Soils. Springer-Verlag Berlin Heidelberg, 2010, ISBN 978-3-642-02500-6

Itasca (2008, 2005)
PFC^{3D} – Particle Flow Code in 3 Dimensions,
Manual Itasca Consulting Group Inc., Minneapolis, Minnsota,55401 USA

Iten (2011)
Novel Applications of Distributed Fiber-optic Sensing in Geotechnical Engineering. Dissertation at ETH Zurich, Switzerland

Jakob and Konietzky (2012)
Partikelmethoden – Eine Übersicht. TU Bergakademie Freiberg, Institut für Geotechnik.

Jardine (1991)
The cyclic behavior of offshore piles. Blackie and Son, Glasgow

Jardine et al. (2005)
ICP Design Methods For Driven Piles In Sands And Clay. Imperial College London. Thomas Telford books, London, UK. ISBN: 978-0-7277-3272-9

Jardine et al. 1993
Friction Coefficients for Piles in Sands and Silts. In: Proceedings of the International Confernece on Offshore Site Investigation and Foundation Behaviour. Society for Underwater Technology. Vol. 28, 227 – 244

Jelinek and Ostermayer (1964)
Zur Tragfähigkeit von von Zugpfählen. Felsmechanik und Ingenieursgeologie. Vol. 2, No 3

König (2008)
Zur zeitlichen Traglastentwicklung von Pfählen und der nachträglichen Erweiterung bestehender
Pfahlgründungen. Veröffentlichung des Institutes für Geotechnik und Baubetrieb. Heft 17, TUHH

Körner (1986)
Designing with Geosynthetics. USA: Englewood Cliffs, N. J.: Prentice-Hall (1986)

Lackner (2012)
Prestressed reinforced soil – Concept, investigations and recommendations. Dissertation TU Graz, Institut für Bodenmechanik und Grundbau

Lehane and White (2005)
Lateral stress changes and shaft friction for model displacement piles in sand
Canadian Geotechnical Journal 42, pages 1039-1052

Lehane et al. (1993)
Mechanisms of shaft friction in sand from instrumented pile tests. In: Journal of Geotechnical Engineering, Vol. 119, ASCE, 19 – 35

Lehane et al. (1993)
Mechanisms of Shaft Friction in Sand from Instrumented Pile Tests. Journal of Geotechnical Engineering Vol 119, No 1 pages 19-35

Lehane, Gaudin and Schneider (2005)
Scale effects on tension capacity for rough piles buried in dense sand. Ge´otechnique 55, No. 10, 709-719

Lenzi (2009)
Untersuchungen von mit Pfählen gesicherten Rutschhängen mit der Diskreten Elementmethode. Dissertation, Fakultät für Bauingenierwissenschaften, Technische Universität Graz

Lienhart et al. (2013)
Deformation monitoring of flood prevention dams using geodetic and fibre optic measurements techniques. 6th Conference on Structural Health Monitoring of Intelligent Infrastructure, Hong Kong, China Proceeding, 8 Seiten

Lienhart, Lackner, Supp and Marte (2013)
Evaluation of State of the Art Methods for Surface Monitoring of Earth Filled Dams. 2nd Joint International Symposium on Deformation Measurements, Nottingham, England Proceeding, 9 Seiten

Linder (1977)
Zum Eindring- und Tragverhalten von Pfählen in Sand. Dissertation, Berlin

Liu and Iskander (2009)
Speckle photography for measuring 3-D deformation inside a transparent soil model. Proceedings of the 17th International Conference on Soil Mechanics and Geotechnical Engineering (Volumes 1, 2, 3 and 4) DOI10.3233/978-1-60750-031-5-498

Lüking (2010)
Tragverhalten von offenen Verdrängungspfählen unter Berücksichtigung der Propfenbildung in nichtbindigen Böden. Schriftenreihe Geotechnik, Universität Kassel, Heft23. ISBN 978-3-86219-046-1

Mannheimer und Oswald (1993)
Development of transparent porous media with permeability and porosities comparable to soils, aquifers and petroleum reservoirs. In: Groundwater 31 (5),1993,. 781-788

Marandi and Karimzadeh (2009)
Analysis of the Effect of Pile Skin Resistance Verses Pile Diameter Based on Experimental Research American Journal of Applied Sciences;2009, Vol. 6 Issue 1, p114

Martak and Breit (2014)
Prüfung und Bemessung von Verankerungen (Verpressanker, Verpresspfähle, Nägel) gemäß ÖNORM B
1997-1-1:2013. Proceeding of the 29 CVK-colloquium, Graz, Austria

Marte et al. (2014)
Böschungsbruch Großversuche - begleitet durch ein intensives Messprogramm: In: Geomechanics and Tunneling. Messen in der Geotechnik. Mitteilung des Instituts für Grundbau und Bodenmechanik, Technische Universität Braunschweig, Deutschland, 187 – 204. 2014, Heft 98

Marte, Supp and Lienhart (2014)
Böschungsbruch Großversuche - begleitet durch ein intensives Messprogramm . Messen in der Geotechnik, Braunschweig, Deutschland. Tagungshandbuch, S. 187 – 204

Mayrhofer, Oberhofer, Deutinger, Zangerl, Ghetta, Katzenbach, Leppla, Semprich, Supp, Kolymbas and Breymann(2010)
Der Spinnanker als neuartiges Verankerungssystem. In: Vorträge zum 17. Darmstädter Geotechnik-Kolloquium am 18. März 2010. Mitteilungen des Institutes und der Versuchsanstalt für Geotechnik der Technischen Universität Darmstadt, März 2010, 139 – 152, Heft 86

Meyerhof (1973)
Uplift resistance of inclined anchors and piles. Proceeding of the 8th Conference on Soil Mechanics and Foundation Engineering, Moscow, 2 (1), pages 167-172

Meyerhof and Adams (1968)
The Ultimate Uplift Capacity of Foundations. Canadian Geoetchnical Journal, Vol 5.

Nürnberger (2011)
Korrosionstechnische Beurteilung des "DYWI Drill Hohlstab" Systems für Bodennägel, Pfähle Erdanker. Report

Okonek (2014)
Test report of pull-out tests in the United Arab Emirates, Mardinat Zayed.

ÖNORM B 1997-1-1 (2013)
Eurocode 7: Eurocode 7: Geotechnical design – Part 1: General rules – Nationalwpecifications concerning ÖNORM EN 1997-1 and national supplements. Vienna, Austrian Standards Institute, 2013.

ÖNORM B 4440 (2001)
Geotechnical engineering (foundation engineering) - Large diameter bored piles - Bearing capacity Vienna Austrian Standards Institute, 2011.

ÖNORM EN 12699 (2013)
Execution of special geotechnical work - Displacement piles. Vienna Austrian Standards Institute, 2013.

ÖNORM EN 14199 (2013)
Execution of special geotechnical work – Micropiles. Vienna Austrian Standards Institute, 2013.

ÖNORM EN 14490 (2010)
Execution of special geotechnical works - Soil nailing. Vienna Austrian Standards Institute, 2010.

ÖNORM EN 1537 (2000)
Execution of special geotechnical work - Ground anchors. Vienna Austrian Standards Institute, 2000.

ÖNORM EN 1993-5 (2012)
Eurocode 3 - Design of steel structures - Part 5: Piling (consolidated version)
Vienna Austrian Standards Institute, 2013.

ÖNORM EN 1997-1 (2004, +AC:2009)
Eurocode 7: Geotechnical design - Part 1: General rules (prEN 1997-1:2004, not included)Vienna Austrian Standards Institute, 2004.

Ostermayer (1975)
Construction, carrying behaviour and creep characteristics of ground anchors. - In: Proc. of the Conf. on Diaphragm Walls and Anchorages, London, 18.-20. 9. 1974. - London: Inst. of Givil Engineers 1975. S.141-151.

Ostermayer und Werner (1972)
Neue Erkenntnisse und Entwicklungen in der Verankerungstechnik. In: Vorträge der Baugrundtagung 1972 in Stuttgart. Deutsche Gesellschaft für Erd- und Grundbau, 235-262

Paulos (1989)
Pile behaviour – therory and application. Géotechnique 39,Vol 3, pages365-415

Pohl (2005)
Modellierung von granularen Böden und biegsamen Bauwerken mit Hilfe der Diskreten Elementmethode am Beispiel einer eingebetteten Spundwand
Bergische Universität – Gesamthochschule Wuppertal – Fachbereich Bauingenieurwesen. Shaker Verlag GmbH, S 32-52

Poprask (2014)
Experimentelle Untersuchungen zur Visualisierung von Boden-Bauwerksinteraktionen mit Hilfe synthetischem, transparentem Boden. Masterarbeit: Technische Universität Graz, Institut für Bodenemchanik und Grundbau

Quarg-Vonscheidt (2010)
Berechnungsmodell für die Tragfähigkeit und das Gruppenverhalten von Zugpfählen. Bergische Universität, Gesamthochschule Wuppertal, Fachbereich Bauingenieurwesen. Heft 23, ISBN 3-8265-8259-4

Raffel et al. (2007)
Particle Image Velocimetry. Second Edition Springer Berlin Heidelberg New York, 2007, ISBN 978-3-540-72307-3

Ries (2014)
Pfahlgruppeneffekte bei vorgefertigten Vollverdrängungspfählen in Sanden. 33. Baugrundtagung: Forum für junge Geotechnik-Ingenieure – Beiträge der Spezialsitzung, Berlin, S. 87-96.

Rudolf (2005)
Beanspruchung und Verformung von Gründungskonstruktionen auf Pfahlrosten und Pfahlgruppen unter Berücksichtigung des Teilsicherheitskonzeptes. Schriftenreihe Geotechnik Universität Kassel, Heft 17

Semprich et al. (2012)
Entwurf und Ausführung effektiver Abdichtungsmaßnahmen für den Stauraum der Wasserkraftwerke Gössendorf und Kalsdorf bei Graz. Beiträge zum 27. Christian Veder Kolloquium: Planung und Ausführung von Abdichtungsmaßnahmen in der Geotechnik, Herausgeber: Gruppe Geotechnik Graz, ÖsterreichTagungshandbuch, S 225 -240

Siemens and Peters (2011)
Analysis of a drawdown test displaying the use of transparent soil in unsaturated flow applications.Unsaterated Soils – Alonso & Gens (eds). Taylor & Francis Group, London

Stahlwerk Annahütte (2011)
Allgemein bauaufsichtliche Zulassung. Ankerstab St 900/1100 mit Gewinderippen. Nenndurchmesser 15und 20 mm.Deutsches Institut für Bautechnik, Berlin 2011

Steger (2010)
Experimental and numerical investigations of unsaturated soils with application to tunnelling under compressed air. Dissertation TU Graz, Institut für Bodenmechanik und Grundbau

Supp and Semprich (2010)
Spinnanker – ein neues Konstruktionselement. In: Handbuch 7. Kolloquium Bauen in Boden und Fels. Technische Akademie Esslingen. 259 – 269

Supp und Marte (2014)
Spideranchor Netting - full scale experiment, application and slope stability discussion. In: Geomechanics and Tunneling. Ernst und Sohn. Heft 4 2014, 317 – 327

Supp und Semprich (2012)
Spideranchor - an innovative technology for slope stabilization. In: Proceedings of the 11th International and 2nd North American Symposium on Landslides. Taylor & Francis Group, London, 2012, 1991-1995

Supp et al. (2014)
A transparent soil model for visualizing soil-structure interactions during pull- out tests of small diameter steel rods. In: 16th International Conference on Experimental Mechanics. Cambridge, UK. CD – 3 p

Supp, Poprask and Marte (2014)
A transparent soil model for visualizing soil-structure interactions during pull-out tests of small diameter steel rods. Proceedings of the 16th International Conference on Experimental Mechanics, Cambridge, UK

Supp, Semprich, Breymann, Deutinger, Ghetta, Katzenbach, Kolymbas, Leppla, Mayrhofer and Zangerl (2010)
Spideranchor – a new constructional element . 14th Danube-European Conference on Geotechnical Engineering, Bratislava, Slowakei. Herausgeber: Frankovska, J.: Hulla, J.; Ondrasik, M.; Turcek, P. Proceeding, S 212

Vitton and Hryciw (1991)
Sand-Anchor Interaction in Anchored Geosynthetic Systems , Geotechnical Engineering Congress 1991, ASCE, Vol. 2, Boulder, CO, Proceeding, S. 958-969.

Wernick (1978)
Tragfähigkeit zylindrischer Anker in Sand unter Berücksichtigung des Dilatanzverhaltens Veröffentlichungen des Institutes für Bodenmechanik und Felsmechanik der Universität Fridericiana in Karlsruhe. Heft 75.

White and Bolton (2004)
Displacement and strain paths during plane-strain model pile installation in sand. Géotechnique,Volume 54, Issue 6, pages375 – 397

White and Lehane (2004)
Friction fatigue on displacement piles in sand. Ge´otechnique 54, No. 10, 645–658

White et al. 2005
The Influenceof effecitve Area Ratio on Shaft Friction of Displacement Piles in Sand. In: Proceedings of the Internatiopnal Symposium of in Offshore Geotechnics. Balkema, Rotterdam. 741 -474

Witzel (2004)
Zur Tragfähigkeit und Gebrauchstauglichkeit von vorgefertigten Verdrängungspfählen in bindigen und nichtbindigen Böden. Schriftenreihe Geotechnik Universität Kassel, Heft 15

Zhao (2007)
Development and assessment of transparent soil and particle image

velocimetry in dynamic soil structure interaction. Dissertation at University of Science and Technology, Missouri USA, 2007.

Zöhrer (2006)
Laboratory Experiments and Numerical Modelling of Cone Penetration Tests into various Martian Soil Analogue Materials. Dissertation TU Graz, Institutfür Bodenmechanik und Grundbau